UNIVERSITAT DE BARCELONA

# Tuning the composition and dimensionality of transition metal carbides as possible catalysts for green chemistry related reactions

Martí López Berbel

Tesi Doctoral

Química Teòrica i Modelització Computacional

---

# Tuning the composition and dimensionality of transition metal carbides as possible catalysts for green chemistry related reactions

---

**Martí López Berbel**
Universitat de Barcelona

Dirigida per:

**Prof. Francesc Illas i Riera**
Universitat de Barcelona

**Dr. Francesc Viñes Solana**
Universitat de Barcelona

Tutora:

**Prof. Carme Sousa Romero**
Universitat de Barcelona


UNIVERSITAT DE
BARCELONA

December 2022

# Abstract

Transition metal carbides (TMCs) have acquired a wide potential as a green chemistry catalysts. Their relatively high abundance and their catalytic performance makes them great candidates to replace scarce and pollutant catalysts as Pt, as well as promising catalysts to generate and store clean fuels. Moreover, a new synthesised family of 2D materials called MXenes, derived from the TMCs, has attracted an increasing attention due to its vast reactivity and potential applications. This thesis aims to evaluate possible applications for the TMCs and MXenes to face nowadays climate and energy problematics, as the $CO_2$ atmosphere mitigation or clean hydrogen production for its usage as a fuel, through density functional theory calculations.

First, we explore the $CO_2$ capture, storage, and activation potential of doped TMCs using TiC as a textbook. When the TiC is doped with early transition metals the electron transfer produced upon the $CO_2$ adsorption appear to be the leading feature, as more electrons where transferred, higher the adsorption energy. However, when replacing the Ti for a variety of elements across all the periodic table this tight relation is lost. Instead we observed that the main effect does not come from the electronic structure perturbations but from the distortion that the dopant generates into the surface atomic structure.

The MXenes are evaluated regarding its potential for hydrogen related reactions both in gas-solyd systems and electrochemical pro-

cesses. In gas-solid systems, $W_2N$, $Fe_2C$ and $Mo_2C$ presented the necessary intermediate hydrogen coverage under current reaction conditions to be promising catalyst candidates for further hydrogenation reactions, while the rest of the MXenes where fully passivated. In electrochemical systems, we also studied systematically the surface coverage of the MXenes in aqueous solution. We detailed how to construct the so-called Pourbaix diagrams, useful tool for a proper surface analysis, and show how the most thermodynamic favourable surface in a gas-solid environment could not be the most stable surface under electrochemical conditions. Finally, based on the construction of theoretical Tafel plots, we disclosed the mechanism of the Hydrogen Evolution Reaction (HER) over $V_2C$.

Dedicada als meus àvis, en Juan, la Juana Maria, l'Antoni i la Montserrat.

# Agraïments

M'agradaria començar per donar les gràcies a en Francesc Illas i en Francesc Viñes, els meus dos directors de Tesis, i a la Carme Sousa, la meva tutora, sense els quals res de tot això hagués estat possible. Tot va començar amb una encaixada de mans i un compromís, el resultat del qual és el que es pot llegir en aquesta Tesi. Moltes gràcies per la confiança, la paciència i l'energia dedicada a formar-me i guiar-me durant aquests anys. En especial gràcies a en Francesc Viñes per acompanyar-me de ben a prop durant les primeres passes del doctorat i introduir-me al món de la investigació i a en Francesc Illas per ajudar-me a aconseguir una beca quan no semblava gens fàcil. També, a tots dos, agrair l'oportunitat de poder enriquir aquesta tesi col·laborant amb altres professors i universitats d'arreu. Són infinites les coses que he après de vosaltres.

També vull fer extensiva la meva gratitud a totes aquelles persones amb qui he compartit parts d'aquest camí. Als meus companys de despatx, el Joan, l'Anabel, el Jaunjo, el Raul Morales i l'Oriol. Les memòries forjades al 425 les guardaré per sempre com un tresor. Debats infinits, partides d'escacs, torneigs de battlegrounds i les millors adaptacions de nadales que s'hagin compost mai al departament són només alguns dels records que m'emporto. A la Lorena, que després d'un any de màster molt dur em va donar l'empenta necessària per començar aquest viatge. A la resta de companys, ara ja amics, del departament: Cristina, Pablo Blanco, Ignasi, Ramon, Marc, Pablo

Lozano, Genís, Roger, Dani i Raul Santiago. Entre Ping-Pongs, birres i cafès, he trobat un suport immillorable per segur avançant cada dia. M'heu fet arribar allà on jo sol no hagués pogut mai. També a les últimes incorporacions del departament; Pablo Castro, Eleonora, Riccardo i Jon. Un especial agraïment a la Berta. Vam començar junts el 2012 a l'M2 i acabem junts deu anys més tard. Gràcies per ser-hi, he sigut molt afortunat de poder caminar al teu costat. També als tècnics de l'IQTC, en Jordi i la Irene per fer possible la part tècnica de la feina i solucionar tots i cada un dels problemes que m'han sorgit, que no n'han sigut pocs.

I must also thank the groups and researchers that have hosted me during my visits to University College Cork and to Duisburg-Essen University. In particular, I am grateful to Dr. Michael Nolan and to Dr. Kai S. Exner for giving me the chance of working with them and for teaching me so many new things. Within those groups, I must also thank Stephen, Samad, Shohreh, Amir, and Maksim for welcome me and make my visits unforgettable. También para Nico, con quien tuve la suerte de poder trabajar y aprender durante su visita en Barcelona.

Gràcies, Julián pels dinars a casa teva, per presentar-me a la Maria i la Marta, i fer-me retrobar amb l'Hèctor. Juntament amb la Dèlia meu brindat petits oasis de complicitat, sempre acompanyats d'un bon vi, on he pogut desconnectar, alleugerir les pors i pressions internes i agafar força per continuar. Aquests agraïments no serien complets sense mencionar als companys de la carrera. La vida ens ha anat portant per camins ben diferents, però sempre sabeu trobar moments per retrobar-nos. Gràcies per la vostra amistat.

Un agraïment des de la distància per a en Sotiris i en Xabi. Que tot i separar-nos després del màster per fer el doctorat ens hem continuat

animant i fent costat a durant tots aquests anys. Així mateix, a les companyes de doctorandes en lluita per ensenyar-me tot el que es pot aconseguir quan lluitem organitzades.

Agrair a tot el Reducte Hortenc i Consejo de Sabios per tot el que hem viscut plegats; Arce, Aleix, Barreda, Blai, Grifo, Iu, Javi, Mario, Nil, Xexi, Murillo, Zarpas i Rubén. Créixer i gaudir amb vosaltres durant les rutes de barri, els vespres de bugui, les visites a l'Almodobar, el Dorado i el bar Viu o aconseguir sobreviure per Festes d'Horta em fan sentir la persona més afortunada del món. M'agradaria agrair de manera especial als companys del zoo, el Marc De Juan, el Marc Domingo, la Queralt i l'Oriol. Gràcies per suportar els meus constants "ruidos de padre" i les descripcions detallades de totes les tasques inútils que pretenc fer cada dia. Gràcies per escoltar-me i fer-me sentir tan bé a casa. Han sigut els millors anys de la meva vida i espero que puguem continuar fruint-ne molts més.

També per a l'Álvaro, per alimentar i complementar els plans esbojarrats que portem fent des de fa mil anys i que ben segur continuarem fent en un futur. Són moltes les memòries que em fan morir de riure només de recordar i m'han animat durant aquests anys. A l'Anna i l'Elena, dues de les dones més fortes que he conegut mai. El que he viscut, après i patit a SETEM no hagués estat suportable sense vosaltres. Gràcies per escoltar-me en tot moment, m'heu ajudat a no defallir. També a la banda simfònica de roquetes, als membres de big funk i els TuBieja. Tocar amb vosaltres transformava completament els meus dies, no hi ha millor remei per apujar l'estat d'ànim.

Als companys del Rosario, per acollir-me des del primer dia i poder desfogar-me amb ells de tot i tothom. Sempre ens trobarem al golf. També als companys de l'equip de Lacrosse i en especial al Cassano, al Graham, al Chauncey, al Pol, al Yannick, a la Bex, a l'Arne, al

Tote, al Félix, a la Clara i al Gabo. También para Angie. Gracias por sostener-me y aportar optimismo en esta travesía. Moreover, I cannot forget Robert and Niles together with rest the Dortmund Wolverines lacrosse team for hosting me as one of their own during my days in Essen.

Finalment, a tota la meva família, tiets, tietes, cosins, cosines, avis i àvies, per tot el suport, la paciència i l'estima. Especialment als meus pares, l'Eulàlia i en Joan Andreu, i als meus germans, la Berta i en Roger. Gràcies per fer-me sempre costat incondicionalment. No puc acabar sense fer una menció especial a la meva àvia Montserrat, a qui li dedico aquesta tesi.

# Contents

# List of Figures

# List of Tables

# List of Abbreviations

***bcc*** Body Centered Cubic

**BO** Born-Oppenheimer

**CCS** $CO_2$ Caputure and Storage

**CCU** $CO_2$ Caputure and Usage

**CHE** Computational Hydrogen Electrode

**CI-NEB** Climbing Image Nudged Elastic Band

**DFT** Density Functional Theory

**DORI** Density Overlap Regions Indicator

**DOS** Density Of States

***fcc*** Face Centered Cubic

**FS** Final State

**GDP** Gross Domestic Product

**GGA** Generalized Gradient Approximation

***hcp*** Hexagonal Close Packed

**HER** Hydrogen Evolution Reaction

**HF** Hartree-Fock

**IS** Initial State

**KS** Kohn-Sham

**LDA** Local Density Approximation

**ML** MonoLayer

**NEB** Nudged Elastic Band

**NCI** Non-Covalent Interaction

**OER** Oxygen Evolution Reaction

**ORR** Oxygen Reduction Reaction

**PAW** Projected Augmented Wave

**PBE** Perdew-Burke-Ernzerhof

**PES** Potential Energy Surface

**rds** Rate Determinant Step

**RHE** Reversible Hydrogen Electrode

**RI** Reaction intermediate

**RPA** Random Phase Approximation

**RWGS** Reverse Water-Gas Shift

**SHE** Standard Hydrogen Electrode

**TiC** Titanium Carbide

**TMC** Transition Metal Carbide

**TPSS** Tao-Perdew-Staroverov-Scuseria

**TS** Transition State

**TST** Transition State Theory

**VASP** Vienna Ab Initio Simulation Program

**vdW** van der Waals

**VH** Volmer-Heyrovsky

**VT** Volmer-Tafel

**WGS** Water-Gas Shift

**ZPE** Zero Point Energy

# List of Symbols

| Symbol | Description |
|---|---|
| $B_{0,x}$ | Rotational constant |
| $\boldsymbol{a}, \boldsymbol{b}, \boldsymbol{k}$ | 3D spatial vectors |
| $E[\rho]$ | Energy density functional |
| $E_{xc}[\rho]$ | Exchange-correlation energy functional |
| $E_a$ | Activation energy |
| $F_{HK}[\rho]$ | Hohenberg-Kohn functional |
| $\Gamma_{act}$ | Density of surface sites |
| $\hat{H}$ | Hamiltonian operator |
| $h$ | Planck constant |
| $\hbar$ | Reduced Planck constant |
| $I^{spin}$ | Spin degeneracy of the electronic ground-state |
| $J[\rho]$ | Electronic coulomb repulsion interaction functional |
| $j_0$ | Exchange current density |
| $k_B$ | Boltzmann constant |

| Symbol | Description |
|---|---|
| $\mathrm{N_A}$ | Avogadro constant |
| $p^\circ$ | Standard pressure |
| $Q$ | Partition function |
| $U, \eta$ | Overpotential |
| S | Sticking coefficient |
| $\mathrm{T}[\rho]$ | Kinetic energy functional |
| $\hat{\mathrm{T}}_x$ | Kinetic energy operator |
| $\hat{T}$ | Translational operator |
| $\mathrm{V}_{ee}[\rho]$ | Electronic potential functional |
| $\hat{\mathrm{V}}_x$ | Potential energy operator |
| $\mathrm{V_c}$ | Bravais cell volume |
| $\theta_{rot}$ | Rotational temperature |
| $\theta_x$ | Coverage |
| $\sigma^{sym}$ | Classical symetry number |
| $\mu_x$ | Chemical potential |
| $e$ | Elementary electron charge |
| $\epsilon$ | Non-integer electron transfer |
| $\nu$ | stochiometric number |
| $\Psi$ | Wavefuntion |
| $\psi$ | Monoelectronic wavefuntion |
| $\psi^{KS}$ | Kohn-Sham monoelectronic wavefuntion |
| $\boldsymbol{R}, \boldsymbol{r}$ | 3D spatial coordinates |
| $xc$ | Exchange and Correlation |

Chapter 1:

# Introduction

## 1.1 Motivation and Goals

The challenging transition towards a sustainable energy model has become an urgent need. From the announcement of the Kyoto Protocol in 1997 to control the $CO_2$ emissions and the greenhouse effects we have been done small steps towards such energy and social transition. New policies derived after several United Nations agreements are being coming out from the past decade and many strategies and energy sources have been purposed to eventually phase out fossil fuels, tackle the climate change, and solve the incoming energy shortage but we remain far from our global objectives.[1–4]

Among all the possible strategies and fields rapidly developed for such aim, Transition Metal Carbides (TMCs) and MXenes, 2D materials highly related with the TMCs, have shown a great potential, playing a key role in a variety of promising applications. Their wide versatility makes them a potential candidate as catalysers for many gas-phase reactions, such CO oxidation,[5] water-gas shift (WGS),[6,7] $N_2$ fixation[8,9] or dehydrogenation,[10] and for energy storage purposes[11–13] as well as antimicrobial activity against different strains and ecotoxicity.[14] Moreover, TMCs have been successfully used as bio-sensors for detection of organophosphates pesticides[15] and MXenes are being explored for oncological

applications, both cancer therapy and cancer imaging.[16]

However, from all this extensive variety of applications we focused in two main applications directly linked with the climate emergency and energy shortage problematic. TMCs and MXenes have also exhibit potential for Carbon Capture and Storage (CCS)[17] and Carbon Capture and Usage (CCU)[18] technologies, aiming to mitigate the most direct impact of the climate change, as the global warming,[19] or the rise of the sea acidity,[20] through the direct reduction of the atmospheric $CO_2$, or as a catalysts of electrocatalytic reactions such as the Hydrogen Evolution Reaction (HER),[11,21,22] Oxygen Evolution Reaction (OER),[23] or Oxygen Reduction Reaction (ORR), and water splitting[24,25] key processes for the development of the hydrogen industry and its usage as a clean energy source, aiming to help with the energy shortage without releasing greenhouse gases. Consequently, the research presented in this thesis aim to explore the CCS and CCU potential of the well-known TMCs family and hydrogen related reactions as the heterogeneously catalyzed Hydrogen formation or the HER on the new-synthesised MXenes.

The first part aims at exploring the $CO_2$ adsorption over doped Titanium Carbide (TiC); the specific goals are to:

- Determine the geometric and electronic impact produced by the introduction of a doping agent on the TiC structure.
- Unravel the mechanism of the $CO_2$ adsorption and activation on the doped TiC.
- Explore its capabilities as a CCS and CCU material.
- Rationalize the correlation between the $CO_2$ adsorption energy and the electronic and physical properties involved in the mentioned adsorption.

The second part aims at exploring hydrogen related reactions over MXenes both involving both gas-phase and electrocatalytical processes.

Regarding the gas-phase systems; the main goals are to:

- Understand the $H_2$ adsorption and dissociation over pristine MXenes for hydrogen storage and further hydrogenation purposes on gas-phase systems.
- Rationalize the correlation between the H and $H_2$ adsorptions energy and the electronic and physical properties involved in the mentioned adsorption.
- Show the construction and application of the newly kinetic phase diagrams and their close relation with the well-known thermodynamic phase diagrams.

And regarding the electrocatalytical systems; to:

- Remark the importance of knowing the surface structure of an electrode under specific reaction conditions. Showing how to construct and evaluate a Pourbaix diagram.
- Determine the most stable surface under HER conditions of four 2D materials from the newly discovered MXene family: $Mo_2C$, $Ti_2C$, $Ti_3C_2$, and $V_2C$.
- Explore the capabilities of the functionalized MXene $V_2C$ as a HER catalysts. Determine if it is active for HER and if so, unravel the possible mechanism.
- Show and construct a computational Tafel plot, a proposed link to compare computational and experimental studies of electrochemical reactions, and test it specifically for HER over functionalized $V_2$.

## 1.2 Thesis Structure

The thesis has been organized in the following framework. The fundamentals of the computational tools and approaches employed in this research are explained

in Chapter 2. Starting with the Born-Oppenheimer (BO) approximation and the Schrodinger equation, the basics of Density Functional Theory (DFT), including the most typical functionals and corrections are covered. The goal of Chapter 3 is to provide a complete background for the modeling of the relevant systems. The gas-solid and electrochemical systems are the two system types taken into consideration in this dissertation.

The first section of the chapter discusses how to model gas-solid systems for heterogeneous catlysis, how to obtain the energetic descriptors of total adsorption and Gibbs free energy, and how to find transition states and reaction intermediates after briefly outlining the significance of catalytical processes in the world of today. Sections 3.1.5 and 3.1.6 discuss how to convert DFT data to represent the most stable surfaces under appropriate $p-\mathrm{T}$ circumstances using the widely used formalism defined by Scheffler and Reuter, as well as how to get surface rate processes using Transition State Theory (TST). The second section of the chapter discusses the approximations required to represent an electrochemical environment. First, the Computational Hydrogen Electrode (CHE) is introduced for energetic adjustments, followed by instructions on how to build a Pourbaix Diagram, an analogous phase diagram for surface coverages that depends on pH and overpotential, $U$ instead of the preceding $p-\mathrm{T}$. Finally, a microkinetic analysis of a specific reaction is illustrated, with the goal of obtaining a computational Tafel plot, allowing comparison of computational processes with experimental studies.

Chapter 4 discusses the current problem of greenhouse gases, two of the primary methods utilized for $CO_2$ abatement, one of the key protagonists in this struggle, and analyzes the capacity of tunable TiC(001) for $CO_2$ adsorption and activation, as well as a rationalization of suitable descriptors for unrevealing its leading chemistry properties and further improving the screening potential for discovering prospective CCS and CCU bimetallic carbides candidates. The purpose of Chapter 5 is to highlight the adaptability of MXenes in Hydrogen-involving processes. First, the MXenes are presented, along with their

emergence and geometric and electrical properties. There is also a brief presentation on the overall ongoing work with MXenes. The parts that follow detail the hydrogen adsorption and dissociation, under heterogeneous catalysis considerations, a pedagogical explanation of the relevance of the Pourbaix Diagrams in electrocatalysis, and lastly a discussion of the mechanism of the HER, under the electrocatalytical regime. Finally, Chapter 6 contains the main conclusions of this thesis. The appendix contains the supporting information for all of the articles that have been published and are included in this work.

## References

[1] United Nations, *Kyoto Protoc. to United Nations Framew. Conv. Clim. Chang.*, 1997, (December).

[2] United Nations, *Copenhagen Accord*, 2009, (December).

[3] United Nations, *Paris Agreem.*, 2015, (December).

[4] United Nations, *Glas. Clim. Pact*, 2021, (November).

[5] Y. Meng, J.-x. Liang, C. Zhu, C.-q. Xu, and J. Li, 2022, **65**(5), 1303–1312.

[6] K. D. Sabnis, Y. Cui, M. C. Akatay, M. Shekhar, W. S. Lee, J. T. Miller, W. N. Delgass, and F. H. Ribeiro, *J. Catal.*, 2015, **331**, 162–171.

[7] J. Dong, Q. Fu, Z. Jiang, B. Mei, and X. Bao, *J. Am. Chem. Soc.*, 2018, **140**(42), 13808–13816.

[8] H. Wei, Q. Jiang, C. Ampelli, S. Chen, S. Perathoner, Y. Liu, and G. Centi, *ChemSusChem*, 2020, **13**(21), 5614–5619.

[9] J. D. Gouveia, á. Morales-García, F. Viñes, J. R. Gomes, and F. Illas, *ACS Catal.*, 2020, **10**(9), 5049–5056.

[10] J. Diao, M. Hu, Z. Lian, Z. Li, H. Zhang, F. Huang, B. Li, X. Wang, D. S. Su, and H. Liu, *ACS Catal.*, 2018, **8**(11), 10051–10057.

[11] Y. Zhong, X. Xia, F. Shi, J. Zhan, J. Tu, and H. J. Fan, may , 2016, **3**(5), 1500286.

[12] N. K. Chaudhari, H. Jin, B. Kim, D. San Baek, S. H. Joo, and K. Lee, *J. Mater. Chem. A*, 2017, **5**(47), 24564–24579.

[13] B. Anasori, M. R. Lukatskaya, and Y. Gogotsi, *Nat. Rev. Mater.*, 2017, **2**, 16098.

[14] A. Rozmysłowska-Wojciechowska, E. Karwowska, S. Poźniak, T. Wojciechowski, L. Chlubny, A. Olszyna, W. Ziemkowska, and A. M. Jastrzębska, *RSC Adv.*, 2019, **9**(8), 4092–4105.

[15] L. Zhou, X. Zhang, L. Ma, J. Gao, and Y. Jiang, *Biochem. Eng. J.*, 2017, **128**, 243–249.

[16] A. Sundaram, J. S. Ponraj, J. S. Ponraj, C. Wang, W. K. Peng, R. K. Manavalan, S. C. Dhanabalan, H. Zhang, and J. Gaspar, *J. Mater. Chem. B*, 2020, **8**(23), 4990–5013.

[17] S. Posada-Pérez, F. Viñes, P. J. Ramirez, A. B. Vidal, J. A. Rodriguez, and F. Illas, *Phys. Chem. Chem. Phys.*, 2014, **16**(28), 14912–14921.

[18] C. Kunkel, F. Viñes, and F. Illas, *Energy Environ. Sci.*, 2016, **9**(1), 141–144.

[19] P. M. Cox, R. A. Betts, C. D. Jones, and S. A. Spall, *Nature*, 2000, **408**, 184–187.

[20] S. C. Doney, V. J. Fabry, R. A. Feely, and J. A. Kleypas, *Ann. Rev. Mar. Sci.*, 2009, **1**, 169–192.

[21] W. F. Chen, J. T. Muckerman, and E. Fujita, *Chem. Commun.*, 2013, **49**(79), 8896–8909.

[22] W. F. Chen, C. H. Wang, K. Sasaki, N. Marinkovic, W. Xu, J. T. Muckerman, Y. Zhu, and R. R. Adzic, *Energy Environ. Sci.*, 2013, **6**(3), 943–951.

[23] M. Zubair, M. M. Ul Hassan, M. T. Mehran, M. M. Baig, S. Hussain, and F. Shahzad, *Int. J. Hydrogen Energy*, 2022, **47**(5), 2794–2818.

[24] K. Lee, A. Ishihara, S. Mitsushima, N. Kamiya, and K. I. Ota, *Electrochim. Acta*, 2004, **49**(21), 3479–3485.

[25] J. D. Gouveia, Á. Morales-García, F. Viñes, F. Illas, and J. R. Gomes, *Appl. Catal. B Environ.*, 2020, **260**, 118191.

Chapter 2:

# Methodological Background

The theoretical foundations, computational techniques, and analysis tools employed throughout the Thesis are described in the parts that follow in this Chapter. Therefore, just the theoretical framework is presented here; the simulation objects are not, but addressed in posterior chapters.

## 2.1 The Schrödinger Equation

In order to describe the physical properties of the nature at atomic and subatomic level, it is mandatory to apply a quantum mechanics treatment. Under such formalism, the time-independent Schrödinger equation is the linear partial differential equation that governs the description of such systems and is the fundament of all the *ab initio* wave function-based methods of calculus.

$$\hat{\mathrm{H}}\Psi(\boldsymbol{R},\boldsymbol{r}) = \mathrm{E}\Psi(\boldsymbol{R},\boldsymbol{r})\,, \tag{2.1}$$

where $\hat{\mathrm{H}}$ is the Hamiltonian operator, $\Psi(\boldsymbol{R},\boldsymbol{r})$ is the wavefunction of the system that depends on the position of the nuclei, $\boldsymbol{R}$, and the electrons, $\boldsymbol{r}$, of such system, and E is its total energy. The Hamiltonian operator contains both the kinetic energy operators of the nuclei, $\hat{\mathrm{T}}_N$, and of the electrons, $\hat{\mathrm{T}}_n$, and the potential energies, through the Coulomb operator, including the nuclei-nuclei, $\hat{\mathrm{V}}_N$, and

electron-electron, $\hat{\mathrm{V}}_n$, repulsions, and the nuclei-electron, $\hat{\mathrm{V}}_{Nn}$, attraction, see Eq. 2.2. Expressed in atomic units, the Hamiltonian of a system of $N$ nuclei and $n$ electrons is given by:

$$\hat{\mathrm{H}} = \hat{\mathrm{T}}_N + \hat{\mathrm{T}}_n + \hat{\mathrm{V}}_N + \hat{\mathrm{V}}_n + \hat{\mathrm{V}}_{Nn}\,, \tag{2.2}$$

$$-\frac{1}{2}\sum_{A=1}^{N}\frac{\nabla_i^2}{m_A} - \frac{1}{2}\sum_{i=1}^{n}\nabla_i^2 - \sum_{A=1}^{N}\sum_{B>A}^{N}\frac{Z_A Z_B}{R_{AB}} - \sum_{i=1}^{n}\sum_{j>i}^{n}\frac{1}{R_{ij}} - \sum_{i=1}^{n}\sum_{A=1}^{N}\frac{Z_A}{R_{iA}}\,, \tag{2.3}$$

where $\nabla_A^2$ and $\nabla_i^2$ are the Laplace operator of the $N$ nuclei particles and $n$ electrons coordinates, $m_A$ and $Z_A$ are the mass and the atomic number of the $A$ nuclei, $R_{AB}$ is the distance between $A$ and $B$ nuclei, $r_{ij}$ and $r_{iA}$ are the distance between electron $i$ and $j$, and $r_{iA}$ the distance between electron $i$ and nuclei $A$, respectively. Given the complexity to solve the time-independent Schrödinger equation, the Born-Oppenheimer (BO) approximation[1] is commonly used. It states that due to the difference of mass between the electrons and the nuclei particles, the velocity of the electrons is considerably higher than the velocity of the nuclei, thus it is assumed than the electron motion responds instantly to the nuclei motion, and hence they can be treated decoupled. This allows us to separate the total wavefunction, into the electronic and the nucleic wavefunctions, $\Psi_e(\boldsymbol{r})$ and $\Psi_{nuc}(\boldsymbol{R})$, respectively, and to solve the Schrödinger equation in two steps.

$$\Psi(\boldsymbol{R},\boldsymbol{r}) = \Psi_{nuc}(\boldsymbol{R})\Psi_e(\boldsymbol{r})\,. \tag{2.4}$$

The first step is to solve the electronic Hamiltonian,

$$\hat{\mathrm{H}}_e\Psi_e(\boldsymbol{r}) = \mathrm{E}_e\Psi_e(\boldsymbol{r})\,, \tag{2.5}$$

where $\hat{\mathrm{H}}_e$ is the electronic Hamiltonian operator and $\mathrm{E}_e$ is the electronic energy. Note that within the BO approximation, with the nuclei and electrons motion

decoupled, we can solve the Schrödinger equation of a fixed nuclei configuration, $\hat{\mathrm{T}}_N = 0$, so the nuclei coordinates are taken as a parameter, $\mathrm{V}_N$ is a constant, and the wavefunction depends only on the electron coordinates.

$$\hat{\mathrm{H}}_e = \hat{\mathrm{T}}_n + \hat{\mathrm{V}}_n + \hat{\mathrm{V}}_{Nn} + \mathrm{V}_N \,. \tag{2.6}$$

The so-called potential energy surface (PES), $\mathrm{E}_e(\boldsymbol{R})$, can be obtained by incrementally changing the $\boldsymbol{R}$ coordinates and repeatedly solving the Schrödinger equation. Overall, the PES permits us evaluate the total energy of the system as a function of their atomic configuration and hence find the relevant conformations of any system. For instance, the PES minima correspond to stable states (being the PES absolute minima the ground-state of such system) or its first-order saddle points are associated with transition states as they are the direct path between two stable states. Finally, the second step of the BO approximation is to introduce the nuclei motion to the electronic energy to obtain the total energy of the system.

$$(\hat{\mathrm{T}}_N + \mathrm{E}_e(\boldsymbol{R}))\Psi_{nuc}(\boldsymbol{R}) = \mathrm{E}\Psi_{nuc}(\boldsymbol{R}) \,. \tag{2.7}$$

However, the treatment of the $\hat{\mathrm{H}}_e$ is very challenging. Since there is not an analytical solution for systems with more than two electrons due to the electron-electron interactions, two main families of numerical *ab initio* methods are commonly implemented to solve such setback, wavefunction methods, commonly referred as Hartree-Fock (HF) methods as it was the first model and the base for almost all the upcoming methods of the family, and density functional theory (DFT) methods. Therefore, the fundamental premise is to replace such exact electron-electron interactions with a one-electron problem in an approximate field representing the rest of the electrons. Briefly explained, in HF methods, the simplest detailed wavefunction of a given system is described as linear combination of Hartree produts,

$$\Psi_{\mathrm{HF}} = \frac{1}{\sqrt{N!}} \begin{vmatrix} \psi_1(1) & \psi_2(1) & \dots & \psi_N(1) \\ \psi_1(2) & \psi_2(2) & \dots & \psi_N(2) \\ \vdots & \vdots & \ddots & \vdots \\ \psi_1(N) & \psi_2(N) & \dots & \psi_N(N) \end{vmatrix}, \tag{2.8}$$

where $N$ is the number of electrons, $\frac{1}{\sqrt{N!}}$ is a normalization factor and the rows of the determinant are all the possible liner combinations of the Hartree product, a direct product of monoelectronic spinorbitals:

$$\Psi = \prod_{i=1}^{N} \psi_i \,. \tag{2.9}$$

Applying such wavefunctions to the Schrödinger equation requires to solve equations that need $3N$ electron coordinates, making them nearly impossible to use for big, complicated systems with plenty of electrons. Therefore, they are extremely computationally demanding for systems with numerous delocalized electrons such as the metal systems studied in the present thesis. Nonetheless, the DFT family provides a handful set of functionals to compute their electronic structure within a balanced accuracy-computational cost relation.

## 2.2 Density Functional Theory

The DFT evolved from the first statistical electron gas model purposed by Thomas and Fermi,[2,3] which represented the properties of the ground-state of a system composed of uniformly dispersed electrons (known as Jellium or uniform electron gas) under the effect of a nuclear field as a function of electron density in the late 1920s. Shortly, the model was complemented by Dirac[4,5] and Bloch,[6] however, it was not until Hohenberg and Kohn[7] stated their postulates that the contemporary DFT was established. They demonstrated that the ground-state energy of a non-degenerate system is a functional of the electron density and that the electron density that minimizes the energy functional corresponds to

the real electronic density, which corresponds to the solution of the Schrödinger equation. The first Hohenberg-Kohn theorem states that *"The external potential, $v_{ext}(\boldsymbol{r})$, of a non-degenerate electronic state is (to within a constant) a unique functional of the electron density; since, in turn $v_{ext}(\boldsymbol{r})$ fixes the Hamiltonian, we see that the full many particle ground-state is a unique functional of $\rho(\boldsymbol{r})$"*.

Hence, for any electronic system under an external potential $v_{ext}(\boldsymbol{r})$, exists an energy density functional such:

$$\mathrm{E}[\rho] = \mathrm{F_{HK}}[\rho] + \int v_{ext}(\boldsymbol{r})\rho(\boldsymbol{r})d\boldsymbol{r}\,, \tag{2.10}$$

that determines the energy of the ground-state where the Hohenberg-Kohn functional, $\mathrm{F_{HK}}[\rho]$, is:

$$\mathrm{F_{HK}}[\rho] = \mathrm{T}[\rho] + \mathrm{V}_{ee}[\rho]\,, \tag{2.11}$$

and corresponds to the potential-independent terms of the system, the kinetic energy, $\mathrm{T}[\rho]$, and the electronic repulsion, $\mathrm{V}_{ee}[\rho]$. As such terms are equal for any system with the same number of $n$ electrons the $\mathrm{F_{HK}}[\rho]$ is also known as a universal functional. Moreover, this postulate directly relates the electronic density with the Hamiltonian, the wavefunction, and all the expected values of any observable of the ground-state.

The second Hohenberg-Kohn theorem states that *"The functional that delivers the ground-state energy of the system gives the lowest energy if and only if the input density is the true ground-state density"*. In other words, the electronic density that minimize the $\mathrm{E}(\rho)$ is that of the ground-state. Thus, minimizing 2.11 will give us the ground-state energy of any system. However, the exact form of the $\mathrm{F_{HK}}[\rho]$ remains unknown. Fortunately, one year later Kohn and Sham formulated a mathematical approximation to $\mathrm{F_{HK}}[\rho]$ to solve such set back.[8]

The Kohn-Sham model is based on the construction of a fictitious model of non interacting electrons under an effective external potential, aiming to mimic the real electron density, and by extension its ground state properties. Under

such assumption, the ground-state density is obtained as a sum of one electron non interacting orbitals called Kohn-Sham orbitals:

$$\rho(r) = \sum_{i}^{n} |\psi_i^{KS}(\boldsymbol{r})|^2 \,, \tag{2.12}$$

and $\mathrm{F_{HK}}[\rho]$ can be redefined as:

$$\mathrm{F_{HK}}[\rho] = \mathrm{T}_s[\rho] + \mathrm{J}[\rho] + \mathrm{E}_{xc}[\rho] \,, \tag{2.13}$$

where $\mathrm{T}_s[\rho]$ is the sum of all the individual kinetic energies, and $\mathrm{J}[\rho]$ is the energy of the electron-electron interaction, assumed as a Coulomb repulsion interaction.

$$\mathrm{J}[\rho] = \frac{1}{2} \int\int \frac{\rho(\boldsymbol{r}_1)\rho(\boldsymbol{r}_2)}{|\boldsymbol{r}_1 - \boldsymbol{r}_2|} d\boldsymbol{r}_1 d\boldsymbol{r}_2 \,. \tag{2.14}$$

The final term is the exchange-correlation energy functional, $\mathrm{E}_{xc}[\rho]$, which accounts for all the rest of the energetic terms. Mainly it corrects the difference between the real kinetic energy and the simplified non-interaction kinetic energy, $\mathrm{T}_s[\rho]$, as well as the difference between the internal interaction energies of the real interacting many-body system from those of the made-up auxiliary independent-particle system where just the Coulomb electron-electron interaction term is used. As a result, it and may be defined as:

$$\mathrm{E}_{xc}[\rho] = \mathrm{T}[\rho] - \mathrm{T}_s[\rho] + \mathrm{V}_{ee}[\rho] - \mathrm{J}[\rho] \,, \tag{2.15}$$

As $\mathrm{F_{HK}}[\rho]$, $\mathrm{E}_{xc}[\rho]$ expression is unknown, and it is the key problem in all DFT performance. However, in the Kohn-Sham model, only the interaction terms are approximated, whereas for the $\mathrm{F_{HK}}[\rho]$, we apply the approximations to the entire energy. As a result, any variation from reality will be lower and the approximation will be more precise, than when using the $\mathrm{F_{HK}}[\rho]$ functional.

## 2.3 Exchange Correlation Functionals

Since $E_{xc}[\rho]$ is unknown, a suitable approximation to this functional must be found. According to complexity and computational cost, John P. Perdew defined the Jacob's ladder,[9] which divides existing functionals into five categories or rungs. The first rung starts with the simplest and fastest functionals, moving up to the fifth rung with the most complex functionals, which are presumably more accurate (and ideally exact).

Each group will be further explained at the following paragraph but for a brief explanation of the ladder, the local density approximation (LDA) functionals[8,10] are on the bottom rung. To parameterize the $E_{xc}[\rho]$, they solely rely on the local density at each point of the system. The generalized gradient approximation (GGA) functionals,[11–14] which consider the gradient of the local density in addition to the local density, occupy the second rung of the ladder. The meta-GGA functionals,[15,16] which incorporate the kinetic-energy density or second derivative of the local density, are found on the third rung. The first three rungs are particularly computationally efficient since they are semi-local functionals. The hybrid functionals,[17–19] which include certain amount of exact Hartree-Fock exchange, are found on the fourth rung. Finally, the double-hybrid[20] and the random phase approximation (RPA) functionals,[21,22] which also include the unoccupied Kohn-Sham orbitals and the electron exchange is not approximated, are found on the fifth rung. Although the latter two rungs are theoretically more accurate, their non-local nature permit to include long range interactions such the van der Waals (vdW) but makes them computationally very costly.[23]

The LDA describe accurately an electron gas uniformly distributed. Thus, the idea behind LDA functionals is to describe any real atom or molecule dividing the space with infinitesimal volume elements that locally present a uniform electron distribution. For metallic systems, where the valence electrons are non-localized and capable of wandering relatively freely throughout the entire crystal, the LDA functionals are fairly accurate, indeed they consistently provide lattice

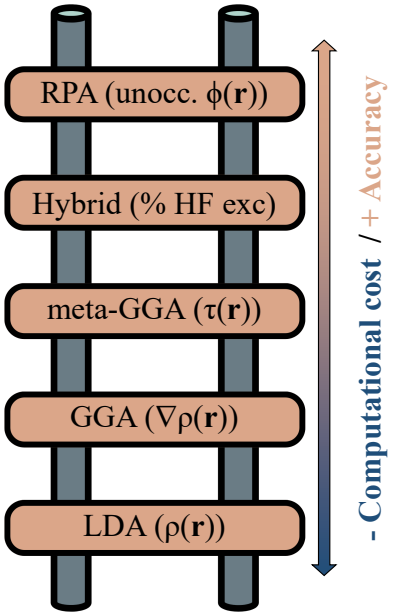


**Figure 2.1: Categorization of the functionals according to the Jacob's ladder of John J. Perdew.** Moving up from the bottom with less expensive and precise functionals to the top with more expensive and accurate ones. $\rho$ equivals to electron density, $\tau$ to kinetic energy density, % HF exc to a percentage of HF exchange functional and $\phi$ to molecular orbitals.

parameters and minimum interatomic distances. However, when describing less homogeneous systems as molecules and by extension bond energies and distances their performance is very poor.[24–26] The GGA functionals provide better results for ground-state energies adsorption energies and molecular geometries but still overestimate bond distances.[27] Within the GGA family, the Perdew-Burke-Ernzerhof (PBE)[14,19] functional is vastly used and it has served as a base for many other improved GGA functionals such RPBE[28] or PBEsol.[29] Indeed, due to its outstanding performance describing transition metal carbide systems,[30] PBE is the exchange-correlation functional used in this research. Meta-GGA functionals generally provide a better thermochemical estimations of molecules but do not improve accuracy when characterizing extended transition metals when compared to GGA functionals.[31] However, all of these functionals (LDA,

GGA, and meta-GGA) suffer from self-interaction errors, as each electron interacts with its own electron density in these approaches.[32] As a result, the energy stability of electronic configurations with electrons delocalized over different atoms is overestimated,[33] leading in a loss of precision when dealing with molecules, clusters, or other strongly correlated systems. Among all of the them, the Tao-Perdew-Staroverov-Scuseria (TPSS)[15] is highly used.

The hybrid functionals include a part of exact HF exchange, cancelling the self-interaction deviation. Moreover, due to the inclusion of the long-range interactions they outperform the GGA appoches when simulating molecules. Nevertheless, the performance of hybrid functionals for solids is less clear. Hybrid functionals produce unsatisfactory results for metals, with inaccurate atomization energies and incorrect broadening of the conduction bands, in contrast to how the inclusion of a fraction of HF exchange improves lattice parameters, bulk moduli, bandgaps, and atomization energies for insulators and semiconductors.[34] Additionally, hybrid functionals are highly computational demanding and tend to localize in excess the electrons, therefore they are not the best choice when simulating metals[35] and thus, they were not use here.

When studying adsorptions and reactions over metallic surfaces of non-magnetic systems the total energies and bond lengths obtained by the spin unrestricted formalism or unrestricted DFT converge with the spin restricted formalism or restricted DFT solution.[36] In the present Thesis, some of the bare systems studied have a metallic character, however as soon as some atom bonds to the surface, a gap opens but without any evidence of spin polarization. Thus, the restricted DFT has been used for the majority of the calculations except for some later explained exceptions.

In order to perform a meaningful DFT calculation, besides choosing an appropriate functional, the Kohn-Sham orbitals must be represented by a sufficient basis set in order to accurately reflect the electron density. Local basis sets are the most common option for atoms and molecules, since they are incredibly

focused around each atom center. On the other hand, extended systems and systems with strongly delocalized electrons, such as metals, are better described by non-local basis sets. Plane waves are a common non-local basis set family used for simulating periodic systems. They cover the whole space rather than being concentrated at the nucleus, therefore plane waves are well suited for computations of extended systems with translational symmetry since they implicitly incorporate the idea of periodic boundary conditions. Their significant disadvantage is that a very large number of them are required in order to adequately represent all of the electrons. Since core electrons are typically not engaged in the processes of forming or breaking bonds, they may be represented by an accurate core potential, also known as a pseudopotential, and as a result, reduce the number of electrons simulated by the plane waves, and thus making the DFT calculations more affordable.

The most common pseudopotentials used with plane waves on periodic models are the projector augmented wave (PAW) potentials,[37] ultrasoft potentials,[38] and norm-conserving pseudopotentials.[39] By taking into account a number of present basis functions to represent the core electrons, the PAW approach allows one to approximate the entire electron wave function. Because it restores the pseudo wavefunction created by the generation of the pseudopotential to the all-electron wavefunction, the PAW approach is specifically employed in this thesis. As a result, it benefits from the all-electron basis. The discrepancy between the precise wave function and the pseudo-wave function is used to simulate the core electrons.

## 2.4 Dispersive Forces Corrections

A particularly difficult challenge in the modeling of molecules and materials is the proper depiction of long-range electron correlation, most notably involving vdW dispersive interactions.[40] The vdW forces are produced by the interplay

of quantum-mechanical fluctuations in the electronic charge density. The semi-local functionals then, are not able to reproduce such non-local effect and often, neglecting such interactions can lead to wrong results. For instance, even when the total energy of a given system is accurately obtained, other observables of the same system, such the interaction energy, can be poorly predicted. Correlated electron mobility, or correlated quantum-mechanical fluctuations of the average electron distribution in the DFT depiction, as mention above, is what accounts for the majority of the missing electronic energy. Moreover, this correlations due to the electron mobility scale non-linearly extremely fast with size and lead polarizable systems.[41,42] This fact adds extra difficulties in simulating such long-range correlation forces and has been a central topic in the quantum chemistry community.

Energy decomposition-based and electron density-based techniques are the two primary families of methodologies that have been designed to accomplish this goal and provide deep comprehension of the long-range interactions. In one hand, the energy decomposition methods are based in the description of the intermolecular energy as a sum of the different interactions involved. Thus, the total energy is decomposed into dispersion interactions exchange-repulsion, electrostatic interactions, polarisation, and high-order terms. Consequently, they allow to perform a quantitatively analysis of the contribution of each energy separately. On the other hand, the electron density-based approaches aim to localize the spatial areas where those interactions are relevant through a screening of the density gradient. Unfortunately, this procedure does not allow us to discriminate between energies but to obtain the total contribution of the intermolecular forces. To do so, Johnson *et al.* introduced the non-covalent interaction (NCI) index.[43,44] The authors of the study observed that the dominant zone of non-covalent interaction is marked by a peak in the regime of low electron densities and a low decreased density gradient, $s$, which is a unit-less measure for the deviation from a homogeneous electron gas[7] given by

$$s = \frac{|\nabla\rho(\boldsymbol{r})|}{2\rho(\boldsymbol{r})k_F}\,, \tag{2.16}$$

where $\nabla\rho(\boldsymbol{r})$ is the gradient density and $k_F$, the Fermi momentum of the free electron gas. This can be understood due to that the low density regions mark the long-range interaction areas and low gradient density regions determine bonding formation. Based on this initial descriptor, more accurate ones have been purposed, *i.e.* density overlap regions indicator (DORI)[45] that complements the NCI by including and depicting both, covalent and non-covalent interactions regions however, not all the long range interactions are captured by such descriptors, for instance, the electrostatic interactions, and further treatment is required for its proper application.

As mentioned above, this thesis has been developed by means of the DFT and therefore a electron density-based approach has been applied. Specially, the methodology chosen was *a posteriori* correction of the semilocal PBE functional, DFT-D3[46]. Initially, a London-type vdW correction was purposed by Wu and Yang[47] but the already obsolete DFT-D purposed by Grimme[48] established the first approach in such regard. DFT-D aims to treats the vdW energy as a $C_6$ pair-wise additive term to the total energy. The main set back of such approximation is the lack of consideration of the electronic screeneing effect and due to that they relay on different semi empiric-wise restricted or damped functions to describe such property. From DFT-D, an enhanced DFT-D2 was purposed.[49] There the effective coefficents were deduced directly from atomic properties. Finally, the DFT-D3 method was implemented and widely used. In comparison with the previous ones, it is also based on $C_6$ atom-pair interaction coefficients, but incorporates local environmental data in the form of fractional coordination numbers driven by geometry. Moreover, the current damped paired-wise functions used has been prove to have minor differences with the final vdW energetics[50] and for such reason DFT-D3 is the model implemented is the present study.

Overall, the DFT is a handful approach that allows us to solve a complex interacting problem, as the the $\hat{\mathrm{H}}_e$, by transforming it to an "exact" equivalent non-interacting problem, much more easy be to solved. Thus, the idea behind DFT is to characterize the system mimicking its electron density, $\rho(\mathrm{r})$, that only depends on 3 spatial coordinates rather than their electronic wavefunctions that depend on $3n$ variables being $n$ the number of electrons of the system.

## References


[1] M. Born and R. Oppenheimer, *Ann. Phys.*, 1927, **84**, 457.

[2] L. H. Thomas, *Math. Proc. Cambridge Philos. Soc.*, 1927, **23**(5), 542–548.

[3] E. Fermi, *Zeitschrift für Phys.*, 1928, **48**(1-2), 73–79.

[4] P. A. M. Dirac, *Proc. R. Soc. A Math. Phys. Eng. Sci.*, 1928, **117**(778), 610–624.

[5] P. A. Dirac, *Math. Proc. Cambridge Philos. Soc.*, 1930, **26**(3), 376–385.

[6] F. Bloch, *Zeitschrift für Phys.*, 1929, **57**, 545–555.

[7] P. Hohenberg and W. Kohn, *Phys. Rev.*, 1964, **136**(3B), B864–B871.

[8] W. Kohn and L. J. Sham, *Phys. Rev.*, 1965, **140**(4A), A1133–A1138.

[9] J. P. Perdew, *MRS Bull.*, 2013, **38**(9), 743–750.

[10] U. Von Barth and L. Hedin, *J. Phys. C Solid State Phys.*, 1972, **5**(13), 1629–1642.

[11] D. C. Langreth and J. P. Perdew, *Phys. Rev. B*, 1980, **21**(12), 5469–5493.

[12] D. C. Langreth and M. J. Mehl, *Phys. Rev. B*, 1983, **28**(4), 1809–1834.

[13] A. D. Becke, *Phys. Rev. A*, 1988, **38**(6), 3098–3100.

[14] J. P. Perdew, K. Burke, and M. Ernzerhof, *Phys. Rev. Lett.*, 1996, **77**(18), 3865–3868.

[15] J. Tao, J. P. Perdew, V. N. Staroverov, and G. E. Scuseria, *Phys. Rev. Lett.*, 2003, **91**(14), 3–6.

[16] J. Sun, R. Haunschild, B. Xiao, I. W. Bulik, G. E. Scuseria, and J. P. Perdew, *J. Chem. Phys.*, 2013, **138**(4), 044113.

[17] A. D. Becke, *J. Chem. Phys.*, 1998, **109**(6), 2092–2098.

[18] J. P. Perdew, M. Ernzerhof, and K. Burke, *J. Chem. Phys.*, 1996, **105**(22), 9982–9985.

[19] M. Ernzerhof and G. E. Scuseria, *J. Chem. Phys.*, 1999, **110**, 5029.

[20] Y. Zhang, X. Xu, and W. A. Goddard, *Proc. Natl. Acad. Sci. U. S. A.*, 2009, **106**(13), 4963–4968.

[21] F. Furche, *Phys. Rev. B - Condens. Matter Mater. Phys.*, 2001, **64**(19), 195120.

[22] J. Harl, L. Schimka, and G. Kresse, *Phys. Rev. B - Condens. Matter Mater. Phys.*, 2010, **81**(11), 115126.

[23] X. Ren, P. Rinke, C. Joas, and M. Scheffler, *J. Mater. Sci.*, 2012, **47**, 7447–7471.

[24] A. D. Becke, *J. Chem. Phys.*, 1992, **96**(3), 2155–2160.

[25] J. P. Perdew, J. A. Chevary, S. H. Vosko, K. A. Jackson, M. R. Pederson, D. J. Singh, and C. Fiolhais, *Phys. Rev. B*, 1992, **48**(7), 4978.

[26] I. H. Lee and R. M. Martin, *Phys. Rev. B - Condens. Matter Mater. Phys.*, 1997, **56**(12), 7197–7205.

[27] M. Fischer, F. O. Evers, F. Formalik, and A. Olejniczak, *Theor. Chem. Acc.*, 2016, **135**(12), 1–19.

[28] B. Hammer, L. B. Hansen, and J. K. Nørskov, *Phys. Rev. B - Condens. Matter Mater. Phys.*, 1999, **59**(11), 7413–7421.

[29] J. P. Perdew, A. Ruzsinszky, G. I. Csonka, O. A. Vydrov, G. E. Scuseria, L. A. Constantin, X. Zhou, and K. Burke, *Phys. Rev. Lett.*, 2008, **100**(13), 1–4.

[30] L. Vega and F. Viñes, *J. Comput. Chem.*, 2020, **41**(30), 2598–2603.

[31] S. Jana, K. Sharma, and P. Samal, *J. Chem. Phys.*, 2018, **149**(16), 164703.

[32] P. Mori-Sánchez, A. J. Cohen, and W. Yang, *J. Chem. Phys.*, 2006, **125**(20), 201102.

[33] A. J. Cohen, P. Mori-Sánchez, and W. Yang, *J. Chem. Phys.*, 2008, **129**(12), 121104.

[34] P. Janthon, S. Luo, S. M. Kozlov, F. Viñes, J. Limtrakul, D. G. Truhlar, and F. Illas, *J. Chem. Theory Comput.*, 2014, **10**(9), 3832–3839.

[35] P. Mori-Sánchez, A. J. Cohen, and W. Yang, *Phys. Rev. Lett.*, 2008, **100**(14), 146401.

[36] J. L. Fajín, M. N. D.s. Cordeiro, J. R. Gomes, and F. Illas, *J. Chem. Theory Comput.*, 2012, **8**(5), 1737–1743.

[37] P. E. Blöchl, *Phys. Rev. B*, 1994, **50**(24), 17953–17979.

[38] D. Vanderbilt, *Phys. Rev. B*, 1990, **41**(11), 7892–7895.

[39] D. R. Hamann, M. Schlüter, and C. Chiang, *Phys. Rev. Lett.*, 1979, **43**(20), 1494–1497.

[40] M. Stöhr, T. Van Voorhis, and A. Tkatchenko, *Chem. Soc. Rev.*, 2019, **48**(15), 4118–4154.

[41] V. V. Gobre and A. Tkatchenko, *Nat. Commun.*, 2013, **4**, 1–6.

[42] J. F. Dobson, A. White, and A. Rubio, *Phys. Rev. Lett.*, 2006, **96**(7), 4–7.

[43] E. R. Johnson, S. Keinan, P. Mori-Sánchez, J. Contreras-García, A. J. Cohen, and W. Yang, *J. Am. Chem. Soc.*, 2010, **132**(18), 6498–6506.

[44] J. Contreras-García, E. R. Johnson, S. Keinan, R. Chaudret, J. P. Piquemal, D. N. Beratan, and W. Yang, *J. Chem. Theory Comput.*, 2011, **7**(3), 625–632.

[45] P. De Silva and C. Corminboeuf, *J. Chem. Theory Comput.*, 2014, **10**(9), 3745–3756.

[46] S. Grimme, J. Antony, S. Ehrlich, and H. Krieg, *J. Chem. Phys.*, 2010, **132**(15), 154104.

[47] Q. Wu and W. Yang, *J. Chem. Phys.*, 2002, **116**(2), 515–524.

[48] S. Grimme, *J. Comput. Chem.*, 2004, **25**(12), 1463–1473.

[49] S. Grimme, *J. Comput. Chem.*, 2006, **27**, 1787–1799.

[50] S. Grimme, *J. Comput. Chem.*, 2011, **32**(7), 1456–1465.

Chapter 3:

# Modelling in Catalysis and Electrocatalysis

Catalysis is the process by which a material enhances the rate of a reaction without being a reactant or product.[1] Moreover, such material is neither consumed or generated during the reaction. A material with such behaviour is known as a catalyst and its efficiency is determined by three parameters: activity, selectivity, and stability.

The activity of a catalyst defines how many orders of magnitude it can boost the rate of a reaction. The active phase of the catalyst is the one that is directly involved in such rate acceleration and must be in contact with the reactants. To maximise its capabilities, the catalyst must be properly distributed in order to optimize the interaction with the reactants. To achieve maximal dispersion, a support material is usually used on which the catalyst is deposited. Even when a catalyst is adequately active, it can be enhanced by the presence of another material known as a promoter, which acts as a sort of catalyst for the catalyst. The selectivity of a catalyst implies that is capable of leading a reaction to certain products, since there are usually other reaction paths that can lead to secondary products. The catalyst might help one path while closing the doors to others, which we then deal with a selective catalyst. The stability of a catalyst

determines its useful life of under reaction conditions. Mechanical or chemical attrition, or the adsorption of impurities or poisons, which are substances that limit catalytic activity, are the most typical ways a catalyst loses activity.

A catalyst, in practice, reduces the activation energy, $E_a$, of a particular process, as it is shown schematically at figure 3.1. Catalysts react with reactants to produce intermediate species, which eventually lead to products and the regenerated catalyst. They effectively give an alternative reaction mechanism with different intermediates and transition-state energies than the non-catalyzed process. Because the reactants and products are the same in both catalyzed and non-catalyzed processes, the thermodynamics of the reaction remain unchanged. As a result, catalysis is dependent on changes in the kinetics of chemical processes.

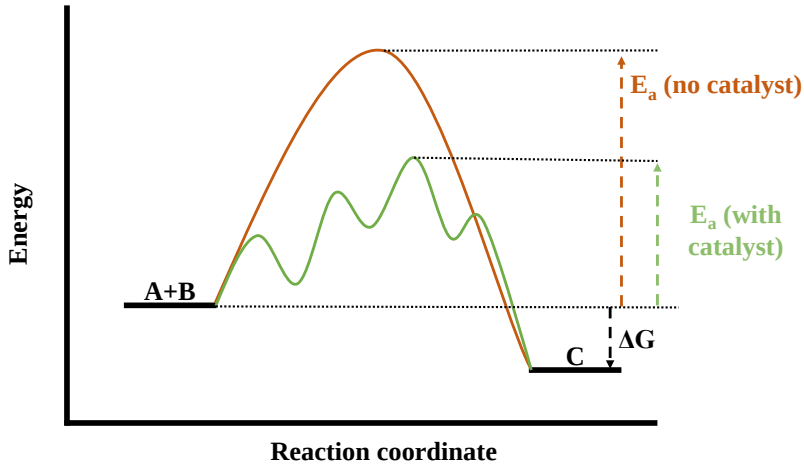


**Figure 3.1: Generic potential energy diagram showing the effect of a catalyst** in an hypothetical exothermic reaction (A+B⇌C). The presence of the catalyst changes the path of the reaction and decreases the $E_a$, in green, respect to the original path, in red. Overall the reaction has the same reactants, A and B, the same product, C, and the same thermodynamics.

Catalysis is a phenomena that has been recognized from very early times, but not so much for its theory or properties. Jöns Jakob Berzelius (1779-1848) coined the term catalysis in 1835,[2] derived from the Greek terms *kata*, which

means "down", and *lyein*, which means "loosen". Since then, uncountable new synthesis methods and catalysts were discovered[3] impacting greatly the industry of the XXth century. Nowadays, it plays a critical part in the production of the great majority of chemicals utilized in our civilization and thus, it represents directly or indirectly to around 35% of the world gross domestic product.[4] Furthermore, catalytical process have a key role at the urgent socioeconomic transformation, that our society is demanding, for facing the many issues arising from forthcoming climate emergencies.[5–7]

Based on the physical state of the matter of the reactants, products and catalysts (solid, liquid or gas) the catalytic process can be divided into homogeneous, enzymatic, and heterogeneous catalysis. Homogeneous catalysis refers to reactions where the catalyst is in the same phase as the reactants, principally in solution. The key advantages of these catalytic reactions are that the reaction mechanism is typically simple, and hence the catalytic process may be readily regulated. Poisoning is also decreased, and high yields and high purity products can be achieved. The fundamental drawback of these procedures is the difficulty in separating the catalyst from the media. In contrast, heterogeneous catalysis describes processes where the catalysts and substrate are in distinct phases. Such reactions not only imply breaking and forming bonds but also multiple interactions with the catalyst surface, complicating their study.

Enzymatic reactions are a particular heterogeneous catalytic systems. They occur inside the living organisms such us and commonly the products and/or reactant are colloids. The enzymes are the catalysts of such reactions. They are proteins in nature, a polypeptide structure formed by one or more long chains of amino acid residues and thus, they are very specific and specialized catalysts. In general, enzymes have outstanding performances, however small environmental modifications such raising the temperature, can denaturalize them very rapidly.

According to the *Sabatier* principle a good catalyst is the one which adsorbs the reactants and Reaction Intermediates (RI) moderately strong, neither too strong or too weak but moderately strong.[8] When a reactant is weakly adsorb,

it will not remain on the surface long enough to let the reaction occur. On the other hand, when the reactant is strongly adsorb, it will remain on the surface without letting the reaction advance and blocking the active sites, poisoning the surface and decreasing the catalyst performance. Moreover, Paul Sabatier also stated that during an heterogeneous catalytic process, the catalyst acts as an additional reactant that leads to the formation of transitory and unstable RIs and the kinetics of the overall process are directly related by the adsorption strength of such intermediates. As more stable and strongly adsorb, the slower will be the reaction. This was complemented later on by Taylor,[9] who introduced the key concept of active sites, which are the parts of the catalyst that are directly involved in the reaction of interest. In this Thesis, we will focus on solid-gas and electrochemical, solid-liquid, processes, which are of great industrial and environmental importance and will be discussed in further detail in the next section and section 3.2, respectively.

## 3.1 Solid-Gas Systems

Within the heterogeneous catalysis processes, solid-gas systems are involved in many relevant processes. Although there are significant catalysts composed of other materials, such as sulfides, phosphates, or ion-exchange resins to name a few,[10–12] the vast majority of catalysts are metals or metallic oxides and carbides.[13–15] In such systems, the reaction take places at the surface of the catalyst due to surfaces are specially reactive. Within the bulk, the atoms are completely surrounded, forming all the bonds that their electronic configuration requires to be stable. The surface atoms, however, suffer from a lack of nearby atoms and hence their electrons will tend to form new bonds easily to fulfill the same coordination than the bulk atoms. In material science the number of neighbouring atoms or complexes is known as the coordination number. Thus, atoms with lower coordination number, as surface atoms, will be more reactive than bulk

ones. As a consequence, both electronic and atomic structure are of great importance when determining the catalyst performance.

In a typical solid-gas catalytic process, see Figure 3.2, the gas reactants first diffuse towards the surface and then they adsorb upon it. The reaction then proceeds on the surface (including any further stages that the entire reaction may have). The products are detached from the catalyst and ultimately discharged at the original gas-phase, leaving the catalyst with the same structure as before the reaction. The three potential limiting stages are the reactants adsorption, the reaction itself, or the products release back at the gas-phase since forming and breaking bonds demand more energy than a gas molecule diffusion in a gas-phase. The catalyst experiences attrition when this process is repeated over time; certain secondary products or chemical intermediates may stay adsorbed on the surface, lowering the number of free active sites, poisoning the surface. Hence, the significance of the *Sabatier principle* in terms of catalyst performance.

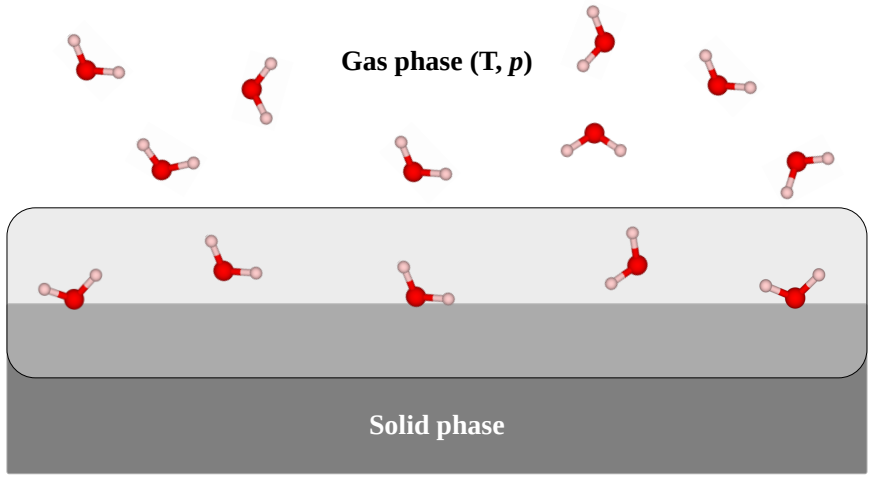


**Figure 3.2: Schematic representation of a solid-gas system**. Typically, a single-crystal metal surface in contact with a surrounding gas phase, which is defined by temperature, T, and pressure, $p$. The shaded area represents the finite interface where the reaction takes place and hence is simulated.

### 3.1.1 Periodic Models

For the correct representation of the solid-gas systems of interest in the present Thesis, it is mandatory to find the appropriated model to depict the condensed phase of the matter as well as the gas molecules involved in the reactions of interest. When it comes to providing significant insight into the behavior of materials as well as the physical, chemical, and catalytic phenomena that occur inside or on their surface, there are two major models: The periodic model and the aggregate or cluster model,[16] with their respective advantages and limitations.

Condensed matter, in the form of crystalline substances, has a periodically ordered atomic structure that can be easily reproduced by the periodic model. Therefore, the totally of the structure can be simulated by studying the smallest portion of the solid, called unit cell, that is able to replicate the entirety of the system when translationally repeated in the three-dimensional space. In this scenario the Schrödinger equation only has to be solved for the unit cell atoms as the electron density (or wave function) at a particular position is unaffected by the translation operator and the calculations are substantially simplified.

The three orthogonal space vectors of the unit cell define the shape crystal lattice (also called Bravias lattice, see Figure 3.3) of the solid. The translational operator ($\hat{T}$) is defined based on the unit cell vectors as,

$$\hat{T} = n_1\mathbf{a}_1 + n_2\mathbf{a}_2 + n_3\mathbf{a}_3\,. \tag{3.1}$$

Applying $\hat{T}$ any point inside the unit cell can be replicated outside by applying entire n translations. Note that the translational and kinetic energy operators are designed by the same symbol, but have different meanings. As mentioned, the unit cell defines the geometrical shape of the crystal lattice, however, within the same unit cell, the atoms can be arranged in multiple variations and hence is both the unit cell and the arrangement of the atoms inside that define the crystal lattice.

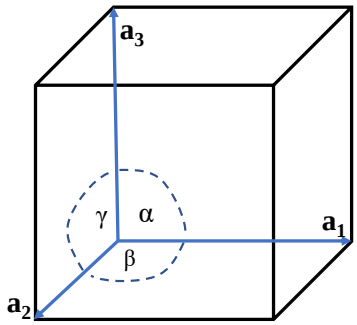


**Figure 3.3: Schematic cubic Bravias lattice** with $\alpha$, $\beta$, and $\gamma = 90^{o}$, and $|\mathbf{a}_1|=|\mathbf{a}_2|=|\mathbf{a}_3|$

There are many possible unit cells that can describe a solid, however there is only one unit cell irreducible and smaller than the rest, the so-called primitive cell. The rest of the unit cells that can be form are just a linear combination of the primitive cell. The most common unit cells are cubic, body-centered cubic (*bcc*), face-centered cubic (*fcc*), and hexagonal closed packed (*hcp*).

For doing analytic analyses of periodic systems, the usage of the reciprocal space is highly convenient. The reciprocal lattice is a mathematical concept that simplifies the characterization of periodic crystalline lattice features. Each crystalline lattice, A=$\{\mathbf{a}_1, \mathbf{a}_2, \mathbf{a}_3\}$, has its corresponding reciprocal lattice, B=$\{\mathbf{b}_1, \mathbf{b}_2, \mathbf{b}_3\}$, which is perfectly defined and satisfies,

$$\mathbf{b}_i = 2\pi \frac{\mathbf{b}_j \times \mathbf{b}_k}{\mathbf{a}_i \cdot (\mathbf{a}_j \times \mathbf{a}_k)} \; \forall_{i,j,k} \in \{1,2,3\}\,, \tag{3.2}$$

$$\mathbf{a}_i \cdot \mathbf{b}_j = 2\pi\delta_{ij}\,. \tag{3.3}$$

The reciprocal lattice has a highly distinct set of features and peculiar points that are inextricably linked to the periodicity and translational symmetry of the Bravais lattice in real space. The reciprocal lattice translational vectors are orthogonal if the crystalline lattice translational vectors are similarly orthogonal.

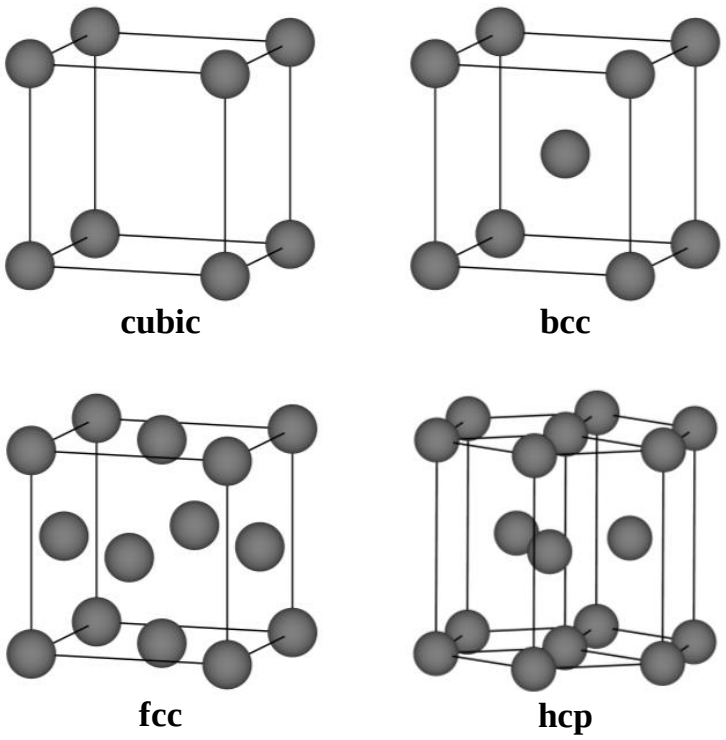


**Figure 3.4: Schematic representation of the most common unit cells**. Depicted are cubic (top left), body-centered cubic (top right), face-centered cubic (bottom left) and hexagonal closed packed (bottom right) unit cells. Grey spheres denote atomic positions

Furthermore, the reciprocal lattice unit cell corresponds to the parallelepiped produced by the three vectors $\{\mathbf{b}_1,\ \mathbf{b}_2,\ \mathbf{b}_3\}$ and its volume equals $(2\pi)^3/\mathrm{V_c}$, where $\mathrm{V_c}$ is the volume of the Bravais unit cell. As a result, bigger real (or direct) unit cells correspond to smaller reciprocal unit cells.

Through the reciprocal space one can easily expand the wavefunction of any system using the Bloch theorem,[17] which offers the theoretical basis for the study of periodic systems utilizing the reciprocal space, describing the electronic

wavefunction in a periodic potential. This theorem asserts, in a nutshell, that the values of all observables at a specific point of a lattice will be the same for analogous places throughout the whole lattice. Therefore, and mimicking $\hat{T}$, when moving one electron from the unit cell to an equivalent outside position, the following expression must hold true,

$$\hat{T}\Psi(\boldsymbol{r}) = \Psi(\boldsymbol{r} + \boldsymbol{R}) = \Psi(\boldsymbol{r})\,. \tag{3.4}$$

Hence, at 3.4 the wavefunction is equal at $\Psi(\boldsymbol{r})$ and $\Psi(\boldsymbol{r} + \boldsymbol{R})$. The periodic potential, $V(\boldsymbol{r})$ that link the periodicity of the wavefunctions with the Bravais lattice can be defined as the multiplication of two functions,

$$V(\boldsymbol{r}) = e^{i\boldsymbol{k}\boldsymbol{r}}\nu_i(\boldsymbol{r})\,, \tag{3.5}$$

where $e^{i\boldsymbol{k}\boldsymbol{r}}$ is a plane wave with wave vector $\boldsymbol{k}$ and $\nu_i(\boldsymbol{r})$ is the function that keeps constraint with the Bravais lattice,

$$\nu_i(\boldsymbol{r} + \boldsymbol{R}) = \nu_i(\boldsymbol{r})\,. \tag{3.6}$$

Moreover, the choice of $\nu_i$ determines the grade of localization of the basis functions of the system.

Once the bulk is properly simulated it is straightforward to model its surface through the slab model. The slab model is simply constructed by enlarging the unit cell in the direction of the plane to be examined, so generating a void wide enough to avoid interactions between a slab and its duplicate in the direction of the void, see Figure 3.5. Metals and covalent solids typically require less vacuum than the ionic compounds. The latest have long-rage Coulomb interactions an requires more vacuum to isolate the simulated surface with its above replica.[18] A vacuum of 10 Å is a good starting point for most any system.

The slab model requires a sufficient number of atomic layers to accurately describe the electronic properties of both the surface and the bulk. In this scenario, it is essential to determine what thickness, measured in atomic layers, is required

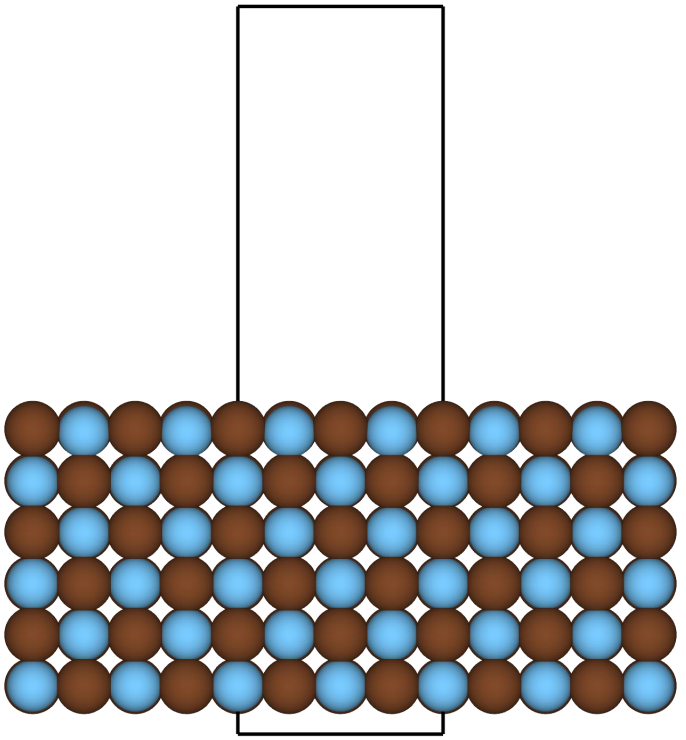

**Figure 3.5: Side view of a generic slab of 6 layers**. Side view of a generic slab of 6 layers. The unit cell, shown in black, is expanded with vacuum over the desired surface to avoid interactions between replicas.

to achieve convergence in a sensitive observable, such as surface energy. A slab model may be built in two ways: Symmetric or non-symmetric. A symmetrical slab is one in which both sides are surface models and may thus relax while investigating the chemistry on their surface, but the interior layers are fixed to replicate the bulk of the material. A non-symmetric slab has one surface side and one fixed bulk side. For an analogous representation, the symmetric model often requires twice as many layers as the non-symmetric model, hence the latter is used for regular surface research. The symmetric model, on the other hand, is beneficial when one wishes to investigate probable interactions between two

species adsorbed on distinct surfaces of the slab via the substrate.

From the same solid, based on how one cuts the bulk to create a surface, many different surface atomic arranges can be generated. To categorize the surface of a given solid the Miller indices are commonly used. Miller indices are three non-co-linear points within the Bravais lattice that determine a plane in it. These indices are defined by the smallest vector of the reciprocal lattice normal to the plane. Thus, having a vector of the reciprocal space with Miller indices $h$, $k$, $l$:

$$h\mathbf{b}_1 + k\mathbf{b}_2 + l\mathbf{b}_3\,, \tag{3.7}$$

we have a plane $(hkl)$ normal to said vector, whose direction is $[hkl]$ when using the Miller indices. $x_1, x_2$, and $x_3$ are the sites where this plane connects with the vectors of the real lattice $a$:

$$x_1\mathbf{a}_1 + x_2\mathbf{a}_2 + x_3\mathbf{a}_3\,. \tag{3.8}$$

The following is the connection between the Miller indices and the points of intersection:

$$h = \frac{1}{x_1};\ k = \frac{1}{x_2};\ l = \frac{1}{x_3}\,. \tag{3.9}$$

A Miller index of 0 indicates that the crossing point is infinite, implying that the plane is parallel to the vector of the direct cell in question and never intersects.

### 3.1.2 Adsorption Energies

For many catalytic processes the adsorption energies of the species involved in such reactions are a popular and effective descriptor to categorize the performance of a given catalyst. By means of DFT optimizations the adsorption energy, $\Delta E_{ads}$, for a gas–solid system can be defined as the total energy difference

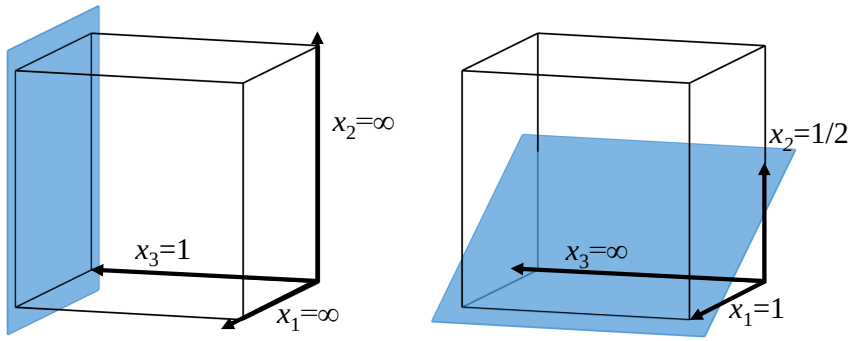


**Figure 3.6: Depiction of the relation between the Miller indices and lattice plains**. At the left is shown in blue the (001) crystallographic plane and so at the right for the (120).

between the surface with the adsorbates on top of it, and the sum of the energies of the clean surface and of the $n$ adsorbates:

$$\Delta E_{ads} = \frac{E_{surf\text{-}ns} - (E_{surf} + nE_s)}{n}, \tag{3.10}$$

where $E_{surf\text{-}ns}$ is the total energy of the surface with $n$ adsorbates on top, $E_{surf}$ is so of the clean surface, and $nE_s$ is so of the $n$ free adsorbates. Within this definition, the more negative $\Delta E_{ads}$ the stronger the adsorption. Overall, to obtain the desired adsorption energy two steps are needed. First, one must optimize the surface with an adsorbate placed on all the existing different symmetric sites, and second, calculate the $\Delta E_{ads}$ with Eq. 3.10. Finally, the scenario with the most stable, negative, energy will determine the adsorption site and the final adsorption energy.

### 3.1.3 Gibbs Free Energies

In order to relate these calculations to macroscopic experimental observables like the Gibbs free energy, thermal effects must be included. For instance, the molecular vibrations derived from the motion of the atomic nuclei at 0 K, known as Zero Point Energy (ZPE), are accounted within the harmonic approximation,

$$\mathrm{ZPE} = \frac{1}{2}\sum h\upsilon_i \,, \tag{3.11}$$

where $h$ is the Planck constant and $\upsilon_i$ stands for the vibrational frequencies. For free gas molecules, the number of frequencies is 3N-6, 3N-5 when the molecule is linear, and correspond to the contribution of each normal mode but when dealing with adsorbates, all the frequencies are accounted, 3N. In addition to the nuclei vibrations, the entropic contribution has to be considered. The entropy of the free gas molecules in standard conditions is well known and can be found in well established thermodynamic tables,[19] however, for the adsorbed molecules, the vibrational entropic contributions can be computed from their vibrational partition functions as,[20,21]

$$\mathrm{TS} = \mathrm{N_A}k_\mathrm{B}\mathrm{T}\sum_{i=1}^{n}\frac{h\upsilon_i/k_\mathrm{B}\mathrm{T}}{e^{h\upsilon_i/k_\mathrm{B}\mathrm{T}}-1} - ln\left(1-e^{-h\upsilon_i/k_\mathrm{B}\mathrm{T}}\right) . \tag{3.12}$$

Due to the energy contribution will be affected by the electronic structure of the surface atoms in addition to the nature of the adsorbate itself. Hence, the adsorption Gibbs free energy can be computed as,

$$\Delta\mathrm{G_{ads}} = \Delta\mathrm{E_{ads}} + \Delta\mathrm{E_{ZPE}} - \mathrm{T}\Delta\mathrm{S} \,, \tag{3.13}$$

where, the $\Delta$ZPE and the T$\Delta$S are evaluated as the adsorption total energy, $\Delta\mathrm{E_{ads}}$ from the section above, 3.1.2, and consequently, $\Delta\mathrm{E_{ZPE}}$ is defined as,

$$\Delta\mathrm{E_{ZPE}} = \mathrm{ZPE_{surf\text{-}}}_{n\mathrm{s}} - (\mathrm{ZPE_{surf}} + n\mathrm{ZPE_s}) \,, \tag{3.14}$$

and $T\Delta S$ as,

$$T\Delta S = TS_{\text{surf-}ns} - (TS_{\text{surf}} + nS_s)\,. \tag{3.15}$$

Commonly, the vibration of the adsorbates are quantitatively higher and can be safely decoupled from the surface vibrations. Thus, the terms $ZPE_{\text{surf}}$ and $TS_{\text{surf}}$ from Eq. 3.14 and Eq. 3.15 can be neglected and the terms $ZPE_{\text{surf-}ns}$ and $TS_{\text{surf-}ns}$ from the same Eqs. only include the frequencies from the adsorbates vibrations.

### 3.1.4 Transition States Finding

The configurations of reactants and products in chemical processes correspond to local minima of the PES. The goal of geometry optimization is to find such structures and their relative energy, determining whether each process is endo- or exothermic. The study of chemical processes, however, is incomplete until the structure of the transition state (TS) and the accompanying energy barrier that the system must overcome to develop from the initial to the final state are determined. Transition states are PES saddle points, which means that their structures maximize energy for the response coordinate while minimizing it for the other coordinates. There are several techniques to discovering the structure of transition states.

**Nudged Elastic Band.** The Nudged Elastic Band (NEB)[22] method starts from the initial and final states of any reaction. From them a series of intermediate configuration are generated. All the images, including the initial and final steps, are linked together with an artificial force or spring. Once all the images are generated, the NEB calculation minimize the energy of each image simulating a path over the PES from the initial step to the final products. Finally, the image with the higher energy is taken as the transition state of such path.

To ensure that the force applied by the springs does not interfere with the minimization of the images, a force projector is used to obtain an estimation of the tangent of the path for each image for each intermediate configuration and

iteration, allowing the true and spring forces to be decomposed into forces parallel and perpendicular to the reaction path. Only the real forces perpendicular to the path and the spring parallel to the path are considered in the optimization procedure.

However, this system has a few drawbacks. The pictures are generated without knowing whether they correspond to the genuine reaction route or, at the very least, the more favorable thermodynamic path. The intermediate pictures are frequently constructed as linear interpolations of the atomic locations between the start and final states to give a meaningful first estimation. Thus, a good practice is that the intermediate pictures are checked to verify that no atoms are too near together. When not, the repulsive potentials between the nuclei can be strong enough to evict such atoms, resulting in an abnormally disordered picture. The generated picture alters the evaluated reaction path to a very artificial path that is distant from reality.

The second major issue is connected to the correctness of the derived TS. The maximal energy picture is used as the TS, although it is only an approximation based on our estimations. To enhance the accuracy of the TS acquired, the number of intermediate photos must be increased. This increases the precision of the pathway over the PES and the possibility of finding an image that is closer to the true TS. However, the computing cost rises considerably and is not always feasible.

**Climbing-Image Nudged Elastic Band.** One improved NEB method to solve the TS precision setback is the Climbing-Image Nudged Elastic band (CI-NEB).[23] Its implementation is identical to the NEB technique, with the difference that after few iterations, the highest image is altered such that it climbs up the PES along the path with the least gradient, until it reaches the saddle point. There is no need to employ a large number of intermediate images. Using such a correction on the high energy image allows for a more precise TS. Thus, the addition of intermediate images raises the computational cost without enhancing the accuracy of the final TS, resulting in a waste of effort.

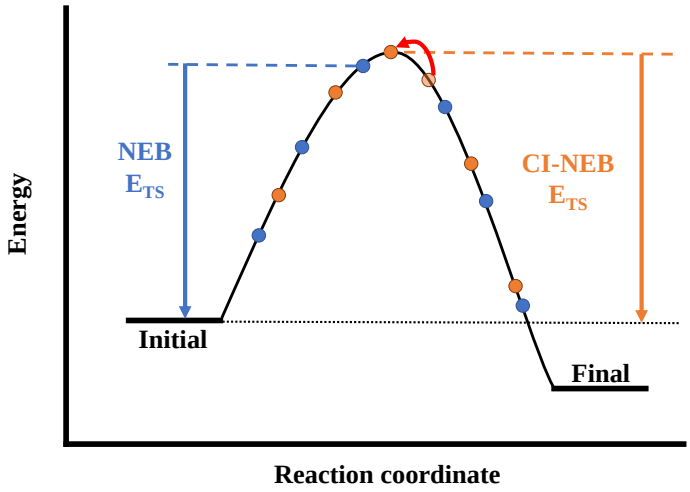


**Figure 3.7: NEB and CI-NEB schematic representation**. The six images of the NEB are represented in blue spheres while the five images of the CI-NEB are represented in orange spheres. The orange transparent sphere is added to exemplify the effect of the CI-NEB method at highest energy image.

**Dimer method.** The Dimer method for identifying saddle points implies working with two pictures (a dimer) of the same system that have nearly identical coordinates but are offset by a defined distance.[24,25] The saddle point search implies advancing the dimer uphill on the PES, from the starting state potential energy minimum to a saddle point. The dimer is rotated along the route to discover the lowest curvature mode of the potential energy at the location where it is positioned. When such a mode is found, the dimer proceeds in that direction. This procedure is repeated until the saddle point is found. The convergence of the saddle point is set minimizing the forces acting on each dimer atoms. Usually the net force resulting of this procedure fits the lowest curvature PES path but acts towards a minimum. In such scenario, the final force is inverted to ensure that dimer moves uphill the curve. One of the major benefits of the Dimer technique is that it allows to start from any beginning configuration and search for a nearby saddle point without knowing the endpoint of the reaction under investigation. It may also take less computing work than a NEB calculation with

many pictures, because the latter are explicitly computed at each stage of the NEB run. Nevertheless, if the initial guess is not close to a saddle point, the Dimer method can lead to TS unrelated to the reaction under discussion.

**Improved dimer method.** Instead of beginning with a dimer generated by two nearby structures, the Improved dimer method[26] allows to begin with a unique geometry. The dimer complex is formed by employing the finite differences of the initial structure's vibration. This limited displacement can be delivered pointing towards the TS direction, and hence accelerating the desired TS discovery.

A mixture of these strategies was employed in this thesis. The CI-NEB approach was used to determine the TS directly, and when it was not enough accurate, the TS was refined using the Improved dimer method.

### 3.1.5 Surface Phase Diagrams

When studying solid-gas heterogeneous catalysis, as the one in Figure 3.2, is of crucial importance to determine the most stable catalytic phase, *i.e.* the solid surface, under reaction conditions. The surface phase diagram indicates the thermodynamic equilibrium surface structure in contact with a given gaseous environment and different conditions of temperature, T, and pressure, $p$. From a theoretical point of view this is achieved by using the *ab initio* thermodynamics formalism developed by Reuter and Scheffler.[27,28] In a typical surface diagram the logarithm of the gas pressure divided by the standard pressure, $\log(p_s/p^\circ)$, is represented on the vertical axis and the T on the horizontal one. The different areas in the diagram correspond to different surface structures, and the lines indicate where two structures are in thermodynamic equilibrium. This implies that the Gibbs free energy of surface structures A and B at a given T and $p$ are equal, *i.e.*, $G_A(T,p) = G_B(T,p)$, or, employing a given reference state for A and B, when the relation $\Delta G_A(T,p) = \Delta G_B(T,p)$ is met. The free energy of the a solid-gas system can be obtained by accounting for the contributions of each part of the system. Thus, the free energy can be determined as the sum of

the free energy of bulk of the solid, $G_{solid}$, the gas-phase, $G_{gas}$, and the surface formation, $\Delta G_{surface}$.

$$G = G_{solid} + G_{gas} + G_{surface}\,. \tag{3.16}$$

When we move deep into the solid and the gas phase there is a distance where the $G_{solid}$ and $G_{gas}$ remain unaffected by the surface. Therefore, within the same finite portion of the system, independently from the surface state, such values will be constant and consequently neglected when computing free energy differences. Moreover, if the reference is chosen to be the clean surface the equation can be further simplified. As the surface free energy of creating the clean metal surface will be equal for all systems such term can be cancelled when computing differences. The remaining term of the $G_{surface}$ will be the free energy contribution of the different coverages that can be form, in other words, the $G_{surface}$ from 3.16 becomes $\Delta G_{ads}$. Moreover, the entropic configurations of the adsorptions are neglected for simplicity as they do not affect qualitatively the surface phase diagrams.[29]

$$\Delta G_{ads}(T,p) = -\frac{1}{A}\left(\Delta E_{ads} + \Delta E_{ZPE} - N_s \Delta\mu_s(T,p)\right)\,, \tag{3.17}$$

where $\Delta E_{ads}$ and $\Delta E_{ZPE}$ are computed as Eq. 3.10 and 3.14 respectively. $N_s$ is the number of adsorbates and $\Delta\mu_s(T,p)$ is the chemical potential of the s specie determined by the condition of thermodynamic equilibrium with the surrounding gas phase reservoir of s. Finally, the $-1/A$ term is introduced to normalize the energy respect to the surface area (A is the surface area of the simulated cell) and the sign stands to transform the most favorable negatives energies to positive ones, facilitating its interpretation. When simulating systems with more than one different adsorbate, *i.e.* s = 1, 2, 3, ..., N. Eq.3.17 has to be account for each specie.

Finally $\Delta\mu_s$ can be calculated as,[29]

$$\Delta\mu_{\mathrm{s}}(\mathrm{T},p) = -k_{\mathrm{B}}\Bigg\{ ln\left[\left(\frac{2\pi m_{\mathrm{s}}}{h^2}\right)^{\frac{3}{2}}\frac{(k_{\mathrm{B}}\mathrm{T})^{\frac{5}{2}}}{p_{\mathrm{s}}}\right] + ln\left(\frac{k_{\mathrm{B}}\mathrm{T}}{\sigma_{\mathrm{s}}^{sym}\mathrm{B}_{0,\mathrm{s}}}\right) - \sum_{i}^{n} ln\left[1 - exp\left(\frac{-\hbar v_{i,\mathrm{s}}}{k_{\mathrm{B}}\mathrm{T}}\right)\right] + ln\left(\mathrm{I}_{\mathrm{s}}^{spin}\right)\Bigg\}. \tag{3.18}$$

where $k_{\mathrm{B}}$ is the Boltzmann's constant, $m_{\mathrm{s}}$ is the mass of the molecule s, $h$ is the Planck's constant, $p_{\mathrm{s}}$ is the partial pressure of $p$, $\sigma_{\mathrm{s}}^{sym}$ is th classical symetry number of s,[30] $\mathrm{B}_{0,\mathrm{s}}$ is the rotational constant of s, $\hbar$ is the reduced Planck's constant, $v_{i,\mathrm{s}}$ are the vibrational normal modes of the gas molecule s, and $\mathrm{I}_{\mathrm{s}}^{spin}$ is the ground-state electronic spin degeneracy of s.

The translational free energy is calculated as the translational partition function in the classical limit, assuming ideal gas phase behavior in the first summand of the Eq. 3.18. The rotating free energy is determined as the rotational partition function inside the rigid rotator approximation in the second summand. The vibrational free energy, estimated as the vibrational partition function in the harmonic approximation, is represented by the third summand. There is a missing negative sign in earlier literature,[29] which is appropriately incorporated in this work. Finally, the nuclear and electronic free energy, where the ground-state spin degeneracy is the only important term correspond to the fourth summand.

The only remaining step is to build a surface phase diagram is to draw a 3D plot with the computed $\Delta\mathrm{G}(\mathrm{T},p)$ values and to project it onto the $(\mathrm{T},p)$ plane of more positive Gibbs free energy, resulting in a 2D plot with $\log(p_{\mathrm{s}}/p^{\circ})$ and T as descriptors on the $x$ and $y$ axes, respectively.

### 3.1.6 Kinetic Phase Diagrams

The surface thermodynamic diagrams shown above are a good method for determining the relative thermodynamic stability of a particular surface covering. However, all kinetic factors are ignored in this methodology. In reactions where thermodynamic equilibrium is quickly achieved, *i.e.* energy barriers are small,

introducing the kinetic aspect has no effect on the overall picture obtained by the surface thermodynamic approach; however, for reactions with large barriers, the impact generated by its consideration could indeed cause meaningful changes.

From a theoretical point of view this is achieved by using mirokinetic simulations based on DFT-determined elementary reaction steps. The aim is to determine the reaction conditions of temperature and partial pressure, under which the surface will be covered in a desired manner. In a typical kinetic phase diagram the logarithm of the gas pressure divided by the standard pressure, $\log(p_s/p^\circ)$, is represented on the vertical axis and the T on the horizontal one. The different areas in the diagram correspond to different surface coverage evaluated. When one considers the simple adsorption and dissociation of a diatomic gas molecule, as $H_2$, the kinetic model consists in two bidirectional steps: $A_2 \rightleftharpoons A_2^* \rightleftharpoons 2A^*$. Each of such steps is described different at the microkinetic simulations. For the gas adsorption and desorption we make use of the rates derivated from the gas theory via Hertz-Knudsen equation and for the dissociation and recombination processes happening at the catalyst surface we use statistical thermodynamics via the transition state theory.

The adsorption is computed deriving the Hertz-Knudsen equation,

$$F = \frac{p}{\sqrt{2\pi m_A k_B T}}\,, \tag{3.19}$$

and from Eq. 3.19 is possible to derive the molecular adsorption rate, expressed as,

$$k_{ads} = \frac{p A S}{\sqrt{2\pi m_A k_B T}}\,, \tag{3.20}$$

where $p$ is the partial pressure of the molecular specie and S is the sticking coefficient of such species over the studied surface. When no precise data is available is recommendable to use low conservative values to avoid overestimation. A is the surface area of a single adsorption site, $A = \frac{surface\ area}{nº\ of sites}$, $m$ is the molecular mass and $k_B$ the Boltzmann constant.

The desorption can be computed as:[31]

$$k_{\mathrm{des}} = \frac{k_{\mathrm{B}}\mathrm{T}^3\mathrm{A}(2\pi k_{\mathrm{B}})}{h^3\sigma^{sym}\theta_{rot}} e^{-\frac{\mathrm{E}_{\mathrm{des}}}{k_{\mathrm{B}}\mathrm{T}}} , \tag{3.21}$$

where $\sigma^{sym}$ and $\theta_{rot}$ are the symmetry number and the rotational temperature of the gas molecule studied, respectively.

As mentioned above the kinetic rates for the surface $A_2$ dissociation and recombination processes can be obtained by TST. Adsorbed molecules only have vibrational degrees of freedom and their forward and backwards rates can be estimated by:

$$k = \frac{k_{\mathrm{B}}\mathrm{T}Q^{\mathrm{TS}}}{hQ} e^{-\frac{\mathrm{E}_a}{k_{\mathrm{B}}\mathrm{T}}} , \tag{3.22}$$

where $Q$ and $Q^{\mathrm{TS}}$ are the vibrational partition functions of the initial and TS states and $\mathrm{E}_a$ is the DFT activation energy or the barrier of the process. Once all the reaction rates are determined, we performed the microkinetic simulations using the MKMCXX program.[31] We started the simulations with the surface clean and let the process advance until the stationary state, or the kinetic equilibrium, is reached. From them is possible to obtain the coverage conditions at chosen T and $p$. Once the coverage of interest is selected we made several simulations at different $p$ to determine between which T range the surface will have the desired coverage for the studied reaction.

## 3.2 Electrochemical Systems

Electrocatalysis is the heterogeneous catalysis of electrochemical processes that takes place at the electrode-electrolyte interface and in which the electrode serves as both an electron donor/acceptor and a catalyst. By transforming chemical energy into electrical energy, electrochemical methods for clean energy generation, conversion, and storage are a viable technique for reducing our contemporary

society dependency on fossil fuels.[32–34] Active, selective, and long-lasting catalysts that enhance the kinetics of electrochemical processes are required to move these promising technologies from the scale of basic research to real-world applications.[35] However, numerous issues such as poor catalytic efficiency, limited selectivity, and high prices must yet be solved.[36] To that end, the electrocatalysis scientific community has made significant efforts to uncover fundamental reaction mechanisms and structure-activity relationships, which are now used to guide the fine-tuning of electrocatalyst composition, size, and morphology in order to achieve high activity and selectivity at reasonable costs.[37–39]

As mentioned above, the optimal catalytic surface for a given reaction, according to the *Sabatier principle*, should have an ideal adsorption strength for the reaction intermediates that is neither too strong nor too weak,[8] finding a subtle equilibrium between enhancing the formation of such intermediates and the obtention of the final products. Consequently, the description of the electrode surface and its behaviour with the environmental chemical solution has a critical importance for a proper theoretical and computational description.[40,41] An ilustrative example of how experimental and computational studies can work through such difficulties and the huge impact that the surface structure may have, is the case of the typical electrocatalytic reaction, Hydrogen Evolution Reaction (HER) over $Mo_2S$. $MoS_2$ was initially believed not active for HER,[42] however when further studies related the ideal HER activity with the computational descriptor of $\Delta G_H = 0$ it was shown[43] that meanwhile the bulk surface of $MoS_2$ present a $\Delta G_H$ of 1.92 eV,[44] highly inactive, the edges of the same $MoS_2$ present a $\Delta G_H$ of 0.08 eV.[45] After such findings, a catalyser of $MoS_2$ supported on carbon black support exposing $MoS_2$ edges was synthetized and become the most active non-precious metal catalyser for HER until that date.[46] Moreover, soon after it was confirmed experimentally that the current active sites of the HER over $MoS_2$ where the edges.[47,48] Distinctly from the heterogeneous catalytic reactions, electrocatalytic reactions take place under a diversity

of current densities and acidity conditions, and they may also have an impact on the electrode surface and thus, may affect its selectivity or/and performance.

### 3.2.1 Computational Hydrogen Electrode

As mentioned at the section above, when simulating computational electrochemical systems, many interactions between the reactants, the catalysits and the solvent are present. Accordingly, such interactions have to be incorporate to the simulations. A crucial modelling singularity of the electrochemical systems is how to treat the electron-proton transfer that occurs at each electrochemical step. Nørskov and coworkers proposed an elegant and nowadays frequently applied method of how to relate the gas-phase energetics of gaseous hydrogen to the free energy of a proton and the electrode potential, also referred as the computational hydrogen electrode (CHE) in the literature.[49] Specifically, based on the the redox couple $H^+/H_2$, which is known from experimental electrochemistry as Standard Hydrogen Electrode (SHE), when $H_2$ gas with a pressure of 1 bar is in equilibrium with a solution of protons of activity 1 at 298.15 K,

$$H^+_{(aq)} + e^- \rightleftharpoons \frac{1}{2}H_{2(g)}\,. \tag{3.23}$$

Under equilibrium conditions then, the process in Eq. 3.23 obeys $\Delta G = 0$, and thus we infer:

$$\mu\left(H^+_{(aq)}\right) + \mu\left(e^-\right) = G\left(H^+_{(aq)}\right) + G\left(e^-\right) = \frac{1}{2}G\left(H_{2(g)}\right)\,, \tag{3.24}$$

where $\mu\left(H^+_{(aq)}\right)$ and $\mu\left(e^-\right)$ are the chemical potential of the hydrated proton and electron, respectively. However, such statement present a clear limitation as it assume that the electron-proton transfer is coupled, *i.e.* when a proton is transferred so it is and electron. As a consequence it is not possible to calculate thermodynamic barriers beyond $U = 0$ without any further analysis as non-integer electron transfer are not accountable. The CHE, thus assumes than the proton and the electron are transferred at the same elementary step, however this

it might not be true.[50] Moreover, to account precisely the electron contribution to the changing molecule along the reaction path, as it can be split between the old and the new surface configurations we need to introduce a non-integer electron transfer variable, $\epsilon$, despite we keep number the total electrons quantified. Therefore, we can define the adsorption of an hydrogen atoms as,

$$\mathrm{H}^{+}_{(\mathrm{aq})} + * + (1+\epsilon)e^{-} \rightleftharpoons \mathrm{H}^{*}\,, \tag{3.25}$$

where * denotes a free active site and H* the Hydrogen already adsorbed. Under such assumption and expressed at SHE scale the free energy of such process at a given potential, $\phi$, will be,[51]

$$\Delta \mathrm{G}^{\phi}_{\mathrm{path}} = \mu^{\phi}\left(\mathrm{H}^{*}\right) - \mu^{\phi}\left(*\right) - \epsilon\mu^{\phi}\left(e^{-}\right) - \mu^{\circ}\left(\frac{1}{2}\mathrm{H}_{2(\mathrm{g})}\right) + e\phi\,, \tag{3.26}$$

where $\mu^{\phi}\left(\mathrm{H}^{*}\right)$ is the chemical potential of the adsorbed Hydrogen, $\mu^{\phi}\left(*\right)$ is that of the surface with the free active site, $\epsilon\mu^{\phi}\left(e^{-}\right)$ is that of non-integer electron transfer at a chosen place of the reaction path, $\mu^{\circ}\left(\frac{1}{2}\mathrm{H}_{2(\mathrm{g})}\right)$ is that of half of the hydrogen gas molecule and $e\phi$ is the contribution of the applied potential. Note that the decoupled computational electrode can be easily readjusted to the conventional CHE by forcing $\epsilon = 0$. Regardless this limitation, the CHE permits us the treat with simplicity the energetic of many electrochemical processes, allowing the construction of free energy diagrams, Pourbaix diagrams or other kinetic properties as the exchange current density *via* theoretical Tafel plots construction, as it will be explained above by performing affordable and accurate gas-phase calculations.

### 3.2.2 Pourbaix Diagrams

The Pourbaix diagrams are similar to the standard surface phase diagrams detailed at the previous section 3.1.5 but indicate the thermodynamic equilibrium surface structure under different conditions of pH and applied over potential,

$U$, normally at a given temperature — *e.g.*, 25 °C, pressure — *e.g.*, 1 bar for gas phase components, and activity of 1 for all components of the liquid phase at such defined standard conditions. In a typical Pourbaix diagram, $U$ is represented on the vertical axis and the pH on the horizontal one. The different areas in the diagram correspond to different surface structures, and the lines indicate where two structures are in thermodynamic equilibrium. Equivalently that in section 3.1.5 this implies that the Gibbs free energy of surface structures A and B at a given pH and $U$ are equal, *i.e.*, $\mathrm{G_A(pH},U) = \mathrm{G_B(pH},U)$, or, employing a given reference state for A and B, when the relation $\Delta\mathrm{G_A(pH},U) = \Delta\mathrm{G_B(pH},U)$ is met.

Thus, the construction of a theoretical Pourbaix diagram implies deriving $\mathrm{G(pH},U)$ or $\Delta\mathrm{G(pH},U)$ values for the possible surface structures for a broad range of pH and $U$. Pourbaix diagrams are clearly required to understand the equilibrium structure under reaction conditions, which is a crucial component in the analysis of any electrocatalytic processes employing a specific electrode. The primary principle behind constructing Pourbaix diagrams is as follows: One of the researched surface models is utilized as a reference. In a typical scenario the pristine surface serves as the reference structure. Reaction equations describe the development of adsorbates on the electrode surface, which is related to the clean surface. Please note that any adsorption process can be written as,

$$\sum_i \Delta v_1 A_i = 0\,, \tag{3.27}$$

where $v_i$ and $A_i$ indicate stochiometric coefficients and reactants or products respectively. Eq. 3.28 shows how the change in Gibbs free energy for such an adsorption process may be stated in a generic form,

$$\Delta\mathrm{G} = \mathrm{G_{surf\text{-}ads}} - \mathrm{G_{surf}} - n\mathrm{G_{ads}}\,. \tag{3.28}$$

The right hand side terms ($\mathrm{G_{surf\text{-}ads}}$, $\mathrm{G_{surf}}$, and $\mathrm{G_{ads}}$) denote the free energy of the surface covered by a particular ordered structure containing $n$ ad-

sorbates, the clean surface, and $n$ times the adsorbates. As mentioned at the above section 3.1.5, gas phase molecules provide reference states of the unbound adsorbates at a solid-gas interface. However, in electrochemical systems at the solid/liquid boundary, the adsorbates may not exist in the gas phase or may be radical in character. By means of DFT calculations, it is much easier to calculate the free energy of a gaseous molecule rather than of a molecule in an aqueous environment. This stays true even for water molecules themselves, where for simulating properly liquid water it is necessary the inclusion of hydrogen-bonding interaction between several water molecules, whereas water vapor can be easily simulated.

As a result, introducing a collection of gas-phase reference structures, pertaining to adsorbates found in the electrochemical environment studied, to simulate the adsorbates in aqueous environment is a unified standard. For instance the reference for the $H^+_{(aq)}$ is the already explained SHE conditions or the reference for the common adsorbates O and OH does not refer to the gaseous oxygen molecule but rather to the water molecule at 298.15 K and 0.035 bar, because under these conditions, water vapor is in equilibrium with liquid water, *i.e.*, their chemical potentials are identical.[49]

Similarly to the construction of surface phase diagrams, all surface structures are evaluated by reaction equations, referenced to the clean structure. Rewriting Eq. 3.28 relating to the adsorption process for the formation of any surface phase yields,

$$\Delta G = G_{\text{surf-ads}} - G_{\text{surf}} - n\Delta G_{\text{ads}}\,, \tag{3.29}$$

where the sole difference between Eq. 3.28 and Eq. 3.29 is in the last right-hand side component, which is the adsorbate free energy relative to the selected reference. In the derivation of Eq. 3.29 we did not account for neither pH nor $U$, or, equivalently, we assumed that both are zero, which we indicate as $\Delta G(0,0)$. Assuming that the only contribution to entropy is related to the adsorbates, Eq.

3.29 becomes Eq. 3.13, repeated here for the convenience of the reader,

$$\Delta \mathrm{G}(0{,}0) = \Delta \mathrm{G}_{\mathrm{ads}} = \Delta \mathrm{E}_{\mathrm{total}} + \Delta \mathrm{E}_{\mathrm{ZPE}} - \mathrm{T}\Delta \mathrm{S}\,, \tag{3.30}$$

Note that $\Delta \mathrm{E}_{\mathrm{total}}$ is defined as the Eq. 3.10 at the section 3.1.2 but without normalizing by the numeber of adsorbates,

$$\Delta \mathrm{E}_{\mathrm{total}} = \mathrm{E}_{\text{surf-}ns} - (\mathrm{E}_{\mathrm{surf}} + n\mathrm{E}_{\mathrm{s}})\,. \tag{3.31}$$

$\Delta \mathrm{E}_{\mathrm{ZPE}}$ and $\mathrm{T}\Delta \mathrm{S}$ at Eq. 3.14 and Eq. 3.15 at section 3.1.3. Given the above, the only remaining point now is introducing the potential relative to the SHE and the pH in Eq. 3.30, which is achieved by making use of the CHE model, see Eq. 3.24 at Section 3.2.1. From the reaction equation to form a certain adsorbate structure with respect to the clean surface reference, the number of transferred protons, $\nu(\mathrm{H}^+)$, and electrons, $\nu(\mathrm{e}^-)$, can be deduced. This information is key for the construction of a Pourbaix diagram because the effect of $U$ and pH is not explicitly accounted for in the DFT calculations, but rather is addressed in the form of an a posteriori analysis. Applying an electrochemical thermodynamic approach,[52] we obtain,

$$\Delta \mathrm{G}(\mathrm{pH},U) = \Delta \mathrm{G}(0,0) - \nu(\mathrm{H}^+)k_{\mathrm{B}}\mathrm{T}(ln10)\mathrm{pH} - \nu(e^-)eU\,, \tag{3.32}$$

where $e$ is the elementary charge of an electron and $U$ is the applied electrode potential with respect to the SHE.

To create a surface Pourbaix diagram, all that is left to do is create a 3D plot using the calculated $\Delta \mathrm{G}(\mathrm{pH},U)$ values and project it onto the plane of pH and $U$ with the lowest Gibbs free energy. This creates a 2D plot with pH and $U$ as descriptors on the $x$ and $y$ axes, respectively.

### 3.2.3 Computational Tafel Plot

To study the kinetic of an electrochemical reaction one can use the computational Tafel plots. Tafel plots are the graphical representation of the corresponding Tafel equation relating the rate of an electrochemical reaction, estimated from the current density, to the applied overpotential. Commonly, Tafel plots represent the $log_{10}$ of the current density, as a function of the applied overpotential. The Tafel equation is applied to both half reactions of an electrochemical reaction and can be derived as approximation for sufficiently large overpotentials from the Butler-Volmer theory as:[53,54]

$$log_{10} j(\eta) = log_{10} j_0 + \frac{\eta}{b}\,, \tag{3.33}$$

where $j(\eta)$ and $j_0$ are the current density as a function of the overpotential, $\eta$, and the exchange current density, respectively, and $b$ is Tafel slope, as this equation establishes a linear relation between the applied overpotential and the current density. The Tafel slope contains information about the transfer coefficient which play a role in the description of the kinetics of the process.

The analysis and interpretation of the Tafel Plots can offer insight of the ongoing kinetics, although this involves a quite complex process and several assumptions must be considered. For the simplest two electrons transfer reaction, two main scenarios can be considered, either quasi-equilibrium or steady-state approximations. The quasi-equilibrium approximation assumes that the coverage of the RI remains essentially constant upon rising overpotential. Consequently, the binding energy of the RI does not appear to play a role and is not taken into consideration. With this assumption, the extraction of kinetic parameters, such as the exchange current density and transfer coefficient from Tafel plots with a single linear Tafel line may be fairly done but this is not the case for Tafel plots featuring a change in the Tafel slope.[55] The steady-state approximation offers an alternative even in these cases. Here, one assumes that, at a given overpotential, the RI is generated as fast as it is consumed. Consequently, the concentration

of such species remains constant but depends on the overpotential applied. Under this hypothesis, one can determine the time-dependent RI concentration as described by Eq. 3.34,

$$\left(\frac{d([RI]}{dt}\right)_{\eta} = k_1(\eta)[IS] + k_{-2}(\eta)[FS] - k_{-1}(\eta)[RI] - k_2(\eta)[RI]\,, \tag{3.34}$$

which follows from the overall reaction mechanism as described by Eq. 3.35 and Eq. 3.36,

$$IS \underset{k_{-1}}{\overset{k_1}{\rightleftharpoons}} RI\,, \tag{3.35}$$

$$RI \underset{k_{-2}}{\overset{k_2}{\rightleftharpoons}} FS\,, \tag{3.36}$$

where $k_1(\eta)$ and $k_{-1}(\eta)$ are the rate forward and backward constants of the reaction in Eq. 3.35, $k_2(\eta)$ and $k_{-2}(\eta)$ are the rate forward and backward constants of the reaction in Eq. 3.36, and $[IS]$, $[FS]$, and $[RI]$ are the concentrations of the initial state, final state and the reaction intermediate.

As the typical electrochemical reaction is catalysed by a solid electrode, all the RI will be adsorbed species and thus, their concentration is also given by their coverage at the electrode surface. Moreover, given the nature of IS and FS, we can redefine [IS] and [FS] as $\theta_S$, and [RI] as $\theta_{(S-ads)}$. In this $\theta_S$ scenario corresponds to the initial coverage of free sites at the studied surface and $\theta_{(S-ads)}$ to the coverage of the adsorbed specie at such initial surface. To respect the balance of active sites and the steady state approximation conditions, the two conditions as in Eq. 3.37 and Eq. 3.38 must be fulfilled.

$$r(\eta) = \left(\frac{d([RI]}{dt}\right)_{\eta} = 0\,, \tag{3.37}$$

$$\theta_S(\eta) + \theta_{S-ads}(\eta) = 1\,, \tag{3.38}$$

where the definition of the reaction rate is,

$$r(\eta) = \frac{d[FS]}{dt} = k_2(\eta) \cdot \theta_{S-ads}(\eta) - k_{-2}(\eta) \cdot \theta_S(\eta)\,. \tag{3.39}$$

Then, one can rewrite the reaction rate expression in Eq. 3.34 as,

$$\begin{aligned} r(\eta) = & \frac{k_1(\eta) \cdot k_2(\eta)}{k_1(\eta) + k_{-1}(\eta) + k_2(\eta) + k_{-2}(\eta)} \\ & - \frac{k_{-1}(\eta) \cdot k_{-2}(\eta)}{k_1(\eta) + k_{-1}(\eta) + k_2(\eta) + k_{-2}(\eta)}\,. \end{aligned} \tag{3.40}$$

Finally, it is convenient to translate this reaction rate into the current density,

$$j(\eta) = n \cdot e \cdot r(\eta) \cdot \Gamma_{act}\,. \tag{3.41}$$

The substitution of the expression of $r(\eta)$ in Eq. 3.40 into Eq. 3.41 leads, after some algebra to Eq. 3.42. We additionally make use of the assumption that only the forward reaction is accounted for in the Tafel regime ($\eta > 0.03$ V), because the overpotential applied is large enough to fairly neglect the backward reaction.

$$\begin{aligned} j(\eta) = & \frac{2k_{\mathrm{B}}\mathrm{T}e\Gamma_{act}}{h} \\ & \cdot \frac{exp\left(\frac{(\alpha_1+\alpha_2)\eta e}{k_{\mathrm{B}}\mathrm{T}}\right)}{exp\left(\frac{\mathrm{G}_1^{TS}+\alpha_2\eta e}{k_{\mathrm{B}}\mathrm{T}}\right) + exp\left(\frac{\mathrm{G}_2^{TS}-(1-\alpha_1)\eta e}{k_{\mathrm{B}}\mathrm{T}}\right) + exp\left(\frac{\mathrm{G}_1^{TS}-\Delta\mathrm{G}_{RI}+\alpha_1\eta e}{k_{\mathrm{B}}\mathrm{T}}\right)}\,, \end{aligned} \tag{3.42}$$

where $k_{\mathrm{B}}\mathrm{T}$ is the Boltzmann's constant times the temperature, $h$ is the Planck's constant, $e$ is the elementary charge, $\Gamma_{\mathrm{act}}$ is the density of active sites in $\mathrm{cm}^{-2}$, defined as $\Gamma_{act} = \frac{n^{o}\ of sites}{surface\ area}$, (the inverse of A defined at section 3.1.6 ) $\alpha_1$ and $\alpha_2$ are the partial charge transfer of the first and second steps, $\mathrm{G}_1^{TS}$ and $\mathrm{G}_2^{TS}$ are free energies of TS respect to the initial state, and finally, $\Delta\mathrm{G}_{RI}$, the free

energy of the reaction leading to the intermediate at $\eta = 0$. In order to facilitate the calculations and to compare to experimental values, $j(\eta)$ is not expressed in SI but in A/cm$^{-2}$. Note that to make use of Eq. 3.42 it is necessary to know the $\Delta$G of the RI together with $\Delta G^{TS}$. Hence, from Eq. 3.42 it is possible to estimate the rds along any $\eta$ and, thus, simulate all the Tafel lines. Note that $\Delta$G can be obtained as in Eq. 3.32 in section 3.2.2. As the pH remains constant that term can be neglected and finally, the final expression can be simplified as,

$$\Delta G = \Delta G_0 - (n \cdot e \cdot \eta)\,, \tag{3.43}$$

where $n$ would be equivalent to the stoichiometric number of transferred electrons in the reaction and $\eta$ to the applied overpotential from the Eq. 3.32.

## References


[1] K. J. Laidler, *Pure Appl. Chem.*, 1996, **68**(1), 149–192.

[2] J. J. Berzelius, *Edimbg. New Phylos. Joounal*, 1836, **XXI**, 223–236.

[3] J. Wisniak, *Educ. Quim.*, 2010, **21**(1), 60–69.

[4] J. N. Armor, *Catal. Today*, 2011, **163**(1), 3–9.

[5] S. Chu and A. Majumdar, *Nature*, 2012, **488**(7411), 294–303.

[6] D. G. Nocera and N. S. Lewis, *Proc. Natl. Acad. Sci. U.S.A*, 2006, **103**(42), 15729–15735.

[7] Z. Ma and F. Zaera, *Encyclopedia of Inorganic and Bioinorganic Chemistry*, John Wiley & Sons, Ltd., Hoboken, 2011.

[8] P. Sabatier, *La Catalyse en Chimie Organique*, Béranger, Paris, 2nd ed., 1920.

[9] H. S. Taylor, *Proc. R. Soc. A Math. Phys. Eng. Sci.*, 1925, **108**, 105–111.

[10] A. Clearfield and D. S. Thakur, *Appl. Catal.*, 1986, **26**, 1–26.

[11] C. Geantet, J. Afonso, M. Breysse, N. Allali, and M. Danot, *Catal. Today*, 1996, **28**(1-2), 23–30.

[12] C. M. Domínguez, P. Ocón, A. Quintanilla, J. A. Casas, and J. J. Rodriguez, *Appl. Catal. B Environ.*, 2014, **144**, 599–606.

[13] M. Nolan, S. C. Parker, and G. W. Watson, *Phys. Chem. Chem. Phys.*, 2006, **8**(2), 216–218.

[14] J. A. Rodriguez, J. Evans, L. Feria, A. B. Vidal, P. Liu, K. Nakamura, and F. Illas, *J. Catal.*, 2013, **307**, 162–169.

[15] X. Wang, Z. Li, Y. Qu, T. Yuan, W. Wang, Y. Wu, and Y. Li, *Chem*, 2019, **5**(6), 1486–1511.

[16] F. Viñes, J. R. Gomes, and F. Illas, *Chem. Soc. Rev.*, 2014, **43**(14), 4922–4939.

[17] F. Bloch, *Zeitschrift für Phys.*, 1929, **57**, 545–555.

[18] D. Wolf in *Comput. Simul. Stud. Condens. Matter Phys. VIII;* 1995.

[19] D. R. Lide, *CRC Handbook of Chemistry and Physics*, CRC Press, Boca Raton, 2005.

[20] M. López, F. Viñes, M. Nolan, and F. Illas, *J. Phys. Chem. C*, 2020, **124**(29), 15969–15976.

[21] J. W. Ochterski, Thermochemistry in Gaussian, 2000.

[22] G. Mills and H. Jónsson, *Phys. Rev. Lett.*, 1994, **72**(7), 1124–1127.

[23] G. Henkelman, B. P. Uberuaga, and H. Jónsson, *J. Chem. Phys.*, 2000, **113**(22), 9901–9904.

[24] G. Henkelman and H. Jónsson, *J. Chem. Phys.*, 1999, **111**(15), 7010–7022.

[25] R. A. Olsen, G. J. Kroes, G. Henkelman, A. Arnaldsson, and H. Jónsson, *J. Chem. Phys.*, 2004, **121**(20), 9776–9792.

[26] A. Heyden, A. T. Bell, and F. J. Keil, *J. Chem. Phys.*, 2005, **123**(22), 224101.

[27] K. Reuter and M. Scheffler, *Phys. Rev. B - Condens. Matter Mater. Phys.*, 2001, **65**(3), 035406.

[28] K. Reuter and M. Scheffler, *Phys. Rev. Lett.*, 2003, **90**(4), 046103.

[29] J. Rogal and K. Reuter, *Educ. Notes*, 2007, **2**, 1–18.

[30] M. K. Gilson and K. K. Irikura, *J. Phys. Chem. B*, 2010, **114**(49), 16304–16317.

[31] I. Filot, *Introduction to Microkinetic Modeling*, 2018.

[32] Y. Yang, M. Luo, W. Zhang, Y. Sun, X. Chen, and S. Guo, *Chem*, 2018, **4**(9), 2054–2083.

[33] J. O. Bockris, *Int. J. Hydrogen Energy*, 2013, **38**(6), 2579–2588.

[34] S. Gu, B. Xu, and Y. Yan, *Annu. Rev. Chem. Biomol. Eng.*, 2014, **5**, 429–454.

[35] Z. W. Seh, J. Kibsgaard, C. F. Dickens, I. Chorkendorff, J. K. Nørskov, and T. F. Jaramillo, *Science (80-. ).*, 2017, **355**(6321), eaad4998.

[36] M. K. Debe, *Nature*, 2012, **486**(7401), 43–51.

[37] V. R. Stamenkovic, B. S. Mun, M. Arenz, K. J. Mayrhofer, C. A. Lucas, G. Wang, P. N. Ross, and N. M. Markovic, *Nat. Mater.*, 2007, **6**(3), 241–247.

[38] V. R. Stamenkovic, D. Strmcnik, P. P. Lopes, and N. M. Markovic, *Nat. Mater.*, 2017, **16**, 57–69.

[39] M. Luo and S. Guo, *Nat. Rev. Mater.*, 2017, **2**, 17059.

[40] J. K. Nørskov, T. Bligaard, J. Rossmeisl, and C. H. Christensen, *Nat. Chem.*, 2009, **1**(1), 37–46.

[41] B. Wu and N. Zheng, *Nano Today*, 2013, **8**(2), 168–197.

[42] W. Jaegermann and H. Tributsch, *Prog. Surf. Sci.*, 1988, **29**(1-2), 1–167.

[43] J. K. Nørskov, T. Bligaard, A. Logadottir, J. R. Kitchin, J. G. Chen, S. Pandelov, and U. Stimming, *J. Electrochem. Soc.*, 2005, **152**(3), J23.

[44] C. Tsai, K. Chan, F. Abild-Pedersen, and J. K. Nørskov, *Phys. Chem. Chem. Phys.*, 2014, **16**(26), 13156–13164.

[45] B. Hinnemann, P. G. Moses, J. Bonde, K. P. Jørgensen, J. H. Nielsen, S. Horch, I. Chorkendorff, and J. K. Nørskov, *J. Am. Chem. Soc.*, 2005, **127**(15), 5308–5309.

[46] Y. Wang, Z. Wang, Q. Yang, A. Hua, S. Ma, Z. Zhang, and M. Dong, *New J. Chem.*, 2019, **43**(16), 6146–6152.

[47] H. Wang, Q. Zhang, H. Yao, Z. Liang, H. W. Lee, P. C. Hsu, G. Zheng, and Y. Cui, *Nano Lett.*, 2014, **14**(12), 7138–7144.

[48] T. F. Jaramillo, K. P. Jørgensen, J. Bonde, J. H. Nielsen, S. Horch, and I. Chorkendorff, *Science (80-. ).*, 2007, **317**(5834), 100–102.

[49] J. K. Nørskov, J. Rossmeisl, A. Logadottir, L. Lindqvist, J. R. Kitchin, T. Bligaard, and H. Jónsson, *J. Phys. Chem. B*, 2004, **108**(46), 17886–17892.

[50] I. Katsounaros, T. Chen, A. A. Gewirth, N. M. Markovic, and M. T. Koper, *J. Phys. Chem. Lett.*, 2016, **7**(3), 387–392.

[51] P. Lindgren, G. Kastlunger, and A. A. Peterson, *ACS Catal.*, 2020, **10**(1), 121–128.

[52] K. S. Exner, J. Anton, T. Jacob, and H. Over, *Electrochim. Acta*, 2014, **120**, 460–466.

[53] J. Tafel, *Zeitschrift für Phys. Chemie*, 1905, **50**, 641–712.

[54] R. Parsons, *Trans. Faraday Soc.*, 1951, **47**, 1332–1344.

[55] K. S. Exner, *Electrochem. Sci. Adv.*, 2022, **2**, e2100037.

Chapter 4:

# Carbon Capture on Doped Titanium Carbide

## 4.1 Introduction

Evidence of the substantial effects of global warming on the Earth is reported with increasing frequency yearly.[1,2] When immediate action is not adopted to counter this issue, environmental prediction models forecast a less-than-optimistic future.[3,4] One of the greenhouse gases having the greatest influence on the environment is atmospheric $CO_2$, whose impacts on the environment are particularly detrimental. In addition to well-known ones like ocean acidification,[5] there are forecasts that, as anthropogenic $CO_2$ emissions increase in the atmosphere, the $CO_2$ concentration and corresponding global warming will increase exponentially due to feedback from the carbon cycle.[4]

Innovative approaches are being investigated regarding the $CO_2$ abatement to deal with this main pressing problem. In particular, $CO_2$ capture and storage (CCS)[6–8] and usage (CCU)[9] technologies are the subject of intensive research. Although adsorption or membrane gas separation are additional options that are still in the development research stage, absorption is now the dominating technology being used in several CCS methods.[7,8,10,11] Due to its significant

industrial and economic potential, CCU technology is gradually advancing by adding more value to the collected $CO_2$.[9] It would be tremendously beneficial for the environment and the industry to add $CO_2$ back into the industrial cycle through industrial processes like hydrogenation to methanol or the reverse water gas shift (RWGS) reaction.

Only a limited few privileged materials can selectively and effectively absorb $CO_2$ strongly enough for CCS or CCU technologies because of the high $CO_2$ chemical stability. Moderate to high $CO_2$ adsorption energies often signify activation of the molecule,[12] which frequently happens as a result of charge transfer from a material's surface to the $CO_2$ $6a_1$ anti-bonding molecular orbital, resulting in the weakening of the C-O bonds and a bent geometry.[13] From this point onwards, the $CO_2^{\delta-}$ molecule, is significantly more reactive than the neutral one which is the starting point for every industrial process to reuse $CO_2$. The main materials studied of choice in the industry within CCU perspective are Ni, Pd, or Pt nanoparticles supported by oxides or sulfides,[14] despite substantial attempts to develop an acceptable oxide support. It is also important to note that relatively recent model system experiments have shown that tiny Au, Cu, and Ni nanoparticles supported on TiC(001) work better in the production of methanol than a model of the traditional Cu/ZnO catalyst.[15,16] Indeed, Transition Metal Carbides (TMCs) have shown to be of particular industrial interest. They can adsorb and activate molecules involved in many foremost reactions such $H_2$, $O_2$, $N_2$, CO and other relevant polyatomic organic molecules containing C-H and C-N bonds.[17] Additionally, it has been shown that bare TMCs, such as MoC and $Mo_2C$, are efficient at catalyzing $CO_2$ activation[18] and conversion.[19] This makes them very desirable since they get around the problem of needing expensive and rare late transition metals.

Indeed, according to computational studies done within the context of DFT, early TMCs including TiC, ZrC, WC, NbC, TaC, and $\delta$-MoC are capable of strongly trapping and activating $CO_2$.[13] In addition, there is experimental and/or computational proof that the surfaces of $\delta$-MoC, $\beta$-$Mo_2C$, WC, and NbC (001)

exhibit remarkable selectivity toward $CO_2$ conversion to CO,[18,20,21] a constituent of synthesis gas utilized in many industrial operations. Furthermore, it is important to note that model catalysts that combine late transition metals with TMCs are very appealing. For instance, $Pt/Mo_2C$ demonstrates superior water gas shift (WGS) performance compared to $Pt/CeO_2$ or $Pt/TiO_2$ catalysts at high rates.[22] In conclusion, TMCs have three essential characteristics that give them a great promise for CCU applications: high $CO_2$ adsorption capacity, competitive catalytic performance, and appealing pricing.

Different approaches to adjusting the surface activity towards $CO_2$ might be considered in the quest for custom-made materials for CCS and/or CCU, including the use of surface doping agents. When thinking about the characteristics of metals and metal oxides, this is a typical approach since it allows for the localization of chemical activity or the stabilization of certain facets, as in F-doped $TiO_2$ nanoparticles.[23,24] Additionally, it has been demonstrated that oxygen vacancy generation on $CeO_2$ nanoparticles is encouraged by the presence of surface dopants.[25,26] Additionally, by adding Zr or Ti in large quantities, CO adsorption on ceria may be readily increased, enhancing CO oxidation and releasing $CO_2$ into the environment.[27] Metal alloying is a common, but not yet well understood or regulated, method of controlling surface activity in metals. In the past, step wise reduction of precursor oxides has been used to create bimetallic TMCs utilizing earth-abundant and inexpensive metals, such as $Fe_3Mo_3C$ $Ni_6Mo_6C$,[28] paving the way for an economically sound synthesis method. Furthermore, there have been considerable advancements in our knowledge of nanoalloys,[29] which has made it possible to exercise future control.

Following such mindset, we explored the transition metal doping, or surface metal alloying, on a TMCs surface using the TiC as a textbook example. In order to understand deeper the $CO_2$ adsorption and activation and how the presence of a surface/subsurface doping agent influences its adsorption energy, the work has been divided in two parts that have been published separately. First we considered eight early transition metals, – Zr, Hf, V, Nb, Ta, Cr, Mo, and W –

known for forming TMC with similar electronic properties and behaviour than Ti; secondly, we explored a broad range of atoms from different periodic table groups as *s* block alkaline earth (Mg, Ca, and Sr), *p* block groups XIII (Al, Ga, and In) and XIV (Si and Sn), *d* block late translation metals (Pd, Pt, Rh and Ir), and *f* block lanthanides (La and Ce). The results of both articles are presented together in the following section, at bottom of the 4.2 section are the original articles. The Supporting Information from both articles can be found a the Appendix A and B, respectively.

## 4.2 $CO_2$ Adsorption and Activation on Doped Titanium Carbide

Surface geometry and charge density distortions are the two primary impacts of replacing the Ti atom of the TiC(001) surface with one of the dopants at the surface or beneath atomic layers. These modifications result from the dopants different atomic radii and electrical configurations as compared to Ti. Given that Ti and dopant atoms have different radii, it seems sense that the latter would be better accommodated at surface sites than subsurface ones since lattice distortions are reduced when the dopant occupies a surface site. According to this logic, one would also anticipate that the energetic gap between the surface and subsurface positions would be smaller the closer the dopant is to Ti in the periodic table. This expectation is supported by the calculations shown in Table 4.1, which are also confirmed by experimental evidence. When this circumstance is coupled with a desired chemical activity, the preference for replacement at surface sites may be advantageous for catalytic reasons. This discovery implies that it is consequently feasible to alter the TMC surface chemistry.

The energy cost for cation exchange, indicated above by the notation $\Delta E_{dop}$, is another factor to take into account. These values are reported in Table 4.1 using the reference of isolated atoms in vacuum, where negative energy denote

| Dopant | $R_{dop}$ | $d$(CM) | $\Delta E_{dop}$ | $\Delta E_{sub\text{-}surf}$ |
|---|---|---|---|---|
| $Ti^{4+}$ | 0.65 | 2.17 | - | - |
| $Cr^{3+}$ | 0.76* | 2.12 | 3.03 | 0.64 |
| $Hf^{4+}$ | 0.85* | 2.22 | -1.19 | 0.34 |
| $Mo^{6+}$ | 0.64 | 2.16 | -2.99 | 0.67 |
| $Nb^{5+}$ | 0.78* | 2.19 | -1.26 | 0.39 |
| $Ta^{5+}$ | 0.78* | 2.18 | -0.07 | 0.26 |
| $V^{5+}$ | 0.60 | 2.13 | -2.33 | 0.26 |
| $W^{6+}$ | 0.65 | 2.15 | 0.71 | 0.58 |
| $Zr^{4+}$ | 0.80 | 2.24 | -0.68 | 0.64 |
| $Mg^{2+}$ | 0.80 | 2.26 | 11.42 | 0.74 |
| $Ca^{2+}$ | 1.14* | 2.39 | 10.86 | 1.99 |
| $Sr^{3+}$ | 1.32* | 2.59 | 11.64 | 1.54 |
| $Al^{3+}$ | 0.62 | 2.19 | 8.66 | 0.39 |
| $Ga^{3+}$ | 0.69 | 2.22 | 11.03 | 0.99 |
| $In^{3+}$ | 0.94 | 2.28 | 11.85 | 1.79 |
| $Si^{4+}$ | 0.54* | 2.12 | 8.40 | 0.65 |
| $Sn^{4+}$ | 0.76 | 2.26 | 11.12 | 1.45 |
| $Rh^{4+}$ | 0.74* | 2.20 | 6.50 | 0.26 |
| $Ir^{4+}$ | 0.77* | 2.19 | 4.89 | 0.44 |
| $Pd^{4+}$ | 0.76* | 2.23 | 9.84 | 0.31 |
| $Pt^{4+}$ | 0.77* | 2.21 | 7.64 | 0.32 |
| $La^{3+}$ | 1.18* | 2.46 | 7.14 | 4.86 |
| $Ce^{4+}$ | 1.01* | 2.33 | 6.02 | 3.28 |

**Table 4.1: Ionic crystal radii of metallic dopants**, $R_{dop}$ in Å. These correspond to surface atoms with five fold coordination, when this information is not available, to sixfold coordination, the latter are marked with an asterisk. The dopant distance to carbon in the surface plane distance, $d$(CM) in Å, doping formation energies, $\Delta E_{dop}$ in eV, and energy difference between subsurface and surface doping, where positive values imply a preference for surface doping, $\Delta E_{sub\text{-}surf}$ in eV.

stability, and it is clear that not all replacements are energetically advantageous, see Equation 4.1

$$\Delta E_{dop} = (E_{TiMC} + E_{Ti}) - (E_{TiC} + E_{M}), \tag{4.1}$$

where $E_{TiMC}$ is the energy of the doped slab, $E_{Ti}$ is the energy of single Ti atom in vacuum, $E_{TiC}$ is the energy of the pristine slab surface model, and $E_M$ is the energy of the dopant atom in vacuum. For instance there is a clear difference between the two doping groups. Regarding the transition metals, they present mostly favourable doping energies due to the close position in the periodic table and the consequent similarity in size and electronic properties. In the same group IV, Zr, and Hf doping is driven by thermodynamics. Doping is also thermodynamically possible along group V (Ta, Nb, and V), although the stability steadily declines as one group is descended. Finally, only Mo is energetically driven in group VI, while Cr and W, which lack rocksalt carbide, exhibit unfavorable (positive) exchange doping energies. Therefore, it appears that the TM dopant capacity to crystallize in a rocksalt environment plays a deciding role.

The elements studied in the second article by contrast present strong positive energies based on the increased electronic structure differences between the dopants and Ti. Be aware that while this method is straightforward and practical for determining the relative stabilities of dopants, it produces high $\Delta E_{dop}$ values, for instance, as compared to utilizing alternative condensed doping reservoir sources. As a result, the findings in Table 4.1 regarding the second group suggest that Ti doping is not very thermodynamically advantageous, which is not surprising given the scarcity of mixed transition metal carbides.[30] This is not so significant, though, as experimental methods for making doped carbides will adhere to other well accepted, well-established methods for doping metal oxides. Additionally, the $\Delta E_{dop}$ results show that doping with late transition metals or even lanthanides is slightly more advantageous than doing it with *p* block elements or alkaline earth metals.

Concerning the charge denisity perturbation introduced by the dopant, we examine the net charges on these atoms and the closest neighbours derived from the calculated Bader charges.[31] For the topmost atomic layer C atoms of the pure TiC(001) surface, the Bader analysis reveals a charge of $-1.70$ $e$; and a slightly higher value of $-1.81$ $e$ is discovered for the C atoms in the second layer. Dopants with an oxidation state higher than Ti ($+1.74$ $e$), such as the extreme case of Si, which as a surface dopant exhibits a Bader charge of $+2.32$ $e$, spread this charge excess over directly bonded C atoms; there are four at the surface layer with a charge of $-1.77$ $e$, and one subsurface C with a charge of $-2.05$ $e$. At the other extreme, Pt, with a charge of $+0.31$ $e$, implies a lower charge transfer, and, consequently, the neighboring C atoms are less negatively charged, with computed Bader charges of $-1.43$ $e$ for surface carbon and $-1.52$ $e$ for subsurface carbon, see Table 4.2. It remains difficult to identify a clear trend, however, when analyzing the possible trends within the transition metals set, the larger the element more polarizable is and thus, the dopant is more oxidized. However, when looking at the second group the small elements, without $d$ occupied orbitals are strongly affected by the nearby Cs, for instance Mg, Al, ans Si. In order to prevent potential artifacts created by the default suggested pseudopotentials, which for these three elements have just two, three, and four valence electrons, respectively, we used alternate pseudopotentials with additional core electrons considered as valence electrons.

A detailed investigation of $CO_2$ binding on a variety of TMC (001) surfaces was conducted before, and scenarios in which the molecule axis is parallel or perpendicular to the carbide surface were taken into account.[13] There is no obvious chemisorption when the $CO_2$ molecule approaches the surface in a perpendicular orientation, *i.e.* when it is anchored by one of its O atoms. Contrarily, the $CO_2$ molecule approaches the surface with its molecular axis parallel, which results in chemisorbed states that frequently result in an activated, adsorbed, bent adsorption species. Two primary competitive adsorption configurations are seen in this scenario, both of which suggest a link between the $CO_2$ molecule and a surface

| Dopant | $q^{surf}$ | $q^{sub}$ | $q^{dop}$ |
|---|---|---|---|
| Ti | -1.70 | -1.81 | +1.74 |
| Cr | -1.70 | -1.64 | +1.31 |
| Hf | -1.74 | -1.90 | +2.03 |
| Mo | -1.59 | -1.61 | +1.41 |
| Nb | -1.66 | -1.76 | +1.72 |
| Ta | -1.70 | -1.81 | +1.91 |
| V | -1.64 | -1.73 | +1.56 |
| W | -1.63 | -1.72 | +1.69 |
| Zr | -1.68 | -1.85 | +1.78 |
| Mg | -1.71 | -1.87 | +1.63 |
| Ca | -1.65 | -1.74 | +1.45 |
| Sr | -1.63 | -1.66 | +1.40 |
| Al | -1.82 | -2.00 | +2.23 |
| Ga | -1.61 | -1.79 | +1.20 |
| In | -1.58 | -1.79 | +1.20 |
| Si | -1.77 | -2.05 | +2.32 |
| Sn | -1.63 | -1.86 | +1.53 |
| Rh | -1.50 | -1.53 | +0.62 |
| Ir | -1.51 | -1.57 | +0.80 |
| Pd | -1.48 | -1.56 | +0.49 |
| Pt | -1.43 | -1.52 | +0.31 |
| La | -1.65 | -1.74 | +1.64 |
| Ce | -1.66 | -1.76 | +1.66 |

**Table 4.2: Bader Charges of the doped systems**. Including the C atoms surrounding the dopant at the surface, $q^{surf}$, the C atom just beneath it, $q^{sub}$, and the dopant itself, $q^{dop}$.

C atom and have the O atoms located almost above the surface metal atoms. These two bonding models, known as TopC and MMC, are shown in Figure 4.1. However, when a doping metal is present, the TopC situation has two potential conformations: TopC and TopC-adjacent, depending on how the activated $CO_2$

molecule atoms are arranged in relation to the dopant atom, the surface C atom, and the $CO_2$ molecule C atom, Figure 4.1. The distinction is that in TopC adjacent, there are no direct contacts between the $CO_2$ molecule and the dopant site. Despite the MMC can be close in energy for some dopants, see Appendix A and B TopC and TopC-Adjacent are always the most energetically preferred adsorption sites for all the dopants. Similar modifications to the structure of the adsorbed $CO_2$ molecule occur in all situations where the surface-$CO_2$ interaction results in a C-C type of bond. The C-O distances are stretched with bond lengths in the 1.28-1.30 Å range, bigger than the estimated PBE value of 1.16 Å for $CO_2$ in vacuum, and the O-C-O angle is decreased from 180° to $< 130°$. The symmetry of the $CO_2$ bonds is partially broken in the examined TopC instances, where there is a clear interaction between one of the $CO_2$ O atoms and the dopant, with the C-O distances exhibiting variations of up to 0.02 Å. This is a clear sign that a charge transfer has been produced and that the $CO_2$ remains adsorbed and activated, accessible for its further usage.

Regarding the preference of TopC vs TopC-Adjacent, it is simple to understand then that generally the TopC mode will be preferred when the interaction between the O atoms in $CO_2$ and the surface dopant atom is stronger than the contact with the surface Ti atoms, being Al and Si, and In and Ce, the only exceptions. The Al and Si prefer the TopC-Adjacent despite showing an higher oxidated state that Ti and In and Ce present the *viceversa* behaviour. Moreover, in TopC where the dopant is directly involved, seems clear that as more oxidized becomes the dopant strong is the M-O bond due to a bigger coulombic interaction, being Ta the only exception with higher oxidation state but lower adsorption energy.

Within the first publication, and in order to find more possible related factors that can affect the $CO_2$ adsorption, the impact of dispersion, the steric repulsion, and closeness of the dopant to the adsorption site were explored. To this end, the Hf and W atoms were chosen due to they are the TopC extreme cases from the transition metal doping, showing a $-0.96$ and $-0.22$ eV adsorption energies,

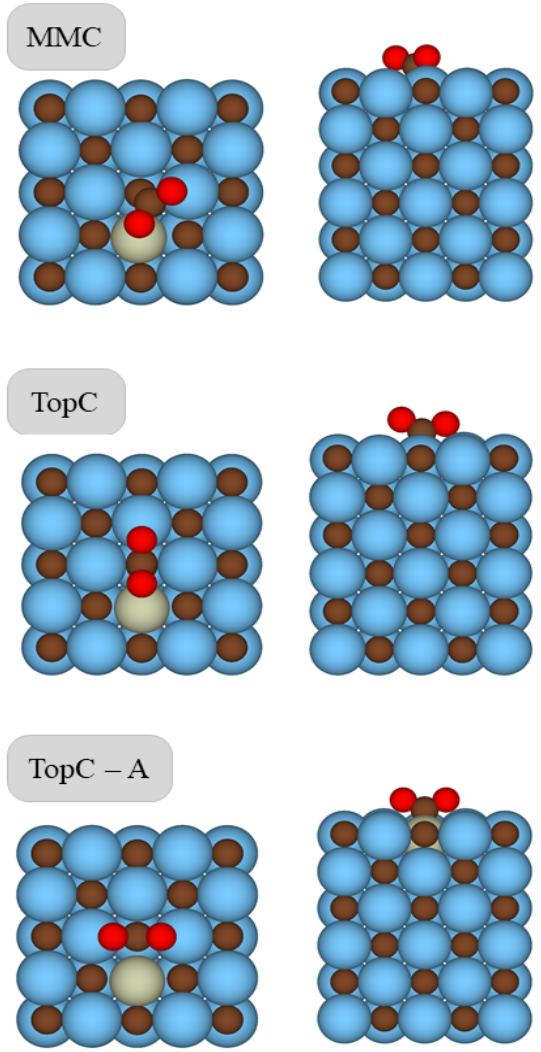


**Figure 4.1: Schematic top view of the MMC, TopC, and TopC-A adsorption modes**, where Ti, C, and O atoms are represented by blue, brown, and red spheres, respectively, whereas the dopant is shown in pale gray.

respectively. Dispersion effects are assessed using Grimme's D3 correction,[32] as was previously examined for $CO_2$ adsorption on TMCs,[13] for all the cases of $CO_2$

adsorption that we have explored, see Appendix A Table S2. As anticipated, the adsorption energies rise (in absolute terms) by 0.24 to 0.29 eV, but more crucially, there are no differences greater than 0.05 eV in this shift between the dopants. As a result, it is reasonable to assume that the influence of vdW type forces on the doping increase or reduction of the $CO_2$ adsorption energies is a constant shift and will not be taken into account in the discussion that follows.

The dopant impact has also been evaluated when the dopant is positioned further from the $CO_2$. This is accomplished by using a bigger $(3\sqrt{2} \times 3\sqrt{2})$R45° supercell, as shown in Figure S1 at Appendix A. The $CO_2$ adsorption energy on undoped TiC(001) is −0.51 eV there due to the varied number of plane waves associated with the cell size and the correspondingly varying density of $k$-points. According to the findings stated above, the estimated adsorption energy increases to −0.89 eV when the $CO_2$ is placed in the TopC condition near Hf. $E_{ads}$, on the other hand, drops to −0.52 eV, which is extremely near to the value of pure, undoped TiC when the $CO_2$ is positioned farther away from the Hf atom. This is more clear evidence of the very local nature of the dopant effect in the carbide–$CO_2$ interactions. Calculations for the W doped surface with a TopC $\Delta E_{ads}$ of −0.14 eV but −0.49 eV when $CO_2$ is at a TopC site further from W, thus revealing a difference of just 0.02 eV from the result for undoped TiC, provide more support for this conclusion. The following permits to conclude that the doping impact is entirely local and focuses on instances when $CO_2$ is close to the doping atom as in Figure 4.1, in accordance with the aforementioned charge density distortions, see also Appendix A Table S1.

Finally, the effects of dopant saturation or coverage on the surface have been assessed using the same two doping agents (Hf and W). To do this, an additional $CO_2$ has been introduced to the $(3\sqrt{2} \times 3\sqrt{2})$R45° unit cell along with its corresponding dopant, thereby boosting the doping concentration and $CO_2$ coverage, see Appendix A Figure S2. The results show that the mean adsorption energies have decreased to −0.77 eV for Hf and −0.13 eV for W, as predicted. Steric factors account for the majority of the decrease compared to the poor

coverage situation. Thus, we automatically assume the same behaviour for the second evaluated doping group.

At this point it is logical to expect some correlation between the net charge on the dopant and the adsorption energy. This plausible correlation is studied together with the charge transfer from the surface to the $CO_2$ molecule to provide additional insight into the observed patterns in $CO_2$ adsorption energy driven by the dopant presence. The first correlation is reasonable accurate with in the transition metal replacement. Figure 4.2 clearly suggests that the higher the $CO_2$ adsorption, the more oxidized the dopant is. This is consistent with the charge alterations of the surface electronic structure caused by the dopant that were previously mentioned. This trend has a very straightforward chemistry. A more oxidized cation results in a greater negative charge on the nearby C atoms that are in direct contact with the adsorbate, see Appendix A Table S1, which is a characteristic that favors electron transfer to the $CO_2$ atoms. The surface C involved in the bonding becomes less negatively charged upon $CO_2$ adsorption, and $CO_2$ is strongly activated, displaying a range of net charges between $-0.76$ and $-0.98$ $e$. The process of adsorption is clearly taking the characteristics of a Lewis acid-base reaction,[33] which has also been seen when $CO_2$ interacts with certain oxides.[34] The surface transfers charge from the acidic $CO_2$ through its base-like action.

However when trying to confirm such tendency considering the dopants from the second article, the correlation of the net charge *vs.* $\Delta E_{ads}$ analysis drops dramatically indicating that the oxidation state of the dopant is not the only key feature involved in such adsorption. Thus, for the second set of dopants more charge transfer involving features were considered, for instance, Figure 4.3 plot of $\Delta E_{ads}$ against the difference in net charge of the C atoms on the surface plane around the dopant atom reveals a stronger link; its values are provided in Table 4.2. This association is more helpful because $CO_2$ adsorption results in the formation of a C-C bond involving a carbon next to the surface dopant, and the incorporation of the dopant into TiC directly impacts the charges on the C

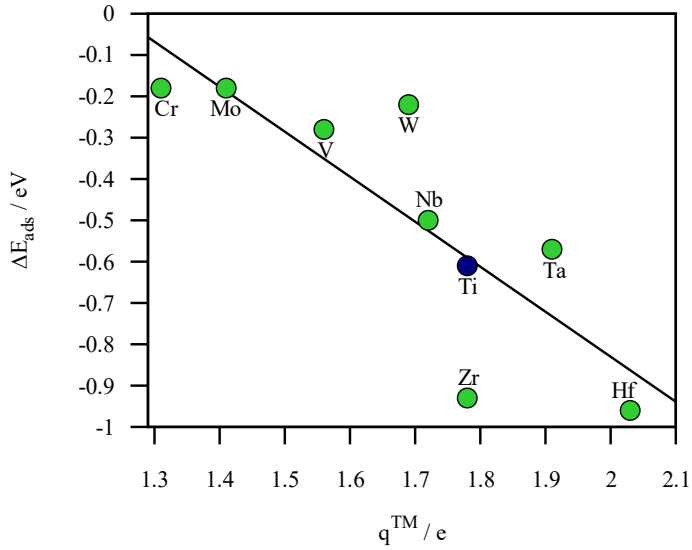


**Figure 4.2: $E_{ads}$ vs. Bader charges of the surface doping TM, $q^{TM}$.** A linear fit (R = 0.76) is shown as a red line.

atoms next to the metal site. In fact, the Figure 4.3 plot demonstrates how the adsorption energy and charge distribution are connected. The adsorption energy increases with the surface charge of the C atoms in the doped system relative to the same quantity for the undoped TiC(001) surface.

Finally, we looked at the effect of dopants atomic sizes to learn more about how they alter the characteristics of $CO_2$ adsorption on TiC (001). The idea behind this is that adding dopants to a Ti site may significantly distort the surface's atomic structure, and how much of a distortion is caused primarily relies on the dopant's ionic radius. The $R_{dop}$ values reported in Table 4.1 and a straightforward plot of $\Delta E_{ads}$ vs dopant radius, however, result in yet another extremely weak association. Instead, when taking into account the geometrical distortions brought on by the dopant, which also depend on the difference in atomic size, the correlation actually becomes much better. To do this, we define $\Delta R$ as,

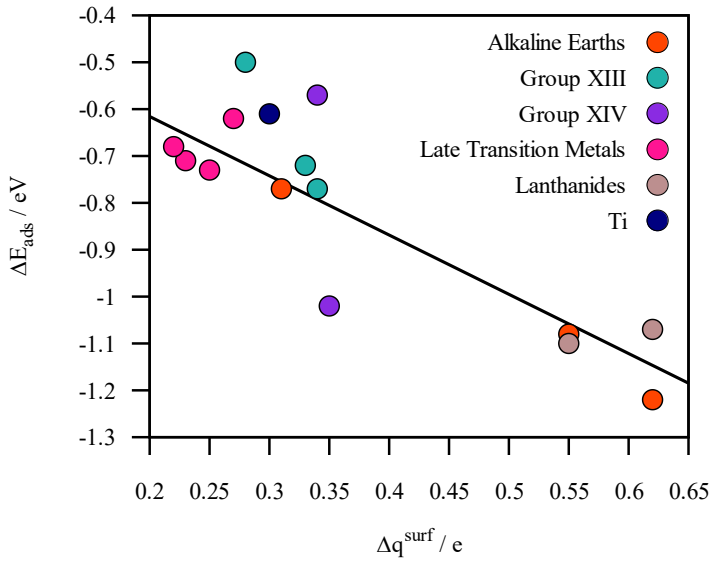


**Figure 4.3: Adsorption energy, $\Delta E_{ads}$, trend versus the difference between the net charge of the surface carbon bonded to $CO_2$ and the net charge of the same carbon for the clean surface, $\Delta q^{surf}$**, that is, $q^{surf}$ values given in Table 4.2, plus 1.70 $e$ accounting for the clean surface. Each group of explored metals is differentiated by colors, as well as the Ti reference in TiC.

$$\Delta R = |R^{M}_{dop} - R^{Ti}_{dop}|\,, \tag{4.2}$$

where $R^{M}_{dop}$ is the dopant ionic crystal radius and $R^{Ti}_{dop}$ is the equivalent value for Ti, both derived from Table 4.1. The surface plane of TiC can become distorted by doping, whether they are concave or convex. Therefore, while examining its impact on the adsorption energy, it is important to take absolute value distortions into account. Figure 4.4 depicts the $\Delta E_{ads}$ *vs.* R plot. Figure 4.4 left panel depicts a clear trend, although this is not truly quantitative since, curiously, Si and In stand out as obvious outliers. We looked at the structure of both doped surfaces in an effort to identify the cause of this disparity. The angle between the surface C and Si atoms and the C from $CO_2$ appears to be around 114° in the case of Si, but it is substantially lower in the other instances and on the undoped TiC (001) surface, at 90° or less. This makes sense given Si has a well-known preference for

tetrahedral coordination and clearly distinguishes it chemically from the other dopants under consideration. The situation of In may also be understood since the ionic radius does not accurately reflect the size of this element in the doped TiC surface because the net charge in In for the doped carbide is substantially less than its formal oxidation number.

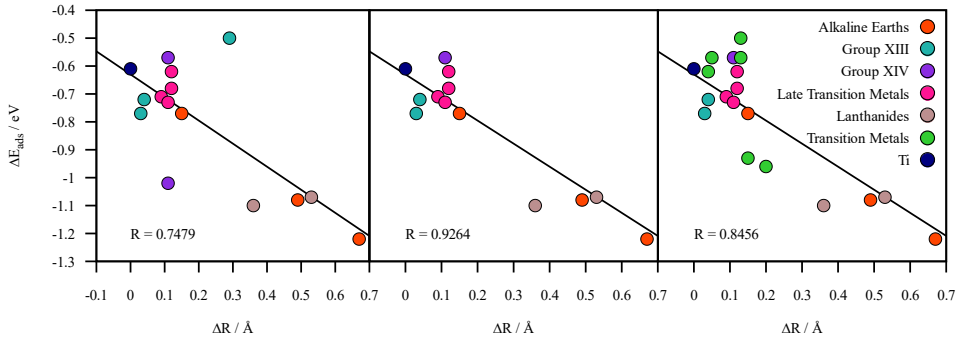


**Figure 4.4: Evolution of the computed adsorption energies, $\Delta E_{ads}$, as a function of the absolute value of $\Delta R$**, as defined in Equation 4.2. The left panel includes all studied elements, whereas the middle panel shows improved correlation when neglecting Si and In outliers. Finally, the right panel considers the elements from the middle panel plus all the early transition metals previously studied. Legend is as shown in Figure 4.3, except for early transition metals, specified.

As can be seen in Figure 4.4, removing the data for Si and In results in a significantly improved correlation. This finding is significant because it enables systematic screening of potential dopants effects on $CO_2$ adsorption without the need for DFT calculations. It also allows one to reasonably estimate the effect of a specific dopant based on intrinsic features of that dopant. As shown in Figure 4.4, the outcomes from the early transition metals analyzed in the prior study incorporated to further confirm the use of R as a descriptor of $CO_2$ adsorption and activation. The presence of the association between $\Delta E_{ads}$ and R is notable given the empirical nature of the ionic crystal radii utilized, Table 4.1, and offers a helpful descriptor for the quick study of a potential dopant impact. Although the association has only been determined for TiC(001), it is likely that other transition metal carbides also exhibit a similar relationship.

The ability of these metal-doped TMCs to adsorb $CO_2$ is influenced by pressure and temperature. The Hertz–Knudsen equation and the transition state theory are used to calculate the rates of adsorption and desorption, respectively[13] which determine whether the $CO_2$ will be quantitatively stored on the surface or desorbed as quickly as it comes into contact with the surface. The working temperature affects both the adsorption and desorption rates, and $T_{eq}$, the temperature at which both processes are equal, establishes the boundary between the two regimes. Figure 4.5 reports the change of both rates with respect to the temperature for each of the materials that were investigated using a typical partial pressure of atmospheric $CO_2$ of 40 Pa.[35] For a given surface, $T < T_{eq}$ denotes the regime in which $CO_2$ capture is promoted because adsorption is quicker than desorption, as opposed to $T > T_{eq}$, when $CO_2$ desorption would predominate.

The $CO_2$ $r_{ads}$ and $r_{des}$ values for TiC(001) and doped-TiC(001) of the first article are shown in Figure 4.5, which makes it evident that a modest increase in the adsorption energies implies a slight rise in the temperature limit between the adsorption and desorption areas. In fact, the equilibrium temperature between adsorption and desorption for Hf-doped TiC is 370 K, which is 135 K higher than the projected 235 K value for stoichiometric TiC. This is because the adsorption energy for Hf-doped TiC is 0.34 eV larger than for undoped TiC(001). As a result, $CO_2$ collection at higher temperature settings would be enabled by Hf-doped TiC. The temperature drops for other doping metals like W, but in these cases, according to the previous research, $CO_2$ would preferentially occupy dopant-free surface areas, thus no change in the equilibrium temperature is to be anticipated.

It is important to note that the desorption rates rely on $\Delta E_{ads}$, which in turn depends on the specific DFT method employed, before examining the T-dependent rates as a plot presented in Figure 4.5. We specifically spoke about how adding dispersion factors, which are not taken into consideration in the current study, may result in greater $\Delta E_{ads}$ values and possibly a change to bigger $T_{eq}$ values. However, since the comparison is between $T_{eq}$ for a given material

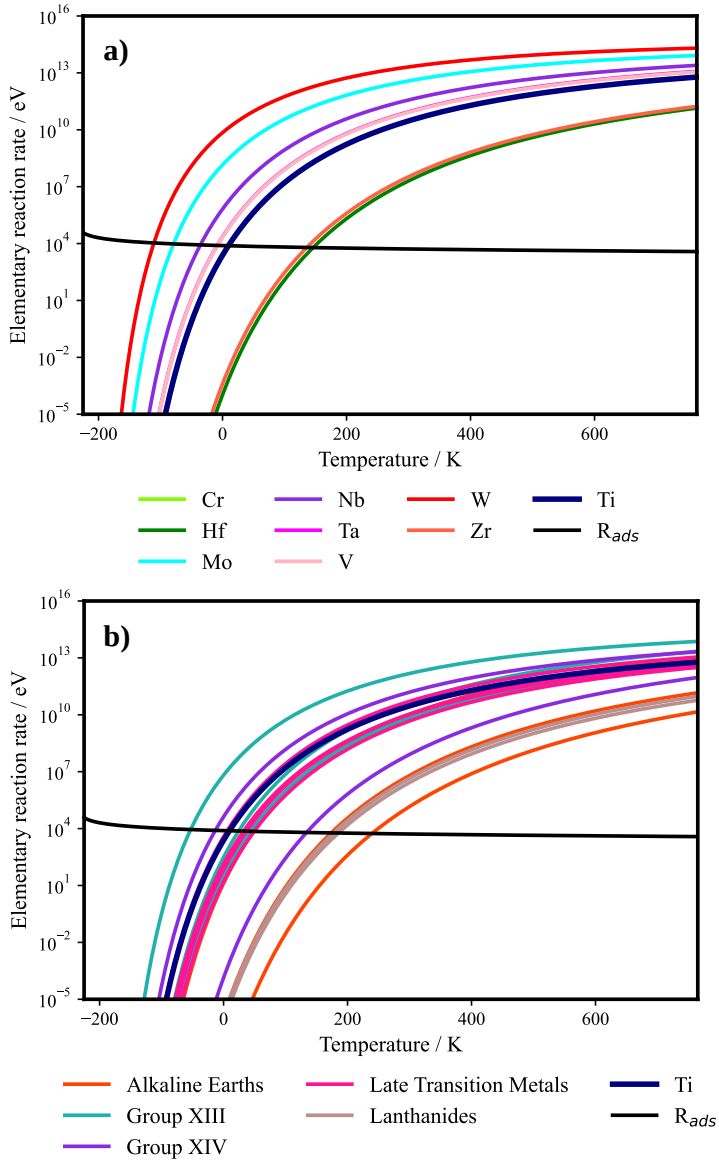


**Figure 4.5: Calculated $CO_2$ desorption rates, $r_{des}$, on doped TiC (001) at the current partial pressure of atmospheric $CO_2$ of 40 Pa**. (a) and (b) correspond to the two different set of dopants considered in the respective articles. Note that the adsorption rate does not depend on the adsorption energy and, hence, is the same for all cases. The desorption rates of the undoped and doped surfaces are shown color-coded

relative to $T_{eq}$ for stoichiometric TiC (001), which we will refer to as $T_{eq}^{TiC}$, these relative values of $T_{eq}$ are therefore resilient to the neglect of dispersion corrections. The effect of the DFT method, including the effect of dispersion, will equally affect all the studied systems.

To sum up, the next points resume the main conclusions reached by this study. The complete publications can be found following the conclusions.[36,37]

- The effects of a dopant on $CO_2$ collection, storage, and activation by two different representative groups of dopants, i) early TMs as Hf, Ta, Zr, Nb, W, Cr, Mo, and V; ii) elements across the periodic table as Mg, Ca, Sr, Al, Ga, In, Si, Sn, Pd, Pt, Rh, Ir, La, and Ce, are reported in the current DFT-based work.

- It is discovered that the dopant influence on the geometric and electrical configurations is highly local. Calculations show that subsurface substitution is never preferable over doping at the very top layer of the surface. Dispersion's impact has been proven to be consistent and to have an equal impact in both doped and undoped circumstances.

- The presence of a doping agent on the TiC(001) surface effects the $CO_2$ adsorption energy affecting its adsorption and desorption rates and, hence, affecting its CCS and possible CCU properties. Moreover, the TMs group shown a correlation by the net charge of the dopant and the $\Delta E_{ads}$. However, the addition of the second group of dopants into that relation drops it dramatically. The results show a qualitative correlation between the net charge of the surface carbons comparing the doped and undoped systems with the $\Delta E_{ads}$. Therefore, the charge transfer is a key feature of the adsorption but not the only one.

- Regarding the systems doped by TMs, the results are expected to be extrapolated to other TMCs, if the TM-TiC have a enhanced adsorption

energy, the pure TMC will show a higher adsorption that the pure TiC. In contrast, the reverse effect is also expected.

- The structural distortion caused by the dopant play a major role. A correlation between the difference in atomic radii of the dopant and the Ti, $\Delta$R, outstand as a valuable relation, due to allow to screen a vast number of elements without carrying out a single DFT calculation.

# References

[1] C. B. Field, V. R. Barros, D. J. Dokken, K. J. Mach, and M. D. Mastrandrea Climate Change 2014 Part A: Global and Sectoral Aspects Technical report, 2014.

[2] O. Edenhofer, R. Pichs-Madruga, Y. Sokona, J. C. Minx, E. Farahani, S. Kadner, K. Seyboth, A. Adler, I. Baum, S. Brunner, P. Eickmeier, B. Kriemann, J. Savolainen, S. Schlömer, C. von Stechow, and T. Zwickel Climate Change 2014: Mitigation of Climate Change Technical report, 2014.

[3] E. J. Kendon, N. M. Roberts, H. J. Fowler, M. J. Roberts, S. C. Chan, and C. A. Senior, *Nat. Clim. Chang.*, 2014, **4**(7), 570–576.

[4] P. M. Cox, R. A. Betts, C. D. Jones, and S. A. Spall, *Nature*, 2000, **408**, 184–187.

[5] S. C. Doney, V. J. Fabry, R. A. Feely, and J. A. Kleypas, *Ann. Rev. Mar. Sci.*, 2009, **1**, 169–192.

[6] L. Espinal, D. L. Poster, W. Wong-Ng, A. J. Allen, and M. L. Green, *Environ. Sci. Technol.*, 2013, **47**(21), 11960–11975.

[7] D. M. D'Alessandro, B. Smit, and J. R. Long, *Angew. Chemie - Int. Ed.*, 2010, **49**(35), 6058–6082.

[8] M. Bui, C. S. Adjiman, A. Bardow, E. J. Anthony, A. Boston, S. Brown, P. S. Fennell, S. Fuss, A. Galindo, L. A. Hackett, J. P. Hallett, H. J. Herzog, G. Jackson, J. Kemper, S. Krevor, G. C. Maitland, M. Matuszewski, I. S. Metcalfe, C. Petit, G. Puxty, J. Reimer, D. M. Reiner, E. S. Rubin, S. A. Scott, N. Shah, B. Smit, J. P. Trusler, P. Webley, J. Wilcox, and N. Mac Dowell, *Energy Environ. Sci.*, 2018, **11**(5), 1062–1176.

[9] P. Markewitz, W. Kuckshinrichs, W. Leitner, J. Linssen, P. Zapp, R. Bongartz, A. Schreiber, and T. E. Müller, *Energy Environ. Sci.*, 2012, **5**(6), 7281–7305.

[10] C. Stewart and M. A. Hessami, *Energy Convers. Manag.*, 2005, **46**(3), 403–420.

[11] C. H. Yu, C. H. Huang, and C. S. Tan, *Aerosol Air Qual. Res.*, 2012, **12**(5), 745–769.

[12] W. Taifan, J. F. Boily, and J. Baltrusaitis, *Surf. Sci. Rep.*, 2016, **71**(4), 595–671.

[13] C. Kunkel, F. Viñes, and F. Illas, *Energy Environ. Sci.*, 2016, **9**(1), 141–144.

[14] J. A. Anderson and M. F. Garcia, *Supported Metals in Catalysis*, Vol. 11, Imperial College Press, London, 2011.

[15] J. A. Rodriguez, J. Evans, L. Feria, A. B. Vidal, P. Liu, K. Nakamura, and F. Illas, *J. Catal.*, 2013, **307**, 162–169.

[16] A. B. Vidal, L. Feria, J. Evans, Y. Takahashi, P. Liu, K. Nakamura, F. Illas, and J. A. Rodriguez, *J. Phys. Chem. Lett.*, 2012, **3**(16), 2275–2280.

[17] G. C. Bond, *Metal-Catalysed reactions of hydrocarbons*, Springer US, New York, 2005.

[18] S. Posada-Pérez, F. Viñes, P. J. Ramirez, A. B. Vidal, J. A. Rodriguez, and F. Illas, *Phys. Chem. Chem. Phys.*, 2014, **16**(28), 14912–14921.

[19] X. Liu, C. Kunkel, P. Ramírez De La Piscina, N. Homs, F. Viñes, and F. Illas, *ACS Catal.*, 2017, **7**(7), 4323–4335.

[20] M. D. Porosoff, S. Kattel, W. Li, P. Liu, and J. G. Chen, *Chem. Commun.*, 2015, **51**(32), 6988–6991.

[21] M. D. Porosoff, X. Yang, J. A. Boscoboinik, and J. G. Chen, *Angew. Chemie - Int. Ed.*, 2014, **53**(26), 6705–6709.

[22] N. M. Schweitzer, J. A. Schaidle, O. K. Ezekoye, X. Pan, S. Linic, and L. T. Thompson, *J. Am. Chem. Soc.*, 2011, **133**(8), 2378–2381.

[23] H. G. Yang, C. H. Sun, S. Z. Qiao, J. Zou, G. Liu, S. C. Smith, H. M. Cheng, and G. Q. Lu, *Nature*, 2008, **453**(7195), 638–641.

[24] O. Lamiel-Garcia, S. Tosoni, and F. Illas, *J. Phys. Chem. C*, 2014, **118**(25), 13667–13673.

[25] I. Yeriskin and M. Nolan, *J. Phys. Condens. Matter*, 2010, **22**(13).

[26] M. Nolan, *J. Mater. Chem.*, 2011, **21**(25), 9160–9168.

[27] Y. Liu, C. Wen, Y. Guo, G. Lu, and Y. Wang, *J. Phys. Chem. C*, 2010, **114**(21), 9889–9897.

[28] Y. N. Regmi and B. M. Leonard, *Chem. Mater.*, 2014, **26**(8), 2609–2616.

[29] S. M. Kozlov, G. Kovács, R. Ferrando, and K. M. Neyman, *Chem. Sci.*, 2015, **6**(7), 3868–3880.

[30] D. J. Ham and J. S. Lee, *Energies*, 2009, **2**(4), 873–899.

[31] R. F. W. Bader, *Atoms in Molecules: A Quantum Theory.*, Oxford University Press, Oxford, 1990.

[32] S. Grimme, J. Antony, S. Ehrlich, and H. Krieg, *J. Chem. Phys.*, 2010, **132**(15), 154104.

[33] P. C. Stair, *J. Am. Chem. Soc.*, 1982, **104**(15), 4044–4052.

[34] G. Pacchioni, J. M. Ricart, and F. Illas, *J. Am. Chem. Soc.*, 1994, **116**(22), 10152–10158.

[35] T. Takahashi and S. C. Sutherland Global ocean surface water partial pressure of CO2 database: mesurements performed during 1967-2018 (version 2018) Technical Report Version 2018, 2019.

[36] M. López, L. Broderick, J. J. Carey, F. Viñes, M. Nolan, and F. Illas, *Phys. Chem. Chem. Phys.*, 2018, **20**(34), 22179–22186.

[37] M. López, F. Viñes, M. Nolan, and F. Illas, *J. Phys. Chem. C*, 2020, **124**(29), 15969–15976.

PCCP

PAPER

View Article Online
View Journal | View Issue



Cite this: *Phys. Chem. Chem. Phys.*, 2018, **20**, 22179

# Tuning transition metal carbide activity by surface metal alloying: a case study on $CO_2$ capture and activation†

Martí López,[a] Luke Broderick,[b] John J. Carey,[b] Francesc Viñes,*[a] Michael Nolan*[b] and Francesc Illas[a]

Received 9th June 2018,
Accepted 6th August 2018

DOI: 10.1039/c8cp03648a

rsc.li/pccp

$CO_2$ is one of the main actors in the greenhouse effect and its removal from the atmosphere is becoming an urgent need. Thus, $CO_2$ capture and storage (CCS) and $CO_2$ capture and usage (CCU) are intensively investigated technologies to decrease the concentration of atmospheric $CO_2$. Both CCS and CCU require appropriate materials to adsorb/release and adsorb/activate $CO_2$, respectively. Recently, it has been theoretically and experimentally shown that transition metal carbides (TMC) are able to capture, store, and activate $CO_2$. To further improve the adsorption capacity of these materials, a deep understanding of the atomic level processes involved is essential. In the present work, we theoretically investigate the possible effects of surface metal doping of these TMCs by taking TiC as a textbook case and Cr, Hf, Mo, Nb, Ta, V, W, and Zr as dopants. Using periodic slab models with large supercells and state-of-the-art density functional theory based calculations we show that $CO_2$ adsorption is enhanced by doping with metals down a group but worsened along the *d* series. Adsorption sites, dispersion and coverage appear to play a minor, secondary constant effect. The dopant-induced adsorption enhancement is highly biased by the charge rearrangement at the surface. In all cases, $CO_2$ activation is found but doping can shift the desorption temperature by up to 135 K.



## 1. Introduction

Every year increasing evidence of the significant impact of global warming on the Earth is being reported.[1,2] The environmental prediction models show a non-optimistic future if no urgent measures are taken to face this issue.[3,4] Atmospheric $CO_2$ is one of the greenhouse gases with the highest impact, and its environmental effects are particularly problematic. Apart from well-known ones such as ocean acidification,[5] there are predictions that while the anthropogenic emissions of $CO_2$ rise in the atmosphere, the $CO_2$ concentration and concomitant global warming will rise exponentially through carbon-cycle feedback.[4] Despite worldwide efforts in controlling and reducing $CO_2$ emissions, as exemplified in active environmental protocols such as Copenhagen, Kyoto, or Paris,[6–8] recently the International Energy Agency (IEA), in its global energy and $CO_2$ status reports, announced an increase of 1.4% in energy-related $CO_2$ emissions.[9]

Among many strategies oriented at reducing $CO_2$ emissions or at decreasing its atmospheric concentration, an appealing one is the removal of atmospheric $CO_2$ *via* scrubber materials.[10,11] Spurred on by the urgent requirements of the Paris protocol, $CO_2$ surface chemistry[12] is experiencing a renewed interest focusing on characterizing scrubber materials and optimizing their properties in $CO_2$ capture and storage (CCS).[13,14] Along this line, a desirable advance is not only in $CO_2$ capture, but its chemical activation and eventual re-use as a carbon feedstock to synthesize other valuable chemicals through the commonly known $CO_2$ capture and usage (CCU) strategies.[15] Given the high $CO_2$ chemical stability, only a few privileged materials are able to selectively adsorb $CO_2$ strongly enough for CCS or CCU technologies. Moderate to high $CO_2$ adsorption energies usually indicate activation of the molecule,[12] which often occurs through charge transfer from the surface of a material to the $CO_2$ $6a_1$ anti-bonding molecular orbital, thus weakening the C–O bonds and leading to a bent geometry.[10] From this point on the $CO_2^{\delta-}$ molecule is much more reactive than the neutral one and the starting point for any industrial process to reuse $CO_2$.

[a] *Departament de Ciència de Materials i Química Física & Institut de Química Teòrica i Computacional (IQTCUB), Universitat de Barcelona, Martí i Franqués 1-11, Barcelona 08028, Spain. E-mail: francesc.vines@ub.edu*
[b] *Tyndall National Institute, Lee Maltings, University College Cork, Cork T12R5CP, Ireland. E-mail: michael.nolan@tyndall.ie*

† Electronic supplementary information (ESI) available: Fig. S1 Top view of the $(3\sqrt{2}\times3\sqrt{2})R45^\circ$ model, the $CO_2$ was adsorbed both in the shown position but the dopant was moved from the near to the far position. Fig. S2 Top view of the slab model used to represent a higher coverage situation. Table S1 Bader charges on all bare surfaces. Table S2 Binding modes, and adsorption energies with and without van der Waals corrections (vdW), as obtained with PBE-D3, as well as geometry parameters, including $CO_2$ angles, C–C bond distances, *d*(C–C), and $CO_2$ molecule C–O bond distances, *d*(C–O). Table S3 Bader charges for all the studied surfaces with adsorbed $CO_2$. See DOI: 10.1039/c8cp03648a

From all known possible materials, transition metal carbides (TMC) have shown promising results in $CO_2$ capture, storage, and activation,[10,16,17] and even conversion to valuable chemicals,[18] while their relatively low cost makes them industrially attractive materials. Diverse density functional theory (DFT) based computational studies, mostly focused on early TMCs, proved that these materials display significant potential for $CO_2$ activation.[19,20] In particular, TiC, WC, and especially α-$Mo_2C$ excel among the family of TMCs, and so, have been studied in deeper detail. These TMCs have proven their CCS potential but also their CCU capabilities, as highlighted by their $CO_2$ based catalytic activity,[17,18] including $CO_2$ hydrogenation towards methanol.[21] Additional systematic DFT based studies report strong $CO_2$ adsorption on the most stable (001) surface of rocksalt crystal group IV (TiC, ZrC, and WC), group V (NbC, and TaC), and group VI (δ-MoC) TMCs with concomitant activation of the adsorbed molecule,[10] indicating that these materials may be adequate for CCU technologies.

In the search for tailor-made materials for CCS and/or CCU, different ways of tuning the surface activity towards $CO_2$ can be envisaged, including the use of surface doping agents. This is a common practice when considering metal and metal oxide properties, thus locally tuning the chemical activity or stabilizing certain facets as in F-doped $TiO_2$ nanoparticles.[22,23] It has also been shown that the presence of surface dopants promotes oxygen vacancy formation on $CeO_2$ nanoparticles.[24,25] Also, CO adsorption on ceria is easily enhanced by adding Zr or Ti in the bulk, improving CO oxidation and releasing $CO_2$ to the atmosphere.[26] In the case of metals, metal alloying is a standard, but not yet fully understood or controlled, approach to modulate the surface activity. Bimetallic TMCs using earth-abundant and cheap metals, such as $Fe_3Mo_3C$ or $Ni_6Mo_6C$, have been previously prepared, *via* stepwise reduction of precursor oxides,[27] opening the path towards an economically reasonable synthesis procedure. Moreover, there have been clear improvements in the understanding of nanoalloys,[28] thus opening the door to future control.

In the present work we explore transition metal doping—or surface metal alloying—on TMC surfaces in the context of $CO_2$ capture, storage, and activation. Here, TiC has been chosen to understand how the $CO_2$ adsorption energy is affected by the presence of a surface or subsurface doping agent. The dopants scrutinized are Zr, Hf, V, Nb, Mo, Cr, Ta, and W; a subset of transition metals that are known to form metal carbides. This work therefore aims to assess the significant possibility of bimetallic/doped TMCs for use in CCS and the implications for design of materials with enhanced $CO_2$ adsorption, following a kinetic rate balance approach successfully used in previous work of some of the authors concerning $CO_2$ adsorption on TMCs.[10] Furthermore, $CO_2$ anchoring and activation is regarded as a first, necessary, and determining step for $CO_2$ conversion through CCU applications.

## 2. Surface models and computational details

Calculations reported in the present work have been carried out within density functional theory (DFT),[29,30] using the Perdew, Burke, and Ernzerhof (PBE) implementation of the generalized gradient approximation (GGA) of the exchange–correlation functional[31] as implemented in the Vienna *Ab Initio* Simulation Package (VASP).[32–34] The electronic density of the valence electrons has been expanded using a plane-wave basis set with an energy cut off of 450 eV. The interactions between the core and valence electrons have been taken into account through the projector augmented wave (PAW) approach of Blöchl,[35] as implemented by Kresse and Joubert.[36] Atomic relaxation optimization has been carried out until forces acting on atoms were less than 0.02 eV $Å^{-1}$, and the electronic energy convergence is set to $10^{-5}$ eV. The convergence of the calculations has been enhanced using a Gaussian smearing method with a smearing width of 0.2 eV, yet final energies are taken extrapolated to 0 K (no smearing). The calculations are non spin-polarized. Calculations incorporating spin polarization have been performed for the pristine and doped surfaces, where the doping metal can show different spin configurations (*e.g.*, for the Cr case, although no solutions were found with an excess of one spin) *i.e.* magnetic minima and the effect of spin polarization on relative energies is negligible. A Monkhorst Pack *k*-point sampling grid[37] of (2×2×1) *k*-points has been used to carry out the necessary numerical integration in reciprocal space.

A $(3\sqrt{2}\times3\sqrt{2})R45^\circ$ supercell slab model has been used to represent the TiC(001) surface. The model consists of six stoichiometric atomic layers extended in the *xy* plane, containing eight C and Ti atoms per layer, with a vacuum gap of 15 Å in the *z* direction. The $CO_2$ molecules have been introduced 2 Å away from the surface along the *z* direction and different initial adsorption sites and orientations relative to the surface have been systematically sampled. The two bottom layers of the slab are fixed to simulate the bulk structure of the materials. The dopants have been placed on the surface of TiC substituting a Ti ion and considering several situations regarding the adsorbed $CO_2$ molecule. Given the lack of work on doped metal carbides to date, we have used a doping concentration of 3.125%, which is typical for doping concentrations in, *e.g.* metal oxides. All ionic relaxations were carried out using the TiC bulk optimized slab geometry. A check on the effect of further optimization of the slabs in the slab plane in which doping atoms are included results in a negligible change to the $CO_2$ adsorption energies which is no larger than 0.04 eV. The necessary calculations for the isolated, gas phase, $CO_2$ molecule, as well as for the isolated metal atoms, have been carried out in an asymmetric box of (9×10×11) Å to force correct molecular orbital occupations. In the case of isolated metal atoms, spin-polarized calculations have been carried out to correctly describe their open shell nature.

## 3. Results and discussion

### 3.1. Dopant effects on the TiC surface

The substitution of the Ti atom of the TiC(001) surface, either at the surface or subsurface atomic layers, by one atom of Cr, Hf, Mo, Nb, Ta, V, W, or Zr as a dopant has two main effects; namely surface geometry and charge density distortions. These changes

 

Table 1 Transition metal cation radii, C-TM distances, $d$(C-TM), of the surface and subsurface carbons, doping formation energies, ($\Delta E_{dop}$) and PBE estimated energy differences ($\Delta E_{sub-surf}$) between surface and subsurface doping sites for TM-TiC(001) surfaces

| Dopant | Radius (Å) | $d$(C-TM) (Å) | $\Delta E_{dop}$ (eV) | $\Delta E_{sub-surf}$ (eV) |
|---|---|---|---|---|
| $Ti^{4+}$ | 0.75 | 2.17, 2.08 | — | — |
| $Cr^{3+}$ | 0.76 | 2.12, 1.86 | 3.03 | 0.64 |
| $Hf^{4+}$ | 0.71 | 2.22, 2.21 | −1.19 | 0.34 |
| $Mo^{6+}$ | 0.73 | 2.16, 1.97 | −2.99 | 0.67 |
| $Nb^{5+}$ | 0.58 | 2.19, 2.07 | −1.26 | 0.39 |
| $Ta^{5+}$ | 0.8 | 2.18, 2.06 | −0.07 | 0.26 |
| $V^{5+}$ | 0.68 | 2.13, 1.93 | −2.33 | 0.26 |
| $W^{6+}$ | 0.51 | 2.15, 1.97 | 0.71 | 0.58 |
| $Zr^{4+}$ | 0.66 | 2.24, 2.26 | −0.68 | 0.62 |

come from the differences of atomic radii and electronic configuration of the transition metal dopants relative to Ti.

For all investigated cases, the dopant at the surface site was energetically preferred over the subsurface one; differences in energies of both situations, $\Delta E_{sub-surf}$, are reported in Table 1, with generally a strong preference for dopants to be at the surface by in between *circa* 0.35 and 0.65 eV with exceptions for V and Ta. Given the mentioned different radii between Ti and dopant atoms, one would think that the latter can be better embedded at the surface sites than at the subsurface ones simply because lattice distortions are minimized when the dopant occupies a surface site, *i.e.*, they are better accommodated. From this reasoning one would also expect that the closer the dopant is to Ti in the periodic table, the smaller the energetic difference between the surface and subsurface positions would be, which is indeed confirmed by the calculations reported in Table 1. The preference for substitution at surface sites may be beneficial for catalytic purposes when this situation is accompanied by a sought for chemical activity. This fact suggests that control of the TMC surface chemistry is therefore possible.

A further point to be considered is the energy cost for cation exchange, here denoted as $\Delta E_{dop}$. Table 1 reports these energies, taking isolated atoms in vacuum as the reference, where negative energies indicate stability, and reveals that not all substitutions are energetically favorable. The doping by the same group IV Zr and Hf is thermodynamically driven. Along group V (Ta, Nb, and V), doping is also thermodynamically feasible, yet gradually the stability decreases by going down a group. Finally, in group VI only Mo is energetically driven whereas Cr and W, which do not feature a rocksalt carbide, show unfavorable (positive) exchange doping energies. Thus, apparently, the ability of the TM dopant to crystallize in a rocksalt environment appears to be a determining factor.

Focusing deeper on the structural aspects, see Table 1, charge density distortions caused by the dopant are present in the neighboring C atoms only, which means that the doping clearly has a local effect. This is also observed when inspecting changes in the electron density affecting both the dopant agent and the surrounding C atoms. For instance, for the pristine TiC(001) surface, the Bader analysis[38] for the C atoms in the outermost atomic layer predicts a charge of −1.70 $e$; a slightly larger value of −1.74 $e$ is found for the C atoms in the second layer. Dopants with an oxidation state higher than Ti (+1.74 $e$), such as the extreme case of Hf, which as a surface dopant exhibits a Bader charge of +2.03 $e$, spread this charge excess over directly bonded C atoms; there are four at the surface layer with a charge of −1.74 $e$, and one subsurface C with a charge of −1.90 $e$. At the other extreme, Cr, with a charge of +1.31 $e$, implies a lower charge transfer, and, consequently, the neighboring C atoms are less negatively charged, with computed Bader charges of −1.58 $e$ for surface carbon and −1.64 $e$ for subsurface carbon. A complete set of calculated Bader charges for the different situations explored in the present work may be found in Table S1 of the ESI.†

### 3.2. Binding modes of $CO_2$ on doped TiC(001)

A previous thorough study explored several binding modes of $CO_2$ on a set of TMC (001) surfaces and considered situations in which the molecular axis lies perpendicular or parallel to the carbide surface.[10] Approaching of the $CO_2$ molecule to the surface in a perpendicular orientation, *i.e.* anchoring by one of its O atoms, results in no clear chemisorption. On the other hand, the approach of the $CO_2$ molecule with its molecular axis parallel to the surface leads to chemisorbed states, which then often lead to an activated, adsorbed, bent adsorption species. In this case, two main competitive adsorption configurations are found, both implying a bond between the $CO_2$ molecule and a surface C atom and with the O atoms nearly above the surface metal atoms. These two bonding models are the so-called TopC and MMC, see Fig. 1. However, in the presence of a doping metal, the TopC situation presents two possible conformations, TopC and TopC-adjacent, depending on the orientation of the plane formed by the atoms of the activated $CO_2$ molecule relative to the plane formed by the dopant atom, the surface C atom, and the C atom of the $CO_2$ molecule (Fig. 1). The difference here is that in TopC adjacent the $CO_2$ molecule does not have any direct interactions with the dopant site. In pristine TiC, both modes present similar binding energies (Table S2, within the accuracy of the PBE calculations, ESI†), both modes having a competitive interaction, but since the MMC mode was never preferred for any doped system, TopC was used for the forthcoming detailed exploration of the doped systems.[10]

### 3.3. $CO_2$ adsorption strength

The $CO_2$ adsorption energy, $E_{ads}$, on the pristine or doped TiC(001) surface, is obtained as in eqn (1)

$$E_{ads} = E_{Sur-CO_2} - (E_{CO_2} + E_{Sur}), \quad (1)$$

where $E_{Sur-CO_2}$ is the energy of the surface with adsorbed $CO_2$, $E_{Sur}$ the energy of the clean pristine or doped TiC surface, and $E_{CO_2}$ the energy of the gas phase molecule. Within this definition, the more negative $E_{ads}$ the stronger the adsorption. From the whole set of investigated dopants, the case with Hf located in the first atomic layer exhibits the largest adsorption energy (−0.96 eV for TopC). This is interpreted in terms of the larger positive charge on Hf compared to Ti (see Table S1, ESI†), which induces a stronger stabilization through a coulombic Hf–O interaction as clearly seen in Fig. 2. This implies that the adsorption energies involving early TMs as dopants are larger than those involving late

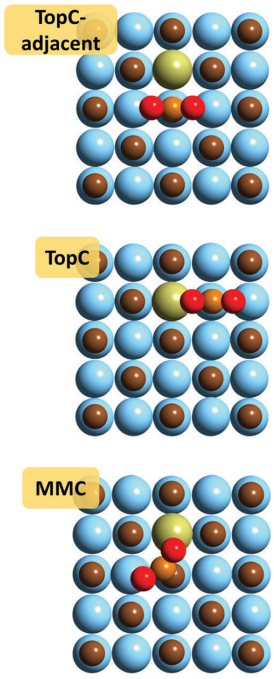


Fig. 1 PBE optimized structure for the most stable three $CO_2$ binding modes in the Hf-doped TiC(001) surface slab model. Hf, Ti, C, and O atoms are represented by green, blue, brown, and red spheres, respectively. The carbon from $CO_2$ is represented by a light brown sphere.

TMs (Table 2), with one of the weakest situations being W (−0.22 eV). However, the case of Ta represents an exception to this rule since even with quite a large charge of +1.91 *e*, it displays a slightly smaller $E_{ads}$ (−0.57 eV) than pristine TiC. In any case, it is clear that the dopant charge is a determining factor although not the only one.

Concerning doping with W, the TopC adjacent situation implies a slightly higher adsorption energy (−0.31 eV), but this is still far from the −0.61 eV for undoped TiC. Hence, the doping effect has still a vicinal, in this case worsening, effect. The opposite applies to Hf, where TopC adjacent leads to a reduced adsorption energy of −0.81 eV. These two limiting situations (Hf and W) are selected to study the effect of dispersion and also of the proximity of the dopant to the adsorption site.

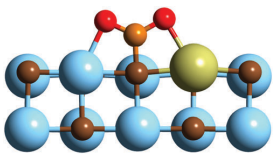

Fig. 2 Relaxed atomic structure of $CO_2$ adsorbed at the Hf-doped TiC(001) surface in TopC binding mode, being the most stable adsorption with an $E_{ads}$ of −0.96 eV. Hf is shown as a pale green sphere. The remaining color code is as in Fig. 1.

Table 2 Binding modes, adsorption energies, $E_{ads}$, and corresponding geometrical data, including $CO_2$ angles, and C–C and C–O bond distances, *d*(C–C) and *d*(C–O), respectively, for the most favorable cases for each transition metal surface dopant at the TiC(001) surface. The remaining adsorption energies and geometries are available in Table S2 of the ESI

| $CO_2$ adsorption | | | | | |
|---|---|---|---|---|---|
| Dopant | Binding mode | $E_{ads}$ (eV) | $CO_2$ angle (°) | *d*(C–C) (Å) | *d*(C–O) (Å) |
| Ti | TopC | −0.61 | 127.5 | 1.48 | 1.29 |
| Cr | TopC-adj | −0.62 | 128.0 | 1.49 | 1.28 |
| Hf | TopC | −0.96 | 126.0 | 1.49 | 1.28, 1.30 |
| Mo | TopC-adj | −0.39 | 128.4 | 1.50 | 1.28 |
| Nb | TopC | −0.50 | 127.0 | 1.49 | 1.28, 1.29 |
| Ta | TopC | −0.57 | 127.1 | 1.49 | 1.28, 1.30 |
| V | TopC-adj | −0.57 | 127.9 | 1.49 | 1.29 |
| W | TopC-adj | −0.31 | 128.6 | 1.50 | 1.28 |
| Zr | TopC | −0.93 | 125.7 | 1.50 | 1.28, 1.30 |

Dispersion effects are evaluated for all the examples of $CO_2$ adsorption that we have studied (see Table S2, ESI†), using the Grimme D3 correction,[39] as earlier studied for $CO_2$ adsorption on TMCs.[10] As expected, the adsorption energies increase (in absolute terms) by −0.24 up to −0.29 eV, but, more importantly, variations in this shift among the dopants are no larger than 0.05 eV. The only exception is $CO_2$ adsorption in MMC mode on Cr–TiC where such an energy difference is −0.32 eV. Consequently, the effect of van der Waals type forces on the doping increase/decrease of the $CO_2$ adsorption energies can be considered a constant shift and can be safely disregarded in the forthcoming discussion.

In a similar fashion, the dopant effect has been tested where the dopant is positioned farther from the $CO_2$ than in the TopC-adjacent situation. To this end, a larger $(3\sqrt{2}\times3\sqrt{2})R45^\circ$ supercell is used, see Fig. S1 (ESI†). There, because of the different number of plane waves associated with the cell dimensions and the concomitant different density of *k*-points, the $CO_2$ adsorption energy on undoped TiC(001) is −0.51 eV. When the $CO_2$ is placed in the TopC situation close to Hf, the computed adsorption energy strengthens to −0.89 eV, in line with the results discussed above. However, when the $CO_2$ is placed farther away from the Hf atom, $E_{ads}$ becomes −0.52 eV, which is very close to that of pristine non-doped TiC. This is more clear evidence of the very local nature of the dopant effect in the carbide–$CO_2$ interactions.

This finding can be further supported by calculations for the W doped surface with a TopC $E_{ads}$ of −0.14 eV but −0.49 eV when $CO_2$ is in a TopC site farther away from W, thus showing a difference of only 0.02 eV from the result for undoped TiC. In line with the above-mentioned charge density distortions (see also Table S1, ESI†), we consider in the following that the doping effect is completely local and focus on the situations where $CO_2$ is close to the doping atom as in Fig. 1.

Finally, the same two doping agents (Hf and W) have been used to evaluate possible effects due to dopant saturation/coverage on the surface. To this end, an extra $CO_2$ with its correspondent dopant has been added to the $(3\sqrt{2}\times3\sqrt{2})R45^\circ$ unit cell, effectively increasing the doping concentration and also the $CO_2$ coverage (see Fig. S2, ESI†). The results, as expected,

reveal a reduction of the mean adsorption energies to −0.77 eV for the case of Hf and −0.13 eV for that of W. Interestingly, the local nature of the dopant effect prevails, a strengthening of the interaction is observed for Hf, and a weakening for W. The reduction with respect to the low coverage case is mostly due to steric repulsion between adsorbates.

### 3.4. Activated $CO_2$ structure

In all cases where the surface–$CO_2$ interaction leads to a C–C type of bond, similar structural changes appear for the adsorbed $CO_2$ molecule. The O–C–O angle is reduced from 180° to <130° and the C–O distances are elongated with bond lengths in the 1.28–1.30 Å range, thus larger than the computed PBE value of 1.16 Å for $CO_2$ in vacuum (Table S3, ESI†). For the studied TopC cases, where a clear interaction exists between one of the O atoms of the $CO_2$ molecule and the dopant, the symmetry of the $CO_2$ bonds is slightly broken with the C–O distances featuring differences of up to 0.02 Å. One can speculate that this lack of symmetry might have an impact on the subsequent $CO_2$ usage since one of the C–O bonds appears to be more activated with a preference for further reactions such as $CO_2$ dissociation upon hydrogenation.[10]

### 3.5. Charge transfer

Additional information to better understand the observed trends in $CO_2$ adsorption energy triggered by the presence of the dopant is gained by analyzing the net charges on relevant atoms as obtained from the Bader's atoms-in-molecules analysis of the total electron density.[38] To this end two possibilities are investigated involving the relationship between $E_{ads}$ and the initial Bader charges of the doped surface (Table S1, ESI†), or the net charge transfer from the doped-surface to $CO_2$ (Table S3, ESI†). The first relationship, summarized in Fig. 3, strongly supports that the more oxidized the dopant, then the stronger the adsorption of $CO_2$. This is in agreement with the previously discussed charge modifications of the surface electronic structure due to the presence of the dopant.

The chemistry behind this trend is quite simple. A more oxidized cation leads to higher negative charge on the neighboring C atoms (Table S1, ESI†) directly interacting with the adsorbate; this is a feature that favors electron transfer to the $CO_2$. On the other hand, comparing the local charges with and without the adsorption, one observes that the charge transferred to the $CO_2$ strongly depends on the binding mode rather than on the dopant (see Table S3, ESI†). Upon $CO_2$ adsorption, the surface C involved in the bonding becomes less negatively charged, and $CO_2$ is highly activated exhibiting a net charge in the −0.76 to −0.98 $e$ range. The emerging picture of the adsorption process can be thought of as a Lewis acid–base reaction,[40] a feature also reported for the interaction of $CO_2$ with some oxides.[41] The surface acts as a base transferring charge to the $CO_2$ acting as an acid.

To further confirm the role played by the charge transfer in $CO_2$ adsorption on the doped TMC surfaces, the same analysis has been repeated for other binding modes with a smaller adsorption energy which all display a smaller degree of charge transfer. Thus, a general trend is present where stronger adsorption

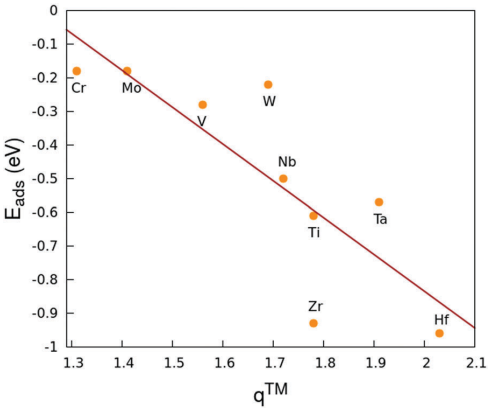


Fig. 3 $E_{ads}$ *vs.* Bader charges of the surface doping TM, $q^{TM}$. A linear fit ($R$ = 0.76) is shown as a red line.

energies involve concomitant larger charge transfer, a point observed in two-dimensional carbides used in ammonia synthesis.[42] Lastly, we note that the negatively charged adsorbate would attract other positively charged species such as $H^+$ with implications for $CO_2$ conversion, especially in its electroreduction.

### 3.6. Work function analysis

The bonding mechanism between doped TiC and $CO_2$ which we have discussed above and which involves charge transfer may have observable consequences. In particular, it is likely to affect the surface work function ($\phi$), a descriptor for base–acid characterization of the surfaces.[40] Several studies, both experimental and theoretical, related to $CO_2$ adsorption on other surfaces such as Ni[43,44] and Co,[45,46] evaluated this property as a chemical activity descriptor although whereas trends along a series are normally trustable[47] it needs to be used with caution.[48]

In the present work only $CO_2$-free doped TiC(001) surfaces were studied to investigate the predictive nature of such a descriptor regarding dopant effects. Within the present surface slab model, the work function was calculated as the energy difference between the electrostatic potential in the vacuum above the surface, $V$, and the Fermi energy, $E_F$. This was carried out for the bare undoped surface model, as well as for the doped cases. A dipole correction has been applied in the direction perpendicular to the surface plane to counteract the small surface dipole created by the doping. The results for metal doped TiC(100) surfaces are summarized in Table 3. These results show that low/high work functions tend to favor/disfavor $CO_2$ adsorption, as expected. However, one must also caution that the relationship between the workfunction and $CO_2$ adsorption is not strong enough so as to conclude a definitive clear direct link between them, which is consistent with previous work.[47,48] Hence, the dopant effects appear to be too local so as to strongly modify the overall surface work function.

### 3.7. Adsorption/desorption rates

Pressure and temperature are important factors to control the $CO_2$ adsorption capacity of such metal doped TMCs. The rates

Table 3 Calculated work function ($\phi$) and work function variation ($\Delta\phi$) of M-TiC doped (001) surfaces

| Dopant | $\phi$ (eV) | $\Delta\phi$ (eV) |
|---|---|---|
| Ti | 3.99 | — |
| Cr | 3.99 | 0.00 |
| Hf | 3.93 | −0.06 |
| Mo | 3.97 | −0.02 |
| Nb | 3.96 | −0.03 |
| Ta | 3.95 | −-0.04 |
| V | 3.99 | 0.00 |
| W | 3.96 | −0.03 |
| Zr | 3.89 | −0.10 |

Table 4 PBE calculated adsorption energies without ($E_{ads}$) and with ($E_{ads}^{ZPE}$) ZPE correction

| Dopant | Binding mode | $E_{ads}$ (eV) | $E_{ads}^{ZPE}$ (eV) |
|---|---|---|---|
| Ti | — | −0.61 | −0.59 |
| Cr | TopC-adj | −0.62 | −0.60 |
| Hf | TopC | −0.96 | −0.93 |
| Mo | TopC-adj | −0.39 | −0.37 |
| Nb | TopC | −0.50 | −0.48 |
| Ta | TopC | −0.57 | −0.55 |
| V | TopC-adj | −0.57 | −0.54 |
| W | TopC-adj | −0.31 | −0.28 |
| Zr | TopC | −0.93 | −0.90 |

of the adsorption and desorption, evaluated through transition state theory, determine whether the $CO_2$ will be quantitatively stored on the surface or will be desorbed as fast as it will contact with the surface. The adsorption and desorption rate estimates, $r_{ads}$ and $r_{des}$, respectively, have been obtained following the set up described by Kunkel *et al.*,[10] at the current atmospheric $CO_2$ partial pressure (40 Pa). Towards this end, the vibrational frequencies of adsorbed $CO_2$ are required, and calculated with the PBE functional through diagonalization of the corresponding block of the Hessian matrix with elements obtained from finite displacements of 0.03 Å of the $CO_2$ molecule analytic gradients. The obtained frequencies allow taking into account the zero point energy (ZPE) in the calculated $E_{ads}$ with values reported in Table 4. Notice that the main effect of the ZPE correction is to reduce the adsorption strength, but it does by up to, at most, 0.03 eV, and therefore can be considered negligible.

Fig. 4 reports the $CO_2$ $r_{ads}$ and $r_{des}$ values for TiC(001) and doped-TiC(001) clearly showing that a small increase in the adsorption energies implies a slight increase of the limit temperature between adsorption and desorption regions. Indeed, for Hf-doped TiC, the adsorption energy is 0.34 eV stronger than for undoped TiC(001), implying an equilibrium temperature between adsorption and desorption of 370 K; this is 135 K higher than the corresponding value for stoichiometric TiC estimated as 235 K.[10] Consequently, Hf-doped TiC would lead to $CO_2$ capture at higher temperature conditions. For other doping metals, such as W, the temperature decreases, but, in such situations, the previous analysis indicates that $CO_2$ will preferentially occupy dopant-free surface regions and, as a result, no change in the equilibrium temperature is to be expected.

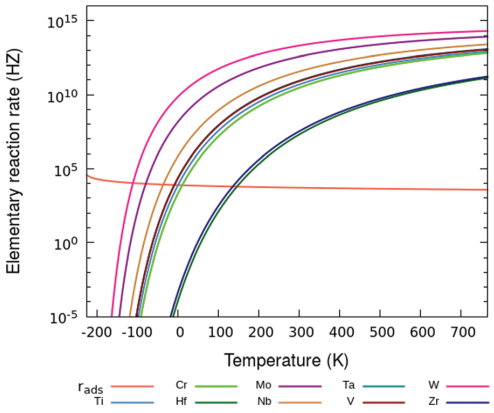


Fig. 4 Calculated rates of desorption, $r_{des}$, and adsorption, $r_{ads}$ of $CO_2$ on the TiC(001) surface at 40 Pa, the current partial pressure of atmospheric $CO_2$. The desorption rates of the undoped and doped surfaces are shown as color-coded lines.

## 4. Summary and conclusions

The present DFT based study reports the effects caused by a dopant in the TiC(001) surface on $CO_2$ capture, storage, and activation. The dopants considered are also early TMs (Hf, Ta, Zr, Nb, W, Cr, Mo, and V) placed either at the surface or at the subsurface layer and always replacing a Ti cation. The dopant effect on the geometric and the electronic configurations is found to be highly local. Calculations predict that doping at the outermost surface layer is always preferred over subsurface substitution. The effect of dispersion has been found to equally affect the undoped and doped situations and, therefore, can be considered as a constant. Depending on the dopant, $CO_2$ adsorption energies can be enhanced, mostly down a group, or reduced, when going along a *d* series.

The results reported in the present work have been obtained for doped TiC but the trends can be easily extrapolated to others TMCs. For instance, according to the observed trends, the Ti-doped VC system would feature an enhanced adsorption energy compared to pure VC. Overall, through surface doping, the $CO_2$ capture conditions can be tuned, while keeping the activated nature of the chemisorbed molecule.

A meaningful analysis of the $CO_2$ interaction with such TMCs reveals that the adsorption is driven by the surface $CO_2$ charge transfer, and ultimately biased by the surface charge rearrangement/transfer when the doping agent is introduced. We hope that the hereby predicted potential of doped TMCs for CCS and CCU technologies would trigger further experimental work in this field.

## Conflicts of interest

The authors declare no competing financial interest.

## Acknowledgements

L. B., J. J. C. and M. N. at Tyndall acknowledge support from the Science Foundation Ireland funded US-Ireland R&D Partnership Program project SusChem grant SFI 14/US/E2915 and from the European Commission funded FP7-NMP project BIOGO, grant number 604296. The SFI/HEA funded Irish Centre for High-end Computing (ICHEC) and SFI funded computing clusters at Tyndall are acknowledged for generous access to computing resources. The work carried out at the Universitat de Barcelona has been supported by Spanish Ministerio de Economía y Competitividad (MINECO/FEDER) CTQ2015-64618-R grant, Generalitat de Catalunya grants 2017SGR13 and XRQTC, and EU H2020 NOMAD project No 676580. F. V. thanks Spanish MINECO for a Ramón y Cajal research contract (RYC-2012-10129) and F. I. acknowledges additional support from the 2015 ICREA Academia Award for Excellence in Research.

## References

1 C. B. Filed, V. R. Barros, D. Jon Dokken, K. J. Mach, M. D. Mastrandrea, T. E. Bilir, M. Chatterejee, K. L. Ebi, Y. O. Estrada, R. C. Genova and B. Girma, *et al.*, *Climate Change 2014: Impacts, Adaptation, and Vulnerability*, 2014.

2 O. Edenhofer; R. Pichs-Madruga; Y. Sokona; J. C. Minx; E. Farahani; K. Susanne; K. Seyboth; A. Adler; I. Baum and S. Brunner; *et al.*, *Climate Change 2014: Mitigation of Climate Change*, 2014.

3 E. Kendon, N. Roberts, H. Fowler, M. Roberts, S. Chan, A. C. Senior, K. Susanne, K. Seyboth, A. Adler, I. Baum and S. Brunner, Heavier Summer Downpours with Climate Change Revealed by Weather Forecast Resolution Model, *Nat. Clim. Change*, 2014, **4**, 570–576.

4 P. M. Cox, R. A. Betts, C. D. Jones, S. A. Spall and I. J. Totterdell, Acceleration of Global Warming due to Carbon-Cycle Feedbacks in a Coupled Climate Model, *Nature*, 2000, **408**, 184–187.

5 S. C. Doney, V. J. Fabry, R. A. Feely and J. A. Kleypas, Ocean Acidification: The other $CO_2$ Problem, *Annu. Rev. Mar. Sci.*, 2009, **1**, 169–192.

6 UN Doc FCCC/CP/1997/7/Add.1. Kyoto Protocol to the United Nations Framework Convention on Climate Change Dec. 10, 1997; 37 ILM 22 1998.

7 UN Doc FCCC/CP/2009/L.7Copenhagen Accord.18 December 2009.

8 UN Doc FCCC/CP/2015/7, Paris Agreement, 2015, https://unfccc.int/sites/default/files/english_paris_agreement.pdf.

9 International Energy agency (©OECD/IEA). Global energy and $CO_2$ status report-2017; 2018.

10 C. Kunkel, F. Viñes and F. Illas, Transition Metal Carbides as Novel Materials for $CO_2$ Capture, Storage, and Activation, *Energy Environ. Sci.*, 2016, **9**, 141–144.

11 Y. Cheng-Hsiu, H. Chihi-Hung and T. Chung-Sung, A Review of $CO_2$ Capture by Absorption and Adsorption, *Aerosol Air Qual. Res.*, 2016, **12**, 745–769.

12 H. Freund and M. W. Roberts, Surface Chemistry of Carbon Dioxide, *Surf. Sci. Rep.*, 1996, **25**, 225–273.

13 L. Espinal, D. L. Poster, W. Wong-Ng, A. J. Allen and M. L. Green, Measurement, Standards, and Data Needs for $CO_2$ Capture Materials: A Critical Review, *Environ. Sci. Technol.*, 2013, **47**, 11960–11975.

14 D. M. D'Alessandro, B. Smit and J. R. Long, Carbon Dioxide Capture: Prospects for New Materials, *Angew. Chem., Int. Ed.*, 2010, **49**, 6058–6082.

15 P. Markewitz, W. Kuckshinrichs, W. Leinter, J. Linssen, P. Zapp, R. Bongartz, A. Schreiber and T. E. Müller, Worldwide Innovations in the Development of Carbon Capture Technologies and the Utilization of $CO_2$, *Energy Environ. Sci.*, 2012, **5**, 7281–7305.

16 S. Posada-Pérez, F. Viñes, J. A. Rodriguez and F. Illas, Fundamentals of Methanol Synthesis on Metal Carbide Based Catalysts: Activation of $CO_2$ and $H_2$, *Top. Catal.*, 2014, **58**, 159–173.

17 S. Posada-Pérez, F. Viñes, P. J. Ramirez, A. B. Vidal, J. A. Rodriguez and F. Illas, The Bending Machine: $CO_2$ Activation and Hydrogenation on δ-MoC(001) and β-$Mo_2C$(001) Surfaces, *Phys. Chem. Chem. Phys.*, 2014, **16**, 14912–14921.

18 N. Li, X. Chen, W.-J. Ong, D. R. MacFarlene, X. Zhao, A. K. Cheetham and C. Sun, Understanding of Electrochemical Mechanisms for $CO_2$ Capture and Conversion into Hydrocarbon Fuels in Transition-Metal Carbides (Mxenes), *ACS Nano*, 2017, **11**, 10825–10833.

19 S. Wu and J. Ho, Adsorption, Dissociation, and Hydrogenation of $CO_2$ on WC (0001) and WC–Co Alloy Surfaces Investigated with Theoretical Calculations, *J. Phys. Chem. C*, 2012, **116**, 13202–13209.

20 A. B. Vidal, L. Feria, J. Evans, Y. Takahashi, P. Liu, K. Nakamura, F. Illas and J. A. Rodriguez, $CO_2$ Activation and Methanol Synthesis on Novel Au/TiC and Cu/TiC Catalysts, *J. Phys. Chem. Lett.*, 2012, **3**, 2275–2280.

21 M. D. Porosoff, S. Kattel, W. Li, P. Liu and J. G. Chen, Identifying Trends and Descriptors for Selective $CO_2$ Conversion to CO over Transition Metal Carbides, *Chem. Commun.*, 2015, **51**, 6988–6991.

22 H. G. Yang, C. H. Sun, S. Z. Qiao, J. Zou, G. Liu, S. C. Smith, H. M. Cheng and G. Q. Lu, Anatase $TiO_2$ Single Crystals With a Large Percentage of Reactive Facets, *Nature*, 2008, **453**, 638–641.

23 O. Lamiel, S. Tosoni and F. Illas., Relative Stability of F-Covered $TiO_2$ Anatase (101) and (001) Surfaces from Periodic DFT Calculations and ab Initio Atomistic Thermodynamics, *J. Phys. Chem. C*, 2014, **118**, 13667–13673.

24 I. Yerskin and M. Nolan, Doping of Ceria Surfaces with Lantanium: a DFT+U Study, *J. Phys.: Condens. Matter*, 2010, **22**, 135004.

25 M. Nolan, Enhanced Oxygen Vacancy Formation in Ceria (111) and (100) Surfaces Doped with Divalent Cations, *J. Mater. Chem.*, 2011, **21**, 9160–9168.

26 Y. Liu, C. Wen, Y. Guo, G. Lu and Y. Wang, Modulated CO Oxidation Activity of M-Doped Ceria (M = Cu, Ti, Zr, and Tb): Role of Pauling Electronegativity of M, *J. Phys. Chem. C*, 2010, **114**, 9889–9897.

27 Y. N. Regmi and B. M. Leonard, General Synthesis Method for Bimetallic Carbides of Group VIIIA First Row Transition Metals with Molybdenum and Tungstenum, *Chem. Mater.*, 2014, **26**, 2609–2616.

28 S. M. Kozlov, G. Kovács, R. Ferrando and K. M. Neyman, How to Determine Accurate Chemical Ordering in Several Nanometer Large Bimetallic Crystallites from Electronic Structure Calculations, *Chem. Sci.*, 2015, **6**, 3868–3880.
29 P. Hohenberg and W. Khon, Inhomogeneous Electron Gas, *Phys. Rev. B: Condens. Matter Mater. Phys.*, 1964, **136**, 846–871.
30 W. Khon and L. Sham, Self-Consistent Equations Including Exchange and Correlaction Effects, *Phys. Rev. A: At., Mol., Opt. Phys.*, 1965, **140**, 1133–1137.
31 J. P. Perdew, K. Burke and M. Ernzerhof, Generalized Gradient Approximation Made Simple, *Phys. Rev. Lett.*, 1996, **77**, 3865–3868.
32 G. Kresse and J. Hafner, Norm-Conserving and Ultrasoft Pseudopotentials for First Row and Transition Elements, *J. Phys.: Condens. Matter*, 1994, **6**, 8245–8257.
33 G. Kresse and J. Furthmüller, Efficiency of *Ab-initio* Total Energy Calculations for Metals and Semiconductors Using a Plane-Wave Basis Set, *Comput. Mater. Sci.*, 1996, **6**, 15–50.
34 G. Kresse and J. Furthmüller, Efficient Iterative Schemes for Ab Initio Total-Energy Calculations Using a Plane-Wave Basis Set, *Phys. Rev. B: Condens. Matter Mater. Phys.*, 1996, **54**, 11169–11186.
35 P. E. Blöchl, Projector Augmented-Wave Method, *Phys. Rev. B: Condens. Matter Mater. Phys.*, 1994, **50**, 17953–17979.
36 G. Kresse and D. Joubert, From Ultrasoft Pseudopotentials to the Projector Augmented-Wave Method, *Phys. Rev. B: Condens. Matter Mater. Phys.*, 1999, **59**, 1758–1775.
37 H. J. Monkhorst and J. D. Pack, Special Points for Brillouin-Zone Integrations, *Phys. Rev. B: Condens. Matter Mater. Phys.*, 1976, **13**, 5188–5192.
38 R. F. W. Bader, Atoms in Molecules, *Encyclopedia of Computational Chemistry*, John Wiley & Sons, Ltd, Chichester, UK, 2002.
39 S. Grimme, J. Antony, S. Ehrlich and H. Krieg, A Consistent and Accurate Ab Initio Parametrization of Density Functional Dispersion Correction (DFT-D) for the 94 Elements H-Pu, *J. Chem. Phys.*, 2010, **132**, 154104.
40 P. C. Stair, The Concept of Lewis Acid and Bases Applied to Surfaces, *J. Am. Chem. Soc.*, 1982, **104**, 4044–4052.
41 G. Pacchioni, J. M. Ricart and F. Illas, Ab initio cluster model calculations on the chemisorption of $CO_2$ and $SO_2$ probe molecules on MgO and CaO(100) surfaces. A theoretical measure of oxide basicity, *J. Am. Chem. Soc.*, 1994, **116**, 10152–10158.
42 L. Miguel-Azofra, N. Li, D. R. MacFarlene and C. Sun, Promising Prospects for 2D $d^2$–$d^4$ $M_3C_2$ Transition Metal Carbides (MXenes) in $N_2$ Capture and Conversion into Ammonia, *Energy Environ. Sci.*, 2016, **9**, 2545–2549.
43 X. Ding, Interaction of Carbon Dioxide with Ni(110): A Combined Experimental and Theoretical Study, *Phys. Rev. B: Condens. Matter Mater. Phys.*, 2007, **76**, 195425.
44 B. Bartos, H. J. Freund, H. Kuhlenbeck, M. Neumann, H. Lindner and K. Müller, Adsorption and Reaction of $CO_2$ and $CO_2$/O CO-Adsorption on Ni(110): Angle Resolved Photoemission (ARUPS) and Electron Energy Loss (HREELS) Studies, *Surf. Sci.*, 1987, **179**, 59–89.
45 M. Frerichs, F. X. Schweiger, F. Voigts, S. Rudenkiy, W. Maus-Friedrichs and V. Kempter, Interaction of $O_2$, CO and $CO_2$ with Co Films, *Surf. Interface Anal.*, 2005, **37**, 633–640.
46 V. A. de la Peña O'Shea, S. González, F. Illas and J. L. G. Fierro, Evidence for Spontaneous $CO_2$ Activation on Cobalt Surfaces, *Chem. Phys. Lett.*, 2008, **454**, 262–268.
47 A. Migani and F. Illas, A systematic study of the structure and bonding of halogens on low index transition metal surfaces, *J. Phys. Chem. B*, 2006, **110**, 11894–11906.
48 A. Migani, C. Sousa and F. Illas, Chemisorption of atomic chlorine on metal surfaces and the interpretation of the induced work function changes, *Surf. Sci.*, 2005, **574**, 297–305 and references therein.

 

THE JOURNAL OF PHYSICAL CHEMISTRY C

pubs.acs.org/JPCC Article

# Predicting the Effect of Dopants on $CO_2$ Adsorption in Transition Metal Carbides: Case Study on TiC (001)

Martí López, Francesc Viñes,* Michael Nolan,* and Francesc Illas

Cite This: J. Phys. Chem. C 2020, 124, 15969−15976 Read Online

ACCESS | Metrics & More | Article Recommendations | Supporting Information

**ABSTRACT:** A previous work has shown that doping the TiC (001) surface with early transition metals significantly affects $CO_2$ adsorption and activation, which opens up a possible way to control this interesting chemistry. In this work, we explore other possibilities, which include nontransition metal elements (Mg, Ca, Sr., Al, Ga, In, Si, and Sn) as well as late transition metals (Pd, Pt, Rh, and Ir) and lanthanides (La and Ce), often used in catalysis. Using periodic slab models with large supercells and state-of-the-art density functional theory (DFT) based calculations, we show that, in all the studied cases, $CO_2$ appears as bent and, hence, activated. However, the effect is especially pronounced for dopants with large ionic crystal radii. This can increase desorption temperature by up to 230 K, almost twice the value predicted when early transition metals are used as dopants. However, a detailed analysis of the results shows that the main effect does not come from the electronic structure perturbations but from the distortion that the dopant generates into the surface atomic structure. A simple descriptor is proposed that would allow predicting the effect of the dopant on $CO_2$ adsorption energy in transition metal carbide surfaces without the need for DFT calculations.

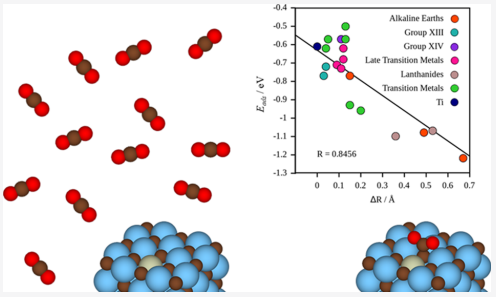




## 1. INTRODUCTION

Finding ways to mitigate global warming, which is primarily driven by the increase in the concentration of $CO_2$ in the Earth's atmosphere as a result of the use of fossil fuels, has become a major research topic. Global warming is predicted to trigger harmful consequences such as ocean acidification,[1] increase in the sea level,[2] or increasing temperatures through the carbon-cycle feedback.[3] Finding alternative, environmentally friendly energy sources to ensure a sustainable industry has become very significant.[4−6] However, although much success has been achieved, the increasing energy demand and the concomitant technical complexity make the translation of such advances into real alternative to finally overcome the fossil fuel energy dependence, in a short-to-medium term, difficult to achieve.

Meanwhile, new strategies are being explored to address more immediate issues. In particular, $CO_2$ capture and storage (CCS),[7−9] and usage (CCU)[10] technologies are being actively investigated. Several CCS approaches are currently being explored with absorption constituting the dominant technology, although adsorption or membrane gas separation are other possibilities, which are in the developmental research stage.[8,9,11,12] To move forward by adding extra value to the captured $CO_2$, CCU technology is slowly growing due to its important industrial and economic potential.[10] Reintroducing $CO_2$ to the industrial cycle through industrial processes including hydrogenation to methanol, or the reverse water gas shift (RWGS) reaction would be extremely positive both for the environment and for the industry.

With CCU in mind, several materials have been tested and Ni, Pd, or Pt nanoparticles supported on oxides or sulfides[13] are the current industry choice, while significant efforts have been made to find an appropriate oxide support. It is also worth mentioning that rather recent experiments on model systems found that small Au, Cu, and Ni nanoparticles supported on TiC (001) exhibit improved performance in methanol synthesis compared to a model of the conventional Cu/ZnO catalyst.[14,15] In addition, bare transition metal carbides such as MoC and $Mo_2C$ have been found to be active in catalyzing $CO_2$ activation[16] and conversion as well,[17] being highly appealing as they surpass the limitation of using scarce and expensive late transition metals.

Indeed, computational studies, carried out in the framework of density functional theory (DFT), have shown that early transition metal carbides (TMCs) such as TiC, ZrC, WC, NbC, TaC, and, δ-MoC are able to strongly trap and activate

Received: May 1, 2020
Revised: June 26, 2020
Published: June 26, 2020

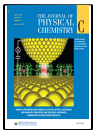

$CO_2$.[18] Besides, there is experimental and/or computational evidence that $\delta$-MoC, $\beta$-$Mo_2C$, WC, and NbC (001) surfaces present high selectivity toward $CO_2$ conversion to CO,[16,19,20] a component of synthesis gas used in many industrial reactions. It is also worth noticing that model catalysts combining late transition metals with TMCs are also attractive, for example, Pt/$Mo_2C$ exhibits high performance toward water gas shift (WGS) with high rates when compared to the widely used Pt/$CeO_2$ or Pt/$TiO_2$ catalysts.[21] In conclusion, TMCs bring together three key properties that confers them with significant potential for CCU applications, namely, high $CO_2$ adsorption capability, competitive performance in catalysis, and attractive cost.

To further enhance the catalytic activity of TMCs, it has been proposed to make use of doping,[22] a strategy already successfully followed to enhance the catalytic performance of metal oxides.[23,24] In particular, the effect of doping on the TiC (001) surface with early transition metals (Hf, Ta, Zr, Nb, W, Cr, Mo, and V) was systematically explored by means of DFT calculations on a series of models where the dopant substituted a Ti atom at the surface atomic layer.[22] Such calculations revealed that the effect was highly local with a strong preference for surface substitution and that the adsorption energy could be enhanced or reduced depending on whether the dopant was chosen down a group or going along a *d* series. In addition, a relationship between the calculated net charge in the doping metal atom directly interacting with $CO_2$ and the corresponding adsorption energy was found, indicating a significant chemical effect. To reach a more complete understanding on this issue and broaden the tuning capabilities well beyond the limited region of early transition metals, we consider, in this work, the effect of other dopants including *s* block alkaline earth (Mg, Ca, and Sr), *p* block groups XIII (Al, Ga, and In) and XIV (Si and Sn) elements, plus some extra late *d* block transition metals (Pd, Pt, Rh, and Ir), even *f* elements such as lanthanides (La and Ce), with the main aim to further assess the capabilities of modified TMCs for use in CCS and CCU technologies.

## 2. SURFACE MODELS AND COMPUTATIONAL DETAILS

We employ the widely studied TiC (001) surface as the dopant host, as used in an earlier work.[22] The corresponding doped models and their interaction with $CO_2$ have been studied in the framework of DFT with calculations carried out with the broadly used Perdew−Burke−Ernzerhof (PBE) exchange−correlation functional,[25] which is among the best functionals to describe the bulk and surface properties of TMCs,[26,27] including elastic and compressive properties,[28] and significantly improving earlier descriptions[29] based on other generalized gradient functionals such as the Perdew−Wang 91 (PW91)[30] or the revised PBE (RPBE).[31] The PBE functional, including a suitable treatment of dispersive forces, has been found to be accurate to assess the experimental interaction of $CO_2$ with diverse TMCs.[17,32] However, in the present work, it was found convenient to neglect the dispersion contribution to the adsorption energy because our previous studies on bare or doped TiC have shown that the main effect of dispersion is a nearly constant increase of ca. −0.26 eV in all calculated adsorption energies, with negligible effects on the $CO_2$ adsorption strength, which arises primarily from the formation of C−C covalent bonds, a substrate→$CO_2$ charge transfer, and the $CO_2^{\delta-}$ Coulombic stabilization with TMC positively charged metal atoms, rather than any dispersion interactions. In addition, the effects of dispersion are also not significant when analyzing the trends across different dopants.[16,18,22] Nevertheless, one should always keep in mind that dispersive forces may play a role in the prediction of quantitative interaction energies[33] and that this can have some effect on the calculated desorption rates and temperature desorption, as discussed in detail in our results.

The TiC (001) surface is represented by a periodic $(3\sqrt{2} \times 3\sqrt{2})R45°$ supercell slab model consisting of six stoichiometric atomic layers periodic in surface directions with eight C and Ti atoms per layer. To provide an adequate description of the surface relaxations, the four uppermost layers were fully allowed to relax during optimization with the two bottommost layers fixed to the pristine TiC bulk structure. To avoid interactions between the periodically repeated slabs in the direction perpendicular to the surface, a vacuum width of 15 Å along the vacuum direction has been added.

Doping has been simulated by substituting one surface Ti atom with the corresponding dopant, a choice which is justified by a previous work indicating that surface doping was always preferred[22] and that subsurface doping has no effect on the $CO_2$ adsorption properties. Indeed, explicit calculations for subsurface doping further confirm this prediction; systematically finding that surface doping is the most favorable case, see Table 1. This is not surprising as surface doping allows a lower energy cost for structural relaxation to adapt to the different atomic sizes of the dopant compared to Ti. The dopant concentration in different models is 3.125 at. %, which is a common value in doped metal oxides and is low enough so as to neglect the distortions in the TiC host, see below.

**Table 1. Ionic Crystal Radii of Metallic Dopants, $R_{dop}$,[a] Dopant Distance to Carbon in the Surface Plane Distance, $d$(CM), and Doping Formation Energies, $\Delta E_{dop}$, as well as when Allowing Surface Relaxation, $\Delta E_{dop}^{relax}$, and Energy Difference between Subsurface and Surface Doping, where Positive Values Imply a Preference for Surface Doping, $\Delta E_{sub\text{-}surf}$[b]**

| dopant | $R_{dop}$ | $d$(CM) | $\Delta E_{dop}$ | $\Delta E_{dop}^{relax}$ | $\Delta E_{sub-surf}$ |
|---|---|---|---|---|---|
| $Ti^{4+}$ | 0.65 | 2.17 | 0 | 0 | 0 |
| $Mg^{2+}$ | 0.80 | 2.26 | 11.42 | 11.09 | 0.74 |
| $Ca^{2+}$ | 1.14* | 2.39 | 10.86 | 10.65 | 1.99 |
| $Sr^{2+}$ | 1.32* | 2.59 | 11.64 | 11.40 | 1.54 |
| $Al^{3+}$ | 0.62 | 2.19 | 8.66 | 8.34 | 0.39 |
| $Ga^{3+}$ | 0.69 | 2.22 | 11.03 | 10.71 | 0.99 |
| $In^{3+}$ | 0.94 | 2.28 | 11.85 | 11.62 | 1.79 |
| $Si^{4+}$ | 0.54* | 2.12 | 8.40 | 8.20 | 0.65 |
| $Sn^{4+}$ | 0.76 | 2.26 | 11.12 | 10.90 | 1.45 |
| $Rh^{4+}$ | 0.74 * | 2.20 | 6.50 | 6.17 | 0.26 |
| $Ir^{4+}$ | 0.77* | 2.19 | 4.89 | 4.54 | 0.44 |
| $Pd^{4+}$ | 0.76* | 2.23 | 9.84 | 9.53 | 0.31 |
| $Pt^{4+}$ | 0.77* | 2.21 | 7.64 | 7.30 | 0.32 |
| $La^{3+}$ | 1.18* | 2.46 | 7.14 | 6.94 | 4.86 |
| $Ce^{4+}$ | 1.01* | 2.33 | 6.02 | 5.85 | 3.28 |

[a]The ionic crystal radii of dopants reported were provided by the Atomistic Simulation Group lead by Prof. Robin Grimes at the Imperial College London. These correspond to surface atoms—with fivefold coordination—or, when this information is not available, to sixfold coordination, the latter are marked with an asterisk. [b]Distances and radii are given in Å, whereas energies in eV. The $Ti^{4+}$ dopant refers to the pristine, undoped surface, used as a reference.



https://dx.doi.org/10.1021/acs.jpcc.0c03893
J. Phys. Chem. C 2020, 124, 15969−15976

All structural optimizations were carried out from the bare TiC-optimized geometry as mentioned in a previous work.[22] The molecular structure and energy of the $CO_2$ molecule in the gas phase and the energy of the isolated metal atoms have been obtained by placing them in an asymmetric box of 9 × 10 × 11 Å to force correct molecular orbital occupation. For the isolated metal atoms, spin-polarized calculations have been performed to properly describe their open shell nature. The interaction of $CO_2$ with different surface models starts by placing the molecule 2 Å away from the surface and exploring all possible surface sites and bonding modes as done in an earlier study.[22]

The $CO_2$ adsorption energy, $E_{ads}$, has been calculated as in eq 1.

$$E_{ads} = E_{CO_2/slab} - (E_{slab} + E_{CO_2}), \quad (1)$$

where $E_{CO_2/slab}$ is the energy of $CO_2$ adsorbed on the slab surface, $E_{slab}$ is the energy of the pristine-relaxed TiC slab surface model, and $E_{CO_2}$ is the energy of the isolated gas phase $CO_2$. Within this notation, the more negative the $E_{ads}$ value, the stronger the interaction. For the most stable situations of the adsorbed molecule, the net charges were estimated using the Bader's atoms-in-molecules analysis of the total electron density.[34]

All calculations employ periodic models and have been carried out by means of the Vienna ab initio simulation package (VASP) code,[35] which uses a plane-wave basis set to expand the valence electron density[36] and includes the effect of the atomic cores on valence electron density by means of the Kresse and Joubert[37] implementation of the projector augmented wave (PAW) approach of Blöchl.[38] In all cases, the core electron PAWs are the ones recommended by default by the VASP developers. More details are provided in the Supporting Information.

An optimized cutoff kinetic energy of 450 eV has been used for the plane-wave basis set expansion and a Monkhorst–Pack[39] grid of (2 × 2 × 1) special **k**-point was used to carry out the necessary numerical integration in the reciprocal space, so as to ensure that the adsorption energies to be converged are below the chemical accuracy of ∼0.04 eV. In the case of isolated atoms or the $CO_2$ molecule, the optimizations were carried out at $\Gamma$ point. The structure optimization has been carried out until forces on all atoms are smaller than 0.02 eV $Å^{-1}$. The threshold convergence for the electronic energy was set to $10^{-5}$ eV. To speed up convergence of the calculations, a Gaussian smearing with a width of 0.2 eV has been used and the final energies are obtained by removing the smearing, that is, by extrapolating to 0 K. In the case of isolated atoms or molecules, the smearing was reduced to 0.001 eV to ensure proper orbital occupation.

## 3. RESULTS AND DISCUSSION

We start this section by considering several features of the doped surfaces including the ionic crystal radius of the dopant, the distance between the dopant and its neighboring atoms, and the relative stability of doping. The latter is defined as

$$\Delta E_{dop} = (E_{TiMC} + E_{Ti}) - (E_{TiC} + E_M), \quad (2)$$

where $E_{TiMC}$ is the energy of the doped slab, $E_{Ti}$ is the energy of a single Ti atom in vacuum, $E_{TiC}$ is the energy of the pristine slab surface model, and $E_M$ is the energy of the dopant atom in vacuum. Within this notation, negative $E_{dop}$ values indicate favorable substitution of a single Ti atom by the doping M atom, having atomic reservoirs of both in vacuum. Notice that this is a practical and direct way of qualitatively assessing the relative stabilities of dopants but results in large $\Delta E_{dop}$ values, for example, as compared to using other condensed doping reservoir sources.

Thus, results in Table 1 show that the substitution of Ti with dopants is apparently not very thermodynamically favorable, which is not surprising because mixed transition metal carbides are scarce although they do exist.[40] However, this is not so important since experimental processes for preparing doped carbides will follow other already well-established routes widely used for the doping of metal oxides. The $\Delta E_{dop}$ values when allowing cell relaxation along the surface directions, $\Delta E_{dop}^{relax}$, change by only ca. ∼0.25 eV on average (see Table 1), reflecting the small impact of the doping agent on the TiC host crystal structure. The $\Delta E_{dop}$ results highlight that it is somewhat more favorable to dope with late transition metals or even lanthanides, rather than with *p* block elements or alkaline earth metals.

Also note that the oxidation state of the dopant reported in Table 1 has been chosen so as to correspond to the most common one. Covalent and ionic crystal atomic radii have been explored due to the mixed character of the M–C bond.[41] An initial analysis of the results shown in Table 1 indicates that the distortion in the C to M dopant atom follows the ionic crystal radii, as expected. Si appears to be an exception which may indicate some inaccuracy on the estimate of the ionic radius of this element or that the reported ionic radius is not adequate for comparison purposes here.

To get additional information about the effects introduced by the dopant, we analyze the net charges on these atoms obtained from the computed Bader charges.[34] Table 2 shows

**Table 2. Bader Charges of the Dopant, $q^{dop}$, and on the C Atoms Surrounding it at the Surface, $q^{surf}$, and Just beneath it, $q^{sub}$[a]**

| dopant | $q^{surf}$ | $q^{sub}$ | $q^{dop}$ |
|---|---|---|---|
| Ti | −1.70 | −1.81 | +1.81 |
| Mg | −1.71 | −1.87 | +1.63 |
| Ca | −1.65 | −1.74 | +1.45 |
| Sr | −1.63 | −1.66 | +1.40 |
| Al | −1.82 | −2.00 | +2.23 |
| Ga | −1.61 | −1.79 | +1.20 |
| In | −1.58 | −1.79 | +1.20 |
| Si | −1.77 | −2.05 | +2.32 |
| Sn | −1.63 | −1.86 | +1.53 |
| Rh | −1.50 | −1.53 | +0.62 |
| Ir | −1.51 | −1.57 | +0.80 |
| Pd | −1.48 | −1.56 | +0.49 |
| Pt | −1.43 | −1.52 | +0.31 |
| La | −1.65 | −1.74 | +1.64 |
| Ce | −1.66 | −1.76 | +1.66 |

[a]All values are given in *e*.

that, in all cases, the dopant atom is partially oxidized, as expected from the rather ionic character of the TiC host.[42] Nevertheless, some differences and trends are clear. For instance, the charge on the dopant in a given group decreases along the group, being larger for lighter atoms such as Mg, Al, or Si. For these three elements, actually, we employed different pseudopotentials with extra core electrons treated as valence


https://dx.doi.org/10.1021/acs.jpcc.0c03893
J. Phys. Chem. C 2020, 124, 15969−15976

electrons to avoid possible artifacts produced by the default recommended pseudopotentials, which have only two, three, and four valence electrons for these elements, respectively. In any case, the values in Table 2 provide a qualitative guide to focus on the trends. For all other dopants, the net charge on the dopant is smaller than the charge corresponding to Ti in the host crystal, which is likely to have an effect on the interaction of the doped surface with $CO_2$.

The study of $CO_2$ adsorption on different doped TiC (001) surfaces follows the approach used in a previous work.[22] Thus, three different adsorption modes are tested and these are: TopC, TopC-A, and MMC, as indicated in Figure 1. The

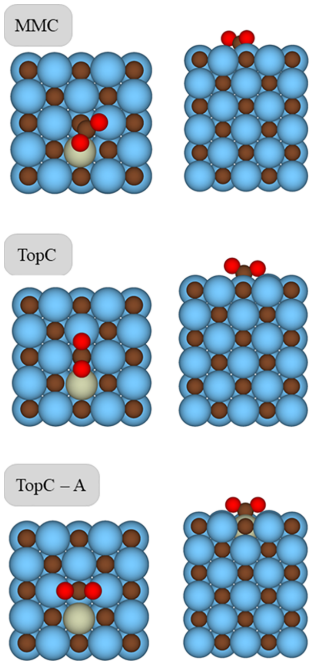


**Figure 1.** Schematic top view of the MMC, TopC, and TopC-A adsorption modes, where Ti, C, and O atoms are represented by blue, brown, and red spheres, respectively, whereas the dopant is shown in pale gray.

TopC and TopC-A modes are equivalent, except for the relative position of the dopant. In the TopC mode, one oxygen atom from $CO_2$ is directly bonded to the dopant. Note that also in the MMC mode, the $CO_2$ plane is slightly bent toward the surface. The summary of results shown in Table 3 clearly shows that, in all cases, the $CO_2$ molecular angle deviates considerably from linearity. In addition, the C−O distances in the adsorbed $CO_2$ elongate from 1.20 Å in free $CO_2$ to between 1.43 and 1.52 Å. These geometrical changes are a clear sign of charge transfer from the substrate to the adsorbed molecule; a feature that is confirmed by the calculated Bader charges. In fact, upon adsorption, the $CO_2$ becomes negatively charged, with the total net charge in the adsorbate going from −0.76 to − 1.28 *e*. Moreover, the cases where the presence of the dopant leads to a large charge transfer are also those where the adsorption energy is particularly large.

**Table 3. Preferred Adsorption Mode, Adsorption Energy, $E_{ads}$, in eV, and Structural Parameters of $CO_2$ on Different Doped TiC (001) Surfaces**[a]

| dopant | mode | $E_{ads}$ | $\alpha$(OCO) | $d$(CC) | $d$(CO) | $q_{CO_2}$ |
|---|---|---|---|---|---|---|
| Ti | TopC | −0.61 | 127.5 | 1.48 | 1.29 | −0.82 |
| Mg | TopC-A | −0.77 | 127.3 | 1.47 | 1.29 | −0.86 |
| Ca | TopC-A | −1.08 | 124.1 | 1.44 | 1.31 | −1.17 |
| Sr | TopC-A | −1.22 | 121.7 | 1.43 | 1.32 | −1.28 |
| Al | TopC-A | −0.77 | 127.7 | 1.47 | 1.29 | −0.82 |
| Ga | TopC-A | −0.72 | 128.0 | 1.48 | 1.29 | −0.83 |
| In | TopC | −0.50 | 125.4 | 1.50 | 1.29 | −0.80 |
| Si | TopC-A | −1.02 | 127.1 | 1.46 | 1.29 | −0.82 |
| Sn | TopC-A | −0.57 | 128.2 | 1.48 | 1.29 | −0.90 |
| Rh | TopC-A | −0.71 | 128.1 | 1.49 | 1.28 | −0.76 |
| Ir | TopC-A | −0.62 | 128.5 | 1.49 | 1.28 | −0.78 |
| Pd | TopC-A | −0.73 | 128.2 | 1.49 | 1.28 | −0.81 |
| Pt | TopC-A | −0.68 | 128.4 | 1.49 | 1.28 | −0.79 |
| La | TopC-A | −1.07 | 123.1 | 1.44 | 1.31 | −1.25 |
| Ce | TopC | −1.10 | 123.4 | 1.52 | 1.29, 1.30 | −0.86 |

[a] $\alpha$(OCO) stands for the bond angle of the adsorbed molecule, given in degrees, whereas $d$(CC) and $d$(CO) stand for the distances between the C atom of $CO_2$ and the closest C atom of the TiC surface, and the C−O distance in the adsorbed molecule − when the two bonds are different, two values are given − both in Å. The $q_{CO_2}$ term refers to the Bader charge of the $CO_2$ molecule, given in *e*.

Not surprisingly, the preferred adsorption mode depends on the nature of each dopant as illustrated in the Supporting Information. This can be easily explained, as the TopC-A mode will be favored when the interaction between O atoms in $CO_2$ and the surface dopant atom is stronger than that with the surface Ti atoms. Therefore, it is logical to expect some correlation between the net charge on the dopant and the adsorption energy. The plot of $E_{ads}$ versus $q^{dop}$ results in a very poor correlation (not shown). However, an improved correlation is found when plotting $E_{ads}$ versus the difference in the net charge of the C atoms in the surface plane surrounding the dopant atom, see Figure 2, and the values are listed in Table 2. This correlation is more useful since a C−C bond involving a carbon neighboring the surface dopant is

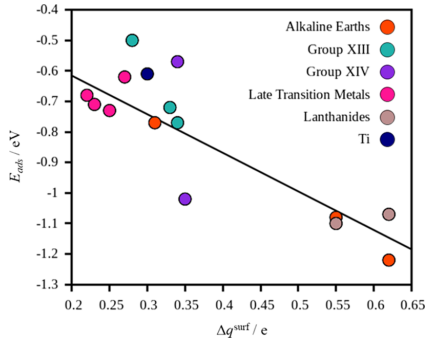


**Figure 2.** Adsorption energy, $E_{ads}$, trend versus the difference between the net charge of the surface carbon bonded to $CO_2$ and the net charge of the same carbon for the clean surface, $\Delta q^{surf}$, that is, $q^{surf}$ values given in Table 1, plus 1.70 *e* accounting for the clean surface. Each group of explored metals is differentiated by colors, as well as the Ti reference in TiC.



https://dx.doi.org/10.1021/acs.jpcc.0c03893
J. Phys. Chem. C 2020, 124, 15969−15976

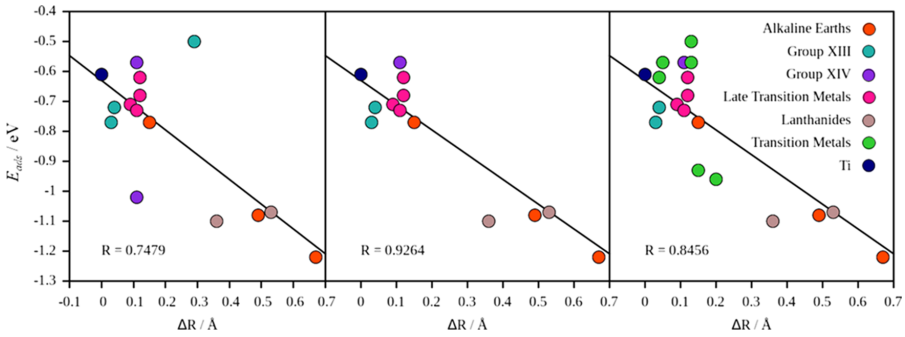


**Figure 3.** Evolution of the computed adsorption energies, $E_{ads}$, as a function of the absolute value of ΔR, as defined in eq 3. The left panel includes all studied elements, whereas the middle panel shows improved correlation when neglecting Si and In outliers. Finally, the right panel considers the elements from the middle panel plus all the early transition metals previously studied.[22] Legend is as shown in Figure 2, except for early transition metals, specified.

formed upon $CO_2$ adsorption, and the incorporation of the dopant into TiC directly affects the charges on the C atoms neighboring the metal site. In fact, the plot in Figure 2 shows that the adsorption energy is related to charge distribution. The larger the charge on the surface C atoms in the doped system relative to the same quantity for the undoped TiC (001) surface, the larger the adsorption energy. Note, however, that Figure 2 only provides a trend which shows that although the electrostatic interactions dominate the differences between the doped systems, they do not fully account for these differences. This implies that some chemical effects are also present.

To further investigate the role of dopants on modifying the adsorption features of $CO_2$ on TiC (001), we analyzed the influence of their atomic size. The rationale here is that substituting dopants on a Ti site can induce significant distortions to the surface atomic structure and the extent of the distortion largely depends on the ionic radius of the dopant. However, a simple plot of $E_{ads}$ versus dopant radius, and using the $R_{dop}$ values listed in Table 1, leads again to a very poor correlation. The correlation actually becomes much better when considering, instead, the geometrical distortions caused by the dopant, which also depend on the difference in atomic size. To this end, we define ΔR as.

$$\Delta R = |R_{dop}^{M} - R_{dop}^{Ti}|, \quad (3)$$

where $R_{dop}^{M}$ is the ionic crystal radius of the dopant, whereas $R_{dop}^{Ti}$ is that corresponding for Ti, both taken from Table 1. Doping involves distortions in the surface plane of TiC, both of the convex or concave type. Therefore, it is advisable to consider the effect of distortions in absolute value when analyzing its effect on the adsorption energy. The plot of $E_{ads}$ versus ΔR is shown in Figure 3. The left panel of Figure 3 shows a clear trend, yet not really quantitative, as, interestingly, Si and In appear as clear outliers.

To try to understand the origin of this discrepancy, we inspected the structure of both doped surfaces. In the case of Si, it appears that the angle between the surface C and Si atoms, and the C from $CO_2$ is ca. 114°, while in the other cases, as well as in the undoped TiC (001) surface, it is significantly smaller, 90° or less. This is understandable from the well-known trend of Si to prefer tetrahedral coordination and represents a clear chemical difference with respect to the rest of the considered dopants. The case of In can also be understood as the net charge in In for the doped carbide is significantly smaller than its formal oxidation number and, hence, the ionic radius does not represent the real size of this element in the doped TiC surface.

Removing the data for Si and In leads to a largely improved correlation as shown in Figure 3. This result is important because it allows one to make a reasonable estimation of the effect of a given dopant based on intrinsic properties of that dopant without the need to perform any DFT calculations and thus can be used for a systematic screening of the effect of possible dopants toward $CO_2$ adsorption.

To further validate the use of ΔR as a descriptor of $CO_2$ adsorption and activation, the results from the early transition metals studied in a previous work using an identical computational setup were added as shown in Figure 3.[22] Taking into account the empirical character of the ionic crystal radii used, cf. Table 1, the existence of the correlation between $E_{ads}$ and ΔR is remarkable, providing a useful descriptor for the fast exploration of the effect of a possible dopant. The correlation has been deduced for TiC (001), yet it is likely that a similar relationship exists for other transition metal carbides.

To further assess the effect of the dopant on the potential for CCS, we used transition state theory (TST) to derive the $CO_2$ desorption rates for each one of the doped TiC surfaces and the Hertz−Knudsen equation to estimate the corresponding adsorption rate; further details can be found in ref 18. Both adsorption and desorption rates depend on the working temperature, and the temperature at which both processes become equal, $T_{eq}$, defines the frontier between the two regimes. The variation of both rates with temperature is reported in Figure 4 for each of the explored materials using a typical partial pressure of atmospheric $CO_2$ of 40 Pa.[43] For a given surface, $T < T_{eq}$ corresponds to the regime where adsorption is faster than desorption, thus fostering $CO_2$ capture, whereas for $T > T_{eq}$, the $CO_2$ desorption would dominate.

Before exploring the $T$-dependent rates as a plot shown in Figure 4, it is worth pointing out that the desorption rates depend on $E_{ads}$, and this, in turn, is also dependent on the particular DFT method used. In particular, we already discussed that including dispersion terms, not accounted for in the present work, would lead to stronger $E_{ads}$ values and


https://dx.doi.org/10.1021/acs.jpcc.0c03893
J. Phys. Chem. C 2020, 124, 15969−15976

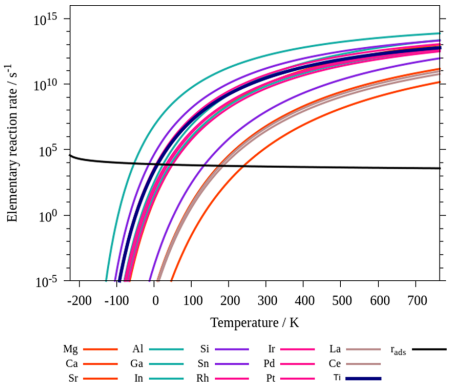


**Figure 4.** Calculated $CO_2$ desorption rates, $r_{des}$, on doped TiC (001) at the current partial pressure of atmospheric $CO_2$ of 40 Pa. Note that the adsorption rate does not depend on the adsorption energy and, hence, is the same for all cases. The desorption rates of the undoped and doped surfaces are shown color-coded.

could therefore result in a shift to larger $T_{eq}$ values. However, the effect of the DFT method, including the effect of dispersion, will equally affect all the studied systems, and since the relevant comparison is $T_{eq}$ for a given material relative to $T_{eq}$ for stoichiometric TiC (001), which we will denote as $T_{eq}^{TiC}$, these relative values of $T_{eq}$ are therefore robust to the neglect of dispersion corrections. From Figure 4, one can see that, for example, for the Sr-doped TiC (001) surface, $T_{eq}$ is 230 K higher than $T_{eq}^{TiC}$, whereas for In-doped TiC (001), the temperature would be ∼80 K lower. In a nutshell, this indicates that doping of metal carbides may broaden the tuning range of $CO_2$ capture and thus can provide a route to further improve their CCS capability.

## 4. CONCLUSIONS

A systematic study of the effect of doping on the TiC (001) surface by different representative elements across the periodic table (Mg, Ca, Sr., Al, Ga, In, Si, Sn, Pd, Pt, Rh, Ir, La, and Ce) on $CO_2$ adsorption has been carried in the framework of DFT. The results show that the introduction of dopants replacing one Ti surface atom has significant effects on the $CO_2$ adsorption properties. In particular, dopants may significantly modify the adsorption energy and, hence, the desorption rate at a given temperature, which will have an impact on the CCS capability of these materials. Most often, the adsorption energy increases, although it is found to decrease when doping with some *p* block elements such as In and Sn.

The analysis of the results provided some trends that can be used for further screening. Thus, the adsorption energy is reasonably correlated with the difference in the net charge of the surface carbon atoms comparing the doped and undoped systems. The surface distortions introduced by the dopant also play a major role. In this sense, it has been found that the adsorption energy correlates rather well with the difference in the (empirical) atomic radii between the dopant and Ti, ΔR. This finding provides a useful descriptor that allows one to predict the effect on the adsorption energy of other dopants without the need to carry out any DFT calculation. The validity of this descriptor has been confirmed by including the cases of early transition metal atoms studied in a previous work. Finally, note that although the ΔR descriptor has been deduced for TiC (001), it is likely to hold for other transition metal carbides. The final rule of thumb is that the larger the ionic crystal size of the dopant, the larger the $CO_2$ adsorption energy.

## ■ ASSOCIATED CONTENT

### Supporting Information

The Supporting Information is available free of charge at https://pubs.acs.org/doi/10.1021/acs.jpcc.0c03893.

Views of the atomic structure of the most favorable adsorption modes of $CO_2$ on doped TiC (001) and valence electron configurations for the dopants studied in this work (PDF)

## ■ AUTHOR INFORMATION


### Corresponding Authors

**Francesc Viñes** − *Departament de Ciència de Materials i Química Física & Institut de Química Teòrica i Computacional (IQTCUB), Universitat de Barcelona, Barcelona 08028, Spain*; orcid.org/0000-0001-9987-8654; Email: francesc.vines@ub.edu

**Michael Nolan** − *Tyndall National Institute, Lee Maltings, University College Cork, Cork T12R5CP, Ireland; Nanotechnology and Integrated Bioengineering Centre, Ulster University, Co Antrim BT37 OQB, Northern Ireland;* orcid.org/0000-0002-5224-8580; Email: michael.nolan@tyndall.ie

### Authors

**Martí López** − *Departament de Ciència de Materials i Química Física & Institut de Química Teòrica i Computacional (IQTCUB), Universitat de Barcelona, Barcelona 08028, Spain*

**Francesc Illas** − *Departament de Ciència de Materials i Química Física & Institut de Química Teòrica i Computacional (IQTCUB), Universitat de Barcelona, Barcelona 08028, Spain*; orcid.org/0000-0003-2104-6123

Complete contact information is available at: https://pubs.acs.org/10.1021/acs.jpcc.0c03893


### Notes

The authors declare no competing financial interest.

The relevant input and output files corresponding to the optimized geometry of a clean doped surface and for $CO_2$ chemisorption thereon have been uploaded to the NOMAD repository and can be found at https://dx.doi.org/10.17172/NOMAD/2020.03.27-1

## ■ ACKNOWLEDGMENTS

The research carried out at the Universitat de Barcelona has been supported by the Spanish MICIUN/FEDER RTI2018-095460-B-I00 and María de Maeztu MDM-2017-0767 grants and, in part, by Generalitat de Catalunya 2017SGR13 grant and by the COST Action 18234, supported by the COST (European Cooperation in Science and Technology). M.N. acknowledges support from the Science Foundation Ireland and the Horizon 2020 M-ERA.net 2 cofund program, through grant agreements No 685451 and 16/M-ERA/3418. M.L acknowledges the HPC-EUROPA3 (INFRAIA-2016-1-730897) project supported by the EC Research Innovation Action under the H2020 Programme, the Tyndall National Institute and the Irish Centre for High-End Computing

(ICHEC) for supporting his stay in Cork. F.V. thanks the Spanish MINECO for postdoctoral contracts under the Ramón y Cajal Program (RYC-2012-10129) and F.I. acknowledges additional support from the 2015 ICREA Academia Award for Excellence in University Research.

## REFERENCES

(1) Doney, S. C.; Fabry, V. J.; Feely, R. A.; Kleypas, J. A. Ocean Acidification: The Other $CO_2$ Problem. *Annu. Rev. Mar. Sci.* **2009**, *1*, 169−192.
(2) Leuliette, E. W.; Willis, J. K. Balancing the Sea Level Budget. *Oceanography* **2011**, *24*, 122−129.
(3) Cox, P. M.; Betts, R. A.; Jones, C. D.; Spall, S. A.; Totterdell, I. J. Acceleration of Global Warming due to Carbon-Cycle Feedbacks in a Coupled Climate Model. *Nature* **2000**, *408*, 184−187.
(4) Atabani, A. E.; Silitonga, A. S.; Badruddin, I. A.; Mahlia, T. M. I.; Masjuki, H. H.; Mekhilef, S. A. Comprehensive Review on Biodiesel as an Alternative Energy Source and its Characteristics. *Renew. Sustain. Energy Rev.* **2012**, *16*, 2070−2093.
(5) Panwar, N. L.; Kaushik, S. C.; Kothari, S. Role of Renewable Energy Sources in Environmental Protection: A Review. *Renew. Sustain. Energy Rev.* **2011**, *15*, 1513−1524.
(6) Balat, M. Potential Alternatives to Edible Oils for Biodiesel Production − A Review of Current Work. *Energy Convers. Manage.* **2011**, *52*, 1479−1492.
(7) Espinal, L.; Poster, D. L.; Wong-Ng, W.; Allen, A. J.; Green, M. L. Measurement, Standards, and Data Needs for $CO_2$ Capture Materials: A Critical Review. *Environ. Sci. Technol.* **2013**, *47*, 11960−11975.
(8) D'Alessandro, D. M.; Smit, B.; Long, J. R. Carbon Dioxide Capture: Prospects for New Materials. *Angew. Chem., Int. Ed.* **2010**, *49*, 6058−6082.
(9) Bui, M.; Adjiman, C. S.; Bardow, A.; Anthony, E. J.; Boston, A.; Brown, S.; Fennell, P. S.; Fuss, S.; Galindo, A.; Hackett, L. A.; et al. Carbon Capture and Storage (CCS): the Way Forward. *Energy Environ. Sci.* **2018**, *11*, 1062−1176.
(10) Markewitz, P.; Kuckshinrichs, W.; Leinter, W.; Linssen, J.; Zapp, P.; Bongartz, R.; Schreiber, A.; Müller, T. E. Worldwide Innovations in the Development of Carbon Capture Technologies and the Utilization of $CO_2$. *Energy Environ. Sci.* **2012**, *5*, 7281−7305.
(11) Hessami, M.-A.; Stewart, C. A Study of Methods of Carbon Dioxide Capture and Sequestration - the Sustainability of a Photosynthetic Bioreactor Approach. *Energy Convers. Manage.* **2005**, *46*, 403−420.
(12) Cheng-Hsiu, Y.; Chihi-Hung, H.; Chung-Sung, T. A Review of $CO_2$ Capture by Absorption and Adsorption. *Aerosol Air Qual. Res.* **2016**, *12*, 745−769.
(13) Fernández-García, M.; Anderson, J. A. Supported Metals in Catalysis, *Catalytic Sciences Series*, Vol. *5*, 2003, Imperial College Press, London.
(14) Rodriguez, J. A.; Evans, J.; Feria, L.; Vidal, A. B.; Liu, P.; Nakamura, K.; Illas, F. $CO_2$ Hydrogenation on Au/TiC, Cu/TiC, and Ni/TiC Catalysts: Production of CO, Methanol, and Methane. *J. Catal* **2013**, *307*, 162−169.
(15) Vidal, A. B.; Feria, L.; Evans, J.; Takahashi, Y.; Liu, P.; Nakamura, K.; Illas, F.; Rodriguez, J. A. $CO_2$ Activation and Methanol Synthesis on Novel Au/TiC and Cu/TiC Catalysts. *J. Phys. Chem. Lett.* **2012**, *3*, 2275−2280.
(16) Posada-Pérez, S.; Viñes, F.; Ramirez, P. J.; Vidal, A. B.; Rodriguez, J. A.; Illas, F. The Bending Machine: $CO_2$ Activation and Hydrogenation on $\delta$-MoC(001) and $\beta$-$Mo_2C$(001) Surfaces. *Phys. Chem. Chem. Phys.* **2014**, *16*, 14912−14921.
(17) Liu, X.; Kunkel, C.; de la Homs, P. R.; Homs, N.; Viñes, F.; Illas, F. Effective and Highly Selective CO Generation from $CO_2$ Using a Polycrystalline $\alpha$-$Mo_2C$ Catalyst. *ACS Catal* **2017**, *7*, 4323−4335.
(18) Kunkel, C.; Viñes, F.; Illas, F. Transition Metal Carbides as Novel Materials for $CO_2$ Capture, Storage, and Activation. *Energy Environ. Sci.* **2016**, *9*, 141−144.
(19) Porosoff, M. D.; Kattel, S.; Li, W.; Liu, P.; Chen, J. G. Identifying Trends and Descriptors for Selective $CO_2$ Conversion to CO over Transition Metal Carbides. *Chem. Commun.* **2015**, *51*, 6988−6991.
(20) Porosoff, M. D.; Yang, X.; Boscoboinik, J. A.; Chen, J. G. Molybdenum Carbide as Alternative Catalysts to Precious Metals for Highly Selective Reduction of $CO_2$ to CO. *Angew. Chem., Int. Ed.* **2014**, *53*, 6705−6709.
(21) Schweitzer, N. M.; Schaidle, J. A.; Ezekoye, O. K.; Pan, X.; Linic, S.; Thompson, L. T. High Activity Carbide Supported Catalysts for Water Gas Shift. *J. Am. Chem. Soc.* **2011**, *133*, 2378−2381.
(22) López, M.; Broderick, L.; Carey, J. J.; Viñes, F.; Nolan, M.; Illas, F. Tuning Transition Metal Carbide Activity by Surface Metal Alloying: a Case Study on $CO_2$ Capture and Activation. *Phys. Chem. Chem. Phys.* **2018**, *20*, 22179−22186.
(23) Yerskin, I.; Nolan, M. Doping of Ceria Surfaces with Lantanium: a DFT+U Study. *J. Phys. Condens. Matter.* **2010**, *22*, 135004.
(24) Nolan, M. Enhanced Oxygen Vacancy Formation in Ceria (111) and (100) Surfaces Doped with Divalent Cations. *J. Mater. Chem.* **2011**, *21*, 9160−9168.
(25) Perdew, J. P.; Burke, K.; Ernzerhof, M. Generalized Gradient Approximation Made Simple. *Phys. Rev. Lett.* **1996**, *77*, 3865−3868.
(26) Quesne, M. G.; Roldán, A.; Leeuw, N. H.; Catlow, C. R. A. Bulk and Surface Properties of Metal Carbides: Implications for Catalysis. *Phys. Chem. Chem. Phys.* **2018**, *20*, 6905−6916.
(27) dos Santos Politi, J. R.; Viñes, F.; Rodriguez, J. A.; Illas, F. Atomic and Electronic Structure of Molybdenum Carbide Phases: Bulk and Low Miller-Index Surfaces. *Phys. Chem. Chem. Phys* **2013**, *15*, 12617−12625.
(28) Ahuja, R.; Eriksson, O.; Wills, J. M.; Johansson, B. Structural, Elastic, and High-Pressure Properties of Cubic TiC, TiN, and TiO. *Phys. Rev. B* **1996**, *53*, 3072−3079.
(29) Viñes, F.; Sousa, C.; Liu, P.; Rodriguez, J. A.; Illas, F. A Systematic Density Functional Theory Study of the Electronic Structure of Bulk and (001) Surface of Transition-Metals Carbides. *J. Chem. Phys.* **2005**, *122*, 174709.
(30) Perdew, J.; Chevary, J. A.; Vosko, S. H.; Jackson, K. A.; Pederson, M. R.; Singh, D. J.; Fiolhais, C. Atoms, Molecules, Solids, and Surfaces: Applications of the Generalized Gradient Approximation for Exchange and Correlation. *Phys. Rev. B* **1992**, *46*, 6671−6687.
(31) Hammer, B.; Hansen, L. B.; Nørskov, J. K. Improved Adsorption Energetics within Density-Functional Theory Using Revised Perdew-Burke-Ernzerhof Functionals. *Phys. Rev. B* **1999**, *59*, 7413−7421.
(32) Kunkel, C.; Viñes, F.; Ramírez, P. J.; Rodriguez, J. A.; Illas, F. Combining Theory and Experiment for Multitechnique Characterization of Activated $CO_2$ on Transition Metal Carbide (001) Surfaces. *J. Phys. Chem. C* **2019**, *123*, 7567−7576.
(33) Vogiatzis, D. K.; Mavrandonakis, A.; Klopper, W.; Froudakis, G. E. Ab initio Study of the Interactions between $CO_2$ and N-Containing Organic Heterocycles. *ChemPhysChem* **2009**, *10*, 374−383.
(34) Bader, R. F. W. *Atoms in Molecules: A Quantum Theory, International Series of Monographs on Chemistry*, ISBN-10: 0198558651, Oxford Clarendon Press, United Kingdom, New Ed. 1994.
(35) Kresse, G.; Furthmüller, J. Efficiency of *Ab-initio* Total Energy Calculations for Metals and Semiconductors Using a Plane-Wave Basis Set. *Comput. Mat. Sci.* **1996**, *6*, 15−50.
(36) Kresse, G.; Furthmüller, J. Efficient Iterative Schemes for Ab Initio Total-Energy Calculations Using a Plane-Wave Basis Set. *Phys. Rev. B* **1996**, *54*, 11169−11186.
(37) Kresse, G.; Joubert, D. From Ultrasoft Pseudopotentials to the Projector Augmented-Wave Method. *Phys. Rev. B* **1999**, *59*, 1758−1775.


https://dx.doi.org/10.1021/acs.jpcc.0c03893
J. Phys. Chem. C 2020, 124, 15969−15976

(38) Blöchl, P. E. Projector Augmented-Wave Method. *Phys. Rev. B* **1994**, *50*, 17953−17979.
(39) Monkhorst, H. J.; Pack, J. D. Special Points for Brillouin-Zone Integrations. *Phys. Rev. B* **1976**, *13*, 5188−5192.
(40) Ham, D. J.; Lee, J. S. Transition Metal Carbides and Nitrides as Electrode Materials for Low Temperature Fuel Cells. *Energies* **2009**, *2*, 873−899.
(41) Cordero, B.; Gómez, V.; Platero-Prats, A. E.; Revés, M.; Echevarría, J.; Cremades, E.; Álvarez, S. Covalent Radii Revisited. *Dalton Trans.* **2008**, *21*, 2832−2838.
(42) Chen, K. Y.; Kamran, S. Bonding Characteristics of TiC and TiN. *Model. Simul. Mater. Sci.* **2013**, *03*, 7−11.
(43) Takahashi, T.; Sutherland, S.; Kozyr, A. *Global Ocean Surface Water Partial Pressure of $CO_2$ Database: Measurements Performed During 1957−2014* (Version 2014). 2015, Environmental Sciences Division,Oak Ridge National Laboratory.



https://dx.doi.org/10.1021/acs.jpcc.0c03893
*J. Phys. Chem. C* 2020, 124, 15969−15976

Chapter 5:

# Hydrogen Related Reactions on MXenes

## 5.1 Introduction

Since the beginning of the industrial revolution in the $18^{th}$ century, fossil fuels such as coal, oil, and natural gas have fuelled the technology and transportation networks that power society. However, continuing to run the globe on fossil fuels endangers our energy supply and places immense burden on the ecosystem. The fossil fuel reserves are predicted to not be enough for maintaining the actual consume in our life-times. [1] Moreover, global oil and gas reserves are concentrated in a few regions of the world, while demand is growing everywhere. As a result, a secure supply is increasingly difficult to assure. Furthermore, the massive usage of fossil fuels produced a concomitant massive release of greenhouse gasses as $CO_2$ having a great negative impact to our environment, as already mentioned at Section 4.

Replacing the source of the primarily energy power will impact our society at transversal levels. Such path requires a massive investment exploring alternative energy sources but ultimately the construction of a complete alternative infrastructure to sustain this necessary change. In the recent years, hydrogen

has been advocated as a substitute to carbon-based fossil fuels, frequently with the goal of moving civilization toward a more ecologically friendly society.[2] It is thought that a system based on hydrogen and electricity can replace the actual model, solving the environmental crisis and offering an alternative able to be produced unlimited an without geographical restrictions. Such energy system is known as hydrogen economy.[3] Briefly explained the hydrogen economy pretend to produce, store and use $H_2$ as a primary energy source. Interestingly the $H_2$ interconnects naturally with fossil fuels, nuclear or electrical energy, among other, adding a flexibility to the hydrogen production, storage or usage and offering robustness to the global energy supply.

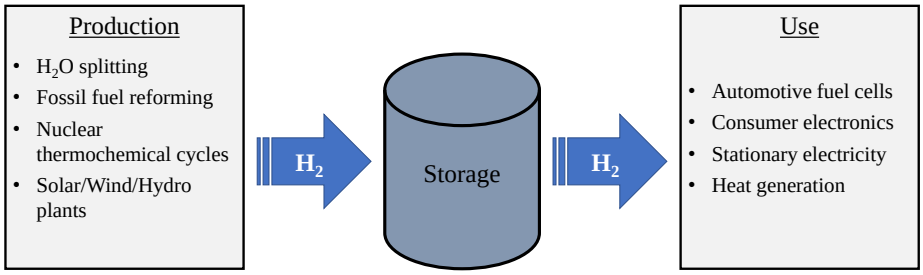


**Figure 5.1: The hydrogen economy** is defined as a network of primary energy sources connected to a variety of end uses using hydrogen as an energy carrier. Hydrogen gives versatility to energy production and usage by naturally connecting with fossil, nuclear, renewable, and electrical energy forms: Any of these energy sources may be used to produce hydrogen.

The development of hydrogen generation technologies that can compete in price with the usage of hydrocarbons is difficult due to the thermodynamics of these processes. For example, electrolysis of $H_2O$ requires around four times more energy per mol of $H_2$ generated than the steam reforming of methane. Another current limitation is the actual price of Hydrogen production. Even though hydrogen can be converted to electricity in fuel cells, the production cost of prototype fuel cells skyrockets: $3000 per kilowatt of power generated

compared to $30 per kilowatt of power produced for gasoline engines.

As a result, new catalysts for reactions that involve hydrogen production, storage, or consumption into valuable commodities are of great importance. Table 5.1 shows some reactions of current interest:

| Reaction | Equation |
|---|---|
| $N_2$ reduction | $N_2 + 3H_2 \rightarrow 2NH_3$ |
| Reverse water-gas shift | $CO_2 + H_2 \rightarrow H_2O + CO$ |
| Water electrolysis | $H_2O \rightarrow H_2 + \frac{1}{2}O_2$ |
| Hydrogen fuel | $H_2 + \frac{1}{2}O_2 \rightarrow H_2O$ |

**Table 5.1: Hydrogen related important reactions**

The new family of two-dimensional (2D) transition metal carbides and nitrides, termed MXenes, is attracting an increasing interest in materials science because of their new, tunable, and unexpected properties.[4–7] These new materials exhibit an outstanding performance in several applications involving batteries,[8,9] supercapacitors,[10] the electrochemical hydrogen evolution,[11,12] $CO_2$ abatement technologies,[13–15] heterogeneous catalysis,[16–20] and antibacterial activity,[21] just to name a few, that include some of the reactions mentioned at Table 5.1.

In this chapter we will discuss the potential of MXenes as catalysts for hydrogenation reactions such the RWGS or the $N_2$ reduction, Section 5.3, we will determine the MXenes surface terminations under suitable electrochemical conditions, Section 5.4, as well as their capabilities as HER catalysts, Section 5.5, a semireaction involved in the water electrolysis but before we will present the MXenes structural and electronic properties to provide some chemical insights regarding their promising performance.

## 5.2 MXenes Structure

The 2D transition-metal carbides, nitrides, and carbonitrides, collectively known as MXenes, are some of the newest members of two-dimension materials family.[4] Since the discovery of $Ti_3C_2T_x$ in 2011,[22] where $T_x$ stands for some of the typical terminations, primarily O, OH, or F, that these materials display when they are first synthesized, this innovative low-dimensional family has swiftly grown.[23] Note that nonstoichiometric terminations are indicated by the subscript x. About 46 distinct MXene materials, without including the surface terminations (only M, X, and n variations), have been reported since the first MXene was created,[24] and more than 150 have been predicted using computational techniques.[4,25] The MXenes are formed from precursors called MAX phases. Such MAX phases are layered 3D bulks, with a general formula $M_{n+1}AX_n$, (n = 1, 2, or 3) where M stand for a transition metal, A is a A-group (or XIII-group) element, and X is C and/or N.[26]

MAX phases have their beginnings in the 1960s, when the Hans-Nowotny group synthesized over 100 novel carbides and nitrides.[27] However, MAX phases received little attention until the 1990s, when Barsoum and El-Rahgy demonstrated an exceptional mix of metallic and ceramic characteristics in $Ti_3SiC_2$.[28] From there on the family was rapidly growing. The MAX phases have unusual chemical, physical, electrical, and mechanical capabilities due to their layered structure and the mixed metallic-ionic-covalent nature of the strong M-X bonds and the comparatively weak M-A bonds. Because of this uncommon property combination, the MAX phases show promise for a variety of applications including high temperature structural applications, protective coatings,[29] sensors,[30] electrical connections[31], and many more.[32]

From them, MXenes may be generated rather readily by selectively chemically exfoliating (or chemically etching) the A in the MAX phase to induce the selective separation of MXene slabs, see Figure 5.2. Because the M-A and M-X bonds are different in nature, they react differently to etchants, destroying the

weak M-A bonds but not the M-X bonds. A high concentration of fluorine (F) is used in the majority of the known synthetic methods since they call for the employment of HF, LiF/HCl, or $NH_4HF_2$ as etchants, and take advantage of their great affinity for the MAX phase A elements, such as Al and Si.[33] The influence of their synthesis on their surface terminations will be examined recently in Section 5.4 This new Family of 2D materials has over passed the already promising MAX capabilities and thus it has attract a wider attention.

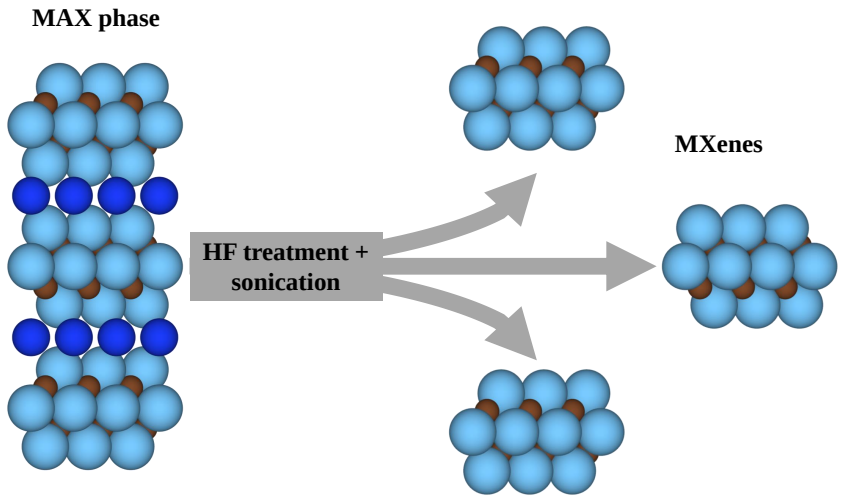


**Figure 5.2: Schematic representation of a MAX phase** of general form $M_3AX_2$. M, A, and X elements are represented by light blue, dark blue, and brown spheres, respectively. The MAX phase (left) after an appropriate treatment is separated removing the A layers and obtaining the respective MXenes sheets (right). From a $M_3AX_2$ MAX phase, $M_3X_2$ MXenes are formed.

### 5.2.1 Geometric Structure

MXenes are 2D transition metal carbides and nitrides with a general formula $M_{n+1}X_nT_x$, (n = 1, 2, or 3) where M stand for a transition metal, primarily M = Sc, Ti, V, Cr, Mn, Zr, Nb, Mo, Hf, Ta, and W, while X stands for C and/or N, and T stands for the surface termination. Similarly to the precursors

MAX phases, MXenes present a vast variety of possible conformations based on the synthesis technique and the MAX precursor used. They can be tailored by changing the number or stacking of layers and the composition of the M and X, including mixtures or defects on their metallic structure. Moreover their surface can be also predetermined by the usage of different etching strategies.

As a result (and avoiding MXenes surface tailoring) the MXene family can be divided into single transition metal MXenes, and double transition metal MXenes. Based on the metal ordering the double transition metals MXenes can be divided into in-plane MXenes, *i*-MXenes and out-of-plane Mxenes, *o*-MXenes, as depicted in Figure 5.3. Moreover all the presented MXenes can be duplicated by changing the conventional ABC (*hpc*) stacking for the ABA (*fcc*).

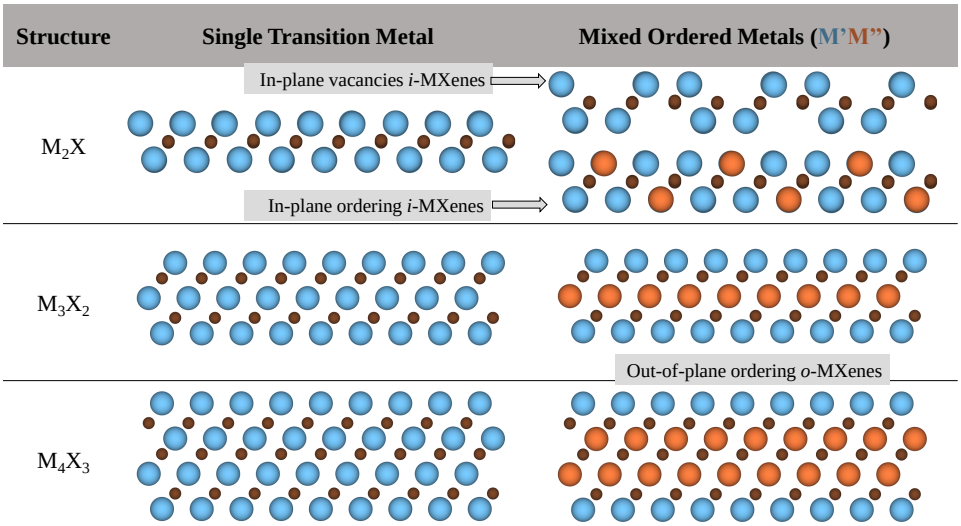


**Figure 5.3: Schematic illustration of MXenes structures**. The bare MXenes have a general formula of $M_{n+1}X_n$ with n = 1, 2, and, 3 resulting in the $M_2X$, $M_3X_2$, and $M_4X_3$. The M can be a single transition metal, as depicted at the second column of the present Table or a double transition metal MXenes. Based on the ordering of the transition metal mixes they can be classified by in-plane ordering, *i*-MXnes, or out-of-plane ordering, *o*-Mxenes. For $M_2X$ are depicted the two *i*-MXenes, including the double transition metal MXenes and the in-plane vacancy MXenes. For $M_3X_2$ and $M_4X_3$ are depicted the most common double transition metals *o*-MXenes. The M are represented by blue and orange spheres while X atoms are represented by brown spheres.

The single transition metal MXenes keep the general formula already presented, $M_{n+1}X_n$. MXenes have a hexagonal close-packed (*hcp*) crystal structure with a $P6_{3/mmc}$ space group symmetry, with the transition metals in the M sites close-packed and the X atoms occupying the octahedral sites between the M atomic planes.[23] For the doble transition metals MXenes we use the general formula $M'_nM''_mX_{n+m-1}$. The overall formula is the same, but the doubling the number of metal atoms involved, adds a level of complication to its expression. For the *i*-MXenes, the two metals are alternatively placed in each layer. All the MXenes reported up to date have the same stoichiometric formula $(M'_{2/3}M''_{1/2})_2X$. Moreover, most *i*-MXenes have M'' atoms that may be selectively etched, resulting in ordered vacancies and an *i*-MXene with the formula $M'_{4/3}X$, previously known as $M'_{1.33}X$. For instance, Tao *et al.*[34] from the *i*-MAX phase $(Mo_{2/3}Sc_{1/2})_2AlC$, with the Mo and Sc atoms exhibiting in-plane chemical ordering, synthesised $Mo_{4/3}C$ MXene by selective etching in 2017.

For the *o*-MXenes, M' and M'' are located in separated layers. The two different composition ratio *o*-MXenes already synthesised (2:1, and 2:2) have this formulas, $M'_2M''_1X_2$ and $M'_2M''_2X_3$. $Cr_2TiC_2$ was the first MXene of the family to be synthesized, as its matching $Cr_2TiAlC_2$ ordered MAX phase structure was the first to be synthesized.[35] Because of the vast number of potential combinations, a broad family of *o*-Mxenes has been predicted.[36] Note that the synthesis of nitride MXenes is still challenging and the research on them has been mainly limted to $Ti_2NT_xx$ and $Ti_4N_3T_xx$.[37,38] Clearly, the precursor MAX phase is critical in generating a particular MXene.

Part of its promising catalytic activity is related with their atomic structure of the exposed (0001) surface. Interestingly, the MXene surface is equivalent to the nonstable but higly active (111) surface of TMCs.[39] For instance, the $CO_2$ total adsorption energy over the stable TiC(001) surface is $-0.61$ eV,[40] as already explored at Chapter 4. However, the adsorption energy of the TiC(111) surface is $-3.47$ eV,[41] which is near to the $-3.69$ eV of the $Ti_2C$ MXene,[15] which is five to six times stronger than the TiC(001).

### 5.2.2 Electronic Structure

The content and structure of MXenes, as well as surface and interlayer chemistry, govern their physical and (electro)chemical properties. The electron transport properties of most MXenes are analogous to metals, with resistivity decreasing linearly with temperature.[42,43] Changing the transition metal type and M site structure in MXenes, on the other hand, can result in a negative temperature dependency of resistivity and, as a result, MXenes with semiconductor-like properties.[44,45] Tuning the M site of *o*-MXenes by changing the outer-layer transition metals is predicted to produce MXenes with attractive magnetic properties, notably antiferromagnetic ones.[46] Mn nitrides and *o*-MXenes with Mn in the intermediate layer are predicted to be ferromagnetic.[46] All bare MXenes are expected to be metallic conductors with transition metal free electron carriers.[43,47] Surface terminations, on the other hand, may change the density of states (DOS) and alter the Fermi level, making them electrically adjustable.[48] The physical properties and chemical stability of MXenes are affected by stoichiometry, surface chemistry, and point defects, mostly vacancies in the M and C sublattices inherited from the precursor or created by etching.[49]

## 5.3 Gas-Phase Surface Hydrogenation

**Introduction**. The interaction of molecular hydrogen with a series of 28 2D carbides and nitrides, known as MXenes, has been studied by means of periodic density functional calculations. This section shows that trends in atomic and molecular adsorption energies can be rationalized in terms of the electrostatic potential above the surface site and the Bader charge on the surface metal atoms. For all systems, molecular hydrogen is found to dissociate with almost negligible barriers, meaning that at low temperature the MXene surface will be passivated by adsorbed atomic hydrogen. The conditions at which the MXene surface is partly covered and, hence, able to participate in hydrogenation reactions are investigated by means of *ab initio* thermodynamics and phase diagrams derived

from microkinetic simulations. The first provide the equilibrium conditions for a given H coverage on the MXene of interest, whereas the second provides the conditions at which a given configuration is reachable at the working conditions. For fast enough processes, both approaches necessarily lead to the same result, but this may differ when high energy barriers are involved, as it the case here for the H adatoms recombination step. With this suite, we show that $Fe_2C$, $W_2N$, and $Mo_2C$ are promising hydrogenation catalysts. This work serves as a first step toward the rational design and implementation of MXene-based hydrogenation catalysts.

**Results**. The first step is to sample all adsorption sites for H and $H_2$ over a $p(3\times3)$ $M_2C(0001)$ surface supercell, see Figure 5.4. For all the tested MXenes Hollow M, site C in Figure 5.4, was the preferred adsorption site for the atomic hydrogen, see table S3 from Appendix C. The only exception was $La_2C$ where H was adsorb stronger at Hollow X, site D in Figure 5.4. Regarding the molecular $H_2$ the preferred adsorption site over all MXenes was Top, site E in Figure 5.4. However, several MXenes shown an spontaneous $H_2$ dissociation upon relaxation, see Table S4 from Appendix C. Such fact is later confirmed by the computed energy barriers for hydrogen dissociation.

The molecular hydrogen tends to easily split into H* + H*. Only $Zr_2C$ and $Hf_2C$ feature energy barriers above 0.10 eV, and for the rest of MXenes, $H_2$ dissociation can be safely considered barrierless, see Table S6 from Appendix C. Thus, we preliminary conclude that MXenes readily dissociate hydrogen and the process does not strongly depend on the M or X components of the MXenes. A consequence of this reactivity is that the MXene surface will be easily covered by hydrogen and, hence, passivated, as the resulting system has no free active sites for other molecules that, eventually, could be hydrogenated. Therefore, determining the conditions at which the MXene surface is eventually partially covered becomes a real need for further applications in catalysis. This involves two well differentiated situations, namely, the conditions at which a thermodynamic equilibrium exists with the MXene surface partially covered and the conditions

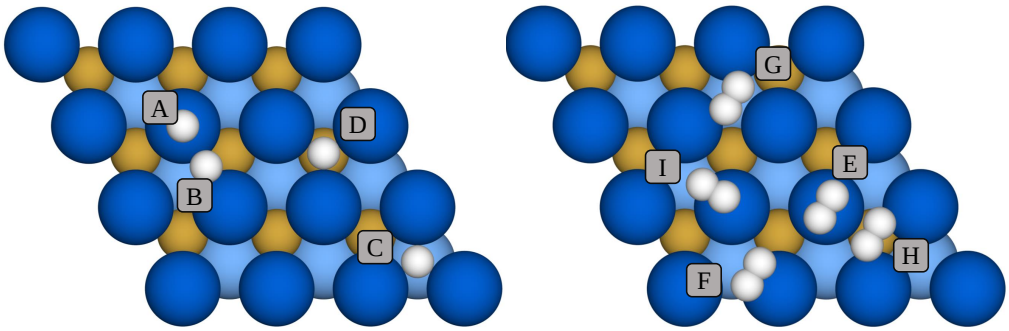


**Figure 5.4: Top views of the main high-symmetry adsorption surface sites for atomic and molecular hydrogen over a $M_2X$ (0001) surface $p$(3×3) supercell**. Metal atoms at the top and bottom layers are represented by bright and light blue spheres, respectively, while C/N atoms are represented by light brown spheres, and H atoms are shown in white. The main high-symmetry adsorption surface sites for H atoms and perpendicular $H_2$ adsorption (left image) are top (A), bridge (B), hollow M (C), and hollow X (D), having either one M or X atom below, respectively. For $H_2$ adsorbed parallel to the $M_2X$(0001) surface (right image), the sampled sites are top (E), XM bridge (F), hollow M (G), hollow X (H), and MM bridge (I)

where such a situation is kinetically reachable during a reasonable contact time in between $H_2$ and the MXene catalyst. Obviously, this also involves determining which of the explored MXenes would exhibit the desired features

To rationalize the trends in $\Delta E_{ads}$ and gain insight into their chemistry, many possible descriptors were analyzed. Among all these, MXene electrostatic potential above the surface adsorption site, $V$, and the surface metal charge, $q$, shown a soft correlation. The electrostatic potential was analyzed by Vaspview software[50] and the surface metal charge were computed following a Bader *Atoms-in-Molecules* analysis of the electron density.[51]

Despite neither one of the descriptors purposed show a correlation good enough, they still provide meaningful information to explain the differences in $\Delta E_{ads}$ of H* and $H_2$*. As shown in Figure 5.5, large negative $V$ values indicate sites with more favorable H adsorption and likely stronger Pauli repulsion for

molecular $H_2$* species.[52] The same view is obtained from the MXene surface metal Bader charge, $q$, thus providing another useful descriptor as shown on related transition metal carbide surfaces.[40,53] This descriptor shows that the more oxidized the metal, the stronger $\Delta E_{ads}$ of H, while negative $q$ would favor $H_2$ physisorption because of the enhancement of dispersion interactions. The charge on the metal sites where H* and $H_2$* present comparable binding strengths, and, hence, can be optimal for hydrogenation purposes, is around 0.7−0.8 $e$, corresponding to Cr, Mo, W, Mn, and Fe, see Table S9 from Appendix C. Moreover, it is possible to observe that the nature of the C/N atom has negligible effect upon adsorption, specially of the atomic H*.

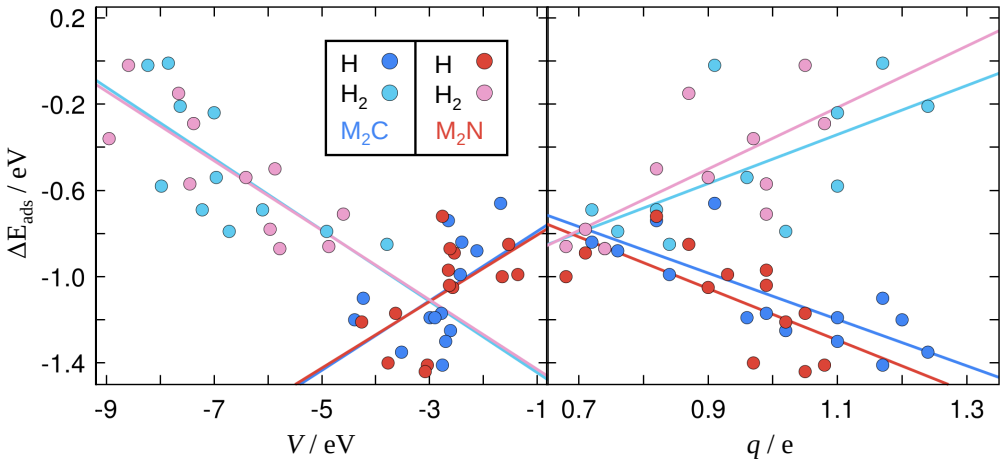


**Figure 5.5: Trends in the adsorption energies of H* and $H_2$*** with respect to the electrostatic potential, $V$, computed 1.5 Åabove the surface plane (left), and with respect to the Bader charges, $q$, on the surface metal M atoms. Values for MCenes/MNenes are represented by blue/red circles, where the dark/light filled circles correspond to $\Delta E_{ads}$ H and $\Delta E_{ads}$ $H_2$, respectively. Linear fits and related statistical data are provided in Table S8 from Appendix C

From the initial set of MXenes we selected the mentioned above MXenes with M = Cr, Mo, W, Mn, and Fe for being the most promising candidates.

However, the barrierless $H_2$ dissociation process may indicate that the surface of all the MXenes will be rapidly passivated with atomic hydrogen, blocking all the adsorption sites for the potential hydrogenable molecules, and hence poisoning the surface. Therefore, is important to settle under which conditions the MXene surface will be partially covered with hydrogen. To do so we employed the thermodynamic formalism described by Reuter *et al.*[54,55] (described in detail at section 3.1.5). We calculated the free H adsorption energies of well-ordered 1/9, 2/9, 4/9, 6/9 and 1 monolayer (ML) coverage surfaces as a function of T and $p$, $\Delta G_{ads}(T,p)$ and projected into the 2D plane of lowest Gibbs free energy. The results are shown in Figure 5.6.

Note that $Fe_2C$ and $W_2N$ diagrams show a wide transition from the clean surface to the fully covered surface in opposition to $Ti_2C$ and $Ti_2N$ where the transition occurs abruptly, in just 50 to 100 K. For instance, the $W_2N$ diagram show that at the 400−600 K temperature range, the MXene will be partially covered in hydrogen, even for relatively high $H_2$ pressures, and thus supporting the hypothesis that such MXenes perform well as a catalyst in hydrogenation reactions.

The *ab initio* thermodynamic approach is undoubtedly extremely useful to determine the relative thermodynamic stability of surfaces with different surface coverage. However, being a purely thermodynamic approach, it does not incorporate any kinetic consideration. For processes reaching the thermodynamic equilibrium in a very fast way, the approach will provide meaningful information. However, for process involving rather large barriers, as is the case for H* + H* recombination leading to $H_2$* which eventually desorbs, the kinetic aspects may introduce noticeable changes. As already established, the $H_2$ dissociation over any of the explored MXenes has a small or negligible barrier, however, the recombination barrier is considerably higher, see Table S5 from Appendix C, and hence the kinetics of such process might have an impact on the T,$p$ surface coverage. From microkinetic simulated, explained in detail in Section 3.1.6 we constructed the kinetic phase diagrams of $W_2N$, $Fe_2C$, $Ti_2C$, and $Ti_2N$ MXenes.

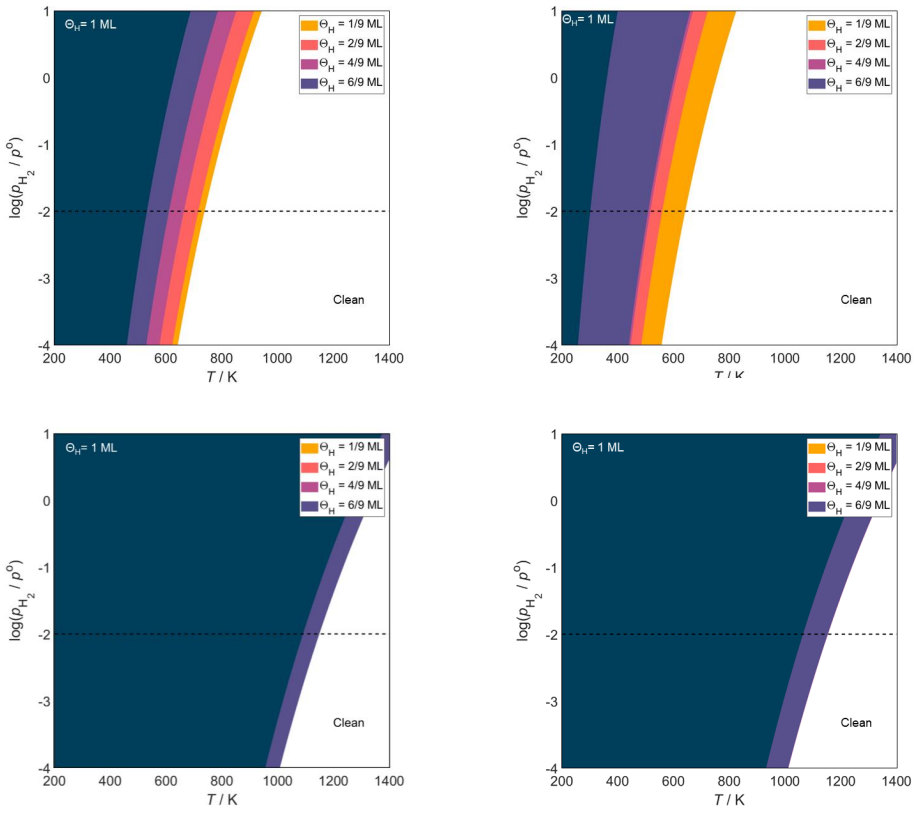


**Figure 5.6: Thermodynamic phase diagram as a function of T and $p_{H_2}$** for $W_2N$ (top loeft), $Fe_2C$ (top right), $Ti_2C$ (bottom left), and $Ti_2N$ (bottom right) (0001) MXenes including different atomic hydrogen coverages, $\theta_H$. It runs from 0 to 1 monolayer (ML). The black dashed line corresponds to a reference $p_{H_2}$ of 10 mbar.

The highlighted regions at Figure 5.7 denote the regions where the H* coverage is 0.4−0.8 ML or free sites coverage is 0.2−0.6. Note that the sum of coverages of the possible surface species, $\theta^* + \theta_H + \theta_{H_2} = 1$ but no $H_2$ population is observed. Equivalently than for the surface phase diagrams $Fe_2C$ and $W_2N$ exhibit potential conditions for hydrogenation processes. at $p_{H_2} = 10$ mbar the range of temperatures that the MXenes present a desirable coverage is 620−707

K and 745−852 K, respectively. Accordingly $Ti_2C$ and $Ti_2N$ will shown a surface fully passivated at very high temperatures, over 1200 K for a broad range of $p_{H_2}$ and hence they will presumably not be good for hydrogenation purposes.

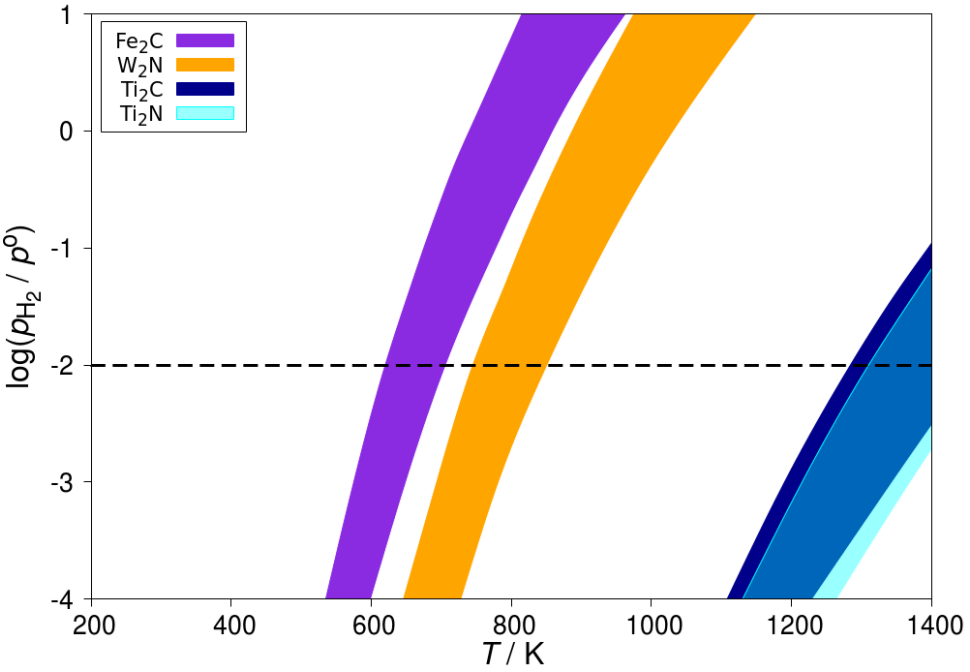


**Figure 5.7: Kinetic phase diagrams as a function of T and $p_{H_2}$** for $Fe_2C$, $W_2C$, $Ti_2C$, and $Ti_2N$ MXenes derived from microkinetic simulations. The colored regions denote conditions with a coverage of free sites between 0.2 (rightmost line of each region) and 0.6 ML (leftmost line of each region), while the rest is covered with H adatoms. Notice that the overlapping region between $Ti_2C$ (dark blue) and $Ti_2N$ (cyan) is colored in light blue. The black dashed line corresponds to a reference $p_{H_2}$ of 10 mbar.

Note that the temperatures for partially covered surfaces diverge from the *ab initio* surface phase diagram and the kinetic phase diagram for about 300 K higher at the latest ones. Such increase in temperature from the purely thermodynamic approach can be attributed at the extra cost generated by the recombination reaction. For the complete $H_2$ adsorption process the negligible barrier of the $H_2$ dissociation make both approaches comparable, however, the

desorption process requires more energy in the kinetic approach due to the high recombination barrier adds an extra energy requirement in comparison with the thermodynamic approach and hence a higher T is required to provoke the desorption. The analysis of the kinetic phase diagrams highlights the role of the energetic barrier for $H_2$ formation in determining the conditions for MXenes to be active hydrogenation catalysts and these are significantly different from those predicted from thermodynamic considerations only.

To sum up, the next points resume the main conclusions reached by this study. The complete publication can be found following the conclusions.[56]

- We provide here the trends in the interaction of H and $H_2$ with $M_2X$ materials by examining their description using the electrostatic potential above the surface and the surface metal Bader charges. The trends in H and $H_2$ adsorption for these two descriptors are diametrically opposed, with the former influenced by electrostatic forces and the latter by dispersive forces.

- $W_2N$, $Fe_2C$, and $Mo_2C$ are promising catalysts of hydrogenation reactions as they appear to be partially covered by hydrogen at common reaction conditions and within their range of thermal stability.

- Despite the kinetic and thermodynamic diagrams are qualitatively equivalent, the kinetic phase diagrams show slightly higher temperatures for the same coverage conditions as they account the extra energy of the kinetic barriers.

- We note that $W_2N$ was anticipated as a viable catalyst for ammonia synthesis,[17] which is a significant commercial hydrogenation process, which is consistent with the current findings.

## 5.4 MXenes Surface Terminations in Electrocatalysis

**Introduction**. As mentioned above, see Section 5.2, MXenes are rarely bare under experimental conditions. Moreover, besides the common -F, -OH, -O, and

-H terminations, derived from their main synthesis mechanism and posterior treatment many more moieties can lay on their surface. However, in addition to its strong corrosiveness, HF is a dangerous reagent that has the potential to be lethal to humans and cause systemic poisoning in the body. In order to make MXene synthesis safer and more environmentally friendly, unique HF-free synthesis techniques have recently emerged.[57–59]. For instance, using two MAX bulks as the cathode and the anode of an electrolytic cell is possible to etch MAX bulk acting as the anode.

Choosing a proper electrolyte such $NH_4Cl$ is possible to break the Ti-Al bonds and exfoliate the MAX phase.[59] Given the amphoteric nature of the Al group, alkali metals can be also used for MAX phases etching, based on a mechanism purposed by K. J. Bayer to extract aluminium from bauxite.[60] In a similar fashion, using a high concentration solution of NaOH at relatively high temperatures, the $OH^-$ are able to attack the insoluble Al compounds to the soluble $Al(OH)_4^-$ ions. Thus, the Al is selectively removed forming F-free MXenes.[57] Moreover, it has been recently reported new experimental techniques to manipulate and modificate MXenes terminations.[61] Due to the existence of such variaty of mechanisms, MXenes can be terminated with a broad spectrum of adsorbates. As a result, finding the most stable surface termination under clear-cut experimental circumstances becomes crucial for tuning the catalyst and is also a necessary component for accurate modeling.

The temperature and partial pressure of the reactants have a major role in determining the surface composition in heterogeneous catalysis. Phase diagrams that show the equilibrium composition for a certain set of circumstances may be constructed there. This is accomplished theoretically by applying the *ab initio* thermodynamics formalism created by Reuter and Scheffler,[54,55], detaily explained before in Section 3.2.2, which produces trustworthy surface phase diagrams. That being said, in electrocatalysis, it is important to understand that the involved reactions typically occur at standard temperatures while also occurring under the application of an external potential in a solution with specific

pH conditions. As a result, $U$ and pH must be taken into account in the modeling to find a reliable surface structure under these operating conditions. This is achieved by using the well-known Pourbaix diagrams,[62–64] which are readily available for a wide range of systems.

Even though they rely on a number of approximations,[65–67] the Pourbaix diagrams may also be computationally produced from first-principles theoretical computations. This is discussed in more detail in the previous section 3.2.2. However, there is no question about their usefulness, and for a number of reactions, including the chlorine evolution reaction on $RuO_2$,[66] the oxygen reduction reaction on metallic electrodes,[65] or the oxygen reduction reaction on lithium-ion batteries,[68] realistic electrocatalyst surface structures have been obtained from simulated Pourbaix diagrams. However, it should be noted that the theoretically produced diagrams only show the surface compositions that have been explicitly examined. This may be considered a restriction. This can be reduced by taking into account a sufficient number of surface motifs. Pourbaix diagrams for the HER on certain MXenes have also been published, but more systematic research that takes into account a larger family of MXenes with various terminations is still absent.

Despite the above-mentioned factors, theoretical investigations with no consideration of the impact of pH and applied voltage on surface composition have been reported,[69–71] which raises severe concerns about the accuracy of the associated predictions. Numerous electrochemical processes, particularly the HER, have been theoretically or empirically investigated over MXenes, as was already indicated. The impact of pH and potential on surface structure is typically only partially or not taken into account in these investigations, for example by assuming a certain surface termination. Some authors restrict the analysis to only take into account the most stable surface without taking pH and $U$ into account. While this may be appropriate for heterogeneous catalysis, it is incorrect when trying to understand the electrocatalytic process.[72] Numerous studies that have been published have only focused on the totally O-terminated MXene surface

without taking into account other factors or using a free energy criteria that ignores the pH-$U$ influence.[69]

In fact, when the oxygen reduction reaction (ORR) had been the reaction under study rather than the HER, the totally O-terminated MXene surface used in these earlier research would have been adequate. Given the foregoing, the goal of this study is to give Pourbaix Diagrams for a number of sample MXenes, such as $V_2C$, $Mo_2C$, $Ti_2C$, and $Ti_3C_2$, as well as to instruct readers on how to construct them by examining various single and double termination options. Our research seeks to wrap up earlier investigations into other scenarios[12,73] and place the findings in the context of earlier studies on MXene models for HER.

**Results**. Pourbaix diagrams may be constructed using a variety of architectures, including mixed instances as well as terminations with a single molecule. There are nine comparable adsorption sites in the supercell used to represent the MXenes most stable surfaces, as shown in Figure 5.9. As a result, 9O, 9OH, 9F, and 9H respectively equals to the surfaces completely covered by O, OH, F, and H. Also keep in mind that there are additional potential adsorption sites that, if permitted, may result in extensive coverage. However, this will result in adsorption at close ranges with correspondingly large steric repulsion.

First, single occupancy has been taken into consideration in all possible adsorption sites to find the most stable adsorption site for each specie, see Figure 5.8 and Table 5.2. Second, in order to explore various intermediate adsorbate coverages, ranges from 1/9 to 1 ML at such sites have been evaluated. And finally, a wide variety of mixed adsorbate scenarios have also been taken into account, all of which reflect complete coverage because a situation with lesser coverage is not preferred under the conditions of interest. For instance, it is evident from theory and experimentation that high temperatures are required to produce partly O-covered MXenes.[74,75] This discovery illustrates a fundamental distinction between electrocatalysis and heterogeneous gas-phase catalysis. In heterogenous catalysis, partly covered surfaces can be created at operational conditions, although this is exceedingly unusual in electrocatalysis. This may be

explained by mentioning the solid/liquid interface, which results in each active site being in direct contact with the electrolyte solution and, as a result, each active site being at least partially covered by a water molecule in the double layer above.

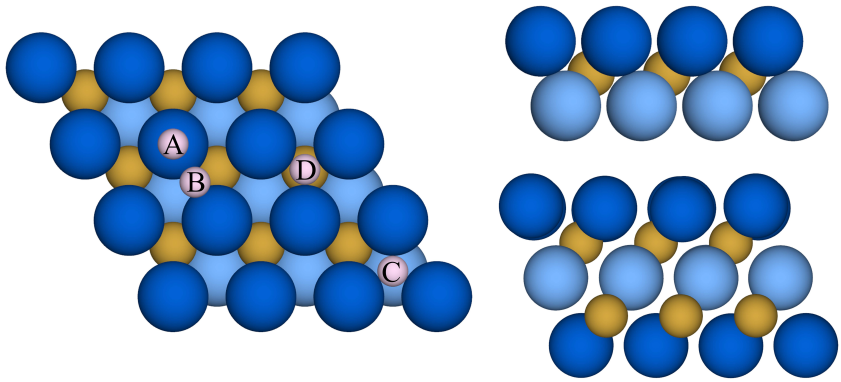


**Figure 5.8: Top (left image) and side (right images) views of a $M_2C(0001)$ (upper right image) and $Ti_3C_2(0001)$ (lower right image) surface $p(3\times3)$ supercell**, M = Ti, Mo, V. Metal atoms at the top and bottom layers are represented by bright and light blue spheres, respectively, while C atoms are represented by light brown spheres, and H atoms are shown in pink. The main high-symmetry surface sites considered are top (A), bridge (B), hollow M (C), and hollow C (D). (C) and (D) sites have either one M or C atom below

As mentioned above, then, for the construction of the four Pourbaix Diagrams -H, -OH, O, and -F will be the considered species together with all the possible distributions of the 3/6 ratio mixtures as illustrated at Figure 5.9. The following adsorption reactions where considered, see Table 5.3.

The adsorption energies indicate that for $V_2C$, $Ti_2C$, and $Ti_3C_2$ hollow M site (C in Figure 5.8) is always slightly preferred for all the adsorbates, however, for $Mo_2C$ it is not case. H still binds stronger at hollow M but the rest of the species prefer a hollow C site (D in Figure 5.8). The results achieved are in con-

| $M_{n+1}C_n(0001)$ | Adsorbate | Top | Hollow C | Hollow M |
|---|---|---|---|---|
| $Mo_2C$ | H | -0.27 | -0.85 | -0.91 |
| | OH | -0.46 | -1.43 | -1.23 |
| | O | -0.55 | -1.44 | -1.35 |
| | F | -3.67 | -3.98 | -3.77 |
| $V_2C$ | H | -0.05 | -1.13 | -1.30 |
| | OH | -1.03 | -2.10 | -2.32 |
| | O | -0.83 | -2.27 | -2.59 |
| | F | -4.12 | -4.72 | -4.98 |
| $Ti_2C$ | H | 0.03 | -1.12 | -1.46 |
| | OH | -1.69 | -2.75 | -2.97 |
| | O | -1.03 | -3.07 | -3.34 |
| | F | -4.76 | -5.43 | -5.73 |
| $Ti_3C_2$ | H | -1.03* | -1.03 | -1.36 |
| | OH | -2.51* | -2.51 | -2.89 |
| | O | -2.52* | -2.52 | -3.15 |
| | F | -5.66* | -5.22 | -5.65 |

**Table 5.2: Reference states for both single and mixed surface terminations**; $n$ and $y$ represent the number of adsorbed species on the studied surface. *For $Ti_3C_2$ the adsorbate at top site move indistinctly to hollow C or M.

cordance with previous literature.[12,73,76] One can next analyze the most likely scenario with either a single kind of moiety or having combinations of two types, as mentioned above, after determining the most stable adsorption site for each adsorbate. The total energy and the ZPE and entropy terms, as discussed in the previous Section 3.2.2, may be obtained from the density functional calculations by correlating vibrational frequencies. This information, along with the stoichiometric coefficients derived from the reaction equations, enables the construction of the Pourbaix diagrams, which are depicted in Figure 5.10 for the systems examined in the current study.

The Pourbaix diagrams for all investigated MXenes show comparable pat-

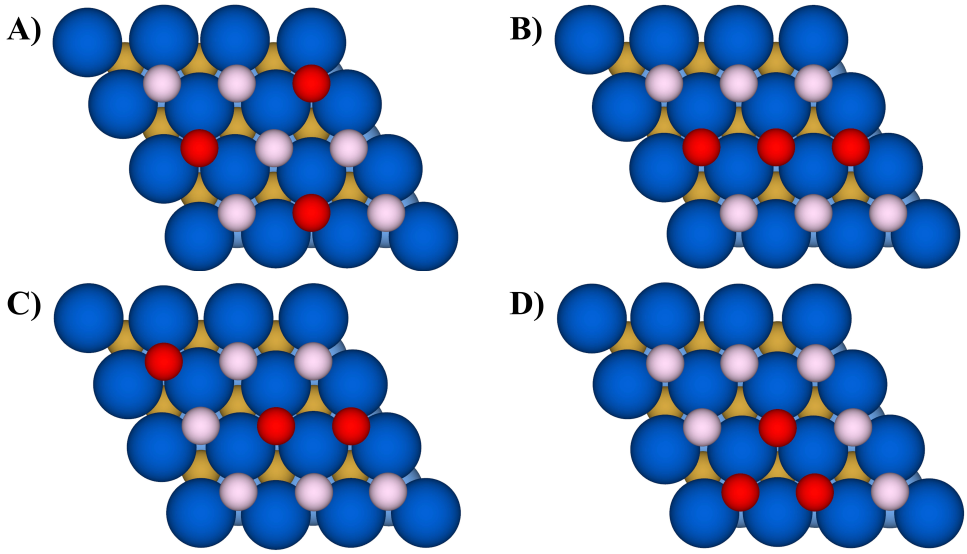


**Figure 5.9: Top view of the four possible 1/3A + 2/3B coverage situation with the adsorbates at their most thermodynamically favored adsorption site, hollow M**. The red and pink spheres represent the A and B adsorbates, respectively. Only for $Mo_2C$ the most thermodynamically stable adsorption site is encountered with hollow C.

terns in the stable surface coverage expected at various pH and $U$ values. Even with $Mo_2C$, when other adsorption sites are involved, this is the case. As a result, MXenes will not display their naked surface in an aqueous environment under any workable pH-$U$ circumstances. As anticipated, all four MXenes surfaces are totally hydrogenated (reduced) at $U_{SHE}$ values below 0.6 V, with H* acting as the only feedstock for any possible reaction. The MXene surface gradually oxidizes when the potential is raised, and OH* begins to replace H*. Being that only for $Ti_2C$ such transition coverages, first 2/3H* + 1/3OH* and then 1/3H* + 2/3OH* appear to be thermodynamically favoured, it is important to note that this process may be strikingly potential sensitive. The surface oxidation process continues as one moves away from negative potentials versus the SHE until $U_{SHE}$ hits 0.55 V, at which point all MXenes are completely covered with oxygen. Despite fluorine presents the highest adsorption energy, it is only present

| Adsorbate | Reaction |
|---|---|
| $n$H | $\frac{n}{2}H_2 + n^* \rightleftharpoons nH^*$ |
| $n$OH | $nH_2O + n^* \rightleftharpoons nOH^* + \frac{n}{2}H_2$ |
| $n$O | $nH_2O + n^* \rightleftharpoons nO^* + nH_2$ |
| $n$F | $\frac{n}{2}F_2 + n^* \rightleftharpoons nF^*$ |
| $n$O/$y$OH | $(n+y)H_2O + (x+y)^* \rightleftharpoons nO^* + yOH^* + (n+\frac{y}{2})H_2$ |
| $n$O/$y$H | $nH_2O + \frac{y}{2}H_2 + (x+y)^* \rightleftharpoons nO^* + yH^* + nH_2$ |
| $n$O/$y$F | $nH_2O + \frac{y}{2}F_2 + (x+y)^* \rightleftharpoons nOH^* + yF^* + nH_2$ |
| $n$OH/$y$H | $nH_2O + \frac{y}{2}H_2 + (x+y)^* \rightleftharpoons nOH^* + yH^* + \frac{n}{2}H_2$ |
| $n$H/$y$F | $nH_2O + \frac{y}{2}F_2 + (x+y)^* \rightleftharpoons nOH^* + yF^* + \frac{n}{2}H_2$ |
| $n$H/$y$F | $\frac{n}{2}H_2 + \frac{y}{2}F_2 + (x+y)^* \rightleftharpoons nH^* + yF^*$ |

**Table 5.3: Reference states for both single and mixed surface terminations**; $n$ and $y$ represent the number of adsorbed species on the studied surface.

on highly acidic conditions for $Ti_2C$ and $Ti_3C_2$ MXenes leading to the idea that F-covered surfaces are not stable for high pH levels. The explanation may be found by looking at Table 5.3 because, as it turns out, the adsorption process for the synthesis of F* results in $v(H_2) = v(H^+) = 0$, which means that there is no pH dependency for the formation of F*. Here, $v(H_2) \neq 0$, and consequently, $v(H^+) \neq 0$, which is significantly different from the situations of H*, O*, and OH* where Table 5.3 displays a definite pH dependency.

In conclusion, the energetics of H*, O*, and OH* are dependent on pH and decrease in free energy as pH rises, but the energetics of F* are not. This explains why F* phases in the Pourbaix diagram may only be seen at low pH values : when pH rises, the free energies of H*, O*, and OH* may surpass those of F*. Regarding the entropy contributions, when analyzing the several mixed coverage distributions, configuration A was always preferred. F/H mixed coverages are one of the deviations. Because F and H have such different electronegativities, the surface is stabilized when the atoms are positioned by groups, closely together, as in configuration D. Even so, the overall effect of the entropy can safely consider

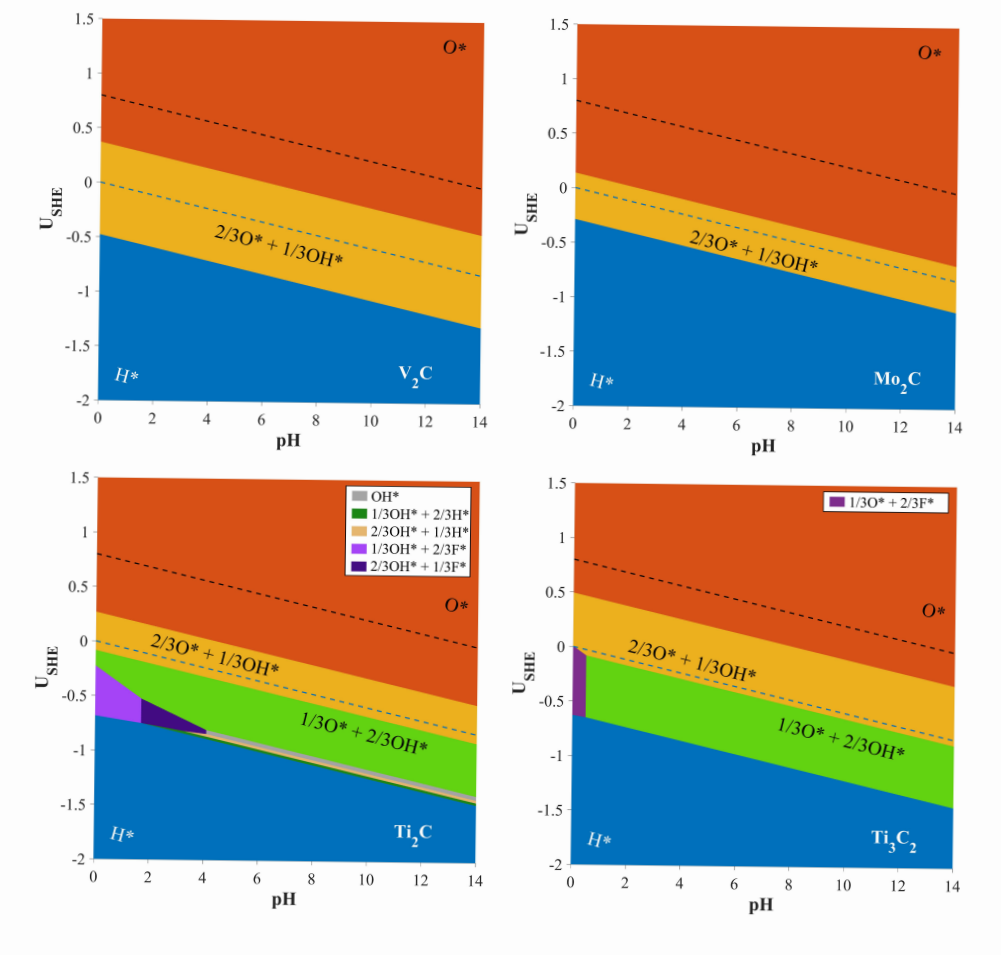


**Figure 5.10: Pourbaix diagrams for $Mo_2C$, $V_2C$, $Ti_2C$, and $Ti_3C_2$.** Note that from negative to positive potentials with respect to the SHE scale the surface becomes progressively oxidized, from full H coverage to full O coverage with intermediate –O/–OH or fully O-covered coverage for HER or ORR conditions, respectively. The HER equilibrium potential ($U = 0$ V vs SHE) as well as typical ORR conditions ($U = 0.8$ V vs SHE) are marked by dashed blue and black lines, respectively

negligible. Looking at Section S1 from Appendix D the difference in energies among all the configurations are mostly within the DFT accuracy.

Once choosing the reaction of interest one has to take a look at the Diagram

to choose a suitable surface terminations under the conditions of interest. Under the typical operation conditions of a considered proper catalyst for ORR, 0.80 eV vs SHE all four MXenes will be fully O-terminated as in concordance with Seh et al.[12] The case of HER is distinct. The combined 2/3O* + 1/3OH* coverage of all MXenes will be present at the equilibrium HER potential (0 eV *versus* SHE). However, the surface for $Ti_2C$ and $Ti_3C_2$ is rearranged to 1/3O* + 2/3OH* when accounting with the necessary applied potential for obtaining a desired $mA/cm^2$ current density, and as a result, such surface must be taken into consideration in a proper analysis. It is important to keep in mind that Pourbaix diagrams for the MXenes under study ($V_2C$, $Mo_2C$, $Ti_2C$, and $Ti_3C_2$) have already been published by Gao *et al.*[77] and others,[12,76,78–80] despite taking a lower number of surface structure possibilities and differing cell sizes into account.

Comparing the Pourbaix diagrams of $Ti_2C$, $Ti_3C_2$, and $V_2C$ with those published by Gao *et al.*[77] reveals that various adsorbates and combinations were chosen for the study even if the general picture is in accord. Thus, even when different mixed ratios of O*/OH* were taken into account, the totally oxygen-covered scenario arises at similar potential for $Ti_2C$, $Ti_3C_2$, and $V_2C$, demonstrating the theoretical approach's predictive effectiveness. In addition, in contrast to other efforts, we choose for a bigger $p(3\times3)$ supercell rather than the $p(2\times2)$[78] or $p(2\times1)$[77,79] ones so that a greater variety of adsorbate patterns may be taken into consideration. The inclusion of H* and F* adsorbates is a significant step up from prior work, even if the calculated Pourbaix diagrams are qualitatively equivalent to the outcomes found in lower cell sizes. For strongly reducing (negative) overpotentials, which may be significant in some electrocatalytic processes involving these MXenes, such as the hydrogen evolution versus electrochemical nitrogen reduction or the hydrogen evolution versus electrochemical $CO_2$ reduction, the fully H* covered situation is actually preferred. It is also important to emphasize the existence of mixed coverages containing F* adsorbates in highly acidic conditions for $Ti_2C$ and $Ti_3C_2$, as they are a factor to be taken into consideration in HER conditions, which could affect the overall surface electrocatalytic

activity but was largely disregarded in earlier studies.[80] However, it is important to be cautious when analyzing some regions of the Pourbaix Diagrams. While the ORR and HER zones are well characterized for the $V_2C$ and $Mo_2C$ MXenes and the more advantageous surfaces are strongly favoured energetically, this is not the case for $Ti_2C$ and $Ti_3C_2$. Several surface adsorbate mixes at the HER regime have extremely near $\Delta G$ energies, and when they are below the DFT accuracy, even though they are not depicted in the diagram (only the lowest energy surface is displayed), they might be current surface at working condition.

To sum up, the next points resume the main conclusions reached by this study. The complete publication can be found following the conclusions.[81]

- We reported a detailed analysis of all the elements needed for the construction of a reliable surface Pourbaix diagram for a set of representative MXenes; $Ti_2C$, $Ti_3C_2$, $V_2C$, and $Mo_2C$, evaluating the most common terminations.

- We have shown how for a wide range of pH and $U$ variables the MXenes are not fully O* or OH* covered but rather other mixed terminations. Moreover, the H* ML coverage is also important for overpotentials under -0.6 vs SHE.

- At ORR conditions the MXenes surface terminations will be a monolayer of O for all the studied cases but for the HER $Mo_2C$ and $V_2C$ will have 2/3O* + 1/3OH* whereas for $Ti_2C$ and $Ti_3C_2$ more considerations have to be done.

- At very acidic conditions the presence of -F moieties at the $Ti_2C$ and $Ti_3C_2$ MXenes has been predicted, and cannot be neglected when studying reactions such HER where its presence must effect its catalytic performance. Additionally, under HER conditions 2/3O* + 1/3OH* and 1/3O* + 2/3OH* coverages are extremely close in energy and thus, both terminations must be considered to evaluate the HER performance.

- Entropy can be safely neglected as it is not influenced by pH and $U$ conditions and the energies of all the different contributions are close enough.

## 5.5 Hydrogen Evolution Reaction over MXenes

**Introduction**. The hydrogen economy pretends to introduce the hydrogen as a candidate energy source to replace the highly pollutant fossil fuels.[3,82] Water splitting is a critical step in the creation of clean electrochemical hydrogen, and the processes that occur at the cathode and anode, respectively, are known as the HER and the OER.[83–85] However, these technologies still have a few drawbacks in terms of large-scale implementation. Currently, $Pt^{-}$ and Ir/Ru-based materials are among the best catalysts for HER[86,87] and OER,[88] respectively, and materials based on non-scarce metals are required to replace $Pt^{-}$ and Ir/Ru-based catalysts.[89]

Focusing on alternatives for HER catalysts Seh *et al.*[12] investigated the suitability of the broadly used Gibbs free energy of adsorbed hydrogen, $\Delta G_H$ descriptor,[90] to evaluate the electrocatalytic potential of several O-terminated early Transition Metal MXenes as HER catalysts. Subsequent research looked at an even broader variety of MXenes, regarding their HER activity.[71,73,91,92] However, despite the large number of studies addressing the HER catalytic activity of MXenes, they rely solely on thermodynamic considerations, ignoring the role of kinetics in the HER process. A survey of the available literature on the HER mechanism in MXenes, including the most recent review,[93] reveals that the majority of the published research depend on thermodynamic reasoning and descriptors such as the previously stated $\Delta G_H$. However, the thermodynamic method may not be sufficient to describe all electrocatalytic processes since, in certain circumstances, the fundamental hypothesis, assuming a thermodynamically driven process, does not always true.[94]

In the present Section, we propose a complete analysis in which the kinetics of HER over the $V_2C$, an example case of the MXenes $M_2C$ family, is accounted for

for the first time. This is accomplished by invoking new formalisms that employ first-principles computations to get kinetic information by modeling Tafel plots.

From the Pourbaix Diagram of the $V_2C$[81] the most thermodynamically preferred surface termination was selected as the current termination for the present HER stuyd, $T_x = 1/3$ OH* + 2/3 O*. However, one must recognize that an overpotential is required to start the electrochemical process. In the instance of $V_2C$, the most stable surface at a -0.5 V vs. the reversible hydrogen electrode (RHE) overpotential is that totally covered by adsorbed H*, and this condition is considered in our analysis. We also investigated the case with complete OH* coverage, even though recent research indicates that this state is not thermodynamically favorable at any pH or potential condition.[81]

This is due to the fact that most simulated surface Pourbaix diagrams fail to account for the influence of the surrounding solvent. As a result, six molecules of water are added to the surface to function as proton-electron donors in order to better replicate an electrochemical environment. The atomic structure of the adsorbed water is similar to the ice-like form structure that has previously been used to analyze the HER kinetics in other systems, and includes an extra H bonded to a water molecule, $H_3O^+$. Including explicit water molecules in the computational models with the initial surface coverage of 1/3OH* + 2/3O* results in a novel condition where the surface is completely covered by OH* groups. As a result, the current study we consider the full OH* termination instead, both structures, $T_x$ = H or OH, are depicted at Figure 5.11

The presence of the water layer simulating the reaction environment and acting as a proton-electron donor make us consider the global HER under an acidic equilibrium, Eq. 5.1.

$$2H^+ + 2e^- \rightleftharpoons H_2\,. \tag{5.1}$$

The HER can occur *via* two main mechanisms, the Volmer−Heyrovsky (VH), and the Volmer−Tafel (VT) mechanisms. Both methods have the identical elec-

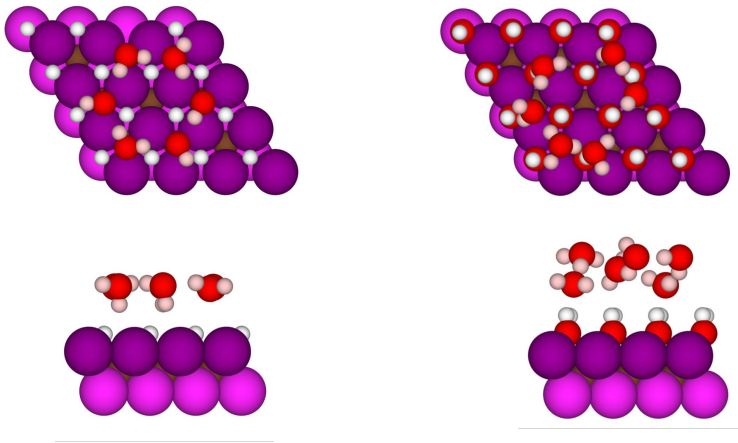

**Figure 5.11: Top and side views of the $p$(3×3) supercells used to represent $V_2C$(0001)** terminated by H (right) and OH (left) with the surface covered by six water molecules in an ice-shaped structure. Metal atoms at the top and bottom layers are represented by bright and light purple spheres while C atoms are represented by dark brown spheres. H atoms adsorbed on the surface and on the water layer are shown in white and pink spheres, respectively, with O atoms in red.

trochemical step of proton reduction at the electrode, the called Volmer step, as shown in Eq. 5.2, but vary in the second step. The second phase in the VH process is likewise electrochemical, the Heyrovsky step, as shown in Eq. 5.3, culminating in the synthesis and release of the $H_2$ molecule. The VT process, on the other hand, comprises the Volmer step in Eq. 5.2 twice plus the Tafel step in Eq. 5.4, a chemical reaction that combines the two adsorbed hydrogen atoms to produce $H_2$, in a similar fashion than the process studied at the Section 5.3 of this Chapter.

$$H^+ + e^- + * \rightarrow H^*\,, \tag{5.2}$$

$$H^+ + e^- + H^* \rightarrow * + H_2\,, \tag{5.3}$$

$$H^* + H^* \rightarrow H_2\,. \tag{5.4}$$

Nevertheless, both mechanisms present a common first step with the electrochemical adsorption of one hydrogen on the catalyst surface. Note that within our model the $V_2C$ surface has already hydrogen adsorbed on it regardless the surface termination considered and hence further considerations are needed. The presence of surface hydrogen might introduce a variation at the order of which the steps of the VH and VT mechanisms might occur. For instance, one hydrogen from the water layer can produce a molecule of $H_2$ *via* a Heyrovsky step and finally an other hydrogen from the water layer can replace the missing hydrogen *via* a Volmer step resulting in an inverse VH mechanism. Following the same logic, exchanging the order of the steps of the VT mechanism two more variants can be introduced. Despite introducing five different alternative mechanisms, not all the possibilities are allowed over all the surfaces. For example, in the H-terminated MXene, $T_x$ = H, the metal top V atoms can attach a H atom from the water layer, allowing any pathway that begins with a Volmer step.

The hydrogen atoms absorbed at the hollow M sites present in the original termination, on the other hand, are tightly adsorbed (*i.e.* $\Delta G$ = -1.05 eV). As a result, the H cannot be employed as a hydrogen source for the HER, and processes that begin with a Heyrovsky or Tafel step cannot and will not be examined, as shown in Figure 5.12. In contrast, on the OH terminated MXene, $T_x$ = OH, the OH groups sterically block the V top sites, leaving no open adsorption sites for the H atoms, as opposed to the $V_2C$-H surface. The H atoms from the surface OH groups, on the other hand, are exposed and can be coupled to one hydrogen from the water layer *via* one Heyrovsky step, or they can form an $H_2$ molecule with another H from the surface OH *via* one Tafel

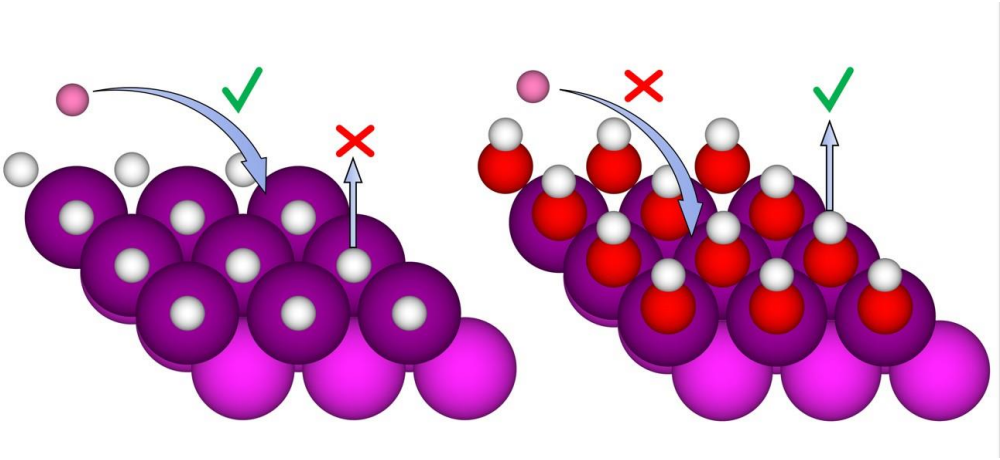

**Figure 5.12: Schematic representation of the initial steps for the HER that are possible in the -H and -OH terminated $V_2C$ MXene surface.** In the $T_x$ = H surface (left image), the Volmer step is allowed as the incoming H (in pink) can be adsorbed on the surface provided there are free sites. However, the Heyrovsky and Tafel steps are forbidden because hydrogen at the surface is too strongly adsorbed (*i. e.* $\Delta$G = -1.05 eV). Therefore, it is not accessible for a forthcoming Heyrovsky or Tafel steps. On the contrary, in the $T_x$ = OH surface (right image), the adsorption sites for the H adsorption are sterically blocked, and consequently the Volmer step is restricted although the H from the OH termination groups are exposed to the ice-liked water layer and available as a hydrogen source for a starting Heyrovsky or Tafel steps.

step, as illustrated schematically in Figure 5.12. Overall, Table 5.4 shows all the mechanisms explored.

In the current model, we use the previously mentioned layer of ice-like water on top of the model as a hydrogen source to get insight into the HER kinetics. To avoid artifacts, we studied a representative number of possibilities and generated the free energy diagrams using an average across these pathways, rather than assuming the lowest energy adsorption approach.

**Results**. From the five purposed mechanisms the two paths more favoured with comparable thermodynamics and kinetics are VH-I and VT-I over $V_2C$-

| MXene | Mechanism | Step I | Step II | Step III |
|---|---|---|---|---|
| $V_2C$-H | VH-I | Volmer Step | Heyrovsky Step | |
| | VT-I | Volmer Step | Volmer Step | Tafel Step |
| | VT-II | Volmer Step | Tafel Step | Volmer Step |
| $V_2C$-OH | VH-II | Heyrovsky Step | Volmer Step | |
| | VT-III | Tafel Step | Volmer Step | Volmer Step |

**Table 5.4: Description of the five HER mechanisms on the $V_2C$ MXene considered in the HER study**. The mechanism column defines the label for the studied VH and VT mechanisms. The last three columns correspond to the order of the steps for each mechanism.

H. Thus despite including a set of alternative paths involving initial surface hydrogen, it appears to be too strongly adsorbed on the surface to be directly involved in the reaction mechanism. Therefore $V_2C$-OH surface appears to be inactive for HER as the O-H interactions are too strong and the H will remain trap on the surface.

Figure 5.13 shows the free energy diagram of the VH-I mechanism. In this first mechanism, a hydrogen atom from the acidic water layer adsorbs on top of the surface before forming the final $H_2$ molecule *via* a Heyrovsky step, thus, the RI of the mechanism will be the surface with a hydrogen adsorbed on it. The adsorption of such hydrogen atom at the surface can be direct, one hydrogen from a $H_3O^+$ molecule is adsorbed on the surface, or indirectly, one hydrogen from the $H_3O^+$ moves to a near by water molecule and finally, one hydrogen from the acceptor water molecule pointing towards the surface adsorbs on the surface. Accordingly, eighteen different possible paths, including direct and indirect adsorptions, starting the from the unit cell described at the left side of Figure 5.11 where evaluated, see Figures S2, S3, and S4 from the Appendix E. As mentioned adobe, this mechanism only can occur at $V_2C$-H as has free adsorption sites for the H.

From all the adsorbed sites and paths the top position is consistently pre-

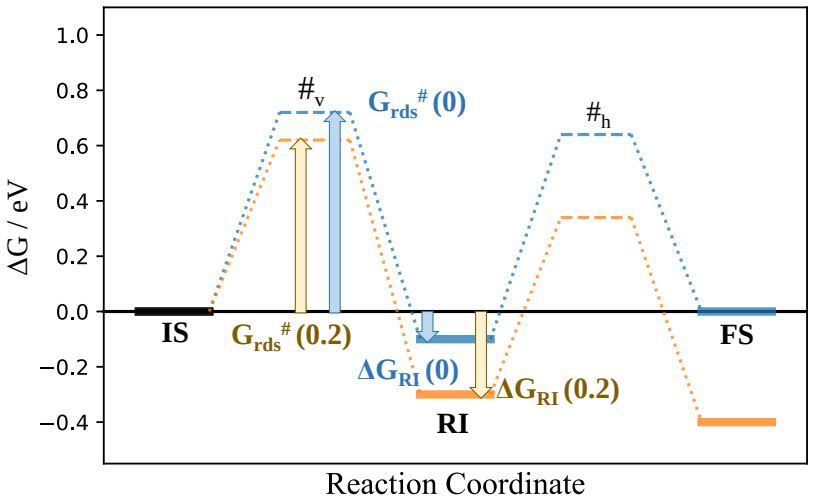


**Figure 5.13: Schematic representation of the Gibbs free energy profile for the VH-I mechanism** at $\eta = 0$ V, in blue, and $\eta = 0.2$ V, in orange. The initial state (IS) is depicted in black. The final states (FS) and the RIs are depicted with a plain line while TS are marked as $\#_{v/h}$ in dashed lines $\Delta G_{RI}(0)$ and $\Delta G_{RI}(0.2)$ are the corresponding values for the RI energies at $\eta = 0$ V, in blue, and $\eta = 0.2$ V, in dark yellow. $G^{\#}_{rds}(0)$ and $G^{\#}_{rds}(0.2)$ correspond to the highest kinetic free energies as a function of the applied overpotential, and are depicted in blue and dark yellow, respectively.

ferred than hollowC, see Figure S1 from the Appendix E, with adsorption energies going from −0.17 to +0.19 eV for top adsorptions and ∼ +0.31 eV for hollowC. The considerable difference between top adsorptions it might be due to in some relaxations, when the water layer is reorganized in response to adsorption, one oxygen atom from the water layer interacts with one V from the surface, stabilizing the RI, and thus, a difference in adsorption energy is observed between the top adsorptions when such stabilization occurs and when not. Because adsorption at hollowC is less stable than at the top site, only one direct and one indirect hollowC channel are examined further. We discover no significant differences between direct and indirect adsorptions when only thermodynamics are considered. Finally, a second hydrogen atom is introduced to

the water layer, where it combines with the hydrogen atom previously adsorbed on the MXene.

Both TSs have equivalent barriers, being the Volmer TS, $\#_v$ higher than the Heyrovsky TS, $\#_v$, and hence becoming the rds of the reaction at $\eta = 0$ in this mechanism. Furthermore, when an overpotential is applied, this profile is kept as the initial barrier of any electrochemical process, *i.e.* $\#_v$ will be lowered by $\alpha_v$ and $\#_h$ by $1+\alpha_h$ in accordance with Eq 3.43. Note that, for TS the number of transferred electrons is a fractional number and the parameter $\alpha$ is introduced to account for it, as in Eq. 5.5.

$$\Delta G^{\#}(\eta) = \Delta G^{\#}(0) - [(n + \alpha)e\eta] \,, \tag{5.5}$$

where $\Delta G^{\#}(\eta)$ and $\Delta G^{\#}(\eta)$ are the free energy change from initial to any TS at zero or $\eta$ overpotential, $n$, the number of transferred electrons, $e$, the elementary charge, and as mentioned above, $\alpha$, is the partial charge transferred on a TS. This value is commonly unknown but commonly approximated to $\alpha = 0.5$. Therefor, we assumed $\alpha_h = \alpha_v = 0.5$. To summarize, the Volmer step is the rds for these processes, and providing an overpotential will have no effect on this; hence, the computational Tafel plot, explained in detail in previous Section 3.2.3, will show just one unique regime.

Regarding the VT-I mechanism, Figure 5.14 shows its free energy diagram. Again, one hydrogen is adsorbed at the surface, however the second step is a second hydrogen adsorption, as distinct to the VH-I process. Finally, the two hydrogens from the surface combine to produce the final hydrogen molecule. Once again, this mechanism is only conceivable in the $V_2C$-H system and, as previously stated, cannot occur in the $V_2C$-OH system. Thus, alternatively to the VH-I, this mechanism has two RI and their two concomitant TS. The mechanism RIs will be the MXene with one H atom adsorbed at its surface, RI1, and MXene with two H atoms adsorbed at its surface, RI2. For simplicity, the first Volmer step, including the described RI1 and TS1, is taken from the VH mechanism.

The second step is evaluated following the same procedure that VH-I, the paths are described at Fiugres S5, S6, and S7 from the Appendix E.

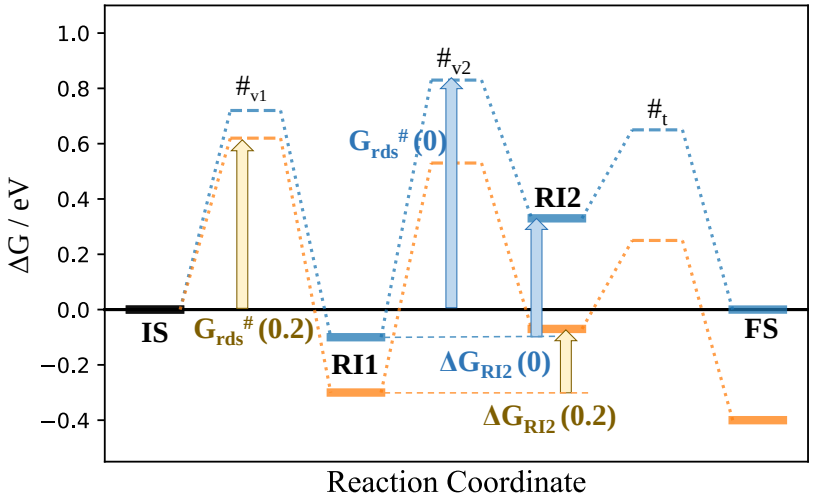


**Figure 5.14: Schematic representation of the Gibbs free energy profile for the VT-I mechanism** at $\eta = 0$ V, in blue, and $\eta = 0.2$ V, in dark yellow. The IS is depicted in black. The FSs and the RIs are depicted with a plain line while TS are marked as $\#_{v/t}$ in dashed lines $\Delta G_{RI}(0)$ and $\Delta G_{RI}(0.2)$ are the corresponding values for the RI energies at $\eta = 0$ V, in blue, and $\eta = 0.2$ V, in dark yellow. $G^{\#}_{rds}(0)$ and $G^{\#}_{rds}(0.2)$ correspond to the highest kinetic free energies as a function of the applied overpotential, and are depicted in blue and dark yellow, respectively.

Again, the RIs with the second hydrogen adsorbing on top sites are more stable; nonetheless, a second hydrogen on the surface does not stabilize as the first Volmer step, with free energy ranging from 0.30 to 0.56 eV. The attractive interactions between the oxygen from the water molecules and the metals on the surface are reduced when more hydrogens are adsorbed on the surface. As a result, the RI created by adding more adsorbed hydrogens to the $V_2C$-H surface may be less favorable than the prior RI with one fewer hydrogen at the surface. In contrast, the hydrogen already adsorbed on the surface does not interfere with the adsorption of additional hydrogens, hence the barriers have equivalent

energies. Finally, we discovered surprisingly low kinetic barriers for Tafel steps ranging from 0.32 to 0.61 eV.

Both Volmer step TSs require similar barriers, but the second barrier is slightly higher, implying that the rds of the reaction will be the second Volmer step at null or low overpotentials, but as the overpotential gradually increases, the first Volmer step will become the new rds as a results of Eq. 5.5. The Tafel plot will display two distinct lineal regimes corresponding to scenarios in which the kinetics of the reaction are dominated first by the second Volmer step and then by the first Volmer step. When a finite overpotential is applied, the second Volmer step ultimately has a lower barrier and the rds changes.

Comparing the kinetics and thermodynamics of both possible candidates it appears that both mechanism will leading the reaction based on the $\eta$ applied. As shown in Figure 5.15. While the VH-I mechanism is energetically preferable for minor overpotentials, it is clear that the VT-I route is kinetically preferred for higher overpotentials. This observation is explained by the fact that when overpotential grows, so does the coverage of adsorbed hydrogen on the top site, which enables chemical recombination of two neighboring hydrogen atoms on the top sites compared to the electrochemical Heyrovsky step in the VH-I process.

The results obtained in terms of the top sites as active species for the HER and the Volmer-Tafel mechanism as the preferred mechanistic description for large overpotentials are somewhat reminiscent of the HER over Pt(111),[95,96] which may be another reason why MXenes are promising electrocatalysts for hydrogen generation. Finally, we examine the influence of the MXene termination (OH*- vs. H*-covered surface) on electrocatalytic performance by comparing the Tafel plot of the merged VH-I and VT-I mechanisms, Figure 5.15, with an empirically reported Tafel plot of the HER over $V_2C$.[97] According to the experimentally reported Tafel plot, $V_2C$ is not active toward the HER in the potential regime of $-0.5$ V $< U$ vs. RHE $< 0$ V. Given that the HER kinetics of this surface termination are poor, we attribute this discovery to the existence of the OH*-covered surface under these potential settings.

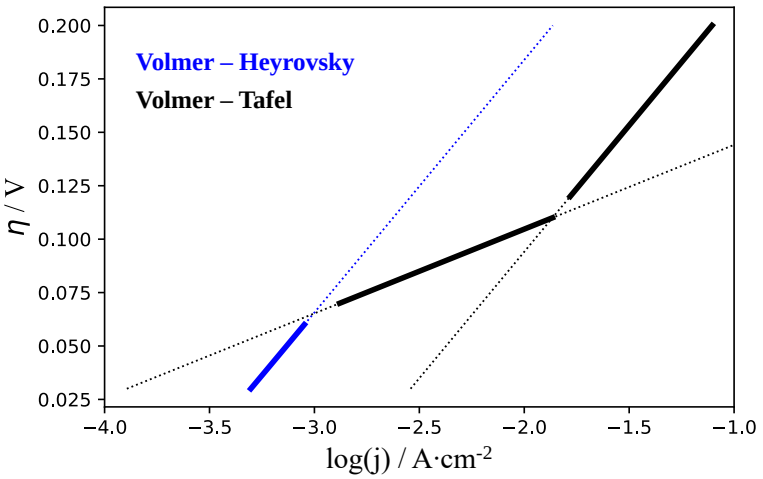


**Figure 5.15: Simulated Tafel plots of the HER over V2C-H via the VH and VT mechanisms** in blue and black, respectively as obtained from the free-energy landscape of Figures 5.13 and 5.14. For small applied overpotential, $\eta \sim 0.07$ V, the Volmer-Heyrovsky mechanism is kinetically preferred whereas for larger overpotentials the Volmer-Tafel mechanism describes the reaction rate.

The experimental Tafel plot, on the other hand, shows hydrogen creation for $U < -0.5$ V vs. RHE, which may be explained by the existence of the H*-covered surface, which has a simple kinetics according to our first-principles model. As a result, tuning the HER kinetics of $V_2C$ requires shifting the transition from the kinetically inactive OH* phase to the active H* phase toward greater positive potentials, which ideally happens at roughly $U = 0$ V vs. RHE.

To sum up, the next points resume the main conclusions reached by this study. The complete submitted text can be found following the conclusions.[81]

- We reported a detailed analysis of the possible mechanisms for HER over $V_2C$ MXene.

- We have presented a detailed explanation on how to compute theoretical Tafel plots for two electron transfer processes, including the VH with only

one reaction intermediate and the VT, with two different intermediates.

- Despite the availability of hydrogen at the surface of $V_2C$-H and $V_2C$-OH MXenes, the standard VH and VT mechanism remain more feasible.
- As the Volmer step is only possible on $V_2C$-H, such surface might be active for HER purposes, in opposition to $V_2C$-OH surface, where the hydrogen adsorption is sterically blocked.
- By comparison of Tafel plots, derived from the free energy diagrams of VH-I and VT-I, with an experimental Tafel plot, we conclude that the HER over $V_2C$, might happen *via* VH mechanism.
- We show that for small overpotentials, the VH pathway corresponds to the preferable mechanistic description, but for greater overpotentials, the VT path becomes kinetically favored. The findings obtained are strikingly comparable to the HER over Pt, demonstrating why MXenes are promising electrocatalysts for the generation of gaseous hydrogen by electrochemical water splitting.

# References

[1] P. B. Weisz, *Phys. Today*, 2004, **57**(7), 47–52.

[2] J. A. Turner, *Science (80-. ).*, 1999, **285**(5428), 687–689.

[3] G. W. Crabtree, M. S. Dresselhaus, and M. V. Buchanan, *Phys. Today*, 2004, **57**(12), 39–44.

[4] B. Anasori, M. R. Lukatskaya, and Y. Gogotsi, *Nat. Rev. Mater.*, 2017, **2**, 16098.

[5] N. K. Chaudhari, H. Jin, B. Kim, D. San Baek, S. H. Joo, and K. Lee, *J. Mater. Chem. A*, 2017, **5**(47), 24564–24579.

[6] Y. Gogotsi and B. Anasori, *ACS Nano*, 2019, **13**(8), 8491–8494.

[7] A. V. Mohammadi, J. Rosen, and Y. Gogotsi, *Science (80-. ).*, 2021, **372**(6547).

[8] D. Er, J. Li, M. Naguib, Y. Gogotsi, and V. B. Shenoy, *ACS Appl. Mater. Interfaces*, 2014, **6**(14), 11173–11179.

[9] X. Liang, A. Garsuch, and L. F. Nazar, *Angew. Chemie - Int. Ed.*, 2015, **54**(13), 3907–3911.

[10] X. Wang, S. Kajiyama, H. Iinuma, E. Hosono, S. Oro, I. Moriguchi, M. Okubo, and A. Yamada, *Nat. Commun.*, 2015, **6**, 6544.

[11] A. D. Handoko, K. D. Fredrickson, B. Anasori, K. W. Convey, L. R. Johnson, Y. Gogotsi, A. Vojvodic, and Z. W. Seh, *ACS Appl. Energy Mater.*, 2018, **1**(1), 173–180.

[12] Z. W. Seh, K. D. Fredrickson, B. Anasori, J. Kibsgaard, A. L. Strickler, M. R. Lukatskaya, Y. Gogotsi, T. F. Jaramillo, and A. Vojvodic, sep , 2016, **1**(3), 589–594.

[13] I. Persson, J. Halim, H. Lind, T. W. Hansen, J. B. Wagner, L. Å. Näslund, V. Darakchieva, J. Palisaitis, J. Rosen, and P. O. Persson, *Adv. Mater.*, 2019, **31**(2), 1805472.

[14] R. Morales-Salvador, Á. Morales-García, F. Viñes, and F. Illas, *Phys. Chem. Chem. Phys.*, 2018, **20**(25), 17117–17124.

[15] Á. Morales-García, A. Fernández-Fernández, F. Viñes, and F. Illas, *J. Mater. Chem. A*, 2018, **6**(8), 3381–3385.

[16] N. Li, X. Chen, W. J. Ong, D. R. Macfarlane, X. Zhao, A. K. Cheetham, and C. Sun, *ACS Nano*, 2017, **11**(11), 10825–10833.

[17] J. D. Gouveia, á. Morales-García, F. Viñes, J. R. Gomes, and F. Illas, *ACS Catal.*, 2020, **10**(9), 5049–5056.

[18] J. D. Gouveia, Á. Morales-García, F. Viñes, F. Illas, and J. R. Gomes, *Appl. Catal. B Environ.*, 2020, **260**, 118191.

[19] H. Wei, Q. Jiang, C. Ampelli, S. Chen, S. Perathoner, Y. Liu, and G. Centi, *ChemSusChem*, 2020, **13**(21), 5614–5619.

[20] T. K. Slot, V. Natu, E. V. Ramos-Fernandez, A. Sepúlveda-Escribano, M. Barsoum, G. Rothenberg, and N. R. Shiju, jul , 2021, **8**(3), 035003.

[21] K. Rasool, M. Helal, A. Ali, C. E. Ren, Y. Gogotsi, and K. A. Mahmoud, *ACS Nano*, 2016, **10**(3), 3674–3684.

[22] M. Naguib, M. Kurtoglu, V. Presser, J. Lu, J. Niu, M. Heon, L. Hultman, Y. Gogotsi, and M. W. Barsoum, *Adv. Mater.*, 2011, **23**(37), 4248–4253.

[23] M. Naguib, V. N. Mochalin, M. W. Barsoum, and Y. Gogotsi, *Adv. Mater.*, 2014, **26**(7), 992–1005.

[24] B. Anasori and Y. Gogotsi, *Graphene 2D Mater.*, 2022, **7**(3), 75–79.

[25] P. O. Persson and J. Rosen, *Curr. Opin. Solid State Mater. Sci.*, 2019, **23**(6), 100774.

[26] M. W. Barsoum, *Prog. Solid State Chem.*, 2000, **28**(1-4), 201–281.

[27] V. H. Nowotny, *Prog. Solid State Chem.*, 1971, **5**, 27–70.

[28] M. W. Barsoum and T. El-Raghy, *J. Am. Ceram. Soc.*, 1996, **79**(7), 1953–1956.

[29] J. Frodelius, M. Sonestedt, S. Björklund, J. P. Palmquist, K. Stiller, H. Högberg, and L. Hultman, *Surf. Coatings Technol.*, 2008, **202**(24), 5976–5981.

[30] P. Eklund, J. Rosen, and P. O. Persson, *J. Phys. D. Appl. Phys.*, 2017, **50**(11).

[31] X. H. Wang and Y. C. Zhou, *J. Mater. Sci. Technol.*, 2010, **26**(5), 385–416.

[32] M. W. Barsoum and M. Radovic, *Annu. Rev. Mater. Res.*, 2011, **41**, 195–227.

[33] M. Alhabeb, K. Maleski, B. Anasori, P. Lelyukh, L. Clark, S. Sin, and Y. Gogotsi, *Chem. Mater.*, 2017, **29**(18), 7633–7644.

[34] Q. Tao, M. Dahlqvist, J. Lu, S. Kota, R. Meshkian, J. Halim, J. Palisaitis, L. Hultman, M. W. Barsoum, P. O. Persson, and J. Rosen, *Nat. Commun.*, 2017, **8**, 1–7.

[35] Z. Liu, E. Wu, J. Wang, Y. Qian, H. Xiang, X. Li, Q. Jin, G. Sun, X. Chen, J. Wang, and M. Li, *Acta Mater.*, 2014, **73**, 186–193.

[36] B. Anasori, Y. Xie, M. Beidaghi, J. Lu, B. C. Hosler, L. Hultman, P. R. Kent, Y. Gogotsi, and M. W. Barsoum, *ACS Nano*, 2015, **9**(10), 9507–9516.

[37] P. Urbankowski, B. Anasori, T. Makaryan, D. Er, S. Kota, P. L. Walsh, M. Zhao, V. B. Shenoy, M. W. Barsoum, and Y. Gogotsi, *Nanoscale*, 2016, **8**(22), 11385–11391.

[38] B. Soundiraraju and B. K. George, *ACS Nano*, 2017, **11**(9), 8892–8900.

[39] Á. Morales-García, F. Calle-Vallejo, and F. Illas, *ACS Catal.*, 2020, **10**(22), 13487–13503.

[40] M. López, L. Broderick, J. J. Carey, F. Viñes, M. Nolan, and F. Illas, *Phys. Chem. Chem. Phys.*, 2018, **20**(34), 22179–22186.

[41] Á. Morales-García, M. Mayans-Llorach, F. Viñes, and F. Illas, *Phys. Chem. Chem. Phys.*, 2019, **21**(41), 23136–23142.

[42] K. Hantanasirisakul and Y. Gogotsi, *Adv. Mater.*, 2018, **30**(52).

[43] M. Khazaei, A. Ranjbar, M. Arai, T. Sasaki, and S. Yunoki, *J. Mater. Chem. C*, 2017, **5**(10), 2488–2503.

[44] J. L. Hart, K. Hantanasirisakul, A. C. Lang, B. Anasori, D. Pinto, Y. Pivak, J. T. van Omme, S. J. May, Y. Gogotsi, and M. L. Taheri, *Nat. Commun.*, 2019, **10**(1).

[45] B. Anasori, C. Shi, E. J. Moon, Y. Xie, C. A. Voigt, P. R. Kent, S. J. May, S. J. Billinge, M. W. Barsoum, and Y. Gogotsi, *Nanoscale Horizons*, 2016, **1**(3), 227–234.

[46] W. Sun, Y. Xie, and P. R. Kent, *Nanoscale*, 2018, **10**(25), 11962–11968.

[47] V. Kamysbayev, A. S. Filatov, H. Hu, X. Rui, F. Lagunas, D. Wang, R. F. Klie, and D. V. Talapin, *Science (80-. ).*, 2020, **369**(6506), 979–983.

[48] N. M. Caffrey, *Nanoscale*, 2018, **10**(28), 13520–13530.

[49] K. Maleski, C. E. Ren, M. Q. Zhao, B. Anasori, and Y. Gogotsi, *ACS Appl. Mater. Interfaces*, 2018, **10**(29), 24491–24498.

[50] T. B. Terriberry, D. F. Cox, and D. A. Bowman, *J. Comput. Chem.*, 2002, **26**, 313–319.

[51] R. F. W. Bader, *Atoms in Molecules: A Quantum Theory.*, Oxford University Press, Oxford, 1990.

[52] S. Zurita, J. Rubio-Martínez, and F. Illas, *Electrochim. Acta*, 1996, **41**(14), 2275–2283.

[53] M. López, F. Viñes, M. Nolan, and F. Illas, *J. Phys. Chem. C*, 2020, **124**(29), 15969–15976.

[54] K. Reuter and M. Scheffler, *Phys. Rev. B - Condens. Matter Mater. Phys.*, 2001, **65**(3), 035406.

[55] K. Reuter and M. Scheffler, *Phys. Rev. Lett.*, 2003, **90**(4), 046103.

[56] M. López, Á. Morales-García, F. Viñes, and F. Illas, nov , 2021, **11**(21), 12850–12857.

[57] T. Li, L. Yao, Q. Liu, J. Gu, R. Luo, J. Li, X. Yan, W. Wang, P. Liu, B. Chen, W. Zhang, W. Abbas, R. Naz, and D. Zhang, *Angew. Chemie - Int. Ed.*, 2018, **57**(21), 6115–6119.

[58] S. Y. Pang, Y. T. Wong, S. Yuan, Y. Liu, M. K. Tsang, Z. Yang, H. Huang, W. T. Wong, and J. Hao, *J. Am. Chem. Soc.*, 2019, **141**(24), 9610–9616.

[59] S. Yang, P. Zhang, F. Wang, A. G. Ricciardulli, M. R. Lohe, P. W. M. Blom, and X. Feng, *Angew. Chemie*, 2018, **130**(47), 15717–15721.

[60] A. R. Hind, S. K. Bhargava, and S. C. Grocott, *Colloids Surfaces A Physicochem. Eng. Asp.*, 1999, **146**(1-3), 359–374.

[61] H. Riazi, M. Anayee, K. Hantanasirisakul, A. A. Shamsabadi, B. Anasori, Y. Gogotsi, and M. Soroush, *Adv. Mater. Interfaces*, 2020, **7**(6), 1–8.

[62] M. Pourbaix, *Corrosion*, 1950, **6**(12), 395–404.

[63] P. Delahay, M. Pourbaix, and P. V. Rysselberghe, *J. Electrochem. Soc.*, 1951, **98**(2), 57.

[64] M. Pourbaix, *Atlas of Electrochemical Equilibria in Aqueous Solutions*, National Association of Corrosion Engineers, Houston, TX, 2n edition ed., 1974.

[65] H. A. Hansen, J. Rossmeisl, and J. K. Norskov, *Phys. Chem. Chem. Phys.*, 2008, **10**(25), 3722–3730.

[66] K. S. Exner, J. Anton, T. Jacob, and H. Over, *Electrochim. Acta*, 2014, **120**, 460–466.

[67] O. Vinogradova, D. Krishnamurthy, V. Pande, and V. Viswanathan, *Langmuir*, 2018, **34**(41), 12259–12269.

[68] K. S. Exner, *ChemElectroChem*, 2017, **4**(12), 3231–3237.

[69] J. Gan, F. Li, and Q. Tang, *J. Phys. Chem. Lett.*, 2021, **12**(20), 4805–4813.

[70] Y. Luo, G. F. Chen, L. Ding, X. Chen, L. X. Ding, and H. Wang, *Joule*, 2019, **3**(1), 279–289.

[71] M. Pandey and K. S. Thygesen, *J. Phys. Chem. C*, 2017, **121**(25), 13593–13598.

[72] D. Opalka, C. Scheurer, and K. Reuter, *ACS Catal.*, 2019, **9**(6), 4944–4950.

[73] D. Jin, L. R. Johnson, A. S. Raman, X. Ming, Y. Gao, F. Du, Y. Wei, G. Chen, A. Vojvodic, Y. Gogotsi, and X. Meng, *J. Phys. Chem. C*, 2020, **124**(19), 10584–10592.

[74] J. D. Gouveia, F. Viñes, F. Illas, and J. R. Gomes, *Phys. Rev. Mater.*, 2020, **4**(5), 1–9.

[75] A. Kurlov, E. B. Deeva, P. M. Abdala, D. Lebedev, A. Tsoukalou, A. Comas-Vives, A. Fedorov, and C. R. Müller, *Nat. Commun.*, 2020, **11**, 4920.

[76] J. Björk and J. Rosen, *Chem. Mater.*, 2021, **33**(23), 9108–9118.

[77] G. Gao, A. P. O'Mullane, and A. Du, *ACS Catal.*, 2017, **7**(1), 494–500.

[78] L. R. Johnson, S. Sridhar, L. Zhang, K. D. Fredrickson, A. S. Raman, J. Jang, C. Leach, A. Padmanabhan, C. C. Price, N. C. Frey, A. Raizada, V. Rajaraman, S. A. Saiprasad, X. Tang, and A. Vojvodic, *ACS Catal.*, 2020, **10**(1), 253–264.

[79] M. Ashton, N. Trometer, K. Mathew, J. Suntivich, C. Freysoldt, S. B. Sinnott, and R. G. Hennig, *J. Phys. Chem. C*, 2019, **123**(5), 3180–3187.

[80] C. Zhan, W. Sun, Y. Xie, D. E. Jiang, and P. R. Kent, *ACS Appl. Mater. Interfaces*, 2019, **11**(28), 24885–24905.

[81] M. López, K. S. Exner, F. Viñes, and F. Illas, *Adv. Theory Simulations*, 2022, p. 2200217.

[82] Y. Li, W. Liu, Z. Zhang, X. Du, L. Yu, and Y. Deng, *Commun. Chem.*, 2019, **2**(1), 1–9.

[83] X. Gao, H. Zhang, Q. Li, X. Yu, Z. Hong, X. Zhang, C. Liang, and Z. Lin, *Angew. Chemie - Int. Ed.*, 2016, **55**(21), 6290–6294.

[84] J. Wang, Y. Gao, D. Chen, J. Liu, Z. Zhang, Z. Shao, and F. Ciucci, *ACS Catal.*, 2018, **8**(1), 364–371.

[85] P. Du and R. Eisenberg, *Energy Environ. Sci.*, 2012, **5**(3), 6012–6021.

[86] J. N. Hansen, H. Prats, K. K. Toudahl, N. Mørch Secher, K. Chan, J. Kibsgaard, and I. Chorkendorff, *ACS Energy Lett.*, 2021, **6**(4), 1175–1180.

[87] S. J. Gutić, A. S. Dobrota, E. Fako, N. V. Skorodumova, N. López, and I. A. Pašti, *Catalysts*, 2020, **10**(3), 290.

[88] M. Tahir, L. Pan, F. Idrees, X. Zhang, L. Wang, J. J. Zou, and Z. L. Wang, *Nano Energy*, 2017, **37**(May), 136–157.

[89] B. Samanta, Á. Morales-García, F. Illas, N. Goga, J. A. Anta, S. Calero, A. Bieberle-Hütter, F. Libisch, A. B. Muñoz-García, M. Pavone, and M. Caspary Toroker, *Chem. Soc. Rev.*, 2022, pp. 3794–3818.

[90] J. K. Nørskov, T. Bligaard, A. Logadottir, J. R. Kitchin, J. G. Chen, S. Pandelov, and U. Stimming, *J. Electrochem. Soc.*, 2005, **152**(3), J23.

[91] C. Ling, L. Shi, Y. Ouyang, and J. Wang, *Chem. Mater.*, 2016, **28**(24), 9026–9032.

[92] Z. Kang, M. A. Khan, Y. Gong, R. Javed, Y. Xu, D. Ye, H. Zhao, and J. Zhang, *J. Mater. Chem. A*, 2021, **9**(10), 6089–6108.

[93] P. Hou, Y. Tian, D. Jin, X. Liu, Y. Xie, F. Du, and X. Meng, *J. Phys. D. Appl. Phys.*, 2022, **55**(46).

[94] K. S. Exner and H. Over, *Acc. Chem. Res.*, 2017, **50**(5), 1240–1247.

[95] P. Lindgren, G. Kastlunger, and A. A. Peterson, *ACS Catal.*, 2020, **10**(1), 121–128.

[96] R. Kronberg and K. Laasonen, *ACS Catal.*, 2021, **11**(111), 8062–8078.

[97] Y. Yoon, A. P. Tiwari, M. Choi, T. G. Novak, W. Song, H. Chang, T. Zyung, S. S. Lee, S. Jeon, and K. S. An, *Adv. Funct. Mater.*, 2019, **29**(30), 1903443.

ACS Catalysis

pubs.acs.org/acscatalysis Research Article

# Thermodynamics and Kinetics of Molecular Hydrogen Adsorption and Dissociation on MXenes: Relevance to Heterogeneously Catalyzed Hydrogenation Reactions

Martí López, Ángel Morales-García, Francesc Viñes, and Francesc Illas*

Cite This: ACS Catal. 2021, 11, 12850−12857 Read Online

ACCESS | Metrics & More | Article Recommendations | Supporting Information

**ABSTRACT:** The interaction of molecular hydrogen with a series of 28 two-dimensional (2D) carbides and nitrides, known as MXenes, has been studied by means of periodic density functional calculations. This study shows that trends in atomic and molecular adsorption energies can be rationalized in terms of the electrostatic potential above the surface site and the Bader charge on the surface metal atoms. For all systems, molecular hydrogen is found to dissociate with almost negligible barriers, meaning that at low temperature the MXene surface will be passivated by adsorbed atomic hydrogen. The conditions at which the MXene surface is partly covered and, hence, able to participate in hydrogenation reactions are investigated by means of ab initio thermodynamics and phase diagrams derived from microkinetic simulations. The first provide the equilibrium conditions for a given H coverage on the MXene of interest, whereas the second provides the conditions at which a given configuration is reachable at the working conditions. For fast enough processes, both approaches necessarily lead to the same result, but this may differ when high energy barriers are involved, as it the case here for the H adatoms recombination step. With this suite, we show that $Fe_2C$, $W_2N$, and $Mo_2C$ are promising hydrogenation catalysts. This work serves as a first step toward the rational design and implementation of MXene-based hydrogenation catalysts.

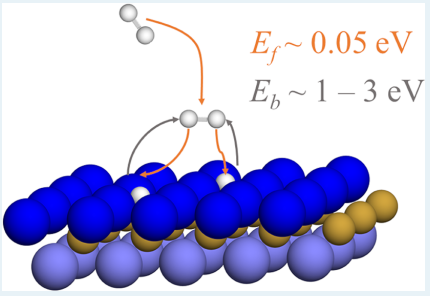


**KEYWORDS:** *MXenes, descriptor-based analysis, microkinetic simulations, hydrogenation, heterogeneous catalysis.*



## 1. INTRODUCTION

The new family of two-dimensional (2D) transition metal carbides and nitrides, termed MXenes, is attracting an increasing interest in materials science because of their new, tunable, and unexpected properties.[1−4] These new materials exhibit an outstanding performance in several applications involving batteries,[5,6] supercapacitors,[7] the electrochemical hydrogen evolution,[8,9] $CO_2$ abatement technologies,[10−12] heterogeneous catalysis,[13−17] and antibacterial activity,[18] just to name a few. MXenes are synthesized following a top-down approach starting from bulk MAX phases as precursors, where M is an early transition metal, A is typically Al or Si, and X is either C or N. In the MXene synthesis, the A component of the MAX phase is etched, generally using hydrofluoric acid (HF), with a subsequent sonication step to separate the as-produced 2D MXene layers.[19,20]

The thus-synthesized MXenes mainly exhibit the (0001) basal surface, which is structurally equivalent to the highly unstable and hard-to-prepare (111) surface of the corresponding bulk rock-salt transition metal carbides (TMCs) and nitrides (TMNs) single crystals.[21] Depending on the synthesis conditions, the MXene surfaces are covered with a variety of chemical species, most often -F, -O, and/or −OH. In the MXene literature, these surface terminations are usually denoted as $T_x$. Not surprisingly, the resulting MXene surface chemistry is heavily influenced by the synthesis conditions, that is, the MAX precursor, the solvent, and the used etchant agent.[22,23] Yet, recent work has shown that $T_x$ terminations can be removed by combining high-temperature treatments with the subsequent hydrogenation of persistent -O groups,[10] which opens new avenues to the experimental study of the chemistry of bare MXene surfaces. Also, a new synthesis route has been reported using alkali metal halides as etchants that leads to MXenes with not so strongly bonded halide ($T_x$ = -Cl, -Br) terminations. This constitutes another pathway toward pristine MXenes[24] and their use in numerous applications.[1,25−27]

Despite several promising applications,[25,28−32] and a salient ability to activate carbon dioxide ($CO_2$),[11,12] the rational selection criteria to choose a given MXene as a catalyst for a specific reaction, based for instance on descriptors determined

Received: July 13, 2021
Revised: September 9, 2021
Published: October 8, 2021




https://doi.org/10.1021/acscatal.1c03150
ACS Catal. 2021, 11, 12850−12857

by their composition and/or electronic structure, remains elusive. The difficulty in finding reactivity descriptors for MXenes can be anticipated from their quite larger affinity for $CO_2$ compared with water ($H_2O$)[11,14] a surprising finding given the larger stability and lower chemical activity of $CO_2$ compared with $H_2O$.

To start addressing this challenge and to spur additional studies, we focus on the adsorption and dissociation of molecular hydrogen over 28 bare $M_2X$ MXenes (M = Sc, Y, La, Ti, Zr, Hf, V, Nb, Ta, Cr, Mo, W, Mn, and Fe; X = C, N) by an interplay of first-principles calculations, ab initio thermodynamics, and microkinetic modeling. These tools allowed us to build not only phase diagrams corresponding to the most stable (more exergonic) surface hydrogen coverage situations but also to predict which of the possible stable surface structures can be kinetically reachable under realistic reaction conditions. In particular, we determine the conditions leading to the catalytically interesting region at which MXenes are not fully covered by atomic hydrogen and, hence, would efficiently operate in hydrogenation reactions, involving, for example, $CO_2$ hydrogenation, wherein a harmful greenhouse gas is converted to methanol or other useful chemicals while contributing to its abatement from the atmosphere,[33,34] or, to name another industrially relevant reaction, in ammonia synthesis.[14] In summary, we show here how combining thermodynamic and kinetic arguments could be useful to predict the conditions at which MXenes can be useful for hydrogenation reactions. We must point out that this constitutes a necessary but not sufficient condition. For the possible favorable cases, the particular hydrogenation reaction would need to be investigated in detail, whereas for the unfavorable ones, this can be directly skipped. Note also that the present analysis can be extended to other catalysts and to different environments.

## 2. COMPUTATIONAL DETAILS

Periodic density functional theory (DFT) calculations were carried employing the Vienna ab initio simulation package (VASP) code.[35] The broadly used Perdew−Burke−Ernzerhof (PBE) functional[36] was chosen to account for exchange and correlation effects, whereas dispersion interactions were included through Grimme's D3 approach.[37] The valence electron density was expanded using a plane-wave basis set with a cutoff kinetic energy of 415 eV, and the effect of the core electrons on the valence density was described through the projector augmented wave (PAW) method[38] as implemented in VASP.[39] The structural optimizations were considered converged when forces acting on atoms were below 0.01 eV $Å^{-1}$. The threshold for electronic energy convergence was set to $10^{-5}$ eV. The tetrahedron smearing method with Blöchl corrections was used in the calculations, with a 0.2 eV width, although the final total energies were always extrapolated to 0 K (no smearing). An optimal $\Gamma$-centered 5×5×1 **k**-point grid was used to sample the Brillouin zone for numerical integration in the reciprocal space. This computational setup, successfully used in previous works,[11,12,15] delivers converged results close to chemical accuracy (i.e., below ∼0.04 eV). For selected cases, spin polarization was accounted for, as described in more detail in the next section.

Adsorption sites for H and $H_2$ adsorption were sampled on a $p(3\times3)$ $M_2C(0001)$ surface supercell, see Figure 1, exposing ABC stacking of the atomic layers as in the parent MAX phases. The slabs are separated by a vacuum layer of at least 10 Å to avoid interaction between the periodically repeated images in the [0001] direction. The possible surface sites were sampled for both H adatoms and the $H_2$ molecule and initially placed ∼2 Å from the surface plane. In the case of $H_2$, several initial orientations were also considered. The corresponding structures were then fully relaxed. The adsorption energy, $E_{ads}^{H_x}$, for either the H adatoms ($x$ = 1) or the $H_2$ molecule ($x$ = 2) was estimated as

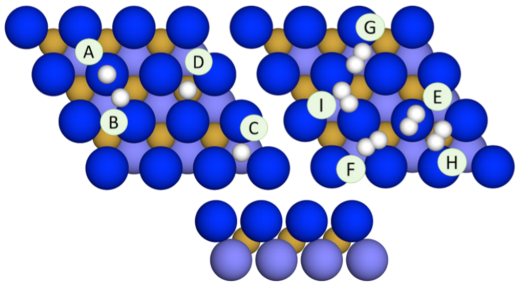


**Figure 1.** Top (upper images) and side (lower image) views of a $M_2X$ (0001) surface $p(3\times3)$ supercell. Metal atoms at the top and bottom layers are represented by bright and light blue spheres, respectively, while C/N atoms are represented by light brown spheres, and H atoms are shown in white. The main high-symmetry surface sites for H atoms and perpendicular $H_2$ adsorption (left upper image) are top (A), bridge (B), hollow M (C), and hollow X (D), having either one M or X atom below, respectively. For $H_2$ adsorbed parallel to the $M_2X(0001)$ surface (right upper image), the sampled sites are top (E), XM bridge (F), hollow M (G), hollow X (H), and MM bridge (I).

$$E_{ads}^{H_x} = E_{H_x/MXene} - \left(E_{MXene} + \frac{x}{2}E_{H_2}\right) \quad (1)$$

where $E_{H_x/MXene}$ is the energy of the surface with H* or $H_2$*, this is, $x$ = 1 or 2, respectively, $E_{MXene}$ is the energy of the pristine MXene surface, and $E_{H_2}$ is the energy of $H_2$ in the gas phase. Note that $E_H$ is obtained with respect to $\frac{1}{2}E_{H_2}$. With these conventions, the adsorption energy is negative for an exothermic process. The lists of $E_{ads}^{H}$ and $E_{ads}^{H_2}$ values including zero-point energy (ZPE) contributions are reported in Tables S1 and S2 of the Supporting Information (SI), respectively.

The search for the transition states (TSs) of $H_2$ dissociation was performed using climbing-image nudged elastic band (CI-NEB) and dimer methods.[40,41] The thus located TS structures were characterized by frequency analysis ensuring that they exhibit just one imaginary frequency along the reaction pathways. The initial atomic configuration used to locate TS structures was the most stable adsorption configuration of $H_2$.

In addition, *ab initio* thermodynamics was employed to build phase diagrams following the method described by Reuter and Scheffler.[42,43] Details on the procedure can be found in a recent article by some of us dealing with the interaction between hydrogen and molybdenum carbides surfaces.[44] The thermodynamic study is complemented with microkinetic analysis,[45] where the Hertz-Knudsen equation is used to determine $H_2$ gas adsorption/desorption rates, in which transition-state theory was invoked to estimate the rates for the dissociation/recombination $H_2$* + * ↔ H* + H*


https://doi.org/10.1021/acscatal.1c03150
ACS Catal. 2021, 11, 12850−12857

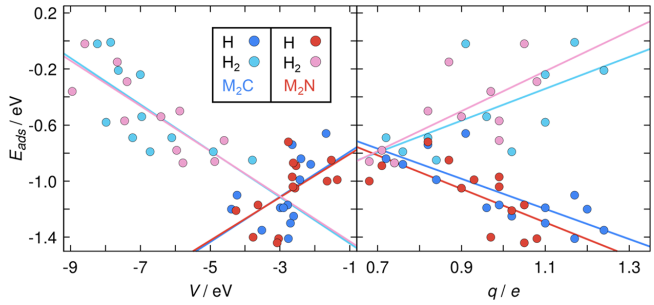


**Figure 2.** Trends in the adsorption energies of H* and $H_2$* with respect to the electrostatic potential, $V$, computed 1.5 Å above the surface plane (left), and with respect to the Bader charges, $q$, on the surface metal M atoms. Values for MCenes/MNenes are represented by blue/red circles, where the dark/light filled circles correspond to $E_{ads}^{H}$ and $E_{ads}^{H_2}$, respectively. Linear fits and related statistical data are provided in Table S8 in the Supporting Information.

elementary surface reaction steps. The microkinetic simulations were carried out using the MKMCXX program,[46] employing an $H_2$ gaseous environment with an explored total pressure ranging from 100 $\mu$bar to 10 bar. Additional details and results on temperature ranges for a coverage of free sites from 0.2 to 0.6 monolayers (ML) are given in the SI.

## 3. RESULTS AND DISCUSSION

**3.1. Atomic and Molecular Hydrogen Adsorption.** We start with this section analyzing the atomic H adsorption on the different MXenes listed in Table S3 of the Supporting Information. In all cases, the most favorable adsorption site is hollow M site ($H_M$) —site C in Figure 1. There is the exception on $La_2C$, where hollow X ($H_x$) is preferred —site I in Figure 1. Geometry optimization starting with H placed above other sites such as bridge (B) and top (T) sites, labeled B and A in the leftmost panel of Figure 1, either lead to the described most stable situation or converged to situations with higher adsorption energies. Shortly, hollow sites accommodate H adatoms. Furthermore, spin-polarization-based calculations were explored for those cases previously reported to exhibit spin-polarized ground states such as $Ti_2C$,[47] $Zr_2C$,[47] $Cr_2N$,[48,49] $Mn_2C$,[50] or $Mn_2N$.[50] However, a systematic study of the different possible spin solutions using functionals not suffering from the well-known limitations of the GGA and GGA+U approaches is still lacking and out of the scope of the present study. Nevertheless, we observed that in most of the explored cases, spin polarization just slightly stabilizes bare MXene surfaces and has no effect on the energy of the H covered MXene. Consequently, it modifies $E_{ads}^{H}$ by less than 0.1 eV. This is because, except for $Fe_2X$ and $Mn_2X$, the presence of adsorbed hydrogen quenches the magnetic moments resulting in an electronic ground state which does not exhibit any spin polarization. Therefore, for the analysis of trends in subsequent sections, spin-polarized results can be safely neglected except, obviously, for the $Fe_2X$ and $Mn_2X$ MXenes. Attending to the results compiled in Table S3 of the Supporting Information, it is difficult to capture a trend in the adsorption energies. In general, the adsorption of atomic H runs between −0.66 and −1.44 eV depending on the MXene composition. The adsorption energy is slightly less exothermic when going down through the groups, except for $Hf_2X$ where the adsorption is more favorable than for $Zr_2X$.

Regarding the $H_2$ molecular adsorption, see Table S4 of the Supporting Information, starting with $H_2$ perpendicular to the surface leads to a systematic physisorption with low $E_{ads}^{H_2}$ values up to −0.09 eV and H−H bond lengths around 0.76 Å, close to the $H_2$ bond length in vacuum of 0.75 Å. Conversely, stronger interactions in the range of −0.15 and −0.90 eV, see Table S4 of the Supporting Information, are observed for $H_2$ adsorption parallel to the surface above top (T) sites (indicated as E in the rightmost panel of Figure 1) locating the mass center of the molecule over such site. There are few cases ($Sc_2C$, $Sc_2N$, $Ti_2C$, $Ti_2N$, $Mn_2C$, and $Mn_2N$) with spontaneous dissociation upon relaxation. Other sites were tested, but the molecular dissociation was always achieved after optimization. Focusing on $d^2$-, $d^3$-, and $d^4$-metals, $E_{ads}^{H_2}$ is more exothermic moving along the series.

**3.2. Molecular Hydrogen Dissociation and Recombination.** In all cases, the energy barriers for molecular hydrogen dissociation, computed from the energy difference corresponding to the molecular adsorption configuration and that of the properly characterized transition state, are very low, see Table S5 of the Supporting Information. The molecular hydrogen tends to easily split into H* + H*. Only $Zr_2C$ and $Hf_2C$ feature energy barriers above 0.10 eV, and for the rest of MXenes, $H_2$ dissociation can be safely considered barrierless. The reaction energy computed as the difference between the energy of the MXene with two H* and that of the MXene with $H_2$* is compiled in Table S6 of the Supporting Information. The analysis of the results clearly indicates that the H* + H* scenario is energetically more favorable than the $H_2$* one.

To further inspect the dissociation reaction step, two different 2H* geometries have been explored, one with both H* at two $H_M$ vicinal positions, which is the situation just after dissociation, and the other one with each H* at the farthest separated $H_M$ sites in the supercell, which corresponds the most stable situation. The results listed in Table S7 indicate that there are no noticeable differences between them. Besides, comparing the adsorption energy per H adatom in any of the two (close or far) situations with the values corresponding to a single H adsorption, indicates that the lateral interactions between H* are negligible. Thus, we preliminarily conclude that MXenes readily dissociate hydrogen and the process does not strongly depend on the M or X components of the MXenes. A consequence of this reactivity is that the MXene surface will be readily covered by hydrogen and, hence,


https://doi.org/10.1021/acscatal.1c03150
ACS Catal. 2021, 11, 12850−12857

passivated, as the resulting system has no free active sites for other molecules that, eventually, could be hydrogenated. Therefore, determining the conditions at which the MXene surface is eventually partially covered becomes a real need for further applications in catalysis. This involves two well differentiated situations, namely, the conditions at which a thermodynamic equilibrium exists with the MXene surface partially covered and the conditions where such a situation is kinetically reachable during a reasonable contact time in between $H_2$ and the MXene catalyst. Obviously, this also involves determining which of the explored MXenes would exhibit the desired features.

**3.3. Trends in Adsorption Energies.** To rationalize the trends in $E_{ads}$, two possible descriptors were analyzed. These are the MXene electrostatic potential above the surface ($V$) and the surface metal charge ($q$). The $V$ values were obtained using the Vaspview software[51] and computed at 1.5 Å above the surface Top and Hollow M positions. No significant variations in the trends were found for the $V$ values at different heights. The net charges over the metal atoms were computed following Bader *Atoms-in-Molecules* analysis of the total electron density.[52] The results are summarized in Figure 2, while the calculated data appear in Tables S8 and S9 of the Supporting Information for $V$ and $q$, respectively. We must point out that even if the correlation between $E_{ads}$ and both descriptors is not good enough, they provide meaningful trends and a possible way to explain the differences in $E_{ads}$ of H* and $H_2$* on MXenes.

Large negative $V$ values indicate sites with more favorable H adsorption and likely stronger Pauli repulsion for molecular $H_2$* species.[53] The same view is obtained from the MXene surface metal Bader charge, $q$, thus providing another useful descriptor as shown on related transition metal carbide surfaces.[54,55] This descriptor shows that the more oxidized the metal, the stronger $E_{ads}$ of H, while negative $q$ would favor $H_2$ physisorption because of the enhancement of dispersion interactions. The charge on the metal sites where H* and $H_2$* present comparable binding strengths and, hence, can be optimal for hydrogenation purposes, is around 0.7−0.8 $e$, corresponding to Cr, Mo, W, Mn, and Fe, see Table S9. All in all, the two descriptors provide consistent trends and help rationalizing the opposing slopes for H* and $H_2$* adsorption. The data corresponding to the linear fits for the plots in Figure 2 are reported in Table S10 of the Supporting Information. The mean absolute errors (MAEs) between the linear fits and the calculated points in Figure 2 are comparable for the two descriptors and in all cases below 0.20 eV, which is an accepted value for the accuracy of DFT at the GGA level. The linear fits relating adsorption energies and either $V$ or $q$ in Table S10 display a clear, yet not quantitative, trend. This provides an indication that these descriptors can be used to make educated guesses of hydrogen adsorption energies in other MXenes and, perhaps, of other adsorbates, although this remains to be proven.

Before ending this section, we want to highlight that, while the hydrogen bonding at the explored MXenes surfaces cannot be described as governed by electrostatics, the electrostatic potential acts as the driving force determining the active sites as shown by some of us for atomic H at several low Miller indexes surfaces Pt surfaces.[53] Thus, the electrostatic potential initiates the interaction, but once the hydrogen is anchored, the short-range interactions govern the chemical bond.

**3.4. Thermodynamic versus Kinetic Phase Diagrams.** The analysis of the results corresponding to the atomic and molecular adsorption of hydrogen discussed in the previous sections reveals that the MXenes with M = Cr, Mo, W, Mn, and Fe, have comparable adsorption energies for H and $H_2$ and are, thus, promising good hydrogenation catalysts. This information is already found from the $V$ and $q$ descriptors as pinpointed in Figure 2, as these MXenes are those close to the crossover between the lines with opposing slope. Nevertheless, the easy dissociation of molecular hydrogen and the large exothermicity of this elementary step for most of the MXenes indicate that the MXene surface will be readily covered by atomic hydrogen thus impeding hydrogenation reactions, as no free sites would be available to the molecule to be hydrogenated. Thus, it is important to explore the conditions where the MXene surface is only partially covered by H* atoms. The atomistic thermodynamics formalism of Reuter et al.[42,43] has been used to build a phase diagram with the relative free energy of well-ordered phases as a function of H* coverage. In Figure 3 we present the phase diagram for $W_2N$

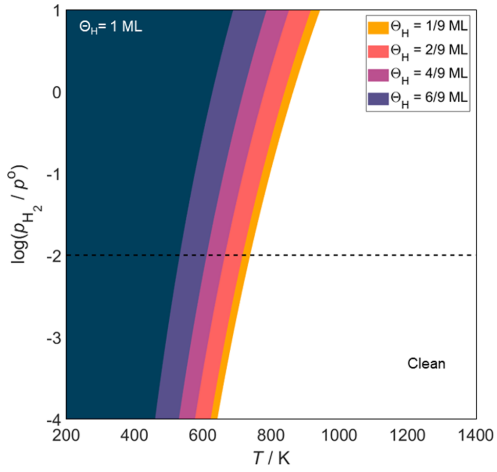


**Figure 3.** Thermodynamic phase diagram as a function of $T$ and $p_{H_2}$ for $W_2N$ (0001) MXenes including different atomic hydrogen coverages, $\theta_H$. It runs from 0 to 1 monolayer (ML). The black dashed line corresponds to a reference $p_{H_2}$ of 10 mbar.

taken as a representative of this set of possibly good candidates. Indeed, Figure 3 shows that even at relatively high $H_2$ partial pressure, the surface is partly covered or even clean at temperatures in the 400−600 K and, therefore, provides support to the hypothesis that these MXenes are likely to perform well in hydrogenation reactions. For comparison, the phase diagrams for $Fe_2C$, a second good candidate for hydrogenation catalyst, and also for $Ti_2C$ and $Ti_2N$, likely to be easily deactivated, are reported in section S5 of the Supporting Information. Note that the phase diagrams for $Ti_2C$ and $Ti_2N$ exhibit an abrupt transition from fully occupied to bare surface which, as predicted, indicates that these represent the worst scenario for hydrogenation.

The ab initio thermodynamic approach is undoubtedly extremely useful to determine the relative thermodynamic stability of surfaces with different surface coverage. However,


https://doi.org/10.1021/acscatal.1c03150
ACS Catal. 2021, 11, 12850−12857

being a purely thermodynamic approach, it does not incorporate any kinetic consideration. For processes reaching the thermodynamic equilibrium in a very fast way, the approach will provide meaningful information. However, for process involving rather large barriers, as is the case for H* + H* recombination leading to $H_2$* which eventually desorbs, the kinetic aspects may introduce noticeable changes. Here, one must advert that the kinetic aspects are not especially relevant for $H_2$ dissociation because the activation barriers are always very low. However, their role is crucial in the recombination step leading to $H_2$ formation that eventually desorbs, thus freeing some surface sites. The complete set of energy barriers for the dissociation and recombination steps is included in Table S5 of the Supporting Information.

To take a step forward in this direction, we propose a new approach in which microkinetic simulations are used to build kinetic, instead of thermodynamic, phase diagrams aiming to determine the reaction temperature, $T$, and hydrogen partial pressure, $p_{H_2}$ at which the $M_2X(0001)$ MXene surfaces will be partially covered. The microkinetic simulations make use of rates derived either from kinetic gas theory via the Hertz-Knudsen equation ($H_2$ adsorption and desorption) or from statistical thermodynamics via transition-state theory ($H_2$* dissociation and H* + H* recombination) as described in detail in Section S1 of the Supporting Information. The results for $Ti_2N$, $Ti_2C$, $Fe_2C$, and $W_2N$ at different $p_{H_2}$ are displayed in Figure 4. This choice is to include MXene with an excessive

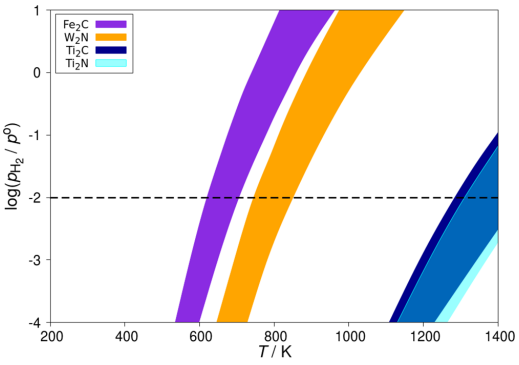


**Figure 4.** Kinetic phase diagrams as a function of $T$ and $p_{H_2}$ for $Fe_2C$, $W_2C$, $Ti_2C$, and $Ti_2N$ MXenes derived from microkinetic simulations. The colored regions denote conditions with a coverage of free sites between 0.2 (rightmost line of each region) and 0.6 ML (leftmost line of each region), while the rest is covered with H adatoms. Notice that the overlapping region between $Ti_2C$ (dark blue) and $Ti_2N$ (cyan) is colored in light blue. The black dashed line corresponds to a reference $p_{H_2}$ of 10 mbar.

affinitive for H adatoms ($Ti_2N$ and $Ti_2C$) and two of the aforementioned promising MXene catalysts for hydrogenation reactions ($Fe_2C$ and $W_2N$). These MXenes do also constitute limiting cases for $H_2$ formation barriers by H* + H* recombination.

The highlighted regions in Figure 4 denote situations where the coverage of free sites is 0.2−0.6 monolayers (ML) and, consequently, with a H* coverage in the range of 0.4−0.8 ML, see section S11 of the Supporting Information. Notice that the sum of coverages of the possible surface species, $\theta_* + \theta_H + \theta_{H_2} = 1$, and no population of $H_2$* moieties is detected in the microkinetic simulations. Despite the high upper limit for H* coverage of 0.8 ML, the thermodynamics and kinetics of hydrogen recombination were estimated at the dilute limit, that is at low H* coverage. This is justified because lateral interactions between adsorbed hydrogen atoms were found to be negligible, see Table S7 of the Supporting Information. In line with the predictions of the descriptor-based analysis, the smallest barriers correspond to $Fe_2C$ and $W_2N$, whereas $Ti_2N$ has one of the largest $H_2$ formation barriers, see Section S5 in the Supporting Information. Besides, $Ti_2C$ is included because it can be considered a prototypical MXene with reactivity close to the first synthesized, and nowadays, broadly used $Ti_3C_2$ MXene.[21] We note that the highest recombination barrier corresponds to $Hf_2C$, yet it is excessively high to be of practical use. In fact, in the presence of oxygen, $Hf_2C$ decomposes into $CO_2$ and the corresponding bulk HfC before reaching the target surface coverage conditions.[56,57]

From the microkinetic analysis for bare Ti-based MXenes, we observe that H adsorption is strong enough to keep the surface fully passivated even above 1200 K for most $p_{H_2}$ conditions, an upper bound for $Ti_2X$ thermal stability.[58] Therefore, bare $Ti_2C$ and $Ti_2N$ MXenes will presumably not be good hydrogenation catalysts, although the presence of other surface species such as -O or -F might change this conclusion. Indeed, Persson et al.[10] used 8 mbar $H_2$ at 973 K to experimentally clean $Ti_3C_2$ surfaces, hydrogenating the surface -O moieties, close to the values for $Ti_2C$ obtained here, see Figure 4. This also indicates that the working temperature can be lowered using smaller $p_{H_2}$. Interestingly, at $p_{H_2}$ = 10 mbar, bare $Fe_2C$ displays a range of temperatures of 620−707 K to meet the target coverages. As Fe is one of the most common and affordable metals on the Earth's crust, Fe-containing carbide MXenes are good candidates for hydrogenation reactions. Since MXene thickness has little influence on their surface chemistry,[21] $Fe_2C$ and $Fe_2C_3$ MXenes probably exhibit similar reactivities toward $H_2$. Note, however, that these MXenes have not been experimentally synthesized yet, and that the effect of surface terminations should be explored.

Although $W_2N$ is slightly worse than $Fe_2C$, with working temperatures ranging from 745 to 852 K at $p_{H_2}$ = 10 mbar, it has already been synthesized.[59] Here it is worth comparing the predictions from the ab initio thermodynamics and the kinetic phase diagrams. Qualitatively, both approaches lead to a similar description in the sense that heating at rather high temperatures will lead to a partial coverage of atomic hydrogen and, hence, to good candidates for hydrogenation reactions. However, the predicted temperature at which the $W_2N$ surface starts to display free sites is significantly larger when kinetic phase diagrams are employed; ∼700 K versus ∼400 K as predicted from the ab initio thermodynamics.

The analysis of the kinetic phase diagrams highlights the role of the energetic barrier for $H_2$ formation in determining the conditions for MXenes to be active hydrogenation catalysts and these are significantly different from those predicted from thermodynamic considerations only. Considering the thermal stability limit for MXenes, a threshold on the $H_2$ formation barrier of ∼2.50 eV can be set, based on the fact that $Zr_2C$ (2.56 eV) has a range of temperatures between 1120 and 1259 K at 10 mbar of $H_2$, already above typical MXene decomposition temperatures.


https://doi.org/10.1021/acscatal.1c03150
ACS Catal. 2021, 11, 12850−12857

## 4. CONCLUSIONS

A systematic theoretical study has been presented on the basis of DFT-D3 calculations for a number of MXene surface models. We disclosed here the trends in the interaction between H and $H_2$ with the $M_2X$ materials by analyzing their description through the electrostatic potential above the surface and the surface metal Bader charges. For these two descriptors, the trends in H and $H_2$ adsorption are opposite, the former being modulated by electrostatic factors and the latter governed by dispersive forces.

Further analysis with ab initio thermodynamics and microkinetic modeling approaches shows that $Fe_2C$, $W_2N$, and $Mo_2C$ are promising hydrogenation catalysts in the sense that the conditions at which the surface of these MXenes is only partially covered by hydrogen, are within the range of thermal stability of these materials and are similar to those used commonly in the chemical industry. Nevertheless, it is important to point out that the predictions from ab initio thermodynamics lead to temperature conditions milder than those predicted from the newly presented kinetic phase diagrams that account for the energy barriers required for atomic hydrogen to recombine and desorb. These differences are likely to be important in other systems as well where the thermodynamic equilibrium will take longer than the chemical reactions that the material of interest is supposed to catalyze.

We note that, in agreement with the predictions in the present work, $W_2N$ was indeed predicted as a potential catalyst for ammonia synthesis,[14] which is an important industrial hydrogenation reaction. In addition, our results likely hold for MXenes involving more atomic layers, as thickness usually bears little effect on MXene surface chemistry.[21] Besides, the predictions made here are to be coupled with the reported favorable $CO_2$ activation on several MXenes[10,12] and experimentally confirmed in some cases, so as to find prospect catalysts for catalytic $CO_2$ reduction.

We hope our observations and specific combination of computational techniques foster further research on the subject and contribute to the elaboration of a quantitative, comprehensive, and data-driven theory of MXene-based catalysis. In particular, the present study calls for future experiments and further studies inspecting surface termination effects.

## ■ ASSOCIATED CONTENT

### Supporting Information

The Supporting Information is available free of charge at https://pubs.acs.org/doi/10.1021/acscatal.1c03150.

Microkinetic modeling and kinetic phase diagrams. Atomic and molecular hydrogen adsorption energies. Molecular hydrogen dissociation energy barrier and reaction energy. Descriptors. Phase diagrams for $Fe_2C$, $Ti_2C$ and $Ti_2N$ and selected results for kinetic phase diagrams (PDF)

## ■ AUTHOR INFORMATION


### Corresponding Author

**Francesc Illas** − *Departament de Ciència de Materials i Química Física & Institut de Química Teòrica i Computacional (IQTCUB), Universitat de Barcelona, Barcelona 08028, Spain;* orcid.org/0000-0003-2104-6123; Email: francesc.illas@ub.edu

### Authors

**Martí López** − *Departament de Ciència de Materials i Química Física & Institut de Química Teòrica i Computacional (IQTCUB), Universitat de Barcelona, Barcelona 08028, Spain*

**Ángel Morales-García** − *Departament de Ciència de Materials i Química Física & Institut de Química Teòrica i Computacional (IQTCUB), Universitat de Barcelona, Barcelona 08028, Spain;* orcid.org/0000-0003-0491-1234

**Francesc Viñes** − *Departament de Ciència de Materials i Química Física & Institut de Química Teòrica i Computacional (IQTCUB), Universitat de Barcelona, Barcelona 08028, Spain;* orcid.org/0000-0001-9987-8654

Complete contact information is available at: https://pubs.acs.org/10.1021/acscatal.1c03150


### Notes

The authors declare no competing financial interest.

## ■ ACKNOWLEDGMENTS

The authors thanks Dr. Federico Calle-Vallejo for many discussions and remarks. Financial support was provided by Spanish *Ministerio de Ciencia, Innovación y Universidades* (MICIUN) through grants RTI2018-095460-B-I00 and *María de Maeztu* MDM-2017-0767 and, in part, by *Generalitat de Catalunya* 2017SGR13 grant. We thank *Red Española de Supercomputación* (*RES*) for supercomputing resources (projects QCM-2018-1-0009, QCM-2018-3-0015). A.M.G. thanks MICIUN for a *Juan de la Cierva* (IJCI-2017-31979) research contract. M.L. thanks *Universitat de Barcelona* for an APIF predoctoral contract.

## ■ REFERENCES


(1) Anasori, B.; Lukatsaya, M. R.; Gogotsi, Y. 2D Metal Carbides and Nitrides (MXenes) for Energy Storage. *Nat. Rev. Mater.* **2017**, *2*, 16098.

(2) Chaudhari, N. K.; Jin, H.; Kim, B.; Baek, D. S.; Joo, S. H.; Lee, K. MXene: An Emerging Two-Dimensional Material for Future Energy Conversion and Storage Applications. *J. Mater. Chem. A* **2017**, *5*, 24564−24579.

(3) Gogotsi, Y.; Anasori, Y. The Rise of MXenes. *ACS Nano* **2019**, *13*, 8491−8494.

(4) VahidMohammadi, A.; Rosen, J.; Gogotsi, Y. The World of Two-Dimensional Carbides and Nitrides (MXenes). *Science* **2021**, *372*, eabf1581.

(5) Er, D.; Li, J.; Naguib, M.; Gogotsi, Y.; Shenoy, V. B. $Ti_3C_2$ MXene as a High Capacity Electrode Material for Metal (Li, Na, K, Ca,) Ion Bateries. *ACS Appl. Mater. Interfaces* **2014**, *6*, 11173−11179.

(6) Liang, X.; Garusch, A.; Nazar, L. F. Sulfur Cathodes Based on Conductive MXene Nanosheets for High-Performance Lithium-Sulfur Batteries. *Angew. Chem., Int. Ed.* **2015**, *54*, 3907−3977.

(7) Wang, X.; Kajiyama, S.; Iinuma, H.; Hosono, E.; Oro, S.; Moriguchi, I.; Okubo, M.; Yamada, A. Pseudocapacitance of MXene Nanosheets for High-Power Sodium-Ion Hybrid Capacitors. *Nat. Commun.* **2015**, *6*, 6544.

(8) Handoko, A. D.; Fredrickson, K. D.; Anasori, B.; Convey, K. W.; Johnson, L. R.; Gogotsi, Y.; Vojvodic, A.; She, Z. W. Tuning the Basal Plane Functionalization of Two-Dimensional Metal Carbides (MXenes) to Control Hydrogen Evolution Activity. *ACS Appl. Energy Mater.* **2018**, *1*, 173−180.

(9) Seh, Z. W.; Fredrickson, K. D.; Anasori, B.; Kibsgaard, J.; Strickler, A. L.; Lukatskaya, M. R.; Gogotsi, Y.; Jaramillo, T. F.; Vojvodic, A. Two-Dimensional Molybdenum Carbide (MXene) as an

Efficient Electrocatalyst for Hydrogen Evolution. *ACS Energy Lett.* **2016**, *1*, 589−594.
(10) Persson, I.; Halim, J.; Linds, H.; Hansen, T. W.; Wagner, J. B.; Näslund, L.; Darakchieva, V.; Palisaitis, J.; Rosen, J.; Persson, P. O. Å. 2D Transition Metal Carbides (MXenes) for Carbon Capture. *Adv. Mater.* **2018**, *31*, 1805472.
(11) Morales-Salvador, R.; Morales-García, Á.; Viñes, F.; Illas, F. Two-Dimensional Nitrides as Highly Efficient Potential Candidates for $CO_2$ Capture and Activation. *Phys. Chem. Chem. Phys.* **2018**, *20*, 17117−17124.
(12) Morales-García, Á.; Fernández-Fernández, A.; Viñes, F.; Illas, F. $CO_2$ abatement using two-dimensional MXenes carbides. *J. Mater. Chem. A* **2018**, *6*, 3381−3385.
(13) Li, N.; Chen, X.; Ong, W. J.; MacFarlane, D. R.; Zhao, X.; Cheetham, A. K.; Sun, C. Understanding of Electrochemical Mechanisms for $CO_2$ Capture and Conversion into Hydrocarbon Fuels in Transition-Metal Carbides (MXenes). *ACS Nano* **2017**, *11*, 10825−10833.
(14) Gouveia, J. D.; Morales-García, Á.; Viñes, F.; Gomes, J. R. B.; Illas, F. Facile Heterogeneously Catalyzed Nitrogen Fixation by MXenes. *ACS Catal.* **2020**, *10*, 5049−5056.
(15) Gouveia, J. D.; Morales-García, Á.; Viñes, F.; Gomes, J. R. B.; Illas, F. MXenes as Promising Catalysts for Water Dissociation. *Appl. Catal., B* **2020**, *260*, 118191.
(16) Wei, H.; Jiang, Q.; Ampelli, C.; Chen, S.; Perathoner, S.; Liu, Y.; Centi, G. Enhancing $N_2$ Fixation Activity by Converting $Ti_3C_2$ MXenes Nanosheets to Nanoribbons. *ChemSusChem* **2020**, *13*, 5614−5619.
(17) Slot, T. K.; Natu, V.; Ramos-Fernandez, E. V.; Sepúlveda-Escribano, A.; Barsoum, M.; Rothenberg, G.; Shiju, N. R. Enhancing catalytic epoxide ring-opening selectivity using surface modified $Ti_3C_2T_x$ MXenes. *2D Mater.* **2021**, *8*, 035003.
(18) Rasool, K.; Helal, M.; Ali, A.; Ren, C. E.; Gogotsi, Y.; Mahmoud, K. A. Antibacterial Activity of $Ti_3C_2T_x$ MXene. *ACS Nano* **2016**, *10*, 3674−3684.
(19) Naguib, M.; Mashtalir, O.; Carle, J.; Presser, V.; Lu, J.; Hultman, L.; Gogotsi, Y.; Barsoum, M. W. Two-Dimensional Transition Metal Carbides. *ACS Nano* **2012**, *6*, 1322−1331.
(20) Naguib, M.; Kurtoglu, M.; Presser, V.; Lu, J.; Niu, J.; Heon, M.; Hultman, L.; Gogotsi, Y.; Barsoum, M. W. Two-Dimensional Nanocrystals Produced by Exfoliation of $Ti_3AlC_2$. *Adv. Mater.* **2011**, *23*, 4248−4253.
(21) Morales-García, Á.; Mayans-Llorach, M.; Viñes, F.; Illas, F. Thickness Biased Capture of $CO_2$ on Carbide MXenes. *Phys. Chem. Chem. Phys.* **2019**, *21*, 23136−23142.
(22) Halim, J.; Cook, K. M.; Naguib, M.; Eklund, P.; Gogotsi, Y.; Rosen, J.; Barsoum, M. W. X-Ray Photoelectron Spectroscopy of Select Multi-layered Transition Metal Carbides (MXenes). *Appl. Surf. Sci.* **2016**, *362*, 406−417.
(23) Xie, Y.; Kent, P. R. Hybrid Density Functional Study of Structural and Electronic Properties of Functionalized $Ti_{n+1}X_n$ (X = C, N) Monolayers. *Phys. Rev. B: Condens. Matter Mater. Phys.* **2013**, *87*, 235441.
(24) Kamysbayev, V.; Filatov, A. S.; Hu, H.; Rui, X.; Lagunas, F.; Wang, D.; Klie, R. F.; Talapin, D. V. Covalent Surface Modifications and Superconductivity of Two-Dimensional Metal Carbide MXenes. *Science* **2020**, *369*, 979−983.
(25) Morales-García, Á.; Calle-Vallejo, F.; Illas, F. MXenes: New Horizons in Catalysis. *ACS Catal.* **2020**, *10*, 13487−13503.
(26) Li, Z.; Wu, Y. 2D Early Transition Metal Carbides (MXenes) for Catalysis. *Small* **2019**, *15*, 1804736.
(27) Handoko, A. D.; Steinmann, S. N.; Seh, Z. W. Theory-Guided Materials Design: Two-Dimensional MXenes in Electro- and Photocatalysis. *Nanoscale Horiz.* **2019**, *4*, 809−827.
(28) Ran, J.; Gao, G.; Li, F. T.; Ma, T. Y.; Du, A.; Qiao, S. Z. $Ti_3C_2$ MXene Co-Catalyst on Metal Sulfide Photo-Absorbers for Enhanced Visible-Light Photocatalytic Hydrogen Production. *Nat. Commun.* **2017**, *8*, 13907.
(29) Zhang, X.; Lei, J.; Wu, D.; Zhao, X.; Jing, Y.; Zhou, Z. A Ti-Anchored $Ti_2CO_2$ Monolayer (MXene) as a Single-Atom Catalyst for CO Oxidation. *J. Mater. Chem. A* **2016**, *4*, 4871−4876.
(30) Zhang, J.; Zhao, Y.; Guo, X.; Chen, C.; Dong, C.-L.; Liu, R.-S.; Han, C.-P. Y.; Li, Y.; Gogotsi, Y.; Wang, G. Single Platinum Atoms Immobilized on an MXene as an Efficient Catalyst for the Hydrogen Evolution Reaction. *Nat. Catal.* **2018**, *1*, 985−992.
(31) Zhao, D.; Chen, Z.; Yang, W.; Liu, S.; Zhang, X.; Yu, Y.; Cheong, W. C.; Zheng, L.; Ren, F.; Ying, G.; Cao, X.; Wang, D.; Peng, Q.; Wang, G.; Chen, C. MXene ($Ti_3C_2$) Vacancy-Confined Single-Atom Catalyst for Efficient Functionalization of $CO_2$. *J. Am. Chem. Soc.* **2019**, *141*, 4086−4093.
(32) Zhang, X.; Zhang, Z.; Li, J.; Zhao, X.; Wu, D.; Zhou, Z. $Ti_2CO_2$ MXene: A Highly Active and Selective Photocatalyst for $CO_2$ Reduction. *J. Mater. Chem. A* **2017**, *5*, 12899−12903.
(33) Ye, R. P.; Ding, J.; Gong, W.; Argyle, M. D.; Zhong, Q.; Wang, Y.; Russell, C. K.; Xu, Z.; Russell, A. G.; Li, Q.; Fan, M.; Yao, Y. G. $CO_2$ Hydrogenation to High-Value Products via Heterogeneous Catalysis. *Nat. Commun.* **2019**, *10*, 5698.
(34) International Energy Agency (IEA). *Putting $CO_2$ to Use*; IEA: Paris, France, 2019
(35) Kresse, G.; Furthmüller, J. Efficient Iterative Scheme for Ab Initio Total-Energy Calculations Using a Plane-Wave Basis Set. *Phys. Rev. B: Condens. Matter Mater. Phys.* **1996**, *54*, 11169.
(36) Perdew, J. P.; Burke, K.; Ernzerhof, M. Generalized Gradient Approximation Made Simple. *Phys. Rev. Lett.* **1996**, *77*, 3865−3868.
(37) Grimme, S.; Antony, J.; Ehrlich, S.; Krieg, S. A Consistent and Accurate Ab Initio Parametrization of Density Functional Dispersion Correction (DFT-D) for the 94 Elements H-Pu. *J. Chem. Phys.* **2010**, *132*, 154104.
(38) Blöch, P. E. Projector augmented-wave method. *Phys. Rev. B* **1994**, *50*, 17953.
(39) Kresse, G.; Joubert, D. From Ultrasoft Pseudopotentials to the Projector Augmented-Wave Method. *Phys. Rev. B: Condens. Matter Mater. Phys.* **1999**, *59*, 1758−1775.
(40) Henkelman, G.; Uberuaga, B. P.; Jónsson, H. A. Climbing Image Nudged Elastic Band Method for Finding Saddle Points and Minimum Energy Paths. *J. Chem. Phys.* **2000**, *113*, 9901.
(41) Henkelman, G.; Jónsson, H. A Dimer Method for Finding Saddle Points on High Dimensional Potential Surfaces Using Only First Derivatives. *J. Chem. Phys.* **1999**, *111*, 7010.
(42) Reuter, K.; Scheffler, M. Composition, Structure, and Stability of $RuO_2(110)$ as a Function of Oxygen Pressure. *Phys. Rev. B* **2002**, *65*, 035406.
(43) Reuter, K.; Scheffler, M. First-Principles Atomistic Thermodynamics for Oxidation Catalysis: Surface Phase Diagrams and Catalytically Interesting Regions. *Phys. Rev. Lett.* **2003**, *90*, 046103.
(44) Posada-Pérez, S.; Viñes, F.; Valero, R.; Rodriguez, J. A.; Illas, F. Adsorption and Dissociation of Molecular Hydrogen on Orthorhombic $\beta$-$Mo_2C$ and Cubic $\delta$-MoC (001) Surfaces. *Surf. Sci.* **2017**, *656*, 24−32.
(45) Filot, I. A. W. *Introduction to Microkinetic Modeling*; Technische Universiteit Eindhoven, 2018.
(46) Filot, I. A.W.; Van Santen, R. A.; Hensen, E. J. M. The Optimally Performing Fischer−Tropsch Catalyst. *Angew. Chem., Int. Ed.* **2014**, *53*, 12746−12750.
(47) Zhao, S.; Kang, W.; Xue, J. Manipulation of Electronic and Magnetic Properties of $M_2C$ (M = Hf, Nb, Sc, Ta, Ti, V, Zr) Monolayer by Applying Mechanical Strains. *Appl. Phys. Lett.* **2014**, *104*, 133106.
(48) Wang, G. Theoretical Prediction of the Intrinsic Half-Metallicity in Surface-Oxygen-Passivated $Cr_2N$ MXene. *J. Phys. Chem. C* **2016**, *120*, 18850−18857.
(49) Kumar, H.; Frey, N. C.; Dong, L.; Anasori, B.; Gogotsi, Y.; Shenoy, V. B. Tunable Magnetism and Transport Properties in Nitride MXenes. *ACS Nano* **2017**, *11*, 7648−7655.
(50) He, J.; Lyu, P.; Nachtigall, P. New two-dimensional Mn-based MXenes with Room-Temperature Ferromagnetism and Half-Metallicity. *J. Mater. Chem. C* **2016**, *4*, 11143−11149.

(51) Terriberry, T. B.; Cox, D. F.; Bowman, D. A. A Tool for the Interactive 3D Visualization of Electronic Structure in Molecules and Solids. *Comput. Chem.* **2002**, *26*, 313−319.
(52) Bader, R. F. W. A Quantum Theory of Molecular Structure and Its Applications. *Chem. Rev.* **1991**, *91*, 893−928.
(53) Zurita, S.; Rubio, J.; Illas, F. Active Sites of Pt Surfaces from Ab Initio Cluster Model Molecular Electrostatic Potential Maps. *Electrochim. Acta* **1996**, *41*, 2275−2283.
(54) López, M.; Broderick, L.; Carey, J. J.; Viñes, F.; Nolan, M.; Illas, F. Tuning Transition Metal Carbide Activity by Surface Metal Alloying: A Case Study on $CO_2$ Capture and Activation. *Phys. Chem. Chem. Phys.* **2018**, *20*, 22179−22186.
(55) López, M.; Viñes, F.; Nolan, M.; Illas, F. Predicting the Effect of Dopants on CO2 Adsorption in Transition Metal Carbides: Case Study on TiC (001). *J. Phys. Chem. C* **2020**, *124*, 15969−15976.
(56) Seredych, M.; Eugene Shuck, C.; Pinto, D.; Alhabeb, M.; Precetti, E.; Deysher, G.; Anasori, B.; Kurra, N.; Gogotsi, Y. High-Temperature Behavior and Surface Chemistry of Carbide MXenes Studied by Thermal Analysis. *Chem. Mater.* **2019**, *31*, 3324−3332.
(57) Salim, O.; Mahmoud, A. K.; Pant, K. K.; Joshi, R. K. Introduction to MXenes: Synthesis and Characteristics. *Mater. Today Chem.* **2019**, *14*, 100191.
(58) Liu, R.; Li, W. High-Thermal-Stability and High-Thermal-Conductivity $Ti_3C_2T_x$ MXene/Poly(vinyl alcohol) (PVA) Composites. *ACS Omega* **2018**, *3*, 2609−2617.
(59) Xiao, X.; Yu, H.; Jin, H.; Wu, M.; Fang, Y.; Sun, J.; Hu, Z.; Li, T.; Wu, J.; Huang, L.; Gogotsi, Y.; Zhou, J. Salt-Templated Synthesis of 2D Metallic MoN and Other Nitrides. *ACS Nano* **2017**, *11*, 2180−2186.


https://doi.org/10.1021/acscatal.1c03150
*ACS Catal.* 2021, 11, 12850−12857

ADVANCED THEORY AND SIMULATIONS
www.advtheorysimul.com

# Computational Pourbaix Diagrams for MXenes: A Key Ingredient toward Proper Theoretical Electrocatalytic Studies

*Martí López, Kai S. Exner,* Francesc Viñes, and Francesc Illas**

**MXenes, a rather new family of 2D carbides and nitrides, have shown to be promising materials in many technological applications, particularly in electrocatalysis. The as-synthesized MXenes exhibit a variety of surface terminations involving mixtures of O, OH, H, or F surface groups. These terminations play a crucial role in the electrocatalytic performance of these materials as these may change depending on the reaction conditions. The Pourbaix diagrams have long being used to provide the thermodynamically stable surface under certain conditions of pH and potential, *U*. However, experimental determination of Pourbaix diagrams may be quite challenging while first-principles studies, considering the most likely terminations, allow deriving reliable insights. Here, Pourbaix diagrams for a series of representative MXenes are provided; the $Ti_2C$, $Ti_3C_2$, $V_2C$, and $Mo_2C$ MXenes, with the novelty of considering single and several double mixed terminations. The possible implications of the obtained results are discussed, especially for a proper choice of models in theoretical electrocatalysis studies, including the water splitting related hydrogen evolution reaction (HER), or the oxygen reduction reaction (ORR), but also serving as a guide to any further computational studies and also to electrocatalytic experiments.**

## 1. Introduction

The challenging transition toward sustainable energy models has become an urgent need. Many strategies and energy sources have been proposed to eventually phase out the use of fossil fuels, while fighting the climate change and solving the approaching energy shortage.[1–4] Electrocatalysis-based synthesis, especially when using power from renewable sources of energy, emerges as a clean alternative to fossil fuels, and, also, to obtain many industrial chemical products with low-carbon fingerprint.[5,6] Highly active and durable catalytic materials are required to facilitate the often sluggish kinetics of the electrochemical processes, thus allowing these promising technologies to move from fundamental research to real-world applications.[6] Currently, the commonly used electrocatalysts exhibit two main drawbacks: either they show low efficiencies, or their price becomes prohibitive, mainly because they involve scarce late transition metals such as Pt.[7–9] Therefore, significant efforts are directed to reveal the fundamental reaction mechanisms in electrocatalysis, to determine the main drawbacks of the existing materials and to foster the discovery of new ones.

During the past decade, a new class of two-dimensional materials, named MXenes,[10] have been a focus of research attention given their growing number of practical applications,[11–13] expanding from energy conversion and storage[14,15] to supercapacitors,[16] $CO_2$ abatement technologies,[17–19] heterogenous catalysis,[20–23] including some examples of single atom catalysts,[24,25] and increasingly in electrocatalysis. For instance, MXenes have been explored as electrocatalysts for the hydrogen evolution reaction (HER),[26–28] the $CO_2$ electroreduction,[29] or even the $N_2$ electroreduction to $NH_3$,[30] among others. MXenes are characterized by the $M_{n+1}C_nT_x$ general formula with $n = 1$–3 and $2n+1$ total number of atomic layers, where M stands generally for an early transition metal, X tends to be C or N, and $T_x$ designates the surface termination that the as-synthesized materials often exhibit, mostly mixtures of –O, –OH, –H, and –F groups, although, depending on the conditions, a specific surface termination of one of these groups can be imposed.[31,32] Indeed, the manipulation and modification of the MXenes termination have also been recently reported.[33] Clearly the termination may largely influence the performance of a given electrocatalyst.[34] Thus, identifying the most stable surface termination under well-defined experimental conditions becomes essential to tune the catalyst and also constitutes an essential ingredient for its proper modeling.

In heterogenous catalysis the surface composition is mostly determined by the temperature and partial pressure of the

M. López, F. Viñes, F. Illas
Departament de Ciència de Materials i Química Física & Institut de Química Teòrica i Computacional (IQTCUB)
Universitat de Barcelona
c/ Martí i Franqués 1-11, Barcelona 08028, Spain
E-mail: francesc.illas@ub.edu

K. S. Exner
University Duisburg-Essen
Faculty of Chemistry
Theoretical Inorganic Chemistry Universitätsstraße 5
45141 Essen, Germany
E-mail: kai.exner@alumni.uni-ulm.de

The ORCID identification number(s) for the author(s) of this article can be found under https://doi.org/10.1002/adts.202200217



**DOI: 10.1002/adts.202200217**

reactants. There, phase diagrams can be built indicating the equilibrium composition for a given set of conditions. From a theoretical point of view, this is achieved by using the ab initio thermodynamics formalism developed by Reuter and Scheffler,[35,36] providing reliable surface phase diagrams. However, in electrocatalysis, one needs to realize that the involved reactions are usually carried out at standard conditions of temperature, but, at the same time, take place under application of an external potential in a solution of given pH conditions, and, therefore, $U$ and pH need to be considered in the modeling to determine a reliable surface structure under these working conditions. This is accomplished by relying on the well-known Pourbaix diagrams,[37,38] available for a broad number of systems.[39] The Pourbaix diagrams can also be computationally obtained from first-principles theoretical calculations, although relying on a series of approximations,[40–42] as commented in detail in a subsequent section. Nevertheless, their utility is out of doubt, and realistic electrocatalysts surface structures have been obtained from simulated Pourbaix diagrams for the oxygen reduction reaction on metallic electrodes,[40] chlorine evolution reaction on $RuO_2$,[41] and lithium-ion batteries,[43] just to mention a few. Note, however, that the theoretically derived diagrams include just the explicitly explored surface compositions, which may constitute a limitation. This can be minimized by considering a large enough number of surface motifs. Pourbaix diagrams have also been reported for the HER on some MXenes,[44] although a more systematic work considering a broader family of MXenes with different terminations is still lacking.

In spite of the considerations above, theoretical studies have been reported where the effect of pH and applied potential on the surface composition is not considered at all[45–47] which cast serious doubts on the reliability of the corresponding predictions. As already mentioned, many electrochemical reactions have been theoretically or experimentally studied over MXenes, especially the HER. In most of these studies, the effect of pH and potential on the surface structure is not considered, or just in part, e.g., assuming a given surface termination, vide infra. Some authors limit the study to consider the most stable surface without including pH and $U$, which can be suitable for heterogeneous catalysis, yet not correct when aiming at studying electrocatalytic process.[48] Many published studies just regarded the fully O-terminated MXene surface without previous considerations or based on a free energy criterion obviating the pH–$U$ influence.[45] For instance, Li et al.[29] reported a complete and accurate analysis of the electrochemical $CO_2$ capture and conversion over bare $M_3X_2$ MXenes, yet completely omitting the role of pH and $U$ on defining the appropriate surface termination. Also, an interesting and simple descriptor such as the number of electrons that the surface O atoms gain was proposed for the HER, but considering fully O-terminated MXenes only.[49] The effect of the metal or carbon vacancies on the same terminated MXenes has also been reported[45] as well as a large screening of the HER limiting potential over 36 carbide and nitride MXenes.[47] However, it has been shown that, at typically HER conditions, the majority of MXenes would be partially covered with –O and –OH moieties, and that this may have a direct impact on the obtained results.[44] Indeed, the fully O-terminated MXene surface chosen in these previous studies would be appropriate if the reaction studied would have been the oxygen reduction reaction (ORR) instead of the HER.

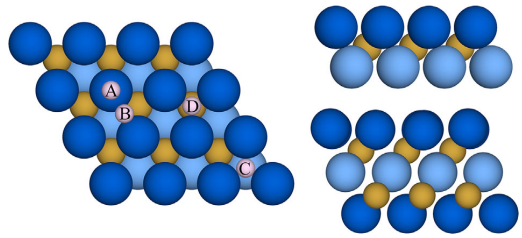


**Figure 1.** Top (left image) and side (right images) views of a $M_2C(0001)$ (upper right image, M = Ti, Mo, V) and $Ti_3C_2(0001)$ (lower right image) surface p(3 × 3) supercell. Metal atoms at the top and bottom layers are represented by bright and light blue spheres, respectively, while C atoms are represented by light brown spheres, and H atoms are shown in pink. The main high-symmetry surface sites considered are top (A), bridge (B), hollow M (C), and hollow C (D). (C) and (D) sites have either one M or C atom below.

Given the above, the purpose of this work is to provide Pourbaix Diagrams for a series of representative MXenes, including $V_2C$, $Mo_2C$, $Ti_2C$, and $Ti_3C_2$, while pedagogically explaining how to build them, thereby considering several possible single and double terminations. Our study aims to complete previous work exploring additional situations[27,28] as well as to set the results into the context of previous investigations of MXene models for HER.

## 2. Computational Details

Appropriate supercell models were used to represent the $M_2C$ (M = Ti, V, and Mo) and $Ti_3C_2$ MXenes (0001) clean surfaces as well as the surfaces with different terminations, described in the next section. For the $M_2C$ bare MXenes, the surface model consists of three atomic layers with a $p(3 \times 3)$ supercell following the ABC stacking, with one layer of carbon in the middle and one transition metal layer above and one below the carbon layer. The $Ti_3C_2$ model is equivalent to $Ti_2C$ but with five atomic layers instead of three, with Ti layers at top, bottom, and middle positions, and C layers in-between them, as illustrated in **Figure 1**. The atomic layers are periodically repeated so as to represent the (0001) basal plane with a perpendicular vacuum gap of at least 12 Å, which is enough to ensure isolation of the translationally repeated MXene layers in the direction perpendicular to the surface.[18,19]

The energy data necessary to build the Pourbaix diagrams were obtained from density functional theory (DFT) calculations carried out with the Perdew–Burke–Ernzerhof (PBE) exchange correlation functional,[50] including the contribution of dispersion through the D3 scheme of Grimme et al.[51] as implemented in the VASP code.[52–54] The effect of the core electrons on the valence electron density was taken into account by means of the projector augmented wave (PAW) approach, and the valence electron density was expressed using a plane-wave basis set with a kinetic energy cutoff of 415 eV. Despite some authors claim that bare MXenes such as $Ti_2C$ exhibit a magnetic ground state,[55] the present calculations were performed without spin polarization.

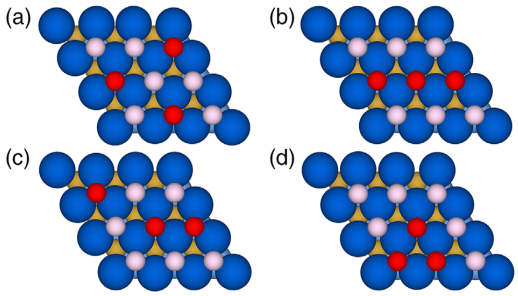


**Figure 2.** Top view of the four possible 1/3A + 2/3B coverage situation with the adsorbates at their most thermodynamically favored adsorption site, hollow M. The red and pink spheres represent the A and B adsorbates, respectively. Only for $Mo_2C$ the most thermodynamically stable adsorption site is encountered with hollow C.

This is because spin polarization vanishes as soon as the MXenes surface is functionalized with moieties such OH*, H*, O*, and F*. As a representative example, the adsorption energy of H* on $Ti_2C$ is affected by 0.06 eV for spin polarized and non-spin polarized calculations, and this effect is negligible for the prediction of the Pourbaix diagrams by DFT calculations. The atomic structure was optimized by a standard energy minimization procedure. In particular, we used the tetrahedron smearing method with a smearing width of 0.2 eV in conjunction with Blöchl corrections. The structure was considered converged when the maximum acting forces on each atom in the supercell were all below 0.01 eV $Å^{-1}$. The threshold for convergence of the total energy along the self-consistent-field was set to $10^{-6}$ eV. The numerical integration in the reciprocal space was carried out by sampling the Brillouin zone with a $5 \times 5 \times 1$ **Γ**-centered grid. This computational setup, used in previous work on similar systems,[18,19,22] achieves numerically converged results within less than 0.04 eV.

To build the Pourbaix diagrams, several possible structures have been considered including terminations with a single moiety, but also mixed cases. In the supercell used to represent the MXenes most stable surfaces, there are nine equivalent adsorption sites, see **Figure 2**. Consequently, 9O, 9OH, 9F, and 9H correspond to the surfaces fully covered by O, OH, F, and H, respectively. Note also that other possible adsorptions sites exist which may lead to large coverage if multiple site occupancy is allowed. Nevertheless, this will lead to adsorbate at small distances with concomitant high steric repulsion. Consequently, single occupancy has been considered in all cases exploring many intermediate adsorbate coverages ranging from 1/9 to 1 monolayer (ML), as described in the Supporting Information (SI). Likewise, a broad range of mixed adsorbate situations has been considered which, in all cases, represent full coverage since, at the conditions of interest, a lower coverage situation is not favored. For instance, both theory and experiments show that partially O-covered MXenes are only attainable at high temperatures.[56,57] This finding represents a general difference between heterogeneous gas-phase catalysis and electrocatalysis. In heterogenous catalysis, partially covered surfaces can be achieved at working conditions whereas this situation is very unlikely in electrocatalysis. This can be explained by referring to the solid/liquid interface, which causes that each active site is in direct contact with the aqueous electrolyte solution, and thus, each active site is at least covered by a water molecule in the double layer above.

Note also that, for each mixed configuration, several possibilities exist. For instance, there are four ways to distribute 3O and 6H in the supercell, see Figure 2, and the most stable one has been chosen to build the Pourbaix diagrams since, as it becomes clear in the next section, the effect of pH and $U$ on the free energy is independent of the surface ordering.

## 3. Step-by-Step Building Pourbaix Diagrams from DFT Based Calculations

The Pourbaix diagrams are similar to the standard pressure–volume phase diagrams but indicate the thermodynamic equilibrium surface structure under different conditions of pH and applied over potential, $U$, normally at a given temperature—e.g., 25 °C, pressure—e.g., 1 bar for gas phase components, and activity of 1 for all components of the liquid phase at such defined standard conditions. In a typical Pourbaix diagram, $U$ is represented on the vertical axis and the pH on the horizontal one. The different areas in the diagram correspond to different surface structures, and the lines indicate where two structures are in thermodynamic equilibrium. This implies that the Gibbs free energy of surface structures A and B at a given pH and $U$ are equal, i.e., $G_A(pH, U) = G_B(pH, U)$, or, employing a given reference state for A and B, when the relation $\Delta G_A(pH, U) = \Delta G_B(pH, U)$ is met. Thus, the construction of a theoretical Pourbaix diagram implies deriving $G(pH, U)$ or $\Delta G(pH, U)$ values for the possible surface structures for a broad range of pH and $U$. Clearly, Pourbaix diagrams are required to know the equilibrium structure under reaction conditions, which is a necessary ingredient in the study of any electrocatalytic processes using a given electrode.

The main idea to construct Pourbaix diagrams is as follows: one of the structures among the set of investigated surface models is used as a reference. In our case, we refer to the pristine MXene surface, 9*, as reference structure. The formation of adsorbates on the electrode surface, referenced to the 9* surface, is described by reaction equations. Please note that any adsorption process can be written as $\sum_i \Delta\nu_i A_i = 0$ where $\nu_i$ and $A_i$ indicate stochiometric coefficients and reactants or products, respectively. The change in Gibbs free energy for such an adsorption process can be written in a general form as indicated by Equation (1):

$$\Delta G = G_{surf-ads} - G_{surf} - n\,G_{ads} \quad (1)$$

The right hand side terms ($G_{surf-ads}$, $G_{surf}$ and $G_{ads}$) correspond to the free energy of the surface covered by a given ordered structure containing $n$ adsorbates, that of the clean surface and $n$ times that of the adsorbates. For a gas–solid interface, the reference state of the free adsorbates is given by the gas phase molecule. However, for electrochemical systems at the solid/liquid interface, the adsorbates may not exist in the gas phase or may have a radical nature. Therefore, it is a unified standard to introduce a set of reference structures relating to the adsorbates observed in an electrochemical environment. Let us recall that the common adsorbates of MXenes under HER conditions refer to O, OH, F, and H groups. The reference state for

O and OH does not refer to the gaseous oxygen molecule but rather to the water molecule at 298.15 K and 0.035 bar, because under these conditions, water vapor is in equilibrium with liquid water, i.e., their chemical potentials are identical.[58] Note that in DFT calculations, it is much easier to calculate the free energy of a gaseous water molecule rather than of liquid water, which necessitates inclusion of hydrogen-bonding between several water molecules, and this renders water vapor under the above conditions as the ultimate choice.

For H and OH groups, an additional reference state refers to the redox couple $H^+/H_2$, which is known from experimental electrochemistry as standard hydrogen electrode (SHE), when $H_2$ gas with a pressure of 1 bar is in equilibrium with a solution of protons of activity 1 at 298.15 K:

$$H^+_{(aq)} + e^- \rightleftharpoons \frac{1}{2}H_{2(g)} \tag{2}$$

Nørskov and co-workers proposed an elegant and nowadays frequently applied method of how to relate the gas-phase energetics of gaseous hydrogen to the free energy of a proton and the electrode potential, also referred as the computational hydrogen electrode (CHE) in the literature.[58]

Under equilibrium conditions, the process in Equation (2) obeys $\Delta G = 0$, and thus we infer:

$$\mu(H^+_{(aq)}) + \mu(e^-) = G(H^+_{(aq)}) + G(e^-) = \frac{1}{2}G(H_{2(g)}) \tag{3}$$

where $\mu(H^+_{(aq)})$ and $\mu(e^-)$ are the chemical potential of the hydrated proton and electron, respectively. This relation is important to factor pH and $U$ into the analysis of Gibbs free energies, as discussed in the following.

Let us recall that all surface structures are evaluated by reaction equations, referenced to the 9* structure. Rewriting Equation (1) relating to the adsorption process for the formation of any surface phase yields:

$$\Delta G = G_{surf-ads} - G_{surf} - n\,\Delta G_{ads} \tag{4}$$

where the only difference with respect to Equation (1) is in the last right hand side term which is the adsorbate free energy relative to the chosen reference. In the derivation of Equation (4) we did not account for neither pH nor $U$, or, equivalently, we assumed that both are zero, which we indicate as $\Delta G(0,0)$. Assuming that the only contribution to entropy is related to the adsorbates, Equation (4) translates to:

$$\Delta G(0,0) = \Delta G = \Delta E_{tot} + \Delta E_{ZPE} - T\Delta S \tag{5}$$

For a gas–solid system, $\Delta E_{tot}$ is the total energy difference between covered surface, and the sum of the energies of the clean surface and of $n$ adsorbates, whereas in an electrochemical environment the energy of the adsorbates is related to the gas phase molecules using the reaction equations in **Table 1**. Hence, it follows:

$$\Delta E_{tot} = E_{surf-ads} - \left(E_{surf} + n\,E_{ads}\right) \tag{6}$$

where the $\Delta E_{ZPE}$ terms correspond to the difference in zero-point energy for the adsorbates at the surface and the free adsorbates

**Table 1.** Reference states for both single and mixed surface terminations; $n$ and $y$ represent the number of adsorbed species on the studied surface.

| Absorbate | Reaction |
|---|---|
| $n$H | $\frac{n}{2}H_2 + n* \rightarrow n$H$*$ |
| $n$OH | $nH_2O + n* \rightarrow n$OH$* + \frac{n}{2}H_2$ |
| $n$O | $nH_2O + n* \rightarrow n$O$* + nH_2$ |
| $n$F | $\frac{n}{2}F_2 + n* \rightarrow n$F$*$ |
| $n$O/$y$OH | $(n+y)H_2O + (n+y)* \rightarrow n$O$* + y$OH$* + (n+\frac{y}{2})H_2$ |
| $n$O/$y$H | $nH_2O + \frac{y}{2}H_2 + (n+y)* \rightarrow n$O$* + y$H$* + nH_2$ |
| $n$O/$y$F | $nH_2O + \frac{y}{2}F_2 + (n+y)* \rightarrow n$O$* + y$F$* + nH_2$ |
| $n$OH/$y$H | $nH_2O + \frac{y}{2}H_2 + (n+y)* \rightarrow n$OH$* + y$H$* + \frac{n}{2}H_2$ |
| $n$OH/$y$F | $nH_2O + \frac{y}{2}F_2 + (n+y)* \rightarrow n$OH$* + y$F$* + \frac{n}{2}H_2$ |
| $n$H/$y$F | $\frac{n}{2}H_2 + \frac{y}{2}F_2 + (n+y)* \rightarrow n$H$* + y$F$*$ |

in the reference state, within the harmonic approximation, as in Equation (7)

$$\Delta E_{ZPE} = ZPE_{surf-ads} - n\,ZPE_{ads} \tag{7}$$

and the same applies for the $T\Delta S$ term, see Equation (8), as only adsorbate contributions are accounted for

$$T\Delta S = TS_{surf-ads} - n\,TS_{ads} \tag{8}$$

The entropy of the gaseous molecules—$S_{ads}$ for $H_2$, $F_2$, and $H_2O$—at room temperature—298 K—has been obtained from thermodynamic tables[59] whereas for the adsorbed phase only the vibrational entropy of adsorbates has been included and estimated as indicated by Equation (9),

$$TS = k_B N_A T \sum_i^n \frac{h\nu_i/k_B T}{e^{h\nu_i/k_B T} - 1} - \ln\left(1 - e^{-h\nu_i/k_B T}\right) \tag{9}$$

where the $\nu_i$ are the vibrational frequencies of adsorbate $i$ gained within the harmonic approximation, with $k_B$, $N_A$ and $h$ denoting the Boltzmann constant, the Avogadro number, and the Planck constant, respectively. Note that the $h\nu_i$ must have the proper energy units of $k_B T$.

Given the above, the only remaining point now is introducing the potential relative to the SHE and the pH in Equation (5), which is achieved by making use of the CHE model. From the reaction equation to form a certain adsorbate structure with respect to the 9* reference, the number of transferred protons, $\nu(H^+)$, and electrons, $\nu(e^-)$, can be deduced. This information is key for the construction of a Pourbaix diagram because the effect of $U$ and pH is not explicitly accounted for in the DFT calculations, but rather is addressed in the form of an a posteriori analysis. Applying an electrochemical-thermodynamic approach,[41] we obtain:

$$\Delta G(pH, U) = \Delta G(0,0) - \nu\left(H^+\right) k_B T(\ln 10) pH - \nu(e^-)\, eU \tag{10}$$

where $e$ is the elementary charge of an electron and $U$ is the applied electrode potential with respect to the SHE. The $\Delta G(0,0)$ values for all considered surface models of the investigated MXenes are collected in Tables S1–S4 (Supporting Information).

Finally, we need to introduce a reference for the F groups. This is achieved in a similar fashion to the popular CHE model by referring to a CFE electrode, that is, a computational fluorine electrode. The elementary processes of the reversible $F^-/F_2$ redox pair with a redox potential of 2.87 V versus SHE at $T = 298.15$ K,[60] is given by Equation (11):

$$\frac{1}{2}F_{2(g)} + e^- \rightleftharpoons F^-_{(aq)} \tag{11}$$

The CFE can be easily implemented into the analysis of Equation (10) by adding an additional term indicating the stoichiometric coefficient of fluoride anions in conjunction with the equilibrium potential of reaction (11). Thus, combining Equations (10) and (11) leads to

$$\Delta G\,(pH,\,U) = \Delta G\,(0,0) - \nu\,(H^+)\,k_B T(\ln 10)pH - \\ -\nu\,(e^-)\,eU - \nu\,(F^-)\,eU_F \tag{12}$$

Let us point out that all reaction equations for the formation of the possible adsorbate structures are compiled in Table 1. Actually, it is possible to obtain the reaction equations for all mixed coverages from simple linear combinations of the four adsorption reactions for the single adsorbates, –O, –H, –OH, and –F—*cf.* Table 1. In our study, we systematically explored all four terminations for coverages of 1/9, 1/3, 2/3, and 1 ML with the adsorbates on their more stable binding site. Full mixed coverages—1/3A + 2/3B—of all the possible combinations were also explored, see Figures 1 and 2. All these structures are considered for the construction of the Pourbaix diagrams, as discussed in Section 3.

Before heading to the results section, we would like to illustrate of how to obtain all terms needed to apply Equation (12). We demonstrate this for the case of a mixed coverage of 1/3 of O* and 2/3 of F*, where * implies an active surface site. The reaction equation to form this surface phase is

$$3H_2O + 3F_2 + 9* \rightarrow 3O^* + 6F^* + 3H_2 \tag{13}$$

and the $\Delta G(pH, U)$ term of this surface includes $\Delta E_{tot}$, $\Delta E_{ZPE}$, $T\Delta S$, $\nu(H^+)$, $\nu(e^-)$, and $\nu(F^-)$, with

$$\Delta E_{tot} = E\,(3O^* + 6F^*) + 3E\,(H_2) - \left[3E\,(H_2O + F_2) + E_{slab}\right] \tag{14}$$

where $E(3O^* + 6F^*)$ is the total energy of the slab surface model with $3O^*$and $6F^*$, $E_{slab}$ the total energy of the bare MXene, $E(H_2)$, the total energy for gas phase hydrogen molecule, and $E(H_2O + F_2)$ the sum of total energies of gas phase water and fluorine molecules. For the ZPE and the entropic correction, we assume that vibrational contributions of the adsorbates are completely decoupled from the slab and neglect the small, phonon vibrations of the electrode and the configurational entropy effects of it, i.e., $ZPE_{slab} = 0$, $S_{slab} = 0$. Using the same notation as in Equation (14) with ZPE or $S$ instead of $E$, we obtain:

$$\Delta E_{ZPE} = \mathrm{ZPE}\,(3O^* + 6F^*) + 3\mathrm{ZPE}\,(H_2) - 3\mathrm{ZPE}\,(H_2O + F_2) \tag{15}$$

$$T\Delta S = T\,S\,(3O^* + 6F^*) + 3T\,S\,(H_2) - 3T\,S\,(H_2O + F_2) \tag{16}$$

Finally, to obtain the stoichiometric coefficients, $\nu$, of the ions relevant to the CHE and CFE models within the adsorption process, the initial surface formation reaction of Equation (13) can be rewritten using Equations (2) and (11):

$$3H_2O + 6F^- + 9* \rightarrow 3O^* + 6F^* + 6H^+ + 12e^- \tag{17}$$

Thus, the stoichiometric coefficients of $\nu(H^+)$, $\nu(e^-)$, and $\nu(F^-)$ amount to 6, 12, and −6, respectively.

Up to this point, we have gathered all the necessary information to compute the $\Delta G(pH, U)$ term, with the implicit approximation that solvation contribution was neglected, which is a common approximation in theoretical electrocatalysis.[44,61] This procedure is carried out for all considered surface terminations, and one can evaluate, for any pH and $U$ conditions, which surface termination has the lowest $\Delta G(pH, U)$. Alternatively, when two terminations compete with each other, one can equal the $\Delta G(pH, U)$ terms, i.e., when $\Delta G_A(pH, U) = \Delta G_B(pH, U)$, vide supra, and isolate the pH versus $U$ conditions that satisfy such thermodynamic equilibrium conditions. The only remaining step is to build a surface Pourbaix diagram is to draw a 3D plot with the computed $\Delta G(pH, U)$ values and to project it onto the (pH, $U$) plane of lowest Gibbs free energy, resulting in a 2D plot with pH and $U$ as descriptors on the $x$ and $y$ axes, respectively.

## 4. Results and Discussion

For the considered adsorbates, –H, –OH, –O, and –F, the most stable adsorption site for $Ti_2C$, $Ti_3C_2$, $V_2C$ is the hollow M—see site C in Figure 1—, while for $Mo_2C$, the situation is slightly different as –OH, –O, and –F prefer the hollow C site—see site D in Figure 1, but –H still prefers hollow M even if the energy difference for H at these two sites is less than 0.09 eV. Apart from the mentioned sites corresponding to the most stable situation, all MXenes show stables adsorption energies at top sites—see site A in Figure 1—except for $Ti_3C_2$, where the adsorbates move toward more stable sites such as hollow M and X. Adsorption at bridge sites—see site B in Figure 1, is not stable in any MXene and consequently are not shown in **Table 2**. The presented results obtained are in agreement with previous studies.[27,28,62] Once the most stable adsorption site for each adsorbate is found, one can proceed to consider the most likely situation with either a single type of moiety, or having mixtures of two types, as described above. From the density functional calculations, one gets the total energy and, from the corresponding vibrational frequencies, the ZPE and entropy terms as described in the previous sections. This data in conjunction with the stoichiometric coefficients based on the reaction equations allows deriving the $\Delta G(pH, U)$ values, necessary to build the Pourbaix diagrams, which, for the systems explored in the present work, are shown in **Figure 3**.

The Pourbaix diagrams for all explored MXenes exhibit similar trends in the predicted stable surface coverage at different values of pH and $U$. This is the case even for $Mo_2C$ where different adsorption sites are involved. Thus, in aqueous environment, MXenes will not show their bare surface at any $pH$-$U$ working conditions. As expected, for $U_{SHE}$ values below −0.6 V the surface of all four MXenes is fully hydrogenated (reduced) with all reaction sites occupied by H* as a feedstock. Upon increasing

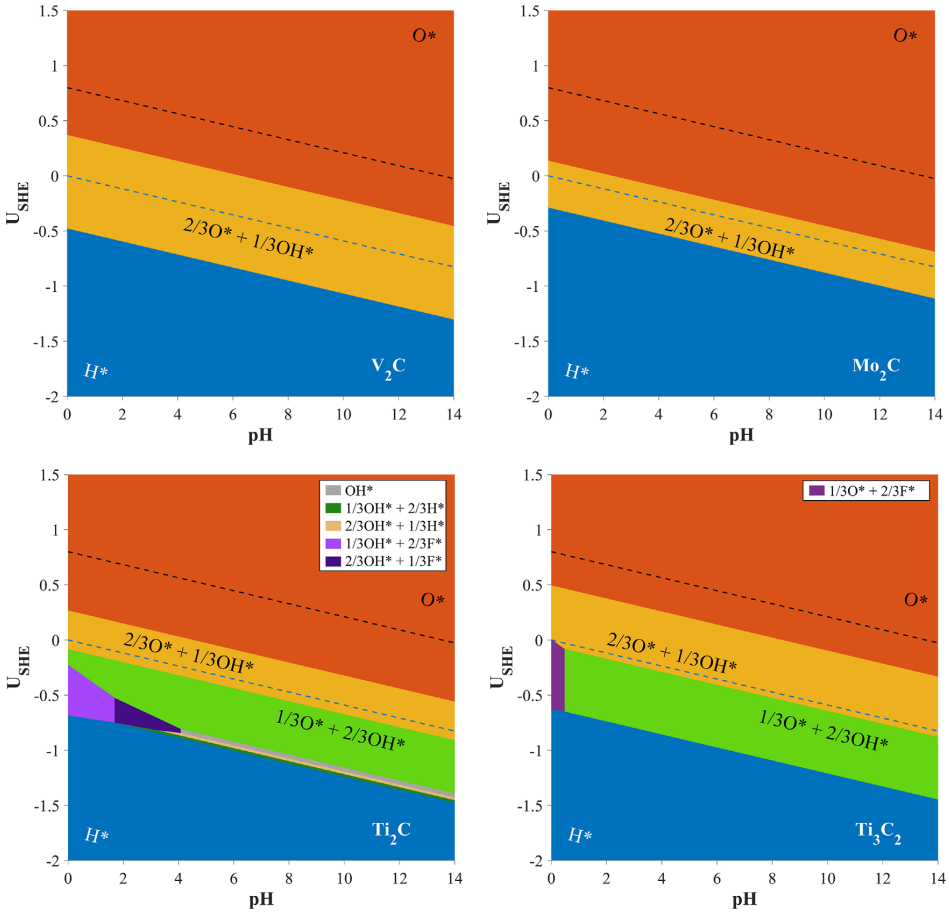


**Figure 3.** Pourbaix diagrams for $Mo_2C$, $V_2C$, $Ti_2C$, and $Ti_3C_2$. Note that from negative to positive potentials with respect to the SHE scale the surface becomes progressively oxidized, from full H coverage to full O coverage with intermediate –O/–OH or fully O-covered coverage for HER or ORR conditions, respectively. The HER equilibrium potential ($U$ = 0 V vs SHE) as well as typical ORR conditions ($U$ = 0.8 V vs SHE) are marked by dashed blue and black lines, respectively.

the potential, the MXene surface becomes progressively oxidized with OH* starting to replace H*. It is worth noting that this process might be remarkably potential sensitive as only for $Ti_2C$ such transition coverages, first 6H* + 3OH* and then 3H* + 6OH*, appear to be thermodynamically preferred. As one move toward positive potentials versus the SHE, the surface oxidation process continues until $U_{SHE}$ reaches 0.55 V, where all MXenes are fully covered by oxygen.

A novelty of the present work is the finding that for $Mo_2C$ and $V_2C$ the 6O* + 3OH* phase is the only mixed surface composition that appears as the thermodynamically favored one for certain *pH*-*U* conditions. Comparing with the values corresponding to both $Ti_2C$ and $Ti_3C_2$, the adsorption energies of O and OH species on these MXene are relatively low, see Table 2. Also, despite fluorine exhibits the strongest adsorption energy on each MXene, stable F-containing surfaces were only found for $Ti_2C$ and $Ti_3C_2$ at highly acidic conditions. This is a direct consequence of the penalty of 2.87 eV for each F* generated according to the CFE part in Equation (12).[38]

An interesting feature that arises from this discussion is why F-covered surfaces are not stable for large pH values. Inspection of Table 1 provides the answer because in the adsorption process for the formation of F*, it turns out that $\nu(H_2) = \nu(H^+) = 0$, and thus, there is no pH dependency for the formation of F*. This is quite in contrast to the cases of H*, O*, and OH* where Table 1 reveals a clear pH dependency because here $\nu(H_2) \neq 0$, and thus, $\nu(H^+) \neq 0$. To summarize, the energetics of H*, O*, and OH* is pH dependent with lower free energy with increasing pH whereas the energetics of F* is not. This is the reason why F* phases are only be observed at small pH values in the Pourbaix diagram because by increasing the pH the free energy of H*, O*, and OH* may excel that of F*.

**Table 2.** Adsorption energies, $E_{ads}$, given in eV, for atomic H, O, and F atoms, and the perpendicularly oriented OH at the obtained local minima on the $M_{n+1}C_n$ (0001) surfaces from calculations using the PBE functional. The results correspond to spin unpolarized calculations.

| $M_{n+1}C_n$ (0001) | Adsorbate | Top | Hollow C | Hollow M |
|---|---|---|---|---|
| $Mo_2C$ | H | −0.27 | −0.85 | −0.91 |
| | OH | −0.46 | −1.43 | −1.23 |
| | O | −0.55 | −1.44 | −1.35 |
| | F | −3.67 | −3.98 | −3.77 |
| $V_2C$ | H | −0.05 | −1.13 | −1.30 |
| | OH | −1.03 | −2.10 | −2.32 |
| | O | −0.83 | −2.27 | −2.59 |
| | F | −4.12 | −4.72 | −4.98 |
| $Ti_2C$ | H | 0.03 | −1.12 | −1.46 |
| | OH | −1.69 | −2.75 | −2.97 |
| | O | −1.03 | −3.07 | −3.34 |
| | F | −4.76 | −5.43 | −5.73 |
| $Ti_3C_2$ | H | −1.03 | −1.03 | −1.36 |
| | OH | −2.51 | −2.51 | −2.89 |
| | O | −2.52 | −2.52 | −3.15 |
| | F | −5.66 | −5.22 | −5.65 |

In the present work we also considered the effect of the configurational entropy by considering more than one possible distribution of the surface adsorbates, see Figure 2. For most of the combinations explored the distribution (a) in Figure 2 was found to be the most stable. Only three coverages (6OH* + 3H*, 3H* + 6F*, and 6H* + 3*) consistently preferred a different arrangement for $Ti_2C$, $Ti_3C_2$, and $V_2C$. For the 6OH* + 3H* coverage, the distribution (d) of Figure 2 was always preferred, yet all the entropic configurations present similar energies, around 0.09 eV. Consequently, we assume that for such mixed surface phases there might not be a specific adsorption pattern energetically preferred. For the F*/H* mixtures the difference in electronegativity between the F and H atoms causes a rearrangement on the order of stability of the different considered configurations. Configuration (a) in Figure 2 is no longer preferred as F* tend to sit at vicinal sites and configurations (b), (c), and (d) are close in energy and around 0.1 eV more stable than (a). The (d) arrangement is the most stable distribution for 3H* + 6F*, and (b) for 6H* + 3F*. $Mo_2C$ shows a similar trend that the previous MXenes in the sense that the (a) pattern is the most stable situation, but for the 3O* + 6OH* and 3O* + 6F* phases all four existing configurations are equally stable; see Table S2 (Supporting Information). However, the small overall differences make us conclude that the effect of the configurational entropy has a low impact on the resulting surface Pourbaix diagrams, and thus can be safely neglected.

Now, depending on the chosen reaction of interest carried out using MXenes as electrocatalysts, the Pourbaix diagrams in Figure 3 provide the equilibrium structure. For ORR, where the typically good catalysts are operating around 0.80 V versus SHE, all four MXenes will be fully covered by oxygen, in agreement with the predictions of Seh et al.[27] Under HER equilibrium conditions, the mixed 2/3O* + 1/3OH* surface termination is thermodynamically preferred for all the studied MXenes, close to the results of Seh et al.[27]. However, for $Ti_2C$ and $Ti_3C_2$, when a modest cathodic overpotential of –100 mV is applied the preferred surface changes to the 1/3O* + 2/3OH* phase. Since this overpotential might be smaller than the necessary overpotential to reach a sufficient HER current density in the order of several mA $cm^{-2}$, one should consider also possible surface compositions of $Ti_2C$ and $Ti_3C_2$ beyond the thermodynamically preferred ones at $U = 0$ V versus SHE (dotted line in Figure 3), i.e., regarding others within a 0.1 V energy window, and so accounting for similarly stable situations within the DFT accuracy.

It is worth noting that Pourbaix diagrams for the studied MXenes, ($V_2C$, $Mo_2C$, $Ti_2C$, and $Ti_3C_2$) were already reported by Gao et al.[44] and others,[27,61–64] although considering a smaller number of possible surface structures and different cell sizes. Comparing the Pourbaix diagrams of $Ti_2C$, $Ti_3C_2$, and $V_2C$ with those reported by Gao et al.[44] one finds that, even if the overall picture is in agreement, different adsorbates and mixtures were chosen for the analysis. Thus, for $Ti_2C$, $Ti_3C_2$ and $V_2C$, the fully oxygen covered situation appears at similar potential even when different mixed ratio of O*/OH* were considered, which indicates the predictive power of this theoretical approach. Moreover, compared to previous works, we choose a larger $p(3 \times 3)$ supercell instead of the $p(2 \times 2)$[61] or $p(2 \times 1)$[44,63] ones used in previous work so that a larger number of adsorbate patterns can be taken into account. While the computed Pourbaix diagrams are qualitatively comparable to the results obtained in smaller cell sizes, it should be noted that an important difference with respect to previous work is the consideration of H* and F* adsorbates. Indeed, the fully H* covered situation is preferred for strongly reducing (negative) overpotentials, which may be important in some electrocatalytic processes involving these MXenes, such as the hydrogen evolution versus electrochemical nitrogen reduction or hydrogen evolution versus electrochemical $CO_2$ reduction. The presence of mixed coverages containing F* adsorbates present at highly acidic conditions for $Ti_2C$ and $Ti_3C_2$ is also to be highlighted, as they are a factor to be regarded in HER conditions, which could indeed affect the overall surface electrocatalytic activity, but has been largely ignored in previous studies.[64]

Note that the presence of F* adsorbates seems to be a singular feature of group IV MXenes, observed for $Ti_2C$ and $Ti_3C_2$, but not seen for group V MXenes ($V_2C$) and group VI MXenes ($Mo_2C$). Therefore, the potential presence of F* adsorbates seems to be also important for earlier MXenes, e.g., Zr- and Hf-based MXenes, independently of their width. Aside, the surface models seem to be rather defined for HER and ORR conditions on group IV and VI ($V_2C$ and $Mo_2C$) considered MXenes, i.e., they are not close to other mixed situations, even if they belong to different *d* series, although for group IV cases ($Ti_2C$ and $Ti_3C_2$), the surface model is clear for ORR conditions; fully O-covered, although for HER, one should regard 1/3O* + 2/3OH* and 2/3O* + 1/3OH* models, and even F-containing models specially at very low pH conditions; 1/3OH* + 2/3F* for $Ti_2C$, and 1/3O* + 2/3F* for $Ti_3C_2$, with the caveat that, even if most stable $\Delta G$ surface terminations are shown in the Pourbaix diagrams shown in Figure 3, close terminations could indeed represent the MXene electrocatalyst surface under such working conditions.

## 5. Conclusions

In summary, we have reported a detailed analysis of all necessary modelling and computational steps that are needed to build Pourbaix diagrams for a series of representative MXenes: $Ti_2C$, $Ti_3C_2$, $V_2C$, and $Mo_2C$. In addition to previous works, we considered the four different most common terminations that can be experimentally encountered under standard MXene synthetic conditions, unless specific cleaning and preparation procedures are involved to remove selected surface terminations.

We have shown here that depending on the pH and $U$ conditions, other terminations rather that the typically assumed fully O* or fully OH* covered surfaces should be considered. In particular, we provide evidence that the fully H* terminated surface is of importance for $U < -0.6$ V versus SHE. In the case of $Ti_2C$ and $Ti_3C$ at strong acidic conditions and slightly negative potentials of $-0.6$ V $< U$ versus SHE $< 0$ V, which are of relevance to the HER, mixed surface phases involving –F moieties with –O or –OH groups should not be disregarded, which may also be important to other early transition metal MXenes, such as Zr- and Hf-based ones. In addition, for HER conditions, the explored Ti-based MXenes feature 1/3O* + 2/3OH* and 2/3O* + 1/3OH* terminations in a close range of potentials, implying that these surface phases should be studied to evaluate the HER performance for any pH conditions.

For the case of mixed configurations, we show that configurational entropy and pH play a negligible role on determining the equilibrium surface structure. Finally under ORR conditions the fully O-covered phase corresponds to the active surface regardless of the explored MXene, while for HER, 2/3O* + 1/3OH* are, apparently, well suited models for all the considered MXenes, although for Ti-based MXenes, the 1/3O* + 2/3OH* model could be also suited.

## Supporting Information

Supporting Information is available from the Wiley Online Library or from the author.

## Acknowledgements

The research carried out at the *Universitat de Barcelona* was supported by the Spanish MCIN/AEI/10.13039/501100011033 funded RTI2018-095460-B-I00 and *María de Maeztu* MDM-2017-0767 grants, including funding from European Union and, in part, by and COST Action CA18234. A significant part of the computational resources has been provided by the *Red Española de Supercomputación* (RES) through QCM-2018-1-0009 and QCM-2018-3-0015 projects. M.L. thanks *Universitat de Barcelona* for an APIF predoctoral contract, the HPC-EUROPA3 (INFRAIA-2016-1-730897) project supported by the EC Research Innovation Action under the H2020 Programme, the University of Duisburg-Essen and the High Performance Computing Center Stuttgart (HRLS) for supporting his stay in Essen. K.S.E. acknowledges funding by the Ministry of Culture and Science of the Federal State of North Rhine-Westphalia (NRW Return Grant). K.S.E. is associated with the CRC/TRR247: "Heterogeneous Oxidation Catalysis in the Liquid Phase" (Project number 388390466-TRR 247), the RESOLV Cluster of Excellence, funded by the Deutsche Forschungsgemeinschaft under Germany's Excellence Strategy—EXC 2033–390677874— RESOLV, and the Center for Nanointegration (CENIDE).

Correction added on 21 September 2022, after first online publication: Table 1 has received two corrections to entries $n$O/$y$H and $n$OH/$y$H. The supplementary information has been updated.

## Conflict of Interest

The authors declare no conflict of interest.

## Data Availability Statement

The data that support the findings of this study are available from the corresponding author upon reasonable request.

## Keywords

density functional calculations, electrochemistry, Gibbs free adsorption energies, MXenes, surface Pourbaix diagrams

Received: April 1, 2022
Revised: May 23, 2022
Published online:

[1] S. Chu, A. Majumdar, *Nature* **2012**, *488*, 294.
[2] J. A. Turner, *Science* **2004**, *305*, 974.
[3] G. W. Crabtree, M. S. Dresselhaus, M. V. Buchanan, *Phys. Today* **2004**, *57*, 39.
[4] D. G. Nocera, N. S. Lewis, *Proc. Natl. Acad. Sci. U. S. A.* **2006**, *103*, 15729.
[5] S. Gu, B. Xu, Y. Yan, *Annu. Rev. Chem. Biomol. Eng.* **2014**, *5*, 429.
[6] Z. W. She, J. Kibsgaard, C. F. Dickens, I. Chorkendorff, J. K. Nørskov, T. F. Jaramillo, *Science* **2017**, *355*, 4998.
[7] M. K. Debe, *Nature* **2012**, *486*, 43.
[8] H. A. Gasteiger, S. S. Kocha, B. Sompalli, F. T. Wagner, *Appl. Catal., B: Environ.* **2005**, *56*, 9.
[9] V. R. Stamenkovic, B. S. Mun, M. Arenz, K. J. J. Mayrhofer, C. A. Lucas, G. Wang, P. N. Ross, N. M. Markovic, *Nat. Mater.* **2007**, *6*, 241.
[10] M. Naguib, M. Kurtoglu, V. Presser, J. Lu, J. Niu, M. Heon, L. Hultman, Y. Gogotsi, M. W. Barsoum, *Adv. Mater.* **2011**, *4*, 4248.
[11] *2D Metal Carbides and Nitrides (MXenes): Structure, Properties and Applications* (Eds: B. Anasori, Y. Gogotsi), Springer Nature Switzerland AG, London, England, UK **2019**
[12] Y. Gogotsi, B. Anasori, *ACS Nano* **2019**, *13*, 8491.
[13] A. Vahid Mohammadi, J. Rosen, Y. Gogotsi, *Science* **2021**, *372*, 1581.
[14] B. Anasori, M. R. Lukatskaya, Y. Gogotsi, *Nat. Rev. Mater.* **2017**, *2*, 16098.
[15] N. K. Chaudhari, H. Jin, B. Kim, D. San Baek, S. H. Joo, K. Lee, *J. Mater. Chem. A* **2017**, *5*, 24564.
[16] X. Wang, S. Kajiyama, H. Iinuma, E. Hosono, S. Oro, I. Moriguchi, M. Okubo, A. Yamada, *Nat. Commun.* **2015**, *6*, 6544.
[17] I. Persson, J. Halim, H. Lind, T. W. Hansen, J. B. Wagner, L. Å. Näslund, V. Darakchieva, J. Palisaitis, J. Rosen, P. O. Å. Persson, *Adv. Mater.* **2019**, *31*, 1805472.
[18] R. Morales-Salvador, Á. Morales-García, F. Viñes, F. Illas, *Phys. Chem. Chem. Phys.* **2018**, *20*, 17117.
[19] Á. Morales-García, A. Fernández-Fernández, F. Viñes, F. Illas, *J. Mater. Chem. A* **2018**, *6*, 3381.
[20] Á. Morales-Garcia, F. Calle-Vallejo, F. Illas, *ACS Catal.* **2020**, *10*, 13487.
[21] J. D. Gouveia, A. Morales-García, F. Viñes, J. R. B. Gomes, F. Illas, *ACS Catal.* **2020**, *10*, 5049.

[22] J. D. Gouveia, Á. Morales-García, F. Viñes, F. Illas, J. R. B. Gomes, *Appl. Catal., B* **2020**, *260*, 118191.
[23] T. K. Slot, V. Natu, E. V. Ramos-Fernandez, A. Sepúlveda-Escribano, M. Barsoum, G. Rothenberg, N. R. Shiju, *2D Mater.* **2021**, *8*, 035003.
[24] Y. Meng, J. Liang, C. Zhu, C. Xu, J. Li, *Sci. China Mater.* **2022**, *65*, 1303.
[25] S. H. Talib, S. Baskaran, X. Yu, Q. Yu, B. Bashir, S. Muhammad, S. Hussain, X. Chen, J. Li, *Sci. China Mater.* **2021**, *64*, 651.
[26] A. D. Handoko, K. D. Fredrickson, B. Anasori, K. W. Convey, L. R. Johnson, Y. Gogotsi, A. Vojvodic, Z. W. Seh, *ACS Appl. Energy Mater.* **2018**, *1*, 173.
[27] Z. W. Seh, K. D. Fredrickson, B. Anasori, J. Kibsgaard, A. L. Strickler, M. R. Lukatskaya, Y. Gogotsi, T. F. Jaramillo, A. Vojvodic, *ACS Energy Lett.* **2016**, *1*, 589.
[28] D. Jin, L. R. Johnson, A. S. Raman, X. Ming, Y. Gao, F. Du, Y. Wei, G. Chen, A. Vojvodic, Y. Gogotsi, X. Meng, *J. Phys. Chem. C* **2020**, *124*, 10584.
[29] N. Li, X. Chen, W. J. Ong, D. R. Macfarlane, X. Zhao, A. K. Cheetham, C. Sun, *ACS Nano* **2017**, *11*, 10825.
[30] J. Zhao, L. Zhang, X. Y. Xie, X. Li, Y. Ma, Q. Liu, W. H. Fang, X. Shi, G. Cui, X. Sun, *J. Mater. Chem. A* **2018**, *6*, 24031.
[31] Z. Kang, M. A. Khan, Y. Gong, R. Javed, Y. Xu, D. Ye, H. Zhao, J. Zhang, *J. Mater. Chem. A* **2021**, *9*, 6089.
[32] J. Halim, K. M. Cook, M. Naguib, P. Eklund, Y. Gogotsi, J. Rosen, M. W. Barsoum, *Appl. Surf. Sci.* **2016**, *362*, 406.
[33] H. Riazi, M. Anayee, K. Hantanasirisakul, A. A. Shamsabadi, B. Anasori, Y. Gogotsi, M. Soroush, *Adv. Mater. Interfaces* **2020**, *7*, 1902008.
[34] Y. Yang, M. Luo, W. Zhang, Y. Sun, X. Chen, S. Guo, *Chem* **2018**, *4*, 2054.
[35] K. Reuter, M. Scheffler, *Phys. Rev. B* **2002**, *65*, 035406.
[36] K. Reuter, M. Scheffler, *Phys. Rev. Lett.* **2003**, *90*, 046103.
[37] M. Pourbaix, *Corrosion* **1950**, *5*, 395.
[38] P. Delahay, M. Pourbaix, P. Van Rysselberghe, *J. Electrochem. Soc.* **1951**, *98*, 57.
[39] M. Pourbaix, *Atlas of Electrochemical Equilibria in Aqueous Solutions*, 2nd English ed., National Association of Corrosion, Houston, TX **1974**.
[40] H. A. Hansen, J. Rossmeisl, J. K. Norskov, *Phys. Chem. Chem. Phys.* **2008**, *10*, 3722.
[41] K. S. Exner, J. Anton, T. Jacob, H. Over, *Electrochim. Acta* **2014**, *120*, 460.
[42] O. Vinogradova, D. Krishnamurthy, V. Pande, V. Viswanathan, *Langmuir* **2018**, *34*, 12259.
[43] K. S. Exner, *ChemElectroChem* **2017**, *4*, 3231.
[44] G. Gao, A. P. O'Mullane, A. Du, *ACS Catal.* **2017**, *7*, 494.
[45] J. Gan, F. Li, Q. Tang, *J. Phys. Chem. Lett.* **2021**, *12*, 4805.
[46] Y. Luo, G. F. Chen, L. Ding, X. Chen, L. X. Ding, H. Wang, *Joule* **2019**, *3*, 279.
[47] M. Pandey, K. S. Thygesen, *J. Phys. Chem. C* **2017**, *121*, 13593.
[48] D. Opalka, C. Scheurer, K. Reuter, *ACS Catal.* **2019**, *9*, 4944.
[49] C. Ling, L. Shi, Y. Ouyang, J. Wang, *Chem. Mater.* **2016**, *28*, 9026.
[50] J. P. Perdew, K. Burke, M. Ernzerhof, *Phys. Rev. Lett.* **1996**, *77*, 3865.
[51] S. Grimme, J. Antony, S. Ehrlich, H. Krieg, *J. Chem. Phys.* **2010**, *132*, 154104.
[52] G. Kresse, J. Hafner, *J. Phys.: Condens. Matter* **1994**, *6*, 8245.
[53] G. Kresse, J. Furthmüller, *Comput. Mater. Sci.* **1996**, *6*, 15.
[54] G. Kresse, J. Furthmüller, *Phys. Rev. B* **1996**, *54*, 11169.
[55] Y. Xie, P. R. C. Kent, *Phys. Rev. B* **2013**, *87*, 235441.
[56] J. D. Gouveia, F. Viñes, F. Illas, J. R. B. Gomes, *Phys. Rev. Mater.* **2020**, *4*, 054003.
[57] A. Kurlov, E. B. Deeva, P. M. Abdala, D. Lebedev, A. Tsoukalou, A. Comas-Vives, A. Fedorov, C. R. Müller, *Nat. Commun.* **2020**, *11*, 4920.
[58] J. K. Nørskov, J. Rossmeisl, A. Logadottir, L. Lindqvist, J. R. Kitchin, T. Bligaard, H. Jónsson, *J. Phys. Chem. B* **2004**, *108*, 17886.
[59] *CRC Handbook of Chemistry and Physics*, 102nd ed., Lide, D. R., Ed., CRC Press, Boca Raton, FL, **2004**.
[60] D. F. Sriver, P. W. Atkins, *Inorganic Chemistry*, 5th ed., W. H. Freeman and Company, New York **2009**.
[61] L. R. Johnson, S. Sridhar, L. Zhang, K. D. Fredrickson, A. S. Raman, J. Jang, C. Leach, A. Padmanabhan, C. C. Price, N. C. Frey, A. Raizada, V. Rajaraman, S. A. Saiprasad, X. Tang, A. Vojvodic, *ACS Catal.* **2020**, *10*, 253.
[62] J. Björk, J. Rosen, *Chem. Mater.* **2021**, *33*, 9108.
[63] M. Ashton, N. Trometer, K. Mathew, J. Suntivich, C. Freysoldt, S. B. Sinnott, R. G. Hennig, *J. Phys. Chem. C* **2019**, *123*, 3180.
[64] C. Zhan, W. Sun, Y. Xie, D. Jiang, P. R. C. Kent, *ACS Appl. Mater. Interfaces* **2019**, *11*, 24885.

# Theoretical Study of the Mechanism of the Hydrogen Evolution Reaction on the $V_2C$ MXene: Thermodynamic and Kinetic Aspects

Martí López,[1] Kai S. Exner,[2]* Francesc Viñes,[1]* Francesc Illas[1]

[1]*Departament de Ciència de Materials i Química Física & Institut de Química Teòrica i Computacional (IQTCUB), Universitat de Barcelona, c/ Martí i Franqués 1-11, Barcelona 08028, Spain.*

[2]*University Duisburg-Essen, Faculty of Chemistry, Theoretical Inorganic Chemistry, Universitätsstraße 5, 45141 Essen, Germany; Cluster of Excellence RESOLV, Bochum, Germany; Center for Nanointegration (CENIDE) Duisburg-Essen, Duisburg, Germany.*

*Corresponding authors: francesc.vines@ub.edu, kai.exner@uni-due.de

## Abstract

Both experimentally and theoretically, the MXene family has shown promising hydrogen evolution reaction (HER) capabilities. However, so far, the theoretical approach has been relying on the well-known thermodynamic descriptor $\Delta G_H$ whereas experimental studies report Tafel plots, containing kinetic rather than thermodynamic information. Aiming to link theory to experiments, the present study explores five different HER pathways over the exemplary $V_2C$ (0001) MXene by density functional theory calculations. While the surface coverage under HER conditions (with either *H or *OH adsorbates) is extracted from a Pourbaix diagram, we determine the energetics of the reaction intermediates and transition states for both surface species as active sites. This enables the construction of free-energy diagrams for the Volmer-Heyrovsky and Volmer-Tafel mechanisms and allows for the simulation of Tafel plots by a rigorous microkinetic framework. While the active-site motif $V_2C$-OH seems to be less relevant for the HER under typical reaction conditions, we demonstrate that the HER is kinetically facile on the $V_2C$-H surface. For this surface termination, we report a potential-depending switching of the preferred mechanism from the Volmer-Heyrovsky to the Volmer-Tafel description with increasing overpotential while encountering similarities to the HER over Pt.

## 1. Introduction

Our society is demanding an urgent socioeconomic transformation to face the many issues arising from forthcoming climate emergencies.[1-4] The increasing energetic demand[5] together with the necessity of reducing our dependency on fossil fuels drives the scientific and technological community to look for environmentally sustainable alternatives.[6,7] Among all the alternative energy sources, the use of molecular hydrogen has attracted a considerable attention due to its multiple capabilities in energy storage or for its direct usage replacing the nowadays employed fossil fuels. [8-10] Water splitting is a key reaction toward the production of green hydrogen, and the hydrogen evolution (HER) and oxygen evolution (OER) reactions take place at the cathode and anode of an electrolyzer, respectively. [11-13] However, these technologies still present few setbacks for their large scale application. Currently, the scarce and expensive Pt- and Ir/Ru-based materials are among the best catalysts for HER[14,15] and OER,[16] respectively, and consequently, materials based on non-scarce metals are called for to replace Pt- and Ir/Ru-based materials.[17]

Currently, materials based on earth-abundant elements are currently tested as alternatives to Pt-based catalysts for the HER, such as transition-metal carbides (TMCs) and nitrides (TMNs),[18-20] transition-metal sulphides,[21-23] phosphides,[24-26] or metallic organic frameworks (MOFs)[27] such as Ni-THT,[28] Co-BHT, and Co-THT.[29] Among them, a new family of 2D materials, named MXenes,[30] is raising considerable expectation.[31] While MXenes are strongly related to TMCs and TMNs in terms of composition, structurally they are very different as MXenes contain a few atomic layers only.[32] Most MXenes adhere to the general formula $M_{n+1}X_n$ where M stands for a metal, usually an early transition metal from groups IV to VI (M = Ti, Zr, Hf, V, Nb, Ta, Cr, Mo, W…) while X stands for carbon or nitrogen. Depending on the synthesis, the surfaces of MXenes are functionalized with groups such as -O, -OH, -H, and -F, and these are normally referred to as $M_{n+1}X_nT_x$ where $T_x$ indicates the termination on both metal surfaces of each MXene sheet. In addition, there are new members of the family involving different metals[33] and even other materials have been proposed where C and N layers can alternate.[34] Meanwhile, MXenes have multiple applications in batteries,[35,36] as supercapacitors,[37] in antibacterial activity,[38] in $CO_2$ abatement technologies,[39-42] and in multiple electrocatalytic processes[43] such as the HER, but they are equally discussed as electrocatalysts for the OER.[44,45]

Relating to the HER activity of MXenes, Seh *et al.*[46] investigated the suitability of the broadly used Gibbs free energy of hydrogen adsorption, $\Delta G_H$,[47] to evaluate the electrocatalytic performance of several O-terminated early transition metal MXenes, such as $Sc_2CO_2$, $V_3C_2O_2$, $Cr_2CO_2$, $Mo_2CO_2$, $Mo_4C_3O_2$, $Cr_2NO_2$, $Nb_2NO_2$. Subsequent studies explored an even wider range of MXenes, also addressing the HER activity of these materials.[48-51] In particular, Ling *et al.*[48] proposed the net charge on the atom(s) directly interacting with adsorbed H as an alternative descriptor, yet this charge is indeed dependent on the MXene $T_x$ termination already mentioned. Additionally, the effect of termination on HER activity has been studied in detail by Hondoko *et al*,[52] pointing out that F-terminated MXenes tend to exhibit lower HER catalytic activity than the O-terminated counterparts.[52] This led to identify the exposed terminal O as the active sites of the HER over MXenes,[53] suggesting that freshly exfoliated MXenes are not active catalysts for the HER and that some surface functionalization is needed.

Despite the considerable number of studies that aim to comprehend the HER activity of MXenes, including the most recent review,[44] so far all theoretical studies rely on thermodynamic considerations only, thus neglecting the effect of the kinetics in the HER. However, the thermodynamic approach may not suffice to explain experimental results in all cases, particularly not if the tacit precondition of Brønsted−Evans−Polanyi relation, which couples the thermodynamic to the kinetic picture, is violated.[54-56] In the present work we present a comprehensive study where, for the first time, the kinetics of the HER over $V_2C$, taken as an exemplary case of the MXene family, is accounted for besides the thermodynamic picture. This is achieved by the coupling of first-principles calculations in the density functional theory (DFT) approximation, including the determination of transition states, with microkinetic considerations to simulate Tafel plots that can be compared to experiments.

## 2. Surface Models and Computational Approach

The $V_2C$ (0001) basal surface is modelled by a *p*(3x3) supercell with three atomic layers stacked in ABC fashion, as in previous works on similar MXenes, see Figure 1.[39,40,57-59] The upper and lower layers contain just V atoms whereas C atoms are placed in the middle layer. A vacuum width of around 12 Å along the *z* direction is added to the supercell to avoid interaction between interleaved MXenes; this is a technicality arising from the use of a computational code that exploits periodic boundary conditions. The surface

termination of the $V_2C$ MXene is chosen by inspecting the corresponding Pourbaix diagram as obtained from theoretical calculations.[44] While most works consider a single surface termination only, a recent study considering various adsorbates, including mixed phases,[60] showed that the most stable surface coverage is predicted to contain $^2/_3$ and $^1/_3$ of surface sites having adsorbed O* and OH* ($^2/_3$O* + $^1/_3$OH*), respectively under HER conditions, in all cases with adsorbates on their most stable HollowM adsorption sites. Accordingly, this surface phase has been adopted as the starting model to explore the HER kinetics. Nevertheless, only if an overpotential is applied, a turnover in terms of hydrogen formation is observed. In the case of $V_2C$, at an applied electrode potential of –0.5 V *vs*. the reversible hydrogen electrode (RHE), the most stable surface is fully covered by adsorbed H*, again on HollowM, and this surface phase is included as second model in our study. We also considered the case with full OH* coverage even if previous work suggests that this situation is not thermodynamically favoured at any pH or potential conditions.[60] This is because, most often, the simulated surface Pourbaix diagrams do not account for the effect of the surrounding solvent. Therefore, to account for the aqueous electrochemical environment, we have added six molecules of water to the surface of the ($^2/_3$O* + $^1/_3$OH*) phase. The atomic structure of the adsorbed water is reminiscent of the ice-like structure, which has already been successfully applied to study the HER kinetics in other systems.[61,62] The explicit water molecules layer includes one extra hydrogen, *i.e.* a $H_3O$ moiety, to prompt the H adsorption. In the computational models with the initial ($^2/_3$O* + $^1/_3$OH*) surface coverage, this leads to a new situation where the surface is fully covered with OH* groups, and this is the reason why the HER kinetics over the fully OH*-covered surface is investigated in the present study as well.

The present theoretical study of the HER kinetics and reaction mechanisms over $V_2C$ is based on calculations carried out in the framework of density functional theory (DFT)[63,64] using the Vienna *ab-initio* simulation package (VASP).[65-67] The Perdew-Burke-Erzenhof (PBE) form of the exchange-correlation potential was used,[68] including dispersion effects through the Grimme's D3 approach.[69] The electronic density of the valence electrons was expanded using a plane-base basis set with an energy cut off of 415 eV. The effect of the core electrons on the valence electron density is accounted for through the projector augmented wave (PAW) approach of Blöchl,[70] as implemented in VASP by Kresse and Joubert.[71] A value of $10^{-5}$ eV was set as a convergence criterion for the electronic energy optimization together with a threshold of 0.01 $Å^{-1}$ for the atomic

forces acting on every single atom of the system. For the calculations, the partial occupancies of the orbitals are considered by the tetrahedron method with Blöchl corrections. Consequently, a **Γ**-cantered **k**-mesh of 5×5×1 dimensions was used to sample the Brillouin zone for the numerical integration in the reciprocal space. At convergence, the total energy was extrapolated to 0 K. Spin polarization was not considered as no magnetism was reported for $V_2C$.[72]

To locate the transition state (TS) structures along the possible reaction paths, we used the climbing-image nudged elastic band[73] (CI-NEB) and the improved dimer method,[74] depending on each single geometrical structure. All the identified TS were characterized by proper frequency analysis, carried out by Hessian matrix construction and diagonalization. We used finite displacements of 0.03 Å in length, verifying that in each case, only one imaginary frequency was present. The structures of interest displayed in this work were represented using the VESTA code.[75]

### 3. Hydrogen Evolution Reaction Mechanism

Strongly acidic solutions are preferably used to carry out the HER, although it is occasionally examined in buffered solutions with an intermediate *p*H or under alkaline conditions. Considering the ice-like water layer as a proton donor, we refer to the acidic HER equilibrium:

$$2H^+ + 2e^- \rightleftharpoons H_2, U^0 = 0\ \text{V}\ \textit{vs.}\ \text{RHE} \quad (1).$$

Two reaction mechanisms are frequently discussed in the literature, denoted as Volmer-Heyrovsky (VH) and Volmer-Tafel (VT);[76,77] their representation is given in Figure 2. Both mechanisms have in common that hydrogen is adsorbed on the electrode within the electrochemical Volmer (cf. Eq. (2)), but they differ in the second step. In the VH mechanism, the Heyrovsky step is also of electrochemical nature (cf. Eq. (3)) in that the adsorbed hydrogen species recombines with another proton from the electrolyte solution to release a single $H_2$ molecule. On the contrary, the VT mechanism consists of two subsequent Volmer steps and the Tafel step of Eq. (4), a chemical recombination step of the two adjacent hydrogen adsorbates to form $H_2$.

$$\text{Volmer step: } H^+ + e^- + * \rightarrow H^* \quad (2),$$

$$\text{Heyrovsky step: } H^+ + e^- + H^* \rightarrow * + H_2 \quad (3),$$

Tafel step: $2H^* \rightarrow * + H_2$ (4).

Given that our $V_2C$ surface models under HER conditions contain already adsorbed hydrogen atoms, some additional considerations are needed. As such, the HER can also proceed starting with the Heyrovsky step to produce $H_2$ using the surface hydrogen without needing an initial Volmer step. Table 1 describes the sequence of steps for the HER mechanisms examined in the current study, employing the two alternative terminations mentioned above and the same line of thought. Nonetheless, based on the terminations considered, not all the mechanisms resulting from combining these steps are allowed. For instance, in the H-terminated MXene ($T_x$ = H), a H from the water layer can bond the metal V Top site and thus any mechanism starting with a Volmer step will be allowed. However, the hydrogen atoms absorbed at HollowM sites that are present in the initial termination are strongly adsorbed (*i.e.* $\Delta G$ = -1.05 eV). Consequently, these H atoms cannot be used as a hydrogen source for the HER, and therefore, mechanisms starting with a Heyrovsky or Tafel step cannot proceed and are not considered (*cf.* Figure 3). In contrast, on the fully OH-terminated $V_2C$ surface, the V Top sites are sterically blocked by the OH groups, thus leaving no free adsorption sites for the H atoms. In contrast to the case of the $V_2C$-H surface, the mechanisms cannot start with a Volmer step. On the other hand, the H atoms from the surface OH groups are exposed and can be combined to one hydrogen from the water layer *via* one Heyrovsky step or, alternatively, can form a $H_2$ molecule with another H from the surface OH *via* one Tafel step as schematically shown in Figure 3. We would like to emphasize that the approximation of the ice-like water layer as hydrogen source on top of the $V_2C$ surface requires caution and, instead of referring to the lowest energy path, we investigated a representative number of options and computed the free-energy diagrams using an average over these paths to reduce possible artifacts.

To finally predict the most favourable mechanism, the free-energy diagrams of all the elementary steps and mechanisms are estimated as indicated in the below. Figure 4 depicts an example of the free-energy diagram for the conventional VH and VT mechanisms at $\eta$ = 0 V and 0.2 V over the $V_2C$-H example; for simplicity, we refer to the absolute value of the HER overpotential in the following even though cathodic overpotentials are formally negative. The free-energy landscape of the HER is directly affected by an increase in the applied overpotential, and the free energies of the reaction intermediates (RI) and transition states are lowered in dependence of the number of

electrons ($n$) transferred according to Eq. (5) and Eq. (6). In the case of TS, the charge transfer between the two involved states is considered not to be complete, which is characterized by the transfer coefficient, α. Its specific value is usually unknown but for a one-electron transfer step, such as encountered with the Volmer and Heyrovsky steps, α is approximated to be $^1/_2$ based on experimental evidence.[78]

$$\Delta G(\eta) = \Delta G(0) - (n \cdot e \cdot \eta) \quad (5),$$

$$\Delta G^{\#}(\eta) = \Delta G^{\#}(0) - [(n + \alpha) \cdot e \cdot \eta] \quad (6).$$

In equations (5) and (6), $\Delta G(\eta)$ and $\Delta G(0)$ denote the free-energy changes from the initial state (*e.g.*, starting surface) to the final state (*e.g.*, reaction intermediate or product $H_2$) at zero overpotential or any arbitrary $\eta$ value, respectively. Similarly, $\Delta G^{\#}$ is the free-energy change from the initial state to a TS, and $n$ or $e$ indicate the number of electrons transferred or the elementary charge, respectively. Based on this framework, the free-energy profile of the VH mechanism is modified in such a way that the Gibbs free energy of TS $\#_1$ is reduced by $\alpha_1 \cdot e \cdot \eta$ and that of RI by $1 \cdot e \cdot \eta$, TS $\#_2$ is lowered by $(1+\alpha_2) \cdot e \cdot \eta$ and the product state by $2 \cdot e \cdot \eta$, see Figure 4a. In a similar way, for the free-energy profile corresponding to the VT mechanism, the first steps are equally affected in that the values for $\#_1$ is reduced by $\alpha_1 \cdot e \cdot \eta$, that of RI1 by $1 \cdot e \cdot \eta$, that of $\#_2$ by $(1+\alpha_2) \cdot e \cdot \eta$, while for RI2, $\#_3$, and the product state the Gibbs free energy is reduced by $2 \cdot e \cdot \eta$, as no more electrons are transferred in the Tafel step, see Figure 4b.

Recent works on the free-energy landscape in electrocatalysis have demonstrated that not the highest free-energy barrier, $\Delta G^{\#}$, but rather the TS with the highest free energy, $G^{\#}_{\mathrm{rds}}$, governs the kinetics of the overall reaction.[74,79] For the HER, $G^{\#}_{\mathrm{rds}}$ is either given by the free-energy difference between TS $\#_1$ and the starting surface ($G^{\#}_1$) or between TS $\#_2$ and the starting surface ($G^{\#}_2$). As such, the free-energy barriers in the free-energy diagram corresponding to the Volmer-Heyrovsky mechanism are related to the respective TS free energies in Eqs. (7) and (8):

$$G^{\#}_1 = \Delta G^{\#}_1 \quad (7),$$

$$G^{\#}_2 = \Delta G^{\#}_2 + \Delta G_{\mathrm{RI}} \quad (8).$$

Inspecting the free-energy profile of Figure 4a, it turns out that $G_2^{\#}$ corresponds to $G_{\mathrm{rds}}^{\#}$ at $\eta$ = 0 V whereas $G_1^{\#}$ is met with $G_{\mathrm{rds}}^{\#}$ at $\eta$ = 0.2 V. Similarly, for the VT free-energy profile one can define $G_1^{\#}$, $G_2^{\#}$, and $G_3^{\#}$ by referring to Eqs. (9)-(11);

$$G_1^{\#} = \Delta G_1^{\#} \tag{9},$$

$$G_2^{\#} = \Delta G_2^{\#} + \Delta G_{\mathrm{RI1}} \tag{10},$$

$$G_3^{\#} = \Delta G_3^{\#} + \Delta G_{\mathrm{RI2}} \tag{11}.$$

Figure 4b reveals that $G_3^{\#}$ and $G_1^{\#}$ are encountered with $G_{\mathrm{rds}}^{\#}$ at $\eta$ = 0 V and $\eta$ = 0.2 V, respectively.

## 4. Computational Construction of Tafel Plots

Tafel plots indicate the rate of an electrochemical reaction, estimated from the current density, in dependence of the applied overpotential, serving as the driving force for the process. Commonly, a logarithmic plot is used in that the $\log_{10}$ of the current density, $j$, is applied. This finding can be traced to the Tafel equation, which can be derived as approximation for sufficiently large overpotentials from the Butler-Volmer theory:[79,80]

$$\log_{10} j(\eta) = \log_{10} j_0 + \frac{\eta}{b} \tag{12},$$

where $j(\eta)$ and $j_0$ are the current density as a function of the overpotential $\eta$, and the exchange current density, respectively, and $b$ denotes the Tafel slope. The Tafel slope contains information about the transfer coefficient which plays an important role for the reaction kinetics relating to the TS (cf. Eq. (6)).

While the analysis and interpretation of Tafel plots can offer valuable insight into the elementary reaction steps and kinetics, it is not straightforward to translate the energetic picture in terms of the free-energy landscape (*cf.* Figure 4) into a Tafel plot. This requires several assumptions which are discussed in the following. The first aspect refers to the description of the RI coverage. The two common approximations refer to the quasi-equilibrium and steady-state assumptions. The quasi-equilibrium approximation, based on thermodynamic considerations in terms of the law of mass action, assumes that the coverage of the RI remains essentially constant upon increasing overpotential, and thus, the quasi-equilibrium model is only a good choice if coverages are not prone to

change. Yet, it was demonstrated that quasi-equilibrium is a valid approximation if there is a single linear regime in the Tafel plot.[77] In case of the steady-state approximation, the RI coverage is described by the rate constants (kinetics) of the elementary steps, thereby taking alterations in the RI concentration on the electrode surface with increasing overpotential into account. Considering the VH mechanism as depicted in Figure 3a, the time-dependent RI concentration as a function of the applied overpotential is described by Eq. (13):

$$\left(\frac{d([\mathrm{RI}])}{dt}\right)_{\eta} = k_1(\eta)\cdot[\mathrm{IS}] + k_{-2}(\eta)\cdot[\mathrm{FS}] - k_{-1}(\eta)\cdot[\mathrm{RI}] - k_2(\eta)\cdot[\mathrm{RI}] \quad (13),$$

which is deduced from the elementary steps of Eqs. (14) and (15):

$$\mathrm{IS} \underset{k_{-1}}{\overset{k_1}{\rightleftharpoons}} \mathrm{RI} \quad (14),$$

$$\mathrm{RI} \underset{k_{-2}}{\overset{k_2}{\rightleftharpoons}} \mathrm{FS} \quad (15).$$

In the above equations, $k_1(\eta)$ and $k_{-1}(\eta)$ are the forward and backward rate constants of the elementary step in Eq. 14; equally, $k_2(\eta)$ and $k_{-2}(\eta)$ correspond to the forward and backward rate constants of the step in Eq. 15. [IS], [FS], and [RI] are the concentrations of the initial state, final state, and the reaction intermediate, respectively. Please note that depending on the surface configuration of $V_2C$ (*cf.* Table 1), the IS can be either a metal atom, *, or adsorbed hydrogen, *-H. This renders whether the RI corresponds to *-H or * + $H_2$, respectively.

Given that all the RIs within the HER are adsorbed species, we can relate their concentrations to their coverage at the electrode surface. In this context, we redefine [IS] and [FS] as $\theta_S$, and [RI] as $\theta_{S-H}$, where $\theta_S$ and $\theta_{S-H}$ correspond to the coverage of vacant sites or the coverage of adsorbed hydrogen on the MXene surface. Considering the balance of active sites and the steady-state approximation, the two conditions of Eq. (16) and Eq. (17) must be fulfilled.

$$\left(\frac{d([\mathrm{RI}])}{dt}\right)_{\eta} = 0 \quad (16),$$

$$\theta_{\mathrm{S}}(\eta) + \theta_{\mathrm{S\text{-}H}}(\eta) = 1 \quad (17),$$

where the definition or reaction rate is

$$r(\eta) = \frac{d[H_2]}{dt} = k_2(\eta)\cdot\theta_{S\text{-}H}(\eta) - k_{-2}(\eta)\cdot\theta_S(\eta) \quad (18).$$

With this, one can rewrite the reaction rate expression in Eq. (13) as;

$$r(\eta) = \frac{k_1(\eta)\cdot k_2(\eta)}{k_1(\eta) + k_{-1}(\eta) + k_2(\eta) + k_{-2}(\eta)} - \frac{k_{-1}(\eta)\cdot k_{-2}(\eta)}{k_1(\eta) + k_{-1}(\eta) + k_2(\eta) + k_{-2}(\eta)} \quad (19).$$

Finally, we apply Faraday's law to obtain the current density in dependence of the applied overpotential:

$$j(\eta) = n\cdot e\cdot r(\eta)\cdot\Gamma_{act} \quad (20).$$

The substitution of the expression of $r(\eta)$ in Eq. (19) into Eq. (20) leads, after some algebra, to Eq. (21). We additionally make use of the assumption that only the forward reaction is accounted for in the Tafel regime ($\eta$ > 0.03 V),[81] because the overpotential applied is large enough to fairly neglect the backward reaction.

$$j(\eta) = \frac{2k_B T e \Gamma_{act}}{h} \cdot \frac{\exp\left(\frac{(\alpha_1 + \alpha_2)\eta e}{k_B T}\right)}{\exp\left(\frac{G_1^{\#} + \alpha_2 \eta e}{k_B T}\right) + \exp\left(\frac{G_2^{\#} - (1 - \alpha_1)\eta e}{k_B T}\right) + \exp\left(\frac{G_2^{\#} - \Delta G_{RI} + \alpha_1 \eta e}{k_B T}\right)} \quad (21),$$

where $k_B$ is Boltzmann's constant, $T$ the temperature in Kelvin, $h$ is Planck's constant, $e$ is the elementary charge, $\Gamma_{act}$ is the density of active sites in $cm^{-2}$, defined as $\Gamma_{act} = \frac{\text{nº of sites}}{\text{surface area}}$, $\alpha_1$ and $\alpha_2$ are the transfer coefficients of the first and second steps, $G_1^{\#}$ and $G_2^{\#}$ are the TS free energies of the first and second step (*cf.* equations (7) and (8)), and finally, $\Delta G_{RI}$ corresponds to the free energy of the reaction intermediate at $\eta$ = 0. In order to facilitate the calculations and to compare them to experimental values, $j(\eta)$ is not expressed in the international system units but in $A/cm^{-2}$. Please note that the evaluation of Eq. (21) requires knowledge of both the energetics of the thermodynamics and kinetics in terms of $\Delta G$ and $\Delta G^{\#}$, respectively. Based on the evaluation of Eq. (21), it becomes possible to simulate Tafel plots in dependence of the applied overpotential and to correlate the Tafel lines to the rate-determining step, as obtained from free-energy diagrams (*cf.* Figure 4).

However, for reactions with more steps as VT, the steady-state assumption requires a more complex expression since more RIs are involved. Yet, the quasi-equilibrium approach offers a simple alternative to simulate the Tafel plot for the VT mechanism. While the quasi-equilibrium approximation is not able to capture the transitions between linear Tafel regimes, indicating a change in the rate-determining step

of the reaction, it can fairly estimate each linear region individually.[82] Thus, by applying the quasi-equilibrium analysis to each TS allows obtaining three linear regimes, and the least favourable regime is reconciled with the rate-determining step in dependence of the applied overpotential, see Figure 5.

The preceding discussion illustrates that the simulation of Tafel plots requires the knowledge of various quantities, such as $\Delta G$ and $G_s^{\#}$ for the RIs and TSs, respectively. These terms are obtained by DFT calculations, analysing the difference in Gibbs free energies for each individual steps. At zero overpotential, $\Delta G_{RI}$, $\Delta G_1^{\#}$ and $\Delta G_2^{\#}$ are obtained from Eq. (21):

$$\Delta G = \Delta E_{TOT} + \Delta E_{ZPE} - T\Delta S \quad (22).$$

For a free-energy change between two intermediate states, $\Delta G_{RI}$, $\Delta E_{TOT}$ refers to the energy difference between the initial and final states whereas for the free-energy barriers $\Delta G_1^{\#}$ and $\Delta G_2^{\#}$, $\Delta E_{TOT}$ correspond to the energy difference between the initial state and the first or the RI and second TS, respectively. In general, for processes involving *n* steps the total free-energy difference from *n*-1 to *n* is obtained according to Eq. (23) and (24) for RIs and TSs, respectively.

$$\Delta E_{TOT} = E_n - E_{n\text{-}1} \quad (23),$$

or,

$$\Delta E_{TOT}^{\#} = E_n^{\#} - E_{n\text{-}1} \quad (24).$$

In Eq. (22), $\Delta E_{ZPE}$ corresponds to the zero-point energy difference between two consecutive steps, *n*-1 and *n*. In the present study we computed the $\Delta E_{ZPE}$ for the two different surfaces in a slightly different way. For $V_2C$-H we assume that the vibrations of the water layer and the H adsorbate involved in the RIs are decoupled from the vibrations of the MXene, including the H layer of the termination. Therefore, the frequencies taken explicitly into account are those from the extra H and of the water layer. However, for the $V_2C$-OH surface, the vibrations of the OH from the MXene termination are accounted for. The reason for such difference is the nature of the RIs involved on the different MXenes. In the case of $V_2C$-H, the H involved in the RIs are adsorbed on V Top site, and the vibrations can be safely decoupled from those of the rest of the MXene, including the termination. However, in the case of $V_2C$-OH, the RIs directly involve the H atoms form

the OH termination and thus, they must be included. Therefore, the $\Delta E_{\mathrm{ZPE}}$ term is computed within the harmonic approximation, as given in Eqs. (25) and (26);

$$\Delta E_{\mathrm{ZPE}} = \mathrm{ZPE}_n - \mathrm{ZPE}_{n\text{-}1} \tag{25},$$

or,

$$\Delta E^{\#}_{\mathrm{ZPE}} = \mathrm{ZPE}^{\#}_n - \mathrm{ZPE}_{n\text{-}1} \tag{26},$$

and similarly, we can obtain the entropy corrections $T\Delta S$, see Eqs. (27) and (28);

$$T\Delta S = TS_n - TS_{n\text{-}1} \tag{27},$$

or,

$$T\Delta S^{\#} = TS^{\#}_n - \mathrm{TS}_{n\text{-}1} \tag{28}.$$

The entropy containing term in Eqs. (27) and (28) is computed by Eq. (29);[60]

$$TS = k_{\mathrm{B}} N_{\mathrm{A}} T \sum_{\mathrm{i}}^{n} \frac{h\nu_{\mathrm{i}}/k_{\mathrm{B}}T}{\mathrm{e}^{h\nu_{\mathrm{i}}/k_{\mathrm{B}}T} - 1} - \ln\left(1 - \mathrm{e}^{-h\nu_{\mathrm{i}}/k_{\mathrm{B}}T}\right) \tag{29},$$

where besides the variables described already in Eq. (21), $N_{\mathrm{A}}$ is the Avogadro number and $\nu_{\mathrm{i}}$ correspond to the vibrational frequencies of the same normal modes considered in the ZPE calculation.

While the DFT calculations are performed for zero electrode potential, we make use of the computational hydrogen electrode (CHE)[83] approach to describe the potential dependence of the free energy. This framework couples the total energy, the zero-point energy, and entropy of the hydrated proton and electron to half of the free energy of a gaseous $H_2$ molecule. This equilibrium is met for a pressure of 1 bar of $H_2$ in a solution of protons with activity 1 at 298.15K:

$$\mathrm{H}^{+}_{(\mathrm{aq})} + \mathrm{e}^{-} \rightleftharpoons \frac{1}{2}\mathrm{H}_{2(\mathrm{g})},\ @\mathrm{U} = 0\ \mathrm{V}\ \textit{vs.}\ \mathrm{RHE} \tag{30},$$

since in equilibrium $\Delta G = 0$ is fulfilled, it can be concluded:

$$G(\mathrm{H}^{+}_{(\mathrm{aq})}) + G(e^{-}) = \frac{1}{2} G(\mathrm{H}_{2(\mathrm{g})}) \tag{31}.$$

Based on the introduced framework, application of Eq. (21) allows compiling Tafel plots for the different HER mechanisms. Note that to compute the Tafel plot, positive values of the current density $j$, are required due to its logarithmic representation in the Tafel plot. Thus, we recall that we use the absolute values of the current density

and applied overpotential for the discussion of the elementary processes in the HER in the following.

## 5. Results and Discussion

To simplify the discussion, the results for $V_2C$-H and $V_2C$-OH are presented separately and, for each case, the different mechanisms are discussed one after the other.

*The $V_2C$-H case*

We start by considering the Volmer Heyrovsky I (VH-I) path by recalling its mechanistic description according to equations (2) and (3):

$$\text{Volmer Step: } H_3O^+ + e^- + M^* \rightleftharpoons M\text{-}H + H_2O \quad (32),$$

$$\text{Heyrovsky Step: } H_3O^+ + e^- + M\text{-}H \rightleftharpoons M^* + H_2 + H_2O \quad (33).$$

In Eqs. (31) and (32), M* indicates a vacant top site at the water covered $V_2C$-H surface. In the first step, one hydrogen is adsorbed at the top site on the surface, see Eq. (32), and subsequently, a second hydrogen recombines with the adsorbed H atom at the top site to form the final hydrogen molecule, see Eq. (33). This mechanism is only possible for the $V_2C$-H system because the top sites on the $V_2C$-OH surface are sterically hindered.

We discuss in the Supplementary Information (SI) that in principle, hydrogen could also be adsorbed on hollow-C as adsorption site, see Figure S1 of the SI. Using the unit cell described in Section 2, a total of eighteen initial different adsorption sites were evaluated, including direct and indirect adsorptions; see additional details in Figures S2-S4 of the SI. Direct adsorptions imply that one hydrogen atom from the $H_3O^+$ adsorbs in a single step on the respective site. In contrast, indirect adsorption involves two steps in that one H from the $H_3O^+$ moves toward a vicinal water molecule first, and in a second step, the hydrogen atom pointing towards the surface of the acceptor water molecule is adsorbed at the surface.

Our thermodynamic analysis indicates that the RI, adsorbed hydrogen, appears to be more stable when bound to the top site (adsorption free energies ranging from -0.17 to +0.19 eV) rather than on the HollowC site (adsorption free energy of about 0.30 eV; see Table S1 in the SI). When the water layer is rearranged in response to adsorption, there

are several situations where one oxygen atom from the water layer interacts with one V atom from the surface. As the adsorption at the HollowC sites is consistently less energetically favoured than at the top sites, one direct and one indirect HollowC paths are further tested, but we do not find any important differences in terms of the thermodynamic picture. Therefore, hydrogen adsorption on the HollowC site is not further pursued.

Finally, a second hydrogen atom is added to the water layer. This hydrogen atom recombines with the hydrogen species adsorbed on the top site in the Heyrovsky step, and the energetics of the TS is quantified following the same procedure as for the Volmer step. Figure 6 depicts the free-energy diagram of the VH-I mechanism at $\eta$ = 0 V and 0.2 V. Given that the Volmer step reveals higher TS free energy than the Heyrovsky step at $\eta$ = 0 V, the Volmer step is reconciled with the rate-determining step, even if the applied overpotential is enhanced. Consequently, the computational Tafel plot reveals a single linear regime as shown in Figure 7.

Next, we have tested the Volmer-Tafel I (VT-I) over the $V_2C$-H surface, and its mechanistic description is given by Eqs. (34) – (36):

$$\text{Volmer Step: } H_3O^+ + e^- + M^* \rightleftharpoons M\text{-}H + H_2O \quad (34),$$

$$\text{Volmer Step: } H_3O^+ + e^- + M\text{-}H + M^* \rightleftharpoons 2(M\text{-}H) + H_2O \quad (35),$$

$$\text{Tafel Step: } 2(M\text{-}H) \rightleftharpoons 2M^* + H_2 \quad (36).$$

While the Volmer steps of Eqs. (32) and (34) are identical, in contrast to the above-discussed VH-I mechanism, the second step contains the adsorption of a second hydrogen atom (*cf.* Eq. (35)). Finally, the two adsorbed hydrogen species recombine under the formation of gaseous hydrogen in the Tafel step (*cf.* Eq. (36)). We recall that the above mechanistic description can only occur on the $V_2C$-H surface, but cannot take place on the $V_2C$-OH phase.

The RIs of the VT-I mechanism are reconciled with one hydrogen atom (RI1) or two hydrogen atoms (RI2) adsorbed at the top site. The energetics of the first Volmer step, including the free energies of RI1 and the TS1, can be directly taken from the VH mechanism. Regarding the second Volmer Step, the number of possible pathways increases exponentially as each single RI from the previous mechanism can be taken as a starting point. Therefore, several Top and Hollow C sites, including direct and indirect

adsorption, are evaluated. Figure S5-S7 show the adsorption sites tested for the first and second Volmer steps, respectively.

It turns out that hydrogen adsorption at the Top site is energetically preferred over the HollowC site. However, a second hydrogen atom on the surface results in a less favourable adsorption energetics compared to the first Volmer step, revealing adsorption free energies of 0.30 to 0.56 eV. We note that the repulsion of adjacent hydrogen species on solid-state electrodes is well documented in the literature.[84] The kinetic barriers for the Tafel step, however, are surprisingly small, given that these are in the range of 0.32 to 0.61 eV, especially in comparison with the formation barriers of hydrogen on bare MXenes.[58] This can be explained by referring to the surface termination: for $V_2C$-H, the most stable sites of H adsorption (HollowM) are already occupied by hydrogen. Consequently, the less stable top adsorption sites are involved in the formation of the hydrogen molecule, and this leads to a facile kinetics.

Figure 8 shows the Gibbs free energy diagram of the VT-I mechanism at $\eta$ = 0 V and 0.2 V. Both Volmer step TSs require similar barriers, but the second barrier is slightly higher, implying that for low overpotentials, the rate-determining step refers to the second Volmer step. However, when gradually increasing the overpotential, the first Volmer step is reconciled with the kinetic bottleneck. Thus, the Tafel plot for the VT-I mechanism consists of two lineal regimes where the kinetics of the reaction are dominated by the second and first Volmer steps (*cf.* Figure 9).

The last mechanism tested over the $V_2C$-H surface refers to an alternative Volmer-Tafel mechanism (VT-II). Essentially, this mechanism corresponds to the initial VT description, but the order between the Volmer and Tafel steps is changed:

$$\text{Volmer Step: } H_3O^+ + e^- + M^* \rightleftharpoons M\text{-}H + H_2O \quad (37),$$

$$\text{Tafel Step: } M\text{-}H + H_{HM} \rightleftharpoons M'^* + H_2 \quad (38),$$

$$\text{Volmer Step: } H_3O^+ + e^- + M'^* \rightleftharpoons H_{HM} + H_2O \quad (39).$$

The first step in Eq. (37) is identical to the two previous mechanisms. Yet, the adsorbed hydrogen species directly recombines with another hydrogen from the HollowM site —$H_{HM}$ in Eq. (38)— to release a hydrogen molecule (*cf.* Eq. (38)). Finally, the resulting vacancy on the HollowM site is filled up by hydrogen again (*cf.* Eq. (39)). Please, note that M'* stands for the MXene surface with a free HollowM site.

Our calculations reveal though that the Tafel step is blocked. This is mainly related to the fact that hydrogen on the HollowM site is strongly bound, and this majorly hampers the HER kinetics. Therefore, this mechanistic description is not further pursued.

*The $V_2C$-OH case*

The HER over the $V_2C$-OH surface can occur via the Volmer Heyrovsky mechanism, but here the steps are inverted, and thus, this mechanism is denoted as VH-II.

$$\text{Heyrovsky Step: } H_3O^+ + e^- + \text{MO-H} \rightleftharpoons \text{MO*} + H_2 + H_2O \quad (40),$$

$$\text{Volmer Step: } H_3O^+ + e^- + \text{MO*} \rightleftharpoons \text{MO-H} + H_2O \quad (41).$$

First, one hydrogen from the water layer recombines with adsorbed hydrogen from the OH adsorbates on the HollowM sites to form gaseous hydrogen in the Heyrovsky step (*cf.* Eq. (40)). Thereafter, one hydrogen atom from the electrolyte replaces the missing hydrogen atom in the Volmer step (*cf.* Eq. (41)). Consequently, the RI in this mechanism is reconciled with surface oxygen, MO*. We note that for the water ice-like layer, we have used the same initial configuration as for $V_2C$-H, but the final configuration differs slightly upon relaxation. Four different reaction paths have been considered, which are summarized in Figure S8 of the SI.

The RIs for all four paths are extremely stable in comparison to the IS, ~ -3.45 eV. Therefore, regardless of any kinetic barrier this mechanism can already be excluded based on thermodynamic reasoning, and thus, is no longer explored.

Finally, the last evaluated pathway corresponds to a third variant of the Volmer Tafel mechanism (VT-III).

$$\text{Tafel Step: MO-H* + MO-H*} \rightleftharpoons 2\text{MO*} + H_2 \quad (42),$$

$$\text{Volmer Step: } H^+ + e^- + 2\ \text{MO*} \rightleftharpoons \text{MO-H*} + \text{MO*} \quad (43).$$

$$\text{Volmer Step: } H^+ + e^- + \text{MO*} + \text{MO-H*} \rightleftharpoons 2\text{MO-H*} \quad (43).$$

Here, two hydrogen atoms from the OH terminating groups recombine *via* a Tafel step to form gaseous hydrogen (*cf.* Eq. (42)), and afterwards, two hydrogen atoms adsorb on the O-covered moieties to close the catalytic cycle (*cf.* Eqs. (42) and (43)). In this case, the RIs are reconciled with 2 MO* and MO* plus a MO-H*.

Our calculations reveal that the free-energy barrier for the initial Tafel step (about 1.43 eV) is the highest among all investigated barriers studied. Therefore, $G_{rds}^{\#}$ for this mechanism is twice as large as for the VH-I and VT-I mechanisms, and thus, is not further considered.

*Comparison of active sites and mechanisms*

In summary, we have investigated the HER kinetics over the $V_2C$-H and $V_2C$-OH surfaces. Our DFT calculations clearly indicate that $V_2C$-H corresponds to the active site motif under HER conditions in that the vacant top sites are responsible for the formation of gaseous hydrogen. This is an important information given that HollowM rather than top corresponds to the energetically preferred adsorption site of $V_2C$ under HER conditions. Using thermodynamic considerations by determining the free energy of adsorbed hydrogen only would likely result in an incorrect result since the hydrogen bond strength on the energetically favoured HollowM site would be evaluated, and this binding energy cannot be related via BEP relation to the kinetics of the HER over the top sites, as resolved in this study. This finding emphasizes the danger of hasty conclusions by thermodynamic approaches and equally underpins the importance of kinetic studies to resolve the entire free-energy landscape.

Relating to the $V_2C$-H surface, we have demonstrated that two mechanistic descriptions are possible, namely the VH-I and VT-I pathways. Figure 10 shows a comparison of the Tafel plot for the two mechanistic descriptions. While for small overpotentials the VH-I mechanism is energetically preferred, it is evident that for larger overpotentials the VT-I pathway is kinetically favoured. This finding can be explained by the fact that with increasing overpotential, the coverage of adsorbed hydrogen on the top site increases, which facilitates the chemical recombination of two adjacent hydrogen atoms on the top sites compared to the electrochemical Heyrovsky step in the VH-I mechanism. The obtained results in terms of the top sites as active species for the HER and the Volmer-Tafel mechanism as the preferred mechanistic description for large overpotentials is somewhat reminiscent of the HER over Pt(111),[61,85] and this may be another cornerstone why MXenes are promising electrocatalysts for the generation of hydrogen. Especially, because Mxenes are 2D versions of transition metal carbide materials,[86] which are known to behave like Pt-group metals in catalysis.[87] Finally, by comparing the Tafel plots of the VH-I and VT-I mechanism with an experimentally reported Tafel plot of the HER over $V_2C$, we observe the impact of the MXene

termination (*OH- vs. *H-covered surface) on the electrocatalytic performance. The experimentally reported Tafel plot[88] indicates that $V_2C$ is not active toward the HER in the potential regime of -0.5 V < U vs. RHE < 0 V. We trace this finding to the presence of the *OH-covered surface under these potential conditions (cf. section 2), given that we demonstrated that the HER kinetics of this surface termination is poor. On the contrary, the experimental Tafel plot indicates hydrogen formation for U < -0.5 V vs. RHE, and this can be explained by the presence of the *H-covered surface, which has a facile kinetics according to our first-principles study. Consequently, the HER kinetics of $V_2C$ can be tuned if the transition from the kinetically inactive *OH phase to the active *H phase is shifted toward more positive potentials and ideally occurs at about $U = 0$ V vs. RHE.

## 5. Conclusions

Taking $V_2C$ (0001) as a representative case of the MXene family, five different hydrogen evolution reaction (HER) mechanisms have been studied for two different surface terminations, which are chosen based on the Pourbaix diagram under HER conditions. The $V_2C$ (0001) surface is either covered by *H or *OH on HollowM sites, and we explicitly account for the presence of water by considering an ice-like monolayer in our simulations.

The present study pinpoints that, despite the availability of a plethora of hydrogen adsorbates on the $V_2C$ surface, the HER is more complex than initially thought. We demonstrate that the *OH termination does not show catalytic activity toward hydrogen formation but rather the *H-covered surface corresponds to the active motif under HER conditions. However, the active hydrogen atoms adsorb on the unoccupied top sites and are not reconciled with the energetically preferred HollowM site. We study the Volmer-Heyrovsky and Volmer-Tafel mechanisms over the H-covered surface, construct free-energy diagrams by resolving the thermodynamics (reaction intermediates) and kinetics (transition states) from density functional theory (DFT), and compile Tafel plots by applying a rigorous microkinetic framework.

Our simulations reveal that the Volmer-Heyrovsky pathway corresponds to the preferred mechanistic description for small overpotentials whereas the Volmer-Tafel path becomes kinetically preferred for larger overpotentials. The obtained results are surprisingly similar to the HER over Pt, thus providing evidence why MXenes are potential electrocatalysts for the formation of gaseous hydrogen by means of

electrochemical water splitting. Also, our combined approach consisting of DFT calculations and microkinetic considerations may serve as a guideline of how to unravel the elementary steps of electrocatalytic processes, such as for the HER, by moving beyond the prototypical thermodynamic framework focusing on adsorption free energies only.

**Acknowledgements**

The research carried out at the *Universitat de Barcelona* has been supported by the Spanish MCIN/AEI/10.13039/501100011033 PID2021-126076NB-I00 project, funded partially by FEDER *Una manera de hacer Europa*, and *María de Maeztu* CEX2021-001202-M grants, including funding from European Union and, in part, by and COST Action CA18234. A significant part of the computational resources has been provided by the *Red Española de Supercomputación* (RES) QS-2020-2-0004 and QS-2020-1-0011. M.L. thanks *Universitat de Barcelona* for an APIF predoctoral contract, the HPC-EUROPA3 (INFRAIA-2016-1-730897) project supported by the EC Research Innovation Action under the H2020 Programme, the University of Duisburg-Essen and the High Performance Computing Center Stuttgart (HRLS) for supporting his stay in Essen. K.S.E. acknowledges funding by the Ministry of Culture and Science of the Federal State of North Rhine-Westphalia (NRW Return Grant). K.S.E. is associated with the CRC/TRR247: "Heterogeneous Oxidation Catalysis in the Liquid Phase" (Project number 388390466-TRR 247), the RESOLV Cluster of Excellence, funded by the Deutsche Forschungsgemeinschaft under Germany's Excellence Strategy – EXC 2033-390677874 – RESOLV, and the Center for Nanointegration (CENIDE).

**Table 1.** Description of the five HER mechanisms over $V_2C$ considered in the present study. The mechanism column defines the label for the studied Volmer-Heyrovsky (VH) and Volmer-Tafel (VT) mechanisms. The last three columns correspond to the order of the steps for each pathway.

| MXene | Mechanism | Step I | Step II | Step III |
|---|---|---|---|---|
| $V_2C$-H | VH-I | Volmer Step | Heyrovsky Step | |
| | VT-I | Volmer Step | Volmer Step | Tafel Step |
| | VT-II | Volmer Step | Tafel Step | Volmer Step |
| $V_2C$-OH | VH-II | Heyrovsky Step | Volmer Step | |
| | VT-III | Tafel Step | Volmer Step | Volmer Step |

**Figure 1.** Top and side views of the *p*(3×3) supercells used to represent a $V_2C$ (0001) basal surface terminated by H (right) and OH (left) with the surface covered by 6 water molecules in an ice-shaped structure. Metal atoms at the top and bottom layers are represented by bright and light purple spheres while C atoms are represented by dark brown spheres. H atoms adsorbed on the surface and on the water layer are shown as white and pink spheres, respectively, with O atoms shown as red spheres.

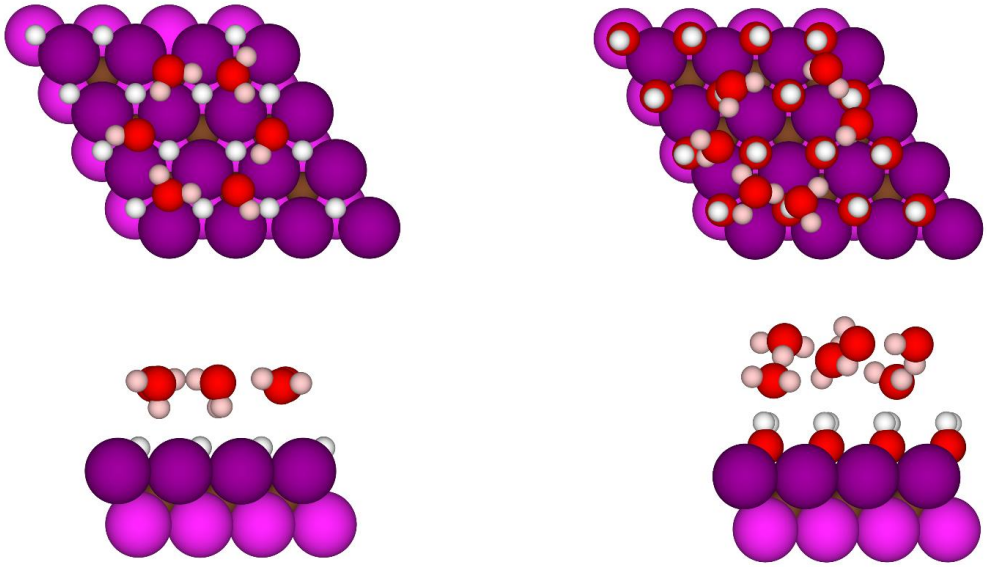

**Figure 2.** Schematic view of the two main HER mechanisms. The cycle with green arrows corresponds to the Volmer-Tafel (VT) mechanism whereas orange arrows refer to the description of Volmer-Heyrovsky (VH). Note that the first step, starting on the top of each cycle is the same for both VT and VH, but the formation of $H_2$ in the VT mechanism is of chemical nature whereas it is an electrochemical step in the VH pathway. Adsorbed H atoms, $H^+$ ions, and electrons are depicted by white, pink, and red spheres, respectively, while the rest of the colour coding is specified in Figure 1.

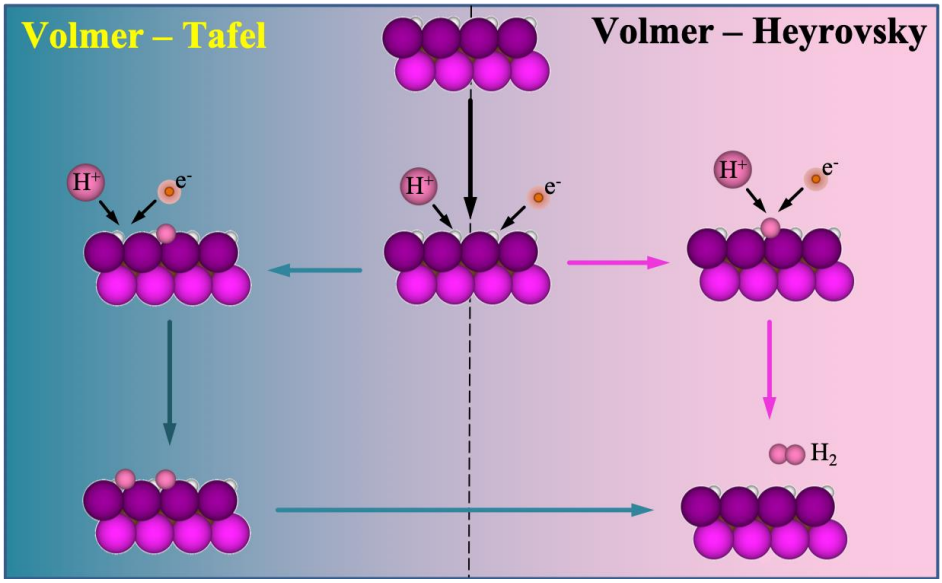

**Figure 3.** Schematic representation of the initial steps for the HER that are possible for the *H and *OH terminated $V_2C$ surface. In case of the $V_2C$-H surface (left image), the Volmer step is the first one because incoming H (shown in pink) can be adsorbed on a vacant surface site (Top). However, the Heyrovsky and Tafel steps are forbidden as the first step because hydrogen at the surface (HollowM) is adsorbed too strongly (*e.g.* $\Delta G$ = -1.05 eV). On the contrary, for the $V_2C$-OH surface (right image), the adsorption sites for H adsorption are sterically blocked by the OH adsorbates on the hollow M position, and consequently, the Volmer step is restrained. Therefore, the mechanistic cycle starts with the release of gaseous hydrogen from the OH groups by a Heyrovsky or a Tafel step.

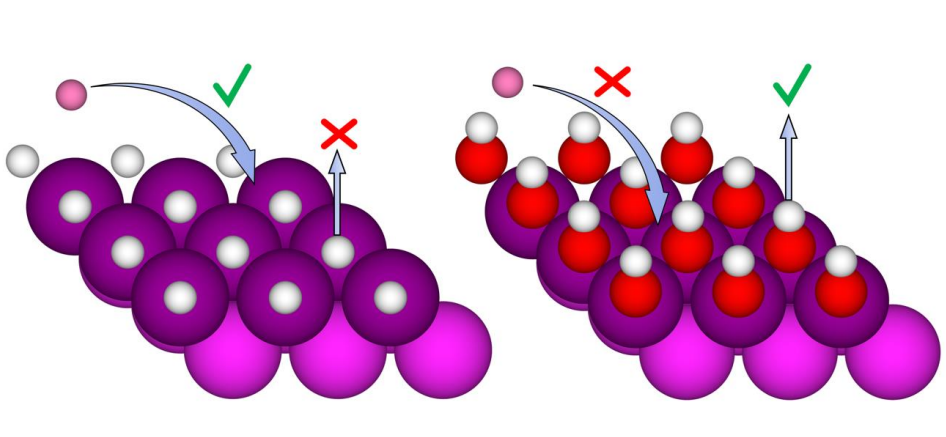

**Figure 4.** Schematic representation of an arbitrarily chosen Gibbs free energy profile based on the $V_2C$-H model for the Volmer-Heyrovsky (a) and Volmer-Tafel (b) mechanisms at $\eta$ = 0 V and $\eta$ = 0.2 V in blue and orange, respectively. The initial state (IS) is depicted in black. The final state (FS) and the reaction intermediate (RI) are depicted by a solid line while transition states (TSs) are marked as $\#_n$ ($n$ = 1, 2) by dashed lines. $G_{RIx}(0)$ and $G_{RIx}(0.2)$ are the corresponding free energies for the reaction intermediate at $\eta$ = 0 V and $\eta$ = 0.2 V, respectively. $G_{rds}^{\#}(0)$ and $G_{rds}^{\#}(0.2)$ correspond to the transition state with highest free energy in dependence of the applied overpotential,. Finally, $\Delta G_2^{\#}$ in light blue corresponds to the barrier of the second elementary step in panel a).

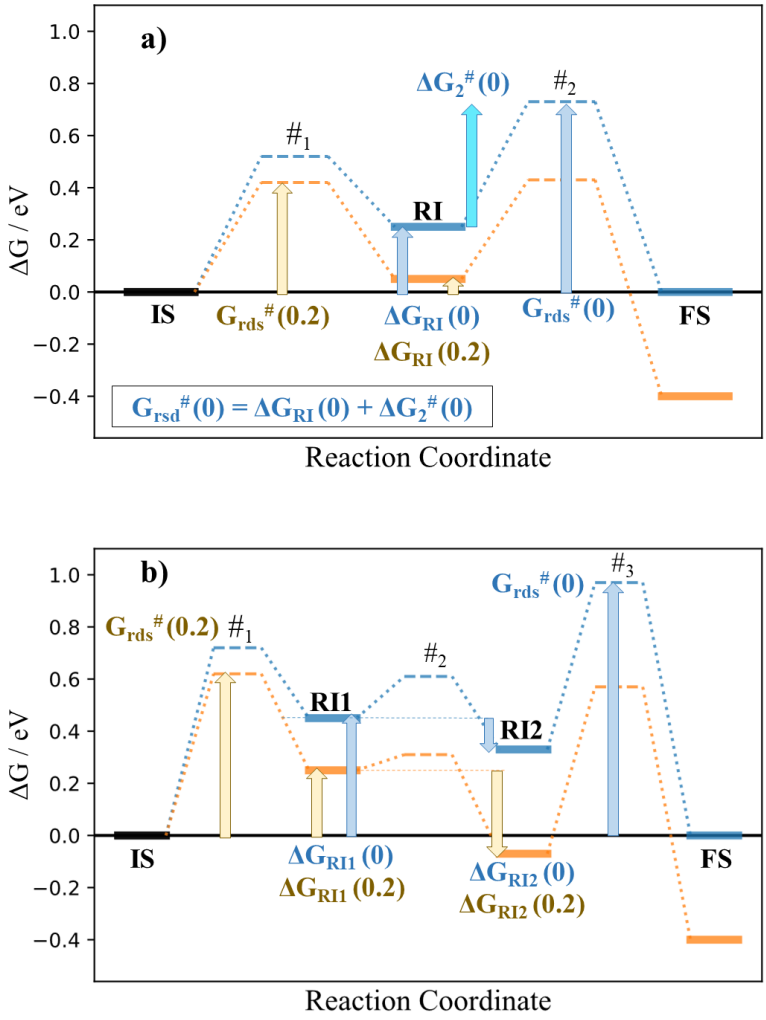

**Figure 5.** Schematic representation of linear Tafel regimes for an arbitrary chosen Volmer-Tafel mechanism. While in a) the linear regimes derived from all the three steps of the mechanism are depicted, and b) shows the final Tafel plot. Green, red, and blue lines indicate the current density in dependence of the applied overpotential for each elementary step. In the present figure, the 3rd step, in blue, governs the kinetics of the reaction for small overpotentials ($\eta$ < 0.1 V) whereas the 1st step, in green, is reconciled with the kinetic bottleneck for larger overpotentials ($\eta$ > 0.13 V). Consequently, the Tafel plot of the V-T mechanism consists of two linear regimes. The transition between the two linear regimes, indicating a change in the rate-determining step, is not captured by the quasi-equilibrium assumption.

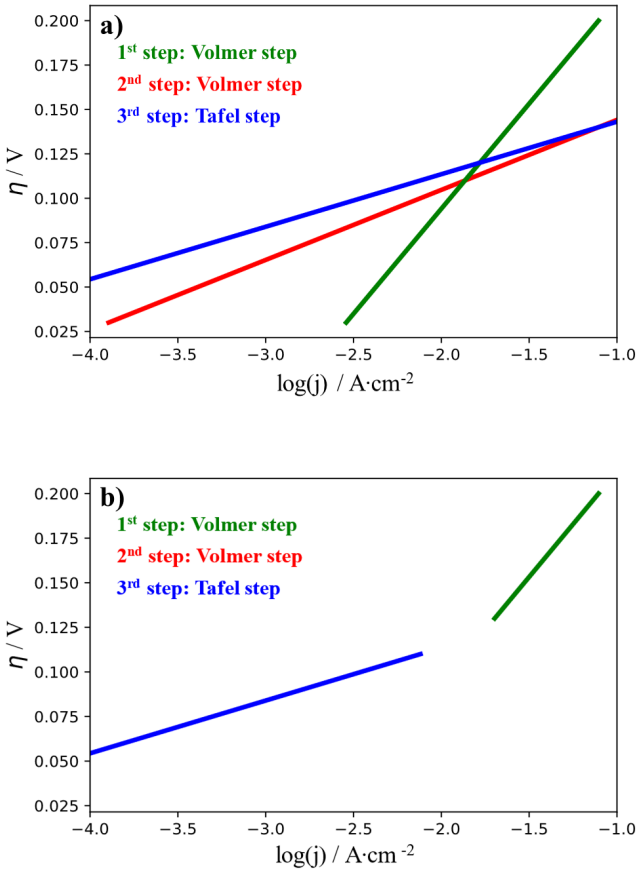

**Figure 6.** Free-energy diagram for the VH-I mechanism over the $V_2C$-H surface at $\eta$ = 0 V and $\eta$ = 0.2 V in blue and orange, respectively. While the initial state (IS) is depicted in black, the reaction intermediate (RI) and final state (FS) are indicated by blue solid lines. Transition states (TS) are marked by dashed lines.

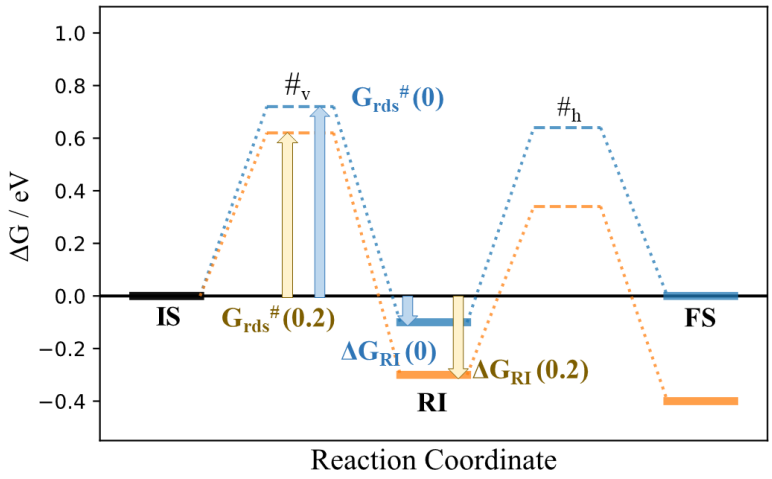

**Figure 7.** Simulated Tafel plot of the HER over $V_2C$-H via the Volmer-Heyrovsky mechanism as obtained from the free-energy landscape of Figure 6. Given that the first transition state of the mechanism is higher in free energy than the second transition state, the mechanism is limited by a single step, and hence, the Tafel plot reveals a single linear regime.

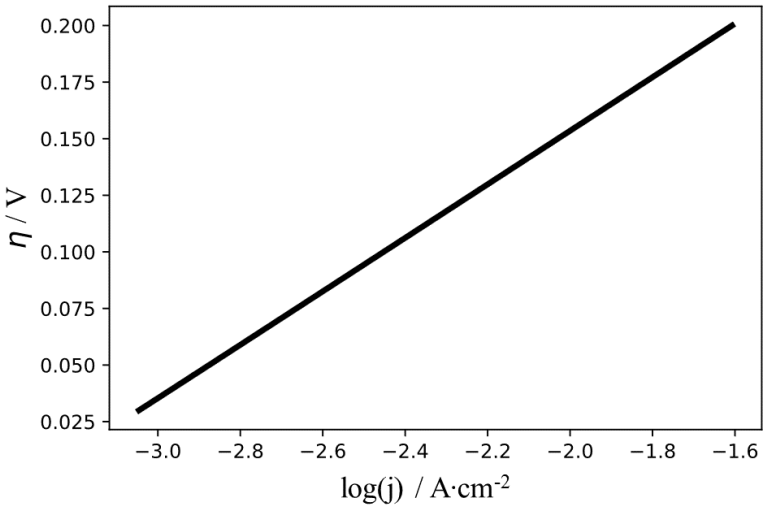

**Figure 8.** Free-energy diagram for the Volmer-Tafel mechanism at $\eta$ = 0 V and $\eta$ = 0.2 V in blue and orange, respectively. While the initial state (IS) is depicted in black, the reaction intermediate (RI) and final state (FS) are indicated by blue solid lines. Transition states (TS) are marked by dashed lines.

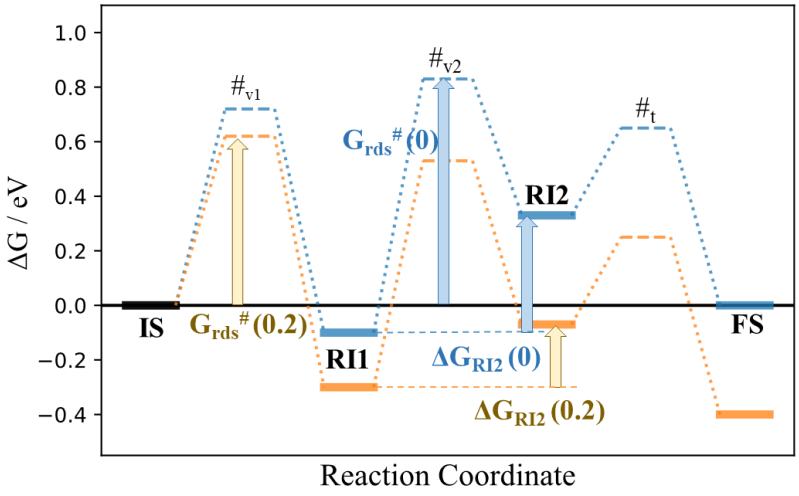

**Figure 9.** Simulated Tafel plot of the HER over $V_2C$-H via the Volmer-Tafel mechanism as obtained from the free-energy landscape of Figure 8. Two linear regimes are obtained in that the second Volmer steps limits the rate for small overpotentials whereas the first Volmer step becomes rate determining for large overpotentials.

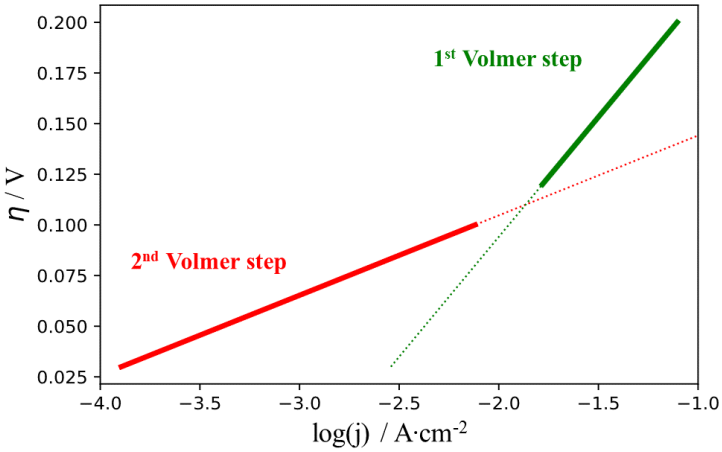

**Figure 10.** Simulated Tafel plots of the HER over $V_2C$-H via the Volmer-Heyrovsky and Volmer-Tafel mechanisms in blue and black, respectively as obtained from the free-energy landscape of Figures 6 and 8. For small applied overpotential, $\eta \sim 0.07$ V, the Volmer- Heyrovsky mechanism is kinetically preferred whereas for larger overpotentials the Volmer-Tafel mechanism describes the reaction rate.

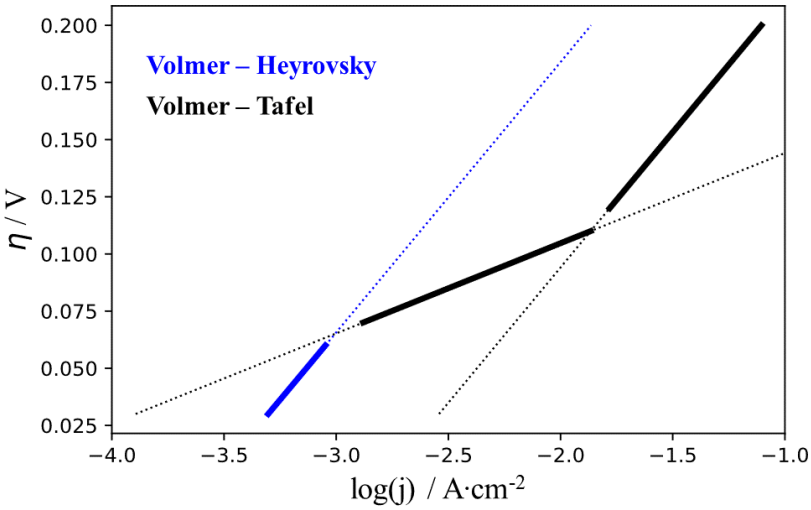

**References**


(1) UN Doc FCCC/CP/1997/7/Add.1. Kyoto Protocol to the United Nations Framework Convention on Climate Change Dec. 10, 1997; 37 ILM 22 1998.

(2) UN Doc FCCC/CP/2009/L.7, Copenhagen Accord.18 December 2009.

(3) UN Doc FCCC/CP/2015/7, Paris Agreement, 2015.

(4) UN Doc FCCC/CP/2021/L.13, Glasgow Climate Pact, 2021.

(5) IEA (2021), Global Energy Review 2021, IEA, Paris

(6) Chu, S.; Majumdar, A. Opportunities and Challenges for a Sustainable Energy Future. *Nature* **2012**, *488* (7411), 294–303.

(7) Nocera, D. G.; Lewis, N. S. Powering the Planet: Chemical Challenges in Solar Energy Utilization. *Proc. Natl. Acad. Sci. U.S.A* **2006**, *103* (42), 15729–15735.

(8) Dincer, I.; Zamfirescu, C. *Sustainable Hydrogen Production*; Elsevier, Ed.; 2016.

(9) Crabtree, G. W.; Dresselhaus, M. S.; Buchanan, M. V. The Hydrogen Economy. *Phys. Today* **2004**, *57* (12), 39–44.

(10) Li, Y.; Liu, W.; Zhang, Z.; Du, X.; Yu, L.; Deng, Y. A Self-Powered Electrolytic Process for Glucose to Hydrogen Conversion. *Commun. Chem.* **2019**, *2* (1), 1–9.

(11) Gao, X.; Zhang, H.; Li, Q.; Yu, X.; Hong, Z.; Zhang, X.; Liang, C.; Lin, Z. Hierarchical $NiCo_2O_4$ Hollow Microcuboids as Bifunctional Electrocatalysts for Overall Water-Splitting. *Angew. Chemie - Int. Ed.* **2016**, *55* (21), 6290–6294.

(12) Wang, J.; Gao, Y.; Chen, D.; Liu, J.; Zhang, Z.; Shao, Z.; Ciucci, F. Water Splitting with an Enhanced Bifunctional Double Perovskite. *ACS Catal.* **2018**, *8* (1), 364–371.

(13) Du, P.; Eisenberg, R. Catalysts Made of Earth-Abundant Elements (Co, Ni, Fe) for Water Splitting: Recent Progress and Future Challenges. *Energy Environ. Sci.* **2012**, *5* (3), 6012–6021.

(14) Hansen, J. N.; Prats, H.; Toudahl, K. K.; Mørch Secher, N.; Chan, K.; Kibsgaard, J.; Chorkendorff, I. Is There Anything Better than Pt for HER? *ACS Energy Lett.* **2021**, *6* (4), 1175–1180.

(15) Gutić, S. J.; Dobrota, A. S.; Fako, E.; Skorodumova, N. V.; López, N.; Pašti, I. A. Hydrogen Evolution Reaction-from Single Crystal to Single Atom Catalysts. *Catalysts* **2020**, *10* (3), 290.

(16) Tahir, M.; Pan, L.; Idrees, F.; Zhang, X.; Wang, L.; Zou, J. J.; Wang, Z. L. Electrocatalytic Oxygen Evolution Reaction for Energy Conversion and Storage: A Comprehensive Review. *Nano Energy* **2017**, *37* (May), 136–157.

(17) Samanta, B.; Morales-García, Á.; Illas, F.; Goga, N.; Anta, J. A.; Calero, S.; Bieberle-Hütter, A.; Libisch, F.; Muñoz-García, A. B.; Pavone, M.; Caspary Toroker, M. Challenges of Modeling Nanostructured Materials for Photocatalytic Water Splitting. *Chem. Soc. Rev.* **2022**, 3794–3818.

(18) Zhong, Y.; Xia, X.; Shi, F.; Zhan, J.; Tu, J.; Fan, H. J. Transition Metal Carbides and Nitrides in Energy Storage and Conversion. *Adv. Sci.* **2016**, *3* (5), 1500286.

(19) Chen, W. F.; Muckerman, J. T.; Fujita, E. Recent Developments in Transition Metal Carbides and Nitrides as Hydrogen Evolution Electrocatalysts. *Chem. Commun.* **2013**, *49* (79), 8896–8909.

(20) Chen, W. F.; Wang, C. H.; Sasaki, K.; Marinkovic, N.; Xu, W.; Muckerman, J. T.; Zhu, Y.; Adzic, R. R. Highly Active and Durable Nanostructured Molybdenum Carbide Electrocatalysts for Hydrogen Production. *Energy Environ. Sci.* **2013**, *6* (3), 943–951.

(21) Voiry, D.; Yamaguchi, H.; Li, J.; Silva, R.; Alves, D. C. B.; Fujita, T.; Chen, M.; Asefa, T.; Shenoy, V. B.; Eda, G.; Chhowalla, M. Enhanced Catalytic Activity in Strained Chemically Exfoliated WS 2 Nanosheets for Hydrogen Evolution. *Nat. Mater.* **2013**, *12* (9), 850–855.

(22) Voiry, D.; Yamaguchi, H.; Li, J.; Silva, R.; Alves, D. C. B.; Fujita, T.; Chen, M.; Asefa, T.; Shenoy, V. B.; Eda, G.; Chhowalla, M. Enhanced Catalytic Activity in Strained Chemically Exfoliated $WS_2$ Nanosheets for Hydrogen Evolution. *Nat. Mater.* **2013**, *12* (9), 850–855.

(23) Jaramillo, T. F.; Jørgensen, K. P.; Bonde, J.; Nielsen, J. H.; Horch, S.; Chorkendorff, I. Identification of Active Edge Sites for Electrochemical $H_2$ Evolution from $MoS_2$ Nanocatalysts. *Science.* **2007**, *317* (5834), 100–102.

(24) Popczun, E. J.; Read, C. G.; Roske, C. W.; Lewis, N. S.; Schaak, R. E. Highly Active Electrocatalysis of the Hydrogen Evolution Reaction by Cobalt Phosphide Nanoparticles. *Angew. Chemie - Int. Ed.* **2014**, *53* (21), 5427–5430.

(25) Yoon, H.; Song, H. J.; Ju, B.; Kim, D. W. Cobalt Phosphide Nanoarrays with Crystalline-Amorphous Hybrid Phase for Hydrogen Production in Universal-PH. *Nano Res.* **2020**, *13* (9), 2469–2477.

(26) Popczun, E. J.; McKone, J. R.; Read, C. G.; Biacchi, A. J.; Wiltrout, A. M.; Lewis, N. S.; Schaak, R. E. Nanostructured Nickel Phosphide as an Electrocatalyst for the Hydrogen Evolution Reaction. *J. Am. Chem. Soc.* **2013**, *135* (25), 9267–9270.

(27) Liu, L.; Xu, Q.; Zhu, Q. Electrically Conductive Metal–Organic Frameworks for Electrocatalytic Applications. *Adv. Energy Sustain. Res.* **2021**, *2* (11), 2100100.

(28) Dong, R.; Pfeffermann, M.; Liang, H.; Zheng, Z.; Zhu, X.; Zhang, J.; Feng, X. Large-Area, Free-Standing, Two-Dimensional Supramolecular Polymer Single-Layer Sheets for Highly Efficient Electrocatalytic Hydrogen Evolution. *Angew. Chemie - Int. Ed.* **2015**, *54* (41), 12058–12063.

(29) Clough, A. J.; Yoo, J. W.; Mecklenburg, M. H.; Marinescu, S. C. Two-Dimensional Metal-Organic Surfaces for Efficient Hydrogen Evolution from Water. *J. Am. Chem. Soc.* **2015**, *137* (1), 118–121.

(30) Gogotsi, Y.; Anasori, B. The Rise of MXenes. *ACS Nano* **2019**, *13* (8), 8491–8494.

(31) Morales-García, Á.; Calle-Vallejo, F.; Illas, F. MXenes: New Horizons in Catalysis. *ACS Catal.* **2020**, *10* (22), 13487–13503.

(32) Naguib, M.; Mashtalir, O.; Carle, J.; Presser, V.; Lu, J.; Hultman, L.; Gogotsi, Y.; Barsoum, M. W. Two-Dimensional Transition Metal Carbides. *ACS Nano* **2012**, *6* (2), 1322–1331.

(33) Naguib, M.; Barsoum, M. W.; Gogotsi, Y. Ten Years of Progress in the Synthesis and Development of MXenes. *Adv. Mater.* **2021**, *33* (39), 2103393.

(34) Gouveia, J. D.; Morales-García, Á.; Viñes, F.; Gomes, J. R. B.; Illas, F. MXenes à La Carte: Tailoring the Epitaxial Growth Alternating Nitrogen and Transition Metal Layers. *ACS Nano* **2022**, *16* (8), 12541–12552.

(35) Liu, S.; Song, Z.; Jin, X.; Mao, R.; Zhang, T.; Hu, F. MXenes for Metal-Ion and Metal-Sulfur Batteries: Synthesis, Properties, and Electrochemistry. *Mater. Reports Energy* **2022**, *2* (1), 100077.

(36) Liang, X.; Garsuch, A.; Nazar, L. F. Sulfur Cathodes Based on Conductive MXene Nanosheets for High-Performance Lithium-Sulfur Batteries. *Angew. Chemie - Int. Ed.* **2015**, *54* (13), 3907–3911

(37) Wang, X.; Kajiyama, S.; Iinuma, H.; Hosono, E.; Oro, S.; Moriguchi, I.; Okubo, M.; Yamada, A. Pseudocapacitance of MXene Nanosheets for High-Power Sodium-Ion Hybrid Capacitors. *Nat. Commun.* **2015**, *6*, 6544.

(38) Rasool, K.; Helal, M.; Ali, A.; Ren, C. E.; Gogotsi, Y.; Mahmoud, K. A. Antibacterial Activity of $Ti_3C_2T_x$ MXene. *ACS Nano* **2016**, *10* (3), 3674–3684.

(39) Morales-Salvador, R.; Morales-García, Á.; Viñes, F.; Illas, F. Two-Dimensional Nitrides as Highly Efficient Potential Candidates for $CO_2$ Capture and Activation. *Phys. Chem. Chem. Phys.* **2018**, *20* (25), 17117–17124.

(40) Morales-García, Á.; Fernández-Fernández, A.; Viñes, F.; Illas, F. $CO_2$ Abatement Using Two-Dimensional MXene Carbides. *J. Mater. Chem. A* **2018**, *6* (8), 3381–3385.

(41) Persson, I.; Halim, J.; Lind, H.; Hansen, T. W.; Wagner, J. B.; Näslund, L. Å.; Darakchieva, V.; Palisaitis, J.; Rosen, J.; Persson, P. O. Å. 2D Transition Metal Carbides (MXenes) for Carbon Capture. *Adv. Mater.* **2019**, *31* (2), 1805472.

(42) Li, N.; Chen, X.; Ong, W. J.; Macfarlane, D. R.; Zhao, X.; Cheetham, A. K.; Sun, C. Understanding of Electrochemical Mechanisms for $CO_2$ Capture and Conversion into Hydrocarbon Fuels in Transition-Metal Carbides (MXenes). *ACS Nano* **2017**, *11* (11), 10825–10833.

(43) Handoko, A. D.; Steinmann, S. N.; Seh, Z. W. Theory-Guided Materials Design: Two-Dimensional MXenes in Electro- and Photocatalysis. *Nanoscale Horizons* **2019**, *4* (4), 809–827.

(44) Hou, P.; Tian, Y.; Jin, D.; Liu, X.; Xie, Y.; Du, F.; Meng, X. Advances in Theoretical Calculations of MXenes as Hydrogen and Oxygen Evolution Reaction (Water Splitting) Electrocatalysts. *J. Phys. D. Appl. Phys.* **2022**, *55* (46).

(45) Browne, M. P.; Tyndall, D.; Nicolosi, V. The Potential of MXene Materials as a Component in the Catalyst Layer for the Oxygen Evolution Reaction. *Curr. Opin. Electrochem.* **2022**, *34*, 101021.

(46) Seh, Z. W.; Fredrickson, K. D.; Anasori, B.; Kibsgaard, J.; Strickler, A. L.; Lukatskaya, M. R.; Gogotsi, Y.; Jaramillo, T. F.; Vojvodic, A. Two-Dimensional Molybdenum Carbide (MXene) as an Efficient Electrocatalyst for Hydrogen Evolution. *ACS Energy Lett.* **2016**, *1* (3), 589–594.

(47) Nørskov, J. K.; Bligaard, T.; Logadottir, A.; Kitchin, J. R.; Chen, J. G.; Pandelov, S.; Stimming, U. Trends in the Exchange Current for Hydrogen Evolution. *J. Electrochem. Soc.* **2005**, *152* (3), J23.

(48) Ling, C.; Shi, L.; Ouyang, Y.; Wang, J. Searching for Highly Active Catalysts for Hydrogen Evolution Reaction Based on O-Terminated MXenes through a Simple Descriptor. *Chem. Mater.* **2016**, *28* (24), 9026–9032.

(49) Jin, D.; Johnson, L. R.; Raman, A. S.; Ming, X.; Gao, Y.; Du, F.; Wei, Y.; Chen, G.; Vojvodic, A.; Gogotsi, Y.; Meng, X. Computational Screening of 2D Ordered Double Transition-Metal Carbides (MXenes) as Electrocatalysts for Hydrogen Evolution Reaction. *J. Phys. Chem. C* **2020**, *124* (19), 10584–10592.

(50) Pandey, M.; Thygesen, K. S. Two-Dimensional MXenes as Catalysts for Electrochemical Hydrogen Evolution: A Computational Screening Study. *J. Phys. Chem. C* **2017**, *121* (25), 13593–13598.

(51) Kang, Z.; Khan, M. A.; Gong, Y.; Javed, R.; Xu, Y.; Ye, D.; Zhao, H.; Zhang, J. Recent Progress of MXenes and MXene-Based Nanomaterials for the Electrocatalytic Hydrogen Evolution Reaction. *J. Mater. Chem. A* **2021**, *9* (10), 6089–6108.

(52) Handoko, A. D.; Fredrickson, K. D.; Anasori, B.; Convey, K. W.; Johnson, L. R.; Gogotsi, Y.; Vojvodic, A.; Seh, Z. W. Tuning the Basal Plane Functionalization of Two-Dimensional Metal Carbides (MXenes) to Control Hydrogen Evolution Activity. *ACS Appl. Energy Mater.* **2018**, *1* (1), 173–180.

(53) Gao, G.; O'Mullane, A. P.; Du, A. 2D MXenes: A New Family of Promising Catalysts for the Hydrogen Evolution Reaction. *ACS Catal.* **2017**, *7* (1), 494–500.

(54) Exner, K. S.; Over, H. Kinetics of Electrocatalytic Reactions from First-Principles: A Critical Comparison with the Ab Initio Thermodynamics Approach. *Acc. Chem. Res.* **2017**, *50* (5), 1240–1247.

(55) Exner, K. S. Does a Thermoneutral Electrocatalyst Correspond to the Apex of a Volcano Plot for a Simple Two-Electron Process? *Angew. Chemie - Int. Ed.* **2020**, *59* (26), 10236–10240.

(56) Gomes, J. R. B.; Bofill, J. M.; Illas, F. Azomethane Decomposition Catalyzed by Pt(111): An Example of Anti-Brönsted-Evans-Polanyi Behavior. *J. Phys. Chem. C* **2008**, *112* (4), 1072–1080.

(57) Gouveia, J. D.; Morales-García, Á.; Viñes, F.; Illas, F.; Gomes, J. R. B. MXenes as Promising Catalysts for Water Dissociation. *Appl. Catal. B Environ.* **2020**, *260*, 118191.

(58) López, M.; Morales-García, Á.; Viñes, F.; Illas, F. Thermodynamics and Kinetics of Molecular Hydrogen Adsorption and Dissociation on MXenes: Relevance to Heterogeneously Catalyzed Hydrogenation Reactions. *ACS Catal.* **2021**, *11* (21), 12850–12857.

(59) Gouveia, J. D.; Morales-García, ángel; Viñes, F.; Gomes, J. R. B.; Illas, F. Facile Heterogeneously Catalyzed Nitrogen Fixation by MXenes. *ACS Catal.* **2020**, *10* (9), 5049–5056.

(60) López, M.; Exner, K. S.; Viñes, F.; Illas, F. Computational Pourbaix Diagrams for MXenes: A Key Ingredient toward Proper Theoretical Electrocatalytic Studies. *Adv. Theory Simulations* **2022**, 2200217.

(61) Lindgren, P.; Kastlunger, G.; Peterson, A. A. A Challenge to the G ∼0 Interpretation of Hydrogen Evolution. *ACS Catal.* **2020**, *10* (1), 121–128.

(62) Tang, M. T.; Liu, X.; Ji, Y.; Norskov, J. K.; Chan, K. Modeling Hydrogen Evolution Reaction Kinetics through Explicit Water–Metal Interfaces. *J. Phys. Chem. C* **2020**, *124* (51), 28083–28092.

(63) Hohenberg, P.; Kohn, W. Inhomogeneous Electron Gas. *Phys. Rev.* **1964**, *136* (3B), B864–B871.

(64) Kohn, W.; J. Sham, L. Self-Consistent Equatios Including Exchange and Correlation Effects. *Phys. Rev.* **1965**, *140* (4A), A1133–A1138.

(65) Kresse, G.; Hafner, J. Norm-Conserving and Ultrasoft Pseudopotentials for First-Row and Transition Elements. *J. Phys. Condens. Matter* **1994**, *6* (40), 8245–8257.

(66) Kresse, G.; Furthmüller, J. Efficient Iterative Schemes for Ab Initio Total-Enery Calculations Using a Plane-Wave Basis Set. *Phys. Rev. B* **1996**, *54*, 11169–11186.

(67) Kresse, G.; Furthmüller, J. Efficiency of Ab-Initio Total Energy Calculations for Metals and Semiconductors Using a Plane-Wave Basis Set. *Comput. Mater. Sci.* **1996**, *6* (1), 15–50.

(68) Perdew, J. P.; Burke, K.; Ernzerhof, M. Generalized Gradient Approximation Made Simple. *Phys. Rev. Lett.* **1996**, *77* (18), 3865–3868.

(69) Grimme, S.; Antony, J.; Ehrlich, S.; Krieg, H. A Consistent and Accurate Ab Initio Parametrization of Density Functional Dispersion Correction (DFT-D) for the 94 Elements H-Pu. *J. Chem. Phys.* **2010**, *132* (15), 154104.

(70) Blöchl, P. E. Projector Augmented-Wave Method. *Phys. Rev. B* **1994**, *50* (24), 17953–17979.

(71) Kresse, G.; Joubert, D. From Ultrasoft Pseudopotentials to the Projector Augmented-Wave Method. *Phys. Rev. B - Condens. Matter Mater. Phys.* **1999**, *59* (3), 1758–1775.

(72) Morales-Salvador, R.; Gouveia, J. D.; Morales-García, Á.; Viñes, F.; Gomes, J. R. B.; Illas, F. Carbon Capture and Usage by MXenes. *ACS Catal.* **2021**, *11* (17), 11248–11255.

(73) Henkelman, G.; Uberuaga, B. P.; Jónsson, H. Climbing Image Nudged Elastic Band Method for Finding Saddle Points and Minimum Energy Paths. *J. Chem. Phys.* **2000**, *113* (22), 9901–9904.

(74) Heyden, A.; Bell, A. T.; Keil, F. J. Efficient Methods for Finding Transition States in Chemical Reactions: Comparison of Improved Dimer Method and Partitioned Rational Function Optimization Method. *J. Chem. Phys.* **2005**, *123* (22), 224101.

(75) Momma, K.; Izumi, F. VESTA 3 for Three-Dimensional Visualization of Crystal, Volumetric and Morphology Data. *J. Appl. Crystallogr.* **2011**, *44* (6), 1272–1276.

(76) Sheng, W.; Gasteiger, H. A.; Shao-Horn, Y. Hydrogen Oxidation and Evolution Reaction Kinetics on Platinum: Acid vs Alkaline Electrolytes. *J. Electrochem. Soc.* **2010**, *157* (11), B1529.

(77) Ledezma-Yanez, I.; Wallace, W. D. Z.; Sebastián-Pascual, P.; Climent, V.; Feliu, J. M.; Koper, M. T. M. Interfacial Water Reorganization as a PH-Dependent Descriptor of the Hydrogen Evolution Rate on Platinum Electrodes. *Nat. Energy* **2017**, *2* (4), 17031.

(78) Brülle, T.; Schneider, O.; Stimming, U. Fundamental Investigation of the HER on a Pt(111) Surface at Temperatures down to 120K. *Zeitschrift fur Phys. Chemie* **2012**, *226* (9–10), 919–934.

(79) Parsons, R. General Equations for the Kinetics of Electrode Processes. *Trans. Faraday Soc.* **1951**, *47*, 1332–1344.

(80) Tafel, J. Über Die Polarisation Bei Kathodischer Wasserstoffentwicklung. *Zeitschrift für Phys. Chemie* **1905**, *50*, 641–712.

(81) Exner, K. S. Why the Microkinetic Modeling of Experimental Tafel Plots Requires Knowledge of the Reaction Intermediate's Binding Energy. *Electrochem. Sci. Adv.* **2021**, *2* (4), e2100037.

(82) Exner, K. S.; Sohrabnejad-Eskan, I.; Over, H. A Universal Approach to Determine the Free Energy Diagram of an Electrocatalytic Reaction. *ACS Catal.* **2018**, *8* (3), 1864–1879.

(83) Nørskov, J. K.; Rossmeisl, J.; Logadottir, A.; Lindqvist, L.; Kitchin, J. R.; Bligaard, T.; Jónsson, H. Origin of the Overpotential for Oxygen Reduction at a Fuel-Cell Cathode. *J. Phys. Chem. B* **2004**, *108* (46), 17886–17892.

(84) Zeradjanin, A. R.; Grote, J. P.; Polymeros, G.; Mayrhofer, K. J. J. A Critical Review on Hydrogen Evolution Electrocatalysis: Re-Exploring the Volcano-Relationship. *Electroanalysis* **2016**, *28* (10), 2256–2269.

(85) Kronberg, R.; Laasonen, K. Reconciling the Experimental and Computational Hydrogen Evolution Activities of Pt(111) through DFT-Based Constrained MD Simulations. *ACS Catal.* **2021**, *11* (111), 8062–8078.

(86) Morales-García, Á.; Mayans-Llorach, M.; Viñes, F.; Illas, F. Thickness Biased Capture of $CO_2$ on Carbide MXenes. *Phys. Chem. Chem. Phys.* **2019**, *21* (41), 23136–23142.

(87) Levy, R. B.; Boudart, M. Platinum-Like Behavior of Tungsten Carbide in Surface Catalysis. *Science*, **1973**, *181*, 547–549.

(88) Yoon, Y.; Tiwari, A. P.; Choi, M.; Novak, T. C.; Song, W.; Chang, H.; Zyung, T.; Lee, S. S.; Jeon, S.; An, K.-S. Precious-MetalFree Electrocatalysts for Activation of Hydrogen Evolution with Nonmetallic Electron Donor: Chemical Composition Controllable Phosphorous Doped Vanadium Carbide MXene. *Adv. Funct. Mater*. **2019**, *29*, 1903443.

# Conclusions

In the present Thesis, several environmental applications of TMCs and MXenes were investigated using DFT simulations. In particular, due its current interest, the capture, storage, and activation properties of doped TiC, as well as the production and dissociation of hydrogen molecules *via* heterogeneous catalysis or electrocatalysis on so-called MXenes, were explored. Despite the fact that the findings of each research have previously been covered at the end of the respective section, the overall conclusions of the thesis are highlighted here.

Regarding the $CO_2$ capture, storage, and activation over of doped TiC, we highlight the following conclusions linked with the objectives presented at the Section 1.1, Motivation and Goals.

- It is discovered that the dopant influence on the geometric and electrical configurations is highly local. Calculations show that subsurface substitution is never preferable over doping at the very top layer of the surface. Dispersion impact has been proven to be consistent and to have an equal impact in both doped and undoped circumstances.

- The presence of a doping agent on the TiC(001) surface effects the $CO_2$ adsorption energy affecting its adsorption and desorption rates and, hence, affecting its CCS and CCU properties. Moreover, the TMs group shown

a correlation by the net charge of the dopant and the $\Delta E_{ads}$. However, the addition of the second group of dopants into that relation drops it dramatically. The results show a qualitative correlation between the net charge of the surface carbons comparing the doped and undoped systems with the $\Delta E_{ads}$. Therefore, the charge transfer is a key feature of the adsorption but not the only one.

- The structural distortion caused by the dopant play a major role. A correlation between the difference in atomic radii of the dopant and the Ti, $\Delta R$, outstand as a valuable relation, due to allow to screen a vast number of elements without carrying out a single DFT calculation.

- Regarding the systems doped by TMs, the results are expected to be extrapolated to other TMCs, if the TM-TiC have a enhanced adsorption energy, the pure TMC will show a higher adsorption that the pure TiC. In contrast, the reverse effect is also expected.

Regarding the study of hydrogen related reactions over MXenes both involving both gas-phase and electrocatalytical processes we highlight the following conclusions linked with the objectives presented at the Section 1.1, Motivation and Goals.

Regarding the gas-phase systems:

- The adsorption of atomic hydrogen, H and molecular hydrogen, $H_2$ over bare MXenes present opposite trends due to the difference in nature of both adsorptions. While the H is chemisorbed on the MXene surface, the $H_2$ remains physisorbed. Thus short range forces derived from the ionic forces will dominate for the H absorption while long range forces derived of the electrostatic potential over the MXene surface will governate the $H_2$ adsorption.

- According to *ab initio* thermodynamics and microkinetic modeling approaches, $Fe_2C$, $W_2N$, and $Mo_2C$ are promising hydrogenation catalysts

in the sense that the conditions under which the surface of these MXenes is only partially covered by hydrogen are within the thermal stability range of these materials and are similar to those commonly used in the chemical industry. Nonetheless, it is crucial to note that the predictions from *ab initio* thermodynamics lead to softer temperature conditions than the recently provided kinetic phase diagrams that account for the energy barriers necessary for atomic hydrogen to recombine and desorb. These distinctions are likely to be significant in other systems where the thermodynamic equilibrium takes longer than the chemical processes that the substance of interest is expected to stimulate.

Regarding the electrocatalytical systems:

- The Pourbaix Diagram is proven to be a useful and necessary tool to characterize the surface of any electrode, including the MXenes, under electrochemical conditions. We exemplified how the most thermodynamically preferred surface coverage in gas-phase conditions it might not be the same that in an aqueous environment. Moreover, we highlighted the necessity of choosing carefully the terminations considered as missing a probably coverage will lead to not accurate results.

- The Pourbaix Diagrams of the four MXenes evaluated, $Ti_2C$, $Ti_3C_2$, $Mo_2C$, and $V_2C$ illustrate that the common MXene termination $T_x = O$ employed in the vast majority of the theoretical studies of MXenes for HER is not the most thermodynamically preferred coverage under typical HER conditions, although it is for the ORR reaction. Alternative coverages based on the studied reaction as $T_x = H$, OH, or mixed terminaions must be considered.

- Despite the most thermdynamically stable surface coverage of $V_2C$ at optimum HER conditions is a mixed coverage of H and OH, when explicitly simulating $H_3O^+$ molecules, the surface become fully covered by OH, highlighting one important limitation of the Pourbaix Diagrams.

- Theoretical Tafel plots are proved to be a handful method to correlate the theoretical studies with the corresponding experimental studies of a given electrochemical reaction, both by the shape of the plot and the decay of the current density as a function of overpotential. Moreover we illustrated how the Tafel plots are constructed from their corresponding free energy diagrams and we stablish a relation between theis kinetic barriers with the rds and the slope of the theoretical Tafel plot.

- Despite the presence of available hydrogen on the $V_2C$ surface we show that it can not be used as a hydrogen source, and thus $V_2C$-H will be active for HER while $V_2C$-OH it will not. The Volmer Heyrovsky mechanism over $V_2C$ MXene is identified as the current mechanism for HER over $V_2C$ and by extension, probably over MXenes in general.

# List of Publications

All of the calculations, basic writting, and images were done by myself in all of the articles included in this Thesis. The final content was refined by discussing with the the rest of the authors.

## Part of this thesis:

**López, M.**, Broerick, L., Carey, J. J., Viñes, F., Nolan, M., Illas, F. Tuning Transition Metal Carbide Activity by Surface Metal Alloying: a Case Study on $CO_2$ Capture and Activation. *Phys. Chem. Chem. Phys.*, 2018, **20**, 22179–22186.

**López, M.**, Viñes, F., Nolan, M., Illas, F.Predicting the Effect of Dopants on $CO_2$ Adsorption in Transition Metal Carbides: Case Study on TiC (001). *Phys. Chem. C*, 2020, **124**, 15969–15976.

**López, M.**, Morales-García, Á., Viñes, F., Illas, F. Thermodynamics and Kinetics of Molecular Hydrogen Adsorption and Dissociation on MXenes: Relevance to Heterogeneously Catalyzed Hydrogenation Reactions. *ACS Catal.*, 2021, **11**, 12850–12857.

**López, M.**, Exner, S. K., Viñes, F., Illas, F. Computational Pourbaix Diagrams for MXenes: A Key Ingredient toward Proper Theoretical Electrocatalytic Studies. *Adv. Theory Simulations*, 2022, 2200217.

**López, M.**, Exner, S. K., Viñes, F., Illas, F. Theoretical Study of Mechanism of Hydrogen Evolution Reaction on the $V_2C$ MXenes: Thermodynamic and Kinetic Aspects. *Submitted to ACS Catalysis*, 2022.

## Other publications:

Flores-González, N., **López, M.**, Minafra, N., Bohnenberger, J., Viñes, F., Rudić, S., Krossing, I., Zeier, W. G., Illas, F., Gregory, D. H. Understanding the effect of lattice polarisability on the electrochemical properties of lithium tetrahaloaluminates, $LiAlX_4$ ( X = Cl, Br, I). *J. Mater. Chem. A*, 2022, **10**, 13467–13475.

**Appendix A:**

# Supporting Information for "Tuning Transition Metal Carbides Activity by Surface Metal Alloying:Case Study on $CO_2$ Capture and Activation"

# Tuning Transition Metal Carbides Activity by Surface Metal Alloying: Case Study on $CO_2$ Capture and Activation

Martí López-Berbel,[a] Luke Broderick, [b] John Carey, [b] Francesc Viñes, [a,*] Michael Nolan, [b*] and Francesc Illas[a]

[a] *Departament de Ciència de Materials i Química Fisica & Institut de Química Teòrica i Computacional (IQTCUB), Universitat de Barcelona, Martí i Franqués 1-11, 08028 Barcelona, Spain.*

[b] *Tyndall National Institute, University College Cork, Cork T12R5CP, Munster, Ireland.*

*Corresponding authors: francesc.vines@ub.edu, michael.nolan@tyndall.ie

**Contents**

**Table S1** Bader charges of all bare surfaces. $q^{sur}$ is the computed charge of surface carbons directly bound to the dopant. $q^{sub}$ is the computed charge on subsurface carbon. $q^{TM}$ is the computed charge of the doping transition metal atom. All values are given in *e*.

| Bare Surfaces | | | |
|---|---|---|---|
| Dopant | $q^{sur}$ | $q^{sub}$ | $q^{TM}$ |
| Ti | -1.70 | -1.81 | - |
| Cr | -1.58 | -1.64 | +1.31 |
| Hf | -1.74 | -1.90 | +2.03 |
| Mo | -1.59 | -1.61 | +1.41 |
| Nb | -1.66 | -1.76 | +1.72 |
| Ta | -1.70 | -1.81 | +1.91 |
| V | -1.64 | -1.73 | +1.56 |
| W | -1.63 | -1.72 | +1.69 |
| Zr | -1.68 | -1.85 | +1.78 |

**Table S2** Binding modes, and adsorption energies ($E_{ads}$) with and without van der Waals corrections (vdW), as obtained PBE-D3, as well as geometry parameters, including $CO_2$ angle, C-C bond distances, *d*(C-C), and $CO_2$ molecule C-O bond distances, *d*(C-O).

| $CO_2$ Adsorption | | | | | | |
|---|---|---|---|---|---|---|
| Dopant | Binding Mode | $E_{ads}$ (eV) | $E_{ads}$ vdW (eV) | $CO_2$ angle (º) | d(C-C) (Å) | d(C-O) (Å) |
| Ti | TopC | -0.61 | -0.87 | 127.5 | 1.48 | 1.29 |
| | TopC-adj | | | | | |
| | MMC | -0.63 | -0.89 | 122.5 | 1.49 | 1.30 |
| Cr | TopC | -0.18 | -0.47 | 126.2 | 1.51 | 1.25,1.32 |
| | TopC-adj | -0.62 | -0.90 | 128.0 | 1.49 | 1.28 |
| | MMC | -0.23 | -0.55 | 122.5 | 1.49 | 1.30,1.29 |
| Hf | TopC | -0.96 | -1.20 | 126.0 | 1.49 | 1.28,1.30 |
| | TopC-adj | -0.56 | -0.81 | 126.9 | 1.48 | 1.29 |
| | MMC | -0.81 | -1.06 | 122.1 | 1.50 | 1.29,1.30 |
| Mo | TopC | -0.18 | -0.45 | 127.8 | 1.49 | 1.29,1.28 |
| | TopC-adj | -0.39 | -0.67 | 128.4 | 1.50 | 1.28 |
| | MMC | -0.13 | -0.42 | 122.8 | 1.50 | 1.29 |
| Nb | TopC | -0.50 | -0.76 | 127.0 | 1.49 | 1.28,1.29 |
| | TopC-adj | -0.40 | -0.67 | 127.8 | 1.49 | 1.29 |
| | MMC | -0.42 | -0.68 | 122.4 | 1.50 | 1.29,1.30 |
| Ta | TopC | -0.57 | -0.83 | 127.1 | 1.49 | 1.28,1.30 |
| | TopC-adj | -0.36 | -0.61 | 128.0 | 1.50 | 1.29 |
| | MMC | -0.52 | -0.78 | 122.1 | 1.50 | 1.29,1.30 |
| V | TopC | -0.28 | -0.55 | 128.2 | 1.48 | 1.29,1.28 |
| | TopC-adj | -0.57 | -0.82 | 127.9 | 1.49 | 1.29 |
| | MMC | -0.36 | -0.63 | 122.6 | 1.49 | 1.30,1.29 |
| W | TopC | -0.22 | -0.48 | 128.0 | 1.48 | 1.28,1.29 |
| | TopC-adj | -0.31 | -0.57 | 128.6 | 1.50 | 1.28 |
| | MMC | -0.18 | -0.45 | 122.4 | 1.50 | 1.29,1.30 |
| Zr | TopC | -0.93 | -1.17 | 125.7 | 1.50 | 1.28,1.30 |
| | TopC-adj | -0.61 | -0.86 | 126.5 | 1.47 | 1.29 |
| | MMC | -0.74 | -0.98 | 122.3 | 1.50 | 1.29,1.30 |

**Table S3** Bader charges for all the studied surfaces with adsorbed $CO_2$ Here $q^{C\text{-}C}$ is the Bader charge of the surface C atom involved in the $CO_2$ adsorption.

| $CO_2$ adsorbed | | | | | | |
|---|---|---|---|---|---|---|
| Dopant | Binding Mode | $q^{surf}$ | $q^{C\text{-}C}$ | $q^{sub}$ | $q^{TM}$ | $q^{CO_2}$ |
| Ti | TopC | -1.67 | -1.40 | -1.81 | - | -0.82 |
| | TopC-adj | | | | | |
| | MMC | -1.65 | -1.33 | -1.83 | +1.81 | -0.86 |
| Cr | TopC | -1.54 | -1.33 | -1.64 | +1.35 | -0.76 |
| | TopC-adj | -1.54 | -1.34 | -1.61 | +1.29 | -0.78 |
| | MMC | -1.48 | -1.27 | -1.69 | +1.35 | -0.81 |
| Hf | TopC | -1.73 | -1.32 | -1.87 | +2.18 | -0.97 |
| | TopC-adj | -1.73 | -1.40 | -1.88 | +2.01 | -0.88 |
| | MMC | -1.72 | -1.37 | -1.88 | +2.16 | -0.90 |
| Mo | TopC | -1.56 | -1.31 | -1.65 | +1.55 | -0.83 |
| | TopC-adj | -1.55 | -1.30 | -1.58 | +1.38 | -0.85 |
| | MMC | -1.53 | -1.29 | -1.69 | +1.53 | -0.82 |
| Nb | TopC | -1.65 | -1.32 | -1.79 | +1.88 | -0.87 |
| | TopC-adj | -1.64 | -1.35 | -1.74 | +1.73 | -0.87 |
| | MMC | -1.62 | -1.32 | -1.81 | +1.84 | -0.85 |
| Ta | TopC | -1.69 | -1.35 | -1.84 | +2.12 | -0.88 |
| | TopC-adj | -1.68 | -1.35 | -1.78 | +1.93 | -0.89 |
| | MMC | -1.68 | -1.34 | -1.86 | +2.11 | -0.88 |
| V | TopC | -1.60 | -1.20 | -1.75 | +1.64 | -0.95 |
| | TopC-adj | -1.61 | -1.37 | -1.73 | +1.57 | -0.80 |
| | MMC | -1.57 | -1.30 | -1.79 | +1.65 | -0.83 |
| W | TopC | -1.60 | -1.34 | -1.68 | +1.76 | -0.82 |
| | TopC-adj | -1.60 | -1.31 | -1.62 | +1.60 | -0.85 |
| | MMC | -1.57 | -1.31 | -1.74 | +1.76 | -0.84 |
| Zr | TopC | -1.69 | -1.27 | -1.83 | +1.98 | -0.98 |
| | TopC-adj | -1.67 | -1.27 | -1.84 | +1.86 | -0.98 |
| | MMC | -1.68 | -1.34 | -1.84 | +1.97 | -0.88 |

**Fig. S1** Top view of the (3√2×3√2)R45º model, the $CO_2$ was adsorbed both in the shown position but the dopant was moved from Near to Far position. The carbon from the $CO_2$ is represented in light brown to contrast the carbons from the slab (dark brown).

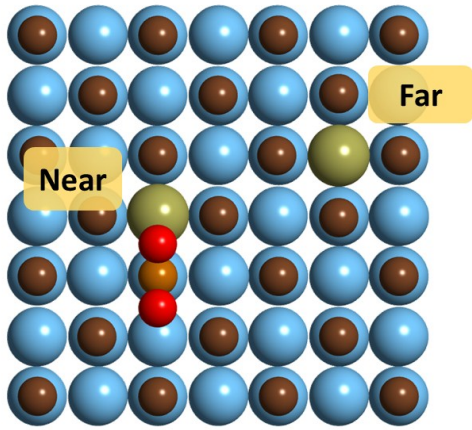

**Fig. S2** Top view of the slab model used to represent a higher coverage situation. Note that due to periodic symmetry, the $CO_2$ adsorbed at the four corners correspond to the same molecule.

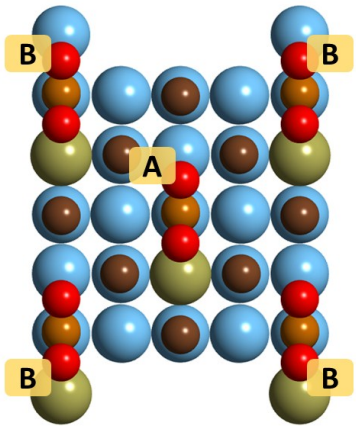

**Appendix B:**

# Supporting Information for "Predicting the Effect of Dopants on $CO_2$ Adsorption in Transition Metal Carbides: Case Study on TiC (001)"

# Supporting Information for

# Predicting the Effect of Dopants on $CO_2$ Adsorption on Transition Metal Carbides: Case Study on TiC (001)

Martí López,[†] Francesc Viñes,[†] Michael Nolan,[*,‡] and Francesc Illas[*,†]

[†] *Departament de Ciència de Materials i Química Física & Institut de Química Teòrica i Computacional (IQTCUB), Universitat de Barcelona, c/ Martí i Franqués 1-11, Barcelona 08028, Spain.*

[‡] *Tyndall National Institute, Lee Maltings, University College Cork, Cork T12R5CP, Ireland.*

*Corresponding authors: francesc.vines@ub.edu, michael.nolan@tyndall.ie

The Supporting Information contains the following

Table S1: Views of the atomic structure of the most favourable adsorption modes of $CO_2$ on doped TiC (001)

Table S2: Valence electron configurations for the dopants studied in this work

**Table S1.** Side and top views of the relaxed structures for the most favourable $CO_2$ adsorption mode for each dopant. Ti, C, and O atoms are represented by blue, brown, and red spheres, respectively, whereas the dopant is coloured differently for each dopant.

| **$CO_2$ adsorbed relaxed structures** | | |
|---|---|---|
| Undoped | Side view | Top view |
| | 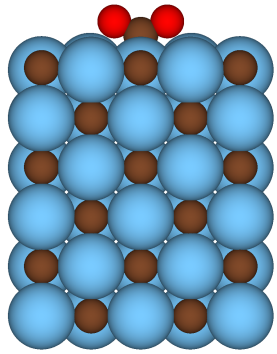 | 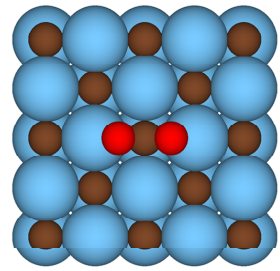 |

| Dopant | Clean doped surface | $CO_2$ adsorbed on doped surface |
|---|---|---|
| Mg | 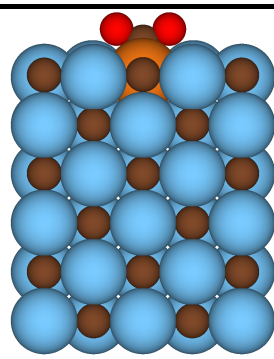 | 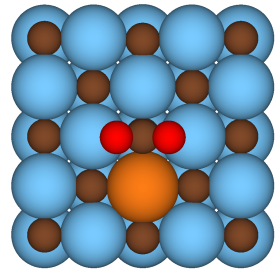 |

Ca

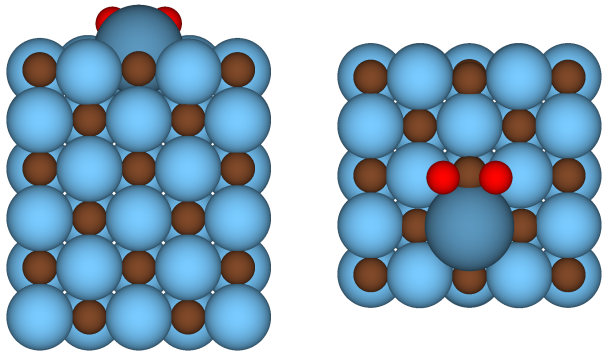

Sr

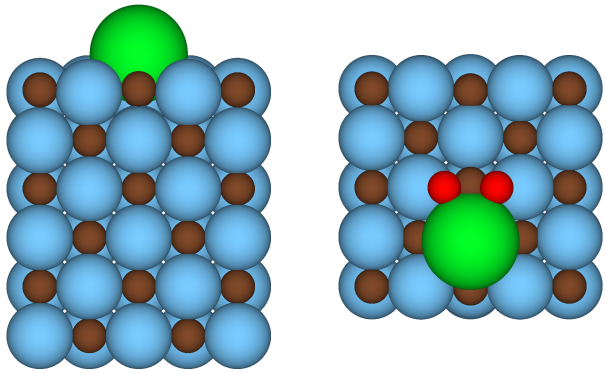

Al

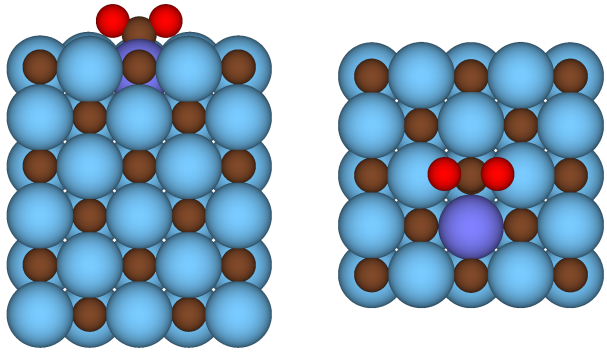

Ga

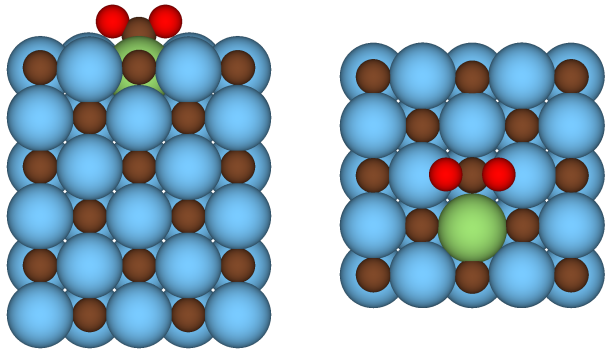

In

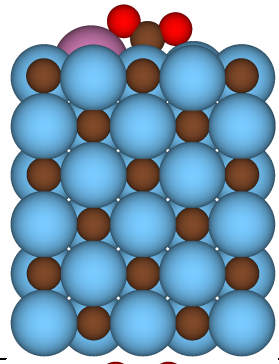

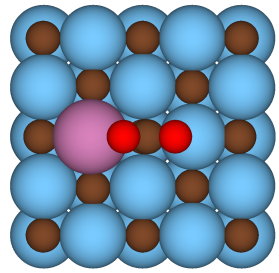

Si

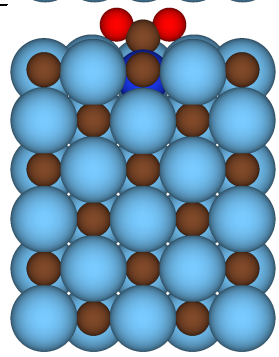

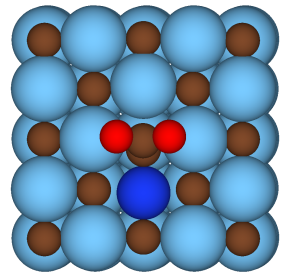

Sn

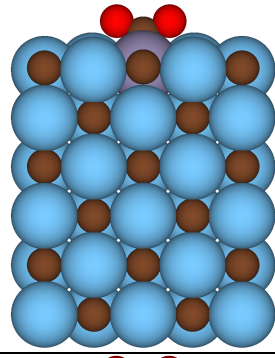

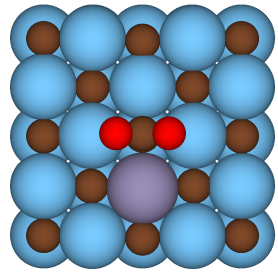

Rh

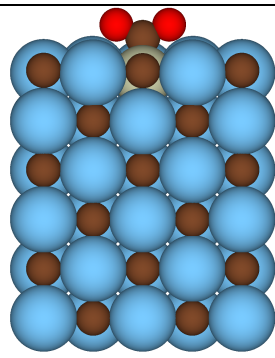

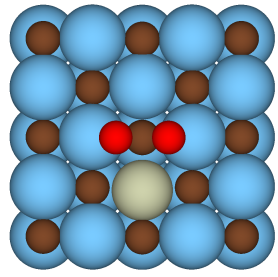

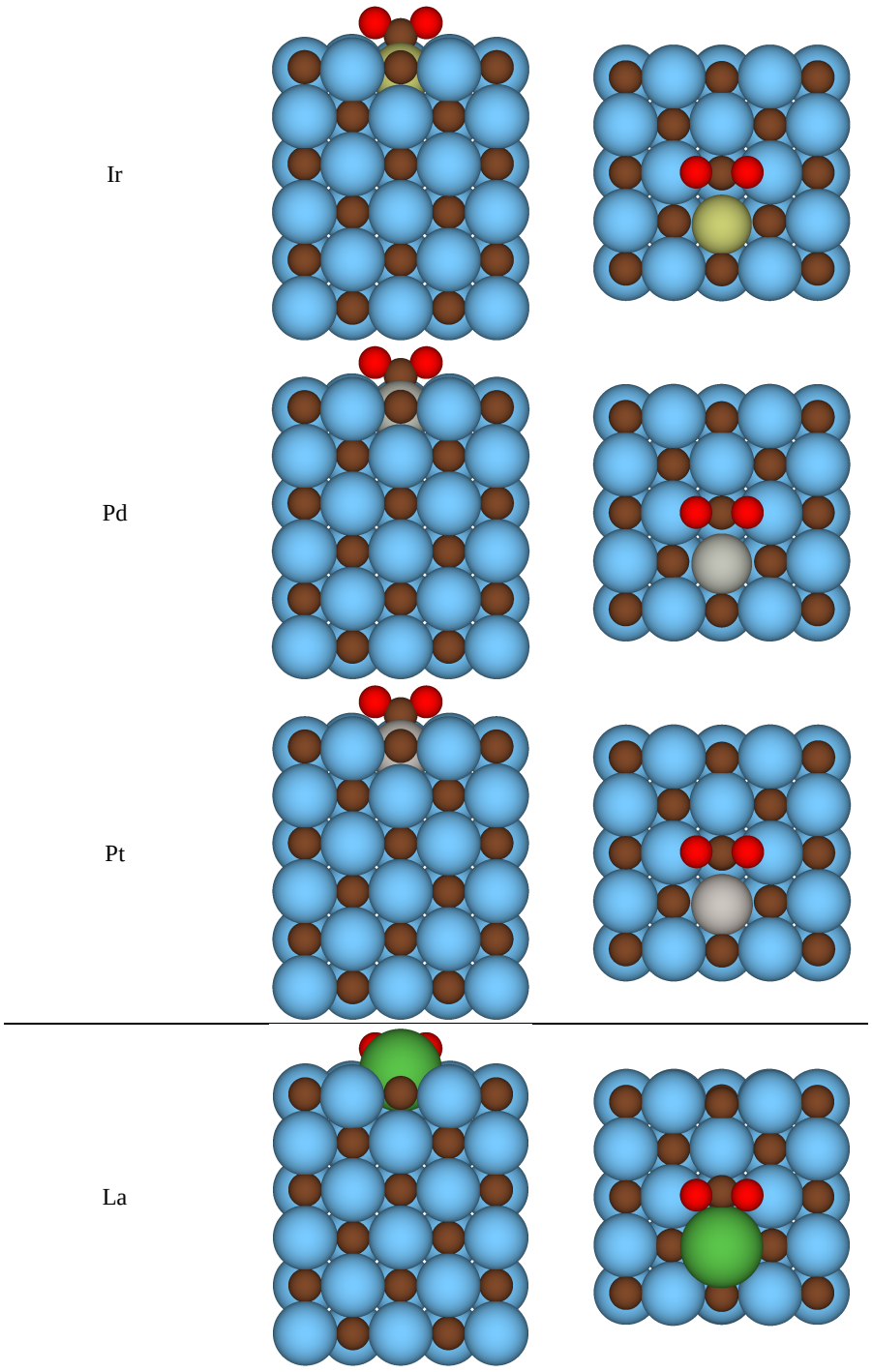
Ir
Pd
Pt
La

Ce

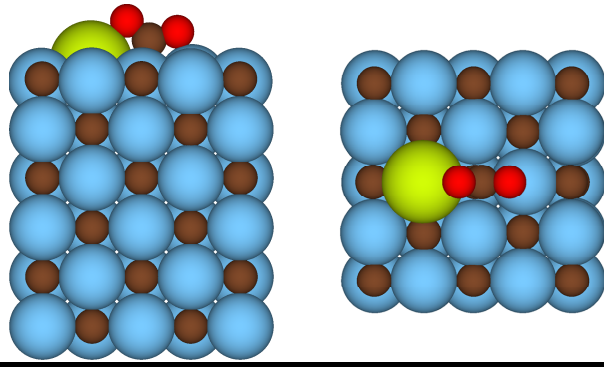

**Table S2.** Electronic configuration of the valence electrons of the employed PAWs used to carry out all the simulations.

| Element | Electronic configuration |
|---|---|
| Ti | $3p^6\ 3d^3\ 4s^1$ |
| C | $2s^2\ 2p^2$ |
| O | $2s^2\ 2p^4$ |
| Mg | $2p^6\ 3s^2$ |
| Ca | $3p^6\ 4s^2$ |
| Sr | $4s^2\ 4p^6\ 5s^2$ |
| Al | $2s^2\ 2p^6\ 3s^2\ 3p^1$ |
| Ga | $4s^2\ 3d^{10}\ 4p^1$ |
| In | $5s^2\ 4d^{10}\ 5p^1$ |
| Si | $2s^2\ 2p^6\ 3s^2\ 3p^2$ |
| Sn | $5s^2\ 4d^{10}\ 5p^2$ |
| Rh | $5s^1\ 4d^8$ |
| Ir | $6s^1\ 5d^8$ |
| Pd | $5s^1\ 4d^9$ |
| Pt | $6s^1\ 5d^9$ |
| La | $5s^2\ 6s^2\ 5p^2\ 5d^1$ |
| Ce | $5s^2\ 6s^2\ 5p^2\ 5d^1\ 4f^1$ |

**Appendix C:**

# Supporting Information for "Thermodynamics and Kinetics of Molecular Hydrogen Adsorption and Dissociation on MXenes: Relevance to Heterogeneously Catalyzed Hydrogenation Reactions"

# Thermodynamics and Kinetics of Molecular Hydrogen Adsorption and Dissociation on MXenes: Relevance to Heterogeneously Catalyzed Hydrogenation Reactions

Martí López, Ángel Morales-García, Francesc Viñes, Francesc Illas*

*Departament de Ciència de Materials i Química Física & Institut de Química Teòrica i Computacional (IQTCUB), Universitat de Barcelona, c/ Martí i Franquès 1-11, Barcelona 08028, Spain.*

*Corresponding author: francesc.illas@ub.edu

**Table of Contents**

**S1. Microkinetic simulations**

For all the studied MXenes, except for $Mn_2C$, $Mn_2N$, $Sc_2C$, $Sc_2N$, $Ti_2C$, and $Ti_2N$ (see below), the model studied consisted of two steps: $H_2 \leftrightarrow H_2^* \leftrightarrow 2{\cdot}H^*$, where $H_2^*$ and $H^*$ refer to adsorbed $H_2$ and H moieties, respectively. Thus, four kinetic constants are required: two for the forward reactions, two for the backward reactions. The forward and backward rate constants for $H_2^*$ dissociation were estimated from transition state theory as:

$$k = \frac{k_B T Q^{TS}}{h \quad Q} e^{-\frac{E_a}{k_B T}} \qquad \text{(S1)},$$

where $Q$ is the partition function for the reactants, which for an adsorbed situation includes only the vibrational partition function. The $Q^{TS}$ term is the partition function of the Transition State (*TS*), in which the imaginary vibration is neglected. Besides, $k_B$ is the Boltzmann constant, $h$ the Planck constant, and $E_a$ is the reaction step activation energy.

For $H_2$ adsorption, the rate has been estimated from the Hertz-Knudsen equation:

$$F = \frac{P}{\sqrt{2\pi m k_B T}} \qquad \text{(S2)},$$

where $m$ is the molecular weight. From Eq. S2 one can derive the molecular adsorption rate, expressed as:

$$k_{ads} = -\frac{pA'}{\sqrt{2\pi m k_B T}} S \qquad \text{(S3)},$$

where $p$ is the partial pressure for the molecular species and $S$ the sticking coefficient, assumed here to be a conservative value of 0.4. Finally, $A'$ is the surface area of a single adsorption site which is obtained dividing the supercell surface area by the number of equivalent sites for a given adsorption mode. Finally, for a free linear molecule, three rotational and two translational degrees of freedom are accounted for in the case of the desorption transition state, so that the desorption rate constant is calculated as:

$$k_{des} = \frac{k_B T^3 A' (2\pi k_B T)}{h^3 \quad \sigma \theta_{rot}} e^{-\frac{E_{des}}{k_B T}} \qquad \text{(S4)},$$

where σ is the symmetry number of $H_2$, and $\theta_{rot}$ the rotational temperature of $H_2$. For $Mn_2C$, $Mn_2N$, $Sc_2C$, $Sc_2N$, $Ti_2C$, $Ti_2N$, we assumed that the molecule dissociates as it adsorbs, simplifying the model to just one step, $H_2 \leftrightarrow 2{\cdot}H^*$. Hence, forward and backward rates are

not required, and Equations S3 and S4 were used instead for the adsorption and desorption rates.

To summarize, for the molecular adsorption of the $H_2$ molecule, and for $Mn_2C$, $Mn_2N$, $Sc_2C$, $Sc_2N$, $Ti_2C$, and $Ti_2N$ MXenes, where it was assumed that the molecule dissociates directly as it adsorbs (see above), the adsorption rate was estimated from the Hertz-Knudsen equation (Eqs. S2 and S3), and the desorption rate from transition state theory (TST) (Eq. S5). See in Tables S1 and S2 the employed parameters for the studied cases; see further details in Section S6.

**Table S1.** Parameters for the adsorption and desorption steps in $H_2$ dissociation.

| $M_2X$ | Adsorbate | A ($m^2$) | m (a. u.) | σ | $\theta_{rot}$ (K) | $E_{ads}$ (eV) |
|---|---|---|---|---|---|---|
| **$Fe_2C$** | $H_2$ | $8.05 \cdot 10^{-20}$ | 2 | 2 | 88.539 | 0.69 |
| **$W_2N$** | $H_2$ | $7.75 \cdot 10^{-20}$ | 2 | 2 | 88.539 | 0.87 |
| **$Ti_2C$** | $H_2$ | $9.52 \cdot 10^{-20}$ | 2 | 2 | 88.539 | 2.83* |
| **$Ti_2N$** | $H_2$ | $8.93 \cdot 10^{-20}$ | 2 | 2 | 88.539 | 2.89* |

*For those MXenes with no explicitly found $H_2$ adsorption we assumed $E_{ads}$ as $E_{ads}^{H_2} = E_{2H/MXene} - (E_{MXene} + E_{H_2})$

For the surface reaction, we used TST rates as in Eq. S1. The parameters needed to perform the microkinetic simulations are the pre-exponential factors for both forward, $\nu_f$, and backward, $\nu_b$, reaction steps, and the corresponding activation energies, again for forward, $E_f$, and backward, $E_b$, reaction steps as estimated from DFT calculations and including the zero point vibrational energy.

**Table S2.** Parameters for $H_2$ dissociation on $Fe_2C$ and $W_2N$ from the physisorbed state.

| $M_2X$ | Reaction | $\nu_f$ ($s^{-1}$) | $\nu_b$ ($s^{-1}$) | $E_f$ (eV) | $E_b$ (eV) |
|---|---|---|---|---|---|
| **$Fe_2C$** | $H_2$* ⇌ 2H* | $5.93 \cdot 10^{13}$ | $5.35 \cdot 10^{14}$ | 0.01 | 0.68 |
| **$W_2N$** | $H_2$* ⇌ 2H* | $2.03 \cdot 10^{13}$ | $2.91 \cdot 10^{11}$ | 0.01 | 0.80 |

## S2. Atomic and molecular hydrogen adsorption energies

**Table S3.** PBE-D3 adsorption energies, in eV, for atomic H on the $M_2X(0001)$ surfaces (X = C,N) calculated with respect the $\frac{1}{2}E_{H_2}$. All values include the ZPE contribution and involve the most stable $H_M$ site except for $La_2C$ which is $H_X$ site. Except for Mn- and Fe-based MXenes, the results correspond to spin unpolarized calculations.

| | $E_{ads}^{H}$ | |
|---|---|---|
| **M** | **$M_2C$** | **$M_2N$** |
| **Sc** | -1.20 | -1.21 |
| **Y** | -1.10 | -1.17 |
| **La** | -0.66 | -0.85 |
| **Ti** | -1.41 | -1.44 |
| **Zr** | -1.30 | -1.40 |
| **Hf** | -1.35 | -1.41 |
| **V** | -1.25 | -1.04 |
| **Nb** | -1.19 | -1.05 |
| **Ta** | -1.19 | -0.97 |
| **Cr** | -0.99 | -0.89 |
| **Mo** | -0.88 | -1.00 |
| **W** | -0.84 | -0.87 |
| **Mn** | -1.17 | -0.99 |
| **Fe** | -0.74 | -0.72 |

**Table S4.** PBE-D3 adsorption energies, in eV, for molecular hydrogen on the $M_2X(0001)$ surfaces (X = C, and N) calculated with respect the $E_{H_2}$. All values involve the most stable Top (T) site and include the ZPE contribution. Except for Mn- and Fe-based MXenes, the results correspond to spin unpolarized calculations.

| | $E_{ads}^{H_2}$ | |
|---|---|---|
| **M** | **$M_2C$** | **$M_2N$** |
| **Sc** | -0.01[a] | -0.01[a] |
| **Y** | -0.01 | -0.02 |
| **La** | -0.02 | -0.15 |
| **Ti** | -0.01[a] | -0.01[a] |
| **Zr** | -0.24 | -0.36 |
| **Hf** | -0.21 | -0.29 |
| **V** | -0.79 | -0.71 |
| **Nb** | -0.54 | -0.54 |
| **Ta** | -0.58 | -0.57 |
| **Cr** | -0.85 | -0.78 |
| **Mo** | -0.79 | -0.86 |
| **W** | -0.69 | -0.87 |
| **Mn** | -0.01[a] | -0.01[a] |
| **Fe** | -0.69 | -0.50 |

*An adsorption energy of -0.01 has been considered for such cases, given the fact that a spontaneous $H_2$ dissociation is observed upon relaxation.

**S3. Molecular hydrogen dissociation energy barriers and reaction energies**

**Table S5.** PBE-D3 calculated energy barriers, for both forward ($E_f$) and backward ($E_b$) reactions, in eV, for the elementary step from physisorbed $H_2$ to the dissociated state involving two vicinal (close in Table S7) H adatoms. All values include the ZPE contribution.

| | $E_f$ | | $E_b$ | |
|---|---|---|---|---|
| **M** | **$M_2C$** | **$M_2N$** | **$M_2C$** | **$M_2N$** |
| **Sc** | ~ 0.01 | ~ 0.01 | 2.41 | 2.50 |
| **Y** | ~ 0.01 | ~ 0.01 | 2.77 | 2.36 |
| **La** | 0.03 | ~ 0.01 | 1.83 | 1.63 |
| **Ti** | ~ 0.01 | ~ 0.01 | 2.84 | 2.90 |
| **Zr** | 0.16 | ~ 0.01 | 2.56 | 2.48 |
| **Hf** | 0.12 | ~ 0.01 | 3.37 | 2.55 |
| **V** | ~ 0.01 | 0.01 | 2.06 | 1.35 |
| **Nb** | 0.02 | 0.09 | 1.92 | 1.58 |
| **Ta** | 0.06 | 0.11 | 1.85 | 1.43 |
| **Cr** | ~ 0.01 | ~ 0.01 | 1.07 | 1.00 |
| **Mo** | ~ 0.01 | ~ 0.01 | 0.93 | 1.09 |
| **W** | ~ 0.01 | ~ 0.01 | 1.00 | 0.80 |
| **Mn** | ~ 0.01 | ~ 0.01 | 2.19 | 1.91 |
| **Fe** | ~ 0.01 | ~ 0.01 | 0.68 | 0.89 |

**Table S6.** PBE-D3 reaction energies for the elementary step from physisorbed $H_2$ to the dissociated state involving two vicinal (close in Table S7) H adatoms. All values in eV include the ZPE contribution.

| | $\Delta E_r$ | |
|---|---|---|
| **M** | **$M_2C$** | **$M_2N$** |
| **Sc** | -2.40 | -2.49 |
| **Y** | -2.76 | -2.35 |
| **La** | -1.80 | -1.62 |
| **Ti** | -2.83 | -2.89 |
| **Zr** | -2.40 | -2.47 |
| **Hf** | -3.25 | -2.54 |
| **V** | -2.05 | -1.34 |
| **Nb** | -1.90 | -1.50 |
| **Ta** | -1.78 | -1.32 |
| **Cr** | -1.06 | -0.99 |
| **Mo** | -0.94 | -1.08 |
| **W** | -0.99 | -0.83 |
| **Mn** | -2.18 | -1.90 |
| **Fe** | -0.71 | -0.88 |

**Table S7.** PBE-D3 adsorption energies, in eV, per H atom, for situations with 2 H adatoms adsorbed nearby (Close), or located far (Far) apart in the *p*(3×3)supercell model. The reference value for a single H adatom on the *p*(3×3) model (I) is given for comparison. The values in this table aim at showing that the interaction between the adsorbed H atoms is almost negligible. Consequently, they do not include the ZPE contribution.

| | $M_2C$ | | | $M_2N$ | | |
|---|---|---|---|---|---|---|
| **M** | **Close** | **Far** | **I** | **Close** | **Far** | **I** |
| **Sc** | -1.23 | -1.24 | -1.23 | -1.29 | -1.28 | -1.26 |
| **Y** | -1.12 | -1.13 | -1.12 | -1.22 | -1.22 | -1.21 |
| **La** | -0.67 | -0.68 | -0.66 | -0.90 | -0.85 | -0.87 |
| **Ti** | -1.46 | -1.45 | -1.46 | -1.51 | -1.50 | -1.50 |
| **Zr** | -1.37 | -1.35 | -1.34 | -1.46 | -1.44 | -1.45 |
| **Hf** | -1.41 | -1.40 | -1.40 | -1.47 | -1.46 | -1.47 |
| **V** | -1.29 | -1.30 | -1.30 | -1.07 | -1.08 | -1.09 |
| **Nb** | -1.24 | -1.26 | -1.24 | -1.07 | -1.07 | -1.09 |
| **Ta** | -1.24 | -1.26 | -1.25 | -1.00 | -1.01 | -1.03 |
| **Cr** | -1.00 | -1.00 | -1.03 | -0.95 | -0.96 | -0.95 |
| **Mo** | -0.90 | -0.91 | -0.91 | -1.03 | -1.01 | -1.05 |
| **W** | -0.90 | -0.93 | -0.91 | -0.90 | -0.91 | -0.93 |
| **Mn** | -1.14 | -1.16 | -1.22 | -1.00 | -1.00 | -1.04 |
| **Fe** | -0.74 | -0.72 | -0.78 | -0.73 | -0.72 | -0.77 |

**S4. Descriptors**

**Table S8.** Electrostatic potential, *V*, above the Top (T) and Hollow M ($H_M$) adsorption site for the studied MXenes, as considered for $H_2$ and H moieties, respectively. All values are given in eV.

| | *V* | | | |
|---|---|---|---|---|
| | $M_2C$ | | $M_2N$ | |
| **M** | $H_M$ | **T** | $H_M$ | **T** |
| **Sc** | -4.39 | -6.48 | -4.26 | -4.87 |
| **Y** | -4.23 | -7.85 | -3.36 | -8.59 |
| **La** | -1.68[a] | -8.23 | -1.53 | -7.66 |
| **Ti** | -2.76 | -5.47 | -3.08 | -5.59 |
| **Zr** | -2.70 | -7.00 | -3.77 | -8.95 |
| **Hf** | -3.52 | -7.63 | -3.04 | -7.38 |
| **V** | -2.61 | -4.91 | -2.63 | -4.60 |
| **Nb** | -2.99 | -6.96 | -2.57 | -6.41 |
| **Ta** | -2.90 | -7.98 | -2.65 | -7.45 |
| **Cr** | -2.43 | -3.79 | -2.54 | -5.96 |
| **Mo** | -2.12 | -6.72 | -1.65 | -4.87 |
| **W** | -2.40 | -7.22 | -2.62 | -5.78 |
| **Mn** | -2.78 | -6.21 | -1.36 | -6.33 |
| **Fe** | -2.65 | -6.10 | -2.76 | -5.78 |

[a] For $La_2C$, Hollow C has been regarded as most stable site.

**Table S9.** Average Bader charges at the MXenes surface metal atoms; *q*, in *e*.

| | *q* | |
|---|---|---|
| **M** | $M_2C$ | $M_2N$ |
| **Sc** | 1.20 | 1.02 |
| **Y** | 1.17 | 1.05 |
| **La** | 0.91 | 0.87 |
| **Ti** | 1.17 | 1.05 |
| **Zr** | 1.10 | 0.97 |
| **Hf** | 1.24 | 1.08 |
| **V** | 1.02 | 0.99 |

| | | |
|---|---|---|
| **Nb** | 0.96 | 0.90 |
| **Ta** | 1.10 | 0.99 |
| **Cr** | 0.84 | 0.71 |
| **Mo** | 0.76 | 0.68 |
| **W** | 0.72 | 0.74 |
| **Mn** | 0.99 | 0.93 |
| **Fe** | 0.82 | 0.82 |

**Table S10.** Linear fits to $p = a \cdot d + b$, where $p$ is the target property, either $E_{ads}$ of H or $H_2$, $E_{ads}^{H}$ or $E_{ads}^{H_2}$, respectively; $d$ is the employed descriptor, either $V$, or $q$; $a$ and $b$ are the linear regression slope and y-axis intercept, respectively; $R$ is the regression coefficient; *MAE* is the mean absolute error between the calculated data points and the predictions of the linear equations. Linear fits for MXenes with X = C or N are shown.

| ***d*** | ***p*** | **X** | ***a*** | ***b*** | ***R*** | ***MAE*** |
|---|---|---|---|---|---|---|
| ***V*** | $E_{ads}^{H}$ | **C** | 0.1615 | -0.6270 | 0.52 | 0.17 |
| | | **N** | 0.1547 | -0.6513 | 0.58 | 0.14 |
| | $E_{ads}^{H_2}$ | **C** | -0.1677 | -1.6245 | 0.72 | 0.19 |
| | | **N** | -0.1612 | -1.5899 | 0.81 | 0.15 |
| ***q*** | $E_{ads}^{H}$ | **C** | -1.0749 | -0.0154 | 0.79 | 0.11 |
| | | **N** | -1.1965 | 0.0220 | 0.71 | 0.13 |
| | $E_{ads}^{H_2}$ | **C** | 1.1533 | -1.6059 | 0.63 | 0.18 |
| | | **N** | 1.4349 | -1.7926 | 0.69 | 0.15 |

## S5. Phase diagrams for $Fe_2C$, $Ti_2C$ and $Ti_2N$

**Figure S1.** Thermodynamic phase diagram as a function of $T$ and $p_{H_2}$ for $Fe_2C$ (0001) MXenes including different atomic hydrogen coverages, $\theta_H$. It runs from 0 to 1 monolayer (ML). The black dashed line corresponds to a reference $p_{H_2}$ of 10 mbar.

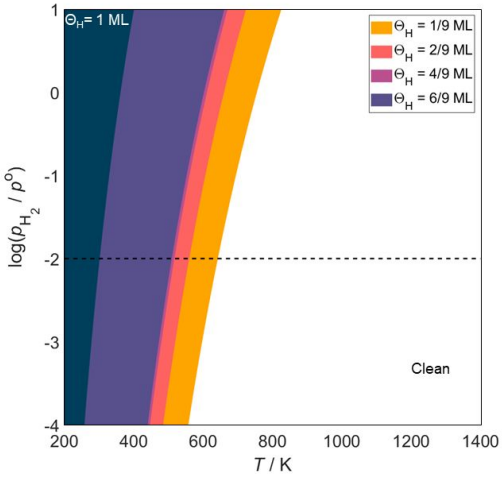

**Figure S2.** Thermodynamic phase diagram as a function of T and $p_{H_2}$ for $Ti_2C$ (0001) MXenes including different atomic hydrogen coverages, $\theta_H$. It runs from 0 to 1 monolayer (ML). The black dashed line corresponds to a reference $p_{H_2}$ of 10 mbar.

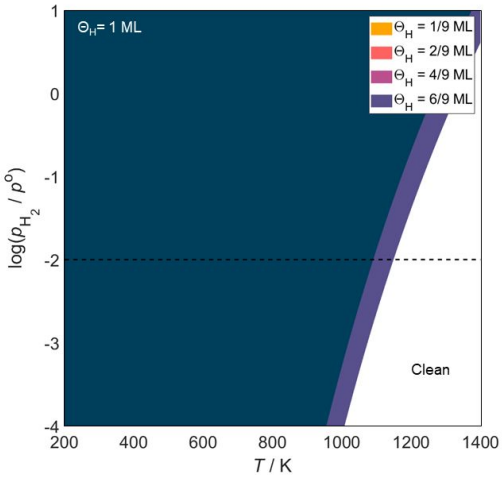

**Figure S3.** Thermodynamic phase diagram as a function of T and $p_{H_2}$ for $Ti_2N$ (0001) MXenes including different atomic hydrogen coverages, $\theta_H$. It runs from 0 to 1 monolayer (ML). The black dashed line corresponds to a reference $p_{H_2}$ of 10 mbar.

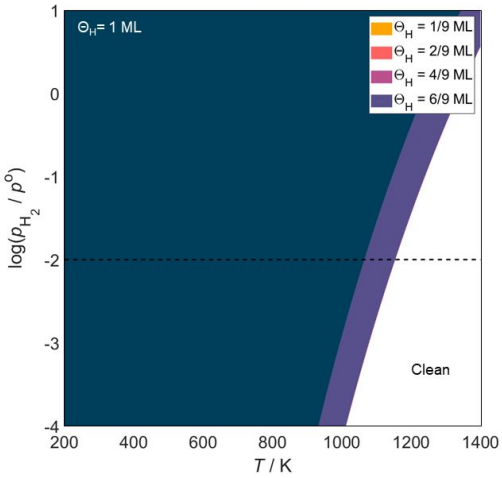

**S6. Selected results for kinetic phase diagrams**

**Table S11.** Range of temperatures, in K, for which the basal surface of $Fe_2C$, $W_2N$, $Ti_2C$, and $Ti_2N$ surface has a coverage of 0.2–0.6 ML of free sites, while the rest is covered with H adatoms. $p_{H_2}$ is given in mbar.

| | **$Fe_2C$** | | **$W_2N$** | | **$Ti_2C$** | | **$Ti_2N$** | |
|---|---|---|---|---|---|---|---|---|
| $p_{H_2}$ | **θ = 0.2** | **θ = 0.6** | **θ = 0.2** | **θ = 0.6** | **θ = 0.2** | **θ = 0.6** | **θ = 0.2** | **θ = 0.6** |
| **$10^{-1}$** | 535 | 600 | 646 | 729 | 1108 | 1775 | 1130 | 1265 |
| **1** | 575 | 650 | 694 | 783 | 1190 | 1344 | 1215 | 1370 |
| **10** | 620 | 707 | 745 | 852 | 1284 | 1463 | 1310 | 1488 |
| **50** | 658 | 756 | 792 | 908 | 1359 | 1559 | 1386 | 1589 |
| **$10^2$** | 675 | 779 | 812 | 934 | 1395 | 1606 | 1420 | 1635 |
| **$5 \cdot 10^2$** | 718 | 853 | 863 | 1000 | 1483 | 1720 | 1511 | 1752 |
| **$10^3$** | 740 | 860 | 887 | 1032 | 1524 | 1775 | 1555 | 1805 |
| **$10^4$** | 815 | 964 | 975 | 1150 | 1677 | 1980 | 1708 | 2016 |

**Appendix D:**

# Supporting Information for "Computational Pourbaix Diagrams for MXenes: A Key Ingredient toward Proper Theoretical Electrocatalytic Studies"

ADVANCED THEORY AND SIMULATIONS

# Supporting Information

for *Adv. Theory Simul.*, DOI 10.1002/adts.202200217

Computational Pourbaix Diagrams for MXenes: A Key Ingredient toward Proper Theoretical Electrocatalytic Studies

*Martí López, Kai S. Exner*, Francesc Viñes and Francesc Illas**

# Computational Pourbaix Diagrams for MXenes: A Key Ingredient towards Proper Theoretical Electrocatalytic Studies

Martí López,[1] Kai S. Exner,[2]* Francesc Viñes,[1] Francesc Illas[1]*

[1]*Departament de Ciència de Materials i Química Física & Institut de Química Teòrica i Computacional (IQTCUB), Universitat de Barcelona, c/ Martí i Franqués 1-11, Barcelona 08028, Spain.*

[2]*University Duisburg-Essen, Faculty of Chemistry, Theoretical Inorganic Chemistry Universitäts straße 5, Essen, 45141, Germany*

*Corresponding authors: francesc.illas@ub.edu , kai.exner@uni-due.de

**Table of Contents**

**S1. Adsorption free energies of adsorbates on $Mo_2C$, $V_2C$, $Ti_2C$, and $Ti_3C_2$**

**Table S1.** Calculated values of the adsorption free energies ($\Delta G$), given in eV, at 298.15 K and 1 bar, given in eV, and stoichiometric coefficients $v(H^+)$, $v(e^-)$, and $v(F^-)$ for the considered surface adsorbate structures on $Mo_2C$, referenced to the clean structure. For the views of the mixed coverages, we refer to Figure 2 of the main article. Coverages values are given as a fraction of a full monolayer (ML).

| **Structure** | | $\Delta G$ | $v(H^+)$ | $v(e^-)$ | $v(F^-)$ |
|---|---|---|---|---|---|
| Single Coverage | Clean | 0 | 0 | 0 | 0 |
| | 1/9 H | -0.70 | -1 | -1 | 0 |
| | 1/3 H | -2.05 | -3 | -3 | 0 |
| | 2/3 H | -3.82 | -6 | -6 | 0 |
| | 1 H | -5.19 | -9 | -9 | 0 |
| | 1/9 OH | -1.19 | 1 | 1 | 0 |
| | 1/3 OH | -2.85 | 3 | 3 | 0 |
| | 2/3 OH | -5.28 | 6 | 6 | 0 |
| | 1 OH | -6.96 | 9 | 9 | 0 |
| | 1/9 O | -1.52 | 2 | 2 | 0 |
| | 1/3 O | -4.93 | 6 | 6 | 0 |
| | 2/3 O | -8.74 | 12 | 12 | 0 |
| | 1 O | -11.9 | 18 | 18 | 0 |
| | 1/9 F | -3.73 | 0 | 1 | -1 |
| | 1/3 F | -11.33 | 0 | 3 | -3 |
| | 2/3 F | -22.54 | 0 | 6 | -6 |
| | 1 F | -33.13 | 0 | 9 | -9 |
| Mixed Coverage **A** | 1/3 O + 2/3 OH | -10.31 | 12 | 12 | 0 |
| | 2/3 O + 1/3 OH | -12.10 | 15 | 15 | 0 |
| | 1/3 O + 2/3 F | -26.21 | 6 | 12 | -6 |
| | 2/3 O +1/3 F | -19.37 | 12 | 15 | -3 |
| | 1/3 OH + 2/3 F | -25.46 | 3 | 9 | -6 |
| | 2/3 OH + 2/3 F | -16.99 | 6 | 9 | -3 |
| Mixed Coverage **B** | 1/3 O + 2/3 OH | -10.31 | 12 | 12 | 0 |

| | | | | | |
|---|---|---|---|---|---|
| | 2/3 O + 1/3 OH | -11.62 | 15 | 15 | 0 |
| | 1/3 O + 2/3 F | -26.19 | 6 | 12 | -6 |
| | 2/3 O + 1/3 F | -19.14 | 12 | 15 | -3 |
| | 1/3 OH + 2/3 F | -25.21 | 3 | 9 | -6 |
| | 2/3 OH + 1/3 F | -16.89 | 6 | 9 | -3 |
| Mixed Coverage **C** | 1/3 O + 2/3 OH | -10.29 | 12 | 12 | 0 |
| | 2/3 O + 1/3 OH | -11.76 | 15 | 15 | 0 |
| | 1/3 O + 2/3 F | -26.27 | 6 | 12 | -6 |
| | 2/3 O + 1/3 F | -19.16 | 12 | 15 | -3 |
| | 1/3 OH + 2/3 F | -25.30 | 3 | 9 | -6 |
| | 2/3 OH + 1/3 F | -16.88 | 6 | 9 | -3 |
| Mixed Coverage **D** | 1/3 O + 2/3 OH | -10.26 | 12 | 12 | 0 |
| | 2/3 O + 1/3 OH | -11.67 | 15 | 15 | 0 |
| | 1/3 O + 2/3 F | -26.25 | 6 | 12 | -6 |
| | 2/3 O + 1/3 F | -19.07 | 12 | 15 | -3 |
| | 1/3 OH + 2/3 F | -25.29 | 3 | 9 | -6 |
| | 2/3 OH + 1/3 F | -16.83 | 6 | 9 | -3 |

**Table S2.** Same as Table S1 for $V_2C$.

| Structure | | $\Delta G$ | $v(H^+)$ | $v(e^-)$ | $v(F^-)$ |
|---|---|---|---|---|---|
| Single Coverage | Clean | 0 | 0 | 0 | 0 |
| | 1/9 H | -1.05 | -1 | -1 | 0 |
| | 1/3 H | -3.13 | -3 | -3 | 0 |
| | 2/3 H | -5.87 | -6 | -6 | 0 |
| | 1 H | -8.30 | -9 | -9 | 0 |
| | 1/9 OH | -2.09 | 1 | 1 | 0 |
| | 1/3 OH | -6.07 | 3 | 3 | 0 |
| | 2/3 OH | -11.29 | 6 | 6 | 0 |
| | 1 OH | -15.12 | 9 | 9 | 0 |
| | 1/9 O | -2.68 | 2 | 2 | 0 |
| | 1/3 O | -8.23 | 6 | 6 | 0 |
| | 2/3 O | -14.54 | 12 | 12 | 0 |
| | 1 O | -18.65 | 18 | 18 | 0 |
| | 1/9 F | -4.60 | 0 | 1 | -1 |
| | 1/3 F | -14.15 | 0 | 3 | -3 |
| | 2/3 F | -28.02 | 0 | 6 | -6 |
| | 1 F | -40.76 | 0 | 9 | -9 |
| Mixed Coverage A | 1/3 O + 2/3 OH | -18.31 | 12 | 12 | 0 |
| | 2/3 O + 1/3 OH | -19.76 | 15 | 15 | 0 |
| | 1/3 O + 2/3 H | -12.60 | 0 | 0 | 0 |
| | 2/3 O + 1/3 H | -16.43 | 9 | 9 | 0 |
| | 1/3 O + 2/3 F | -34.68 | 6 | 12 | -6 |
| | 2/3 O + 1/3 F | -27.55 | -12 | -15 | 3 |
| | 1/3 OH + 2/3 H | -10.87 | -3 | -3 | 0 |
| | 2/3 OH + 1/3 H | -12.99 | 3 | 3 | 0 |
| | 1/3 OH + 2/3 F | -32.76 | 3 | 9 | -6 |
| | 2/3 OH + 1/3 F | -24.12 | 6 | 9 | -3 |
| | 1/3 H + 2/3 F | -29.79 | -3 | 3 | -6 |
| | 2/3 H + 1/3 F | -18.91 | -6 | -3 | -3 |

| | | | | | |
|---|---|---|---|---|---|
| Mixed Coverage B | 1/3 O + 2/3 OH | -17.97 | 12 | 12 | 0 |
| | 2/3 O + 1/3 OH | -19.24 | 15 | 15 | 0 |
| | 1/3 O + 2/3 H | -12.40 | 0 | 0 | 0 |
| | 2/3 O + 1/3 H | -16.01 | 9 | 9 | 0 |
| | 1/3 O + 2/3 F | -34.35 | 6 | 12 | -6 |
| | 2/3 O + 1/3 F | -27.09 | 12 | 15 | -3 |
| | 1/3 OH + 2/3 H | -10.85 | -3 | -3 | 0 |
| | 2/3 OH + 1/3 H | -12.98 | 3 | 3 | 0 |
| | 1/3 OH + 2/3 F | -32.58 | 3 | 9 | -6 |
| | 2/3 OH + 1/3 F | -23.99 | 6 | 9 | -3 |
| | 1/3 H + 2/3 F | -29.80 | -3 | 3 | -6 |
| | 2/3 H + 1/3 F | -19.04 | -6 | -3 | -3 |
| Mixed Coverage C | 1/3 O + 2/3 OH | -18.06 | 12 | 12 | 0 |
| | 2/3 O + 1/3 OH | -19.43 | 15 | 15 | 0 |
| | 1/3 O + 2/3 H | -12.44 | 0 | 0 | 0 |
| | 2/3 O + 1/3 H | -16.14 | 9 | 9 | 0 |
| | 1/3 O + 2/3 F | -34.47 | 6 | 12 | -6 |
| | 2/3 O + 1/3 F | -27.23 | 12 | 15 | -3 |
| | 1/3 OH + 2/3 H | -10.84 | -3 | -3 | 0 |
| | 2/3 OH + 1/3 H | -12.99 | 3 | 3 | 0 |
| | 1/3 OH + 2/3 F | -32.64 | 3 | 9 | -6 |
| | 2/3 OH + 1/3 F | -23.99 | 6 | 9 | -3 |
| | 1/3 H + 2/3 F | -29.82 | -3 | 3 | -6 |
| | 2/3 H + 1/3 F | -18.98 | -6 | -3 | -3 |
| Mixed Coverage D | 1/3 O + 2/3 OH | -17.88 | 12 | 12 | 0 |
| | 2/3 O + 1/3 OH | -19.32 | 15 | 15 | 0 |
| | 1/3 O + 2/3 H | -12.23 | 0 | 0 | 0 |
| | 2/3 O + 1/3 H | -16.09 | 9 | 9 | 0 |
| | 1/3 O + 2/3 F | -34.35 | 6 | 12 | -6 |
| | 2/3 O + 1/3 F | -27.11 | 12 | 15 | -3 |
| | 1/3 OH + 2/3 H | -10.79 | -3 | -3 | 0 |
| | 2/3 OH + 1/3 H | -13.06 | 3 | 3 | 0 |

| | | | | |
|---|---|---|---|---|
| 1/3 OH + 2/3 F | -32.61 | 3 | 9 | -6 |
| 2/3 OH + 1/3 F | -23.95 | 6 | 9 | -3 |
| 1/3 H + 2/3 F | -29.90 | -3 | 3 | -6 |
| 2/3 H + 1/3 F | -18.98 | -6 | -3 | -3 |

**Table S3.** Same as Table S1 for $Ti_2C$.

| Structure | | $\Delta G$ | $v(H^+)$ | $v(e^-)$ | $v(F^-)$ |
|---|---|---|---|---|---|
| Single Coverage | Clean | 0 | 0 | 0 | 0 |
| | 1/9 H | -1.22 | -1 | -1 | 0 |
| | 1/3 H | -3.65 | -3 | -3 | 0 |
| | 2/3 H | -7.46 | -6 | -6 | 0 |
| | 1 H | -10.93 | -9 | -9 | 0 |
| | 1/9 OH | -2.73 | 1 | 1 | 0 |
| | 1/3 OH | -7.63 | 3 | 3 | 0 |
| | 2/3 OH | -15.06 | 6 | 6 | 0 |
| | 1 OH | -22.20 | 9 | 9 | 0 |
| | 1/9 O | -3.42 | 2 | 2 | 0 |
| | 1/3 O | -9.90 | 6 | 6 | 0 |
| | 2/3 O | -19.05 | 12 | 12 | 0 |
| | 1 O | -23.35 | 18 | 18 | 0 |
| | 1/9 F | -5.46 | 0 | 1 | -1 |
| | 1/3 F | -16.07 | 0 | 3 | -3 |
| | 2/3 F | -32.63 | 0 | 6 | -6 |
| | 1 F | -48.82 | 0 | 9 | -9 |
| Mixed Coverage A | 1/3 O + 2/3 OH | -23.90 | 12 | 12 | 0 |
| | 2/3 O + 1/3 OH | -24.15 | 15 | 15 | 0 |
| | 1/3 O + 2/3 H | -15.71 | 0 | 0 | 0 |
| | 2/3 O + 1/3 H | -19.89 | 9 | 9 | 0 |
| | 1/3 O + 2/3 F | -41.00 | 6 | 12 | -6 |
| | 2/3 O + 1/3 F | -32.35 | 12 | 15 | -3 |
| | 1/3 OH + 2/3 H | -14.82 | -3 | -3 | 0 |
| | 2/3 OH + 1/3 H | -18.55 | 3 | 3 | 0 |
| | 1/3 OH + 2/3 F | -40.44 | 3 | 9 | -6 |
| | 2/3 OH + 1/3 F | -31.53 | 6 | 9 | -3 |
| | 1/3 H + 2/3 F | -35.97 | -3 | 3 | -6 |
| | 2/3 H + 1/3 F | -23.31 | -6 | -3 | -3 |

| | | | | | |
|---|---|---|---|---|---|
| Mixed Coverage B | 1/3 O + 2/3 OH | -23.67 | 12 | 12 | 0 |
| | 2/3 O + 1/3 OH | -23.95 | 15 | 15 | 0 |
| | 1/3 O + 2/3 H | -15.52 | 0 | 0 | 0 |
| | 2/3 O + 1/3 H | -19.61 | 9 | 9 | 0 |
| | 1/3 O + 2/3 F | -40.78 | 6 | 12 | -6 |
| | 2/3 O + 1/3 F | -32.28 | 12 | 15 | -3 |
| | 1/3 OH + 2/3 H | -14.81 | -3 | -3 | 0 |
| | 2/3 OH + 1/3 H | -18.54 | 3 | 3 | 0 |
| | 1/3 OH + 2/3 F | -40.34 | 3 | 9 | -6 |
| | 2/3 OH + 1/3 F | -31.46 | 6 | 9 | -3 |
| | 1/3 H + 2/3 F | -36.02 | -3 | 3 | -6 |
| | 2/3 H + 1/3 F | -23.41 | -6 | -3 | -3 |
| Mixed Coverage C | 1/3 O + 2/3 OH | -23.73 | 12 | 12 | 0 |
| | 2/3 O + 1/3 OH | -23.98 | 15 | 15 | 0 |
| | 1/3 O + 2/3 H | -15.54 | 0 | 0 | 0 |
| | 2/3 O + 1/3 H | -19.73 | 9 | 9 | 0 |
| | 1/3 O + 2/3 F | -40.83 | 6 | 12 | -6 |
| | 2/3 O + 1/3 F | -32.28 | 12 | 15 | -3 |
| | 1/3 OH + 2/3 H | -14.79 | -3 | -3 | 0 |
| | 2/3 OH + 1/3 H | -18.55 | 3 | 3 | 0 |
| | 1/3 OH + 2/3 F | -40.38 | 3 | 9 | -6 |
| | 2/3 OH + 1/3 F | -31.48 | 6 | 9 | -3 |
| | 1/3 H + 2/3 F | -36.02 | -3 | 3 | -6 |
| | 2/3 H + 1/3 F | -23.38 | -6 | -3 | -3 |
| Mixed Coverage D | 1/3 O + 2/3 OH | -23.61 | 12 | 12 | 0 |
| | 2/3 O + 1/3 OH | -23.89 | 15 | 15 | 0 |
| | 1/3 O + 2/3 H | -15.39 | 0 | 0 | 0 |
| | 2/3 O + 1/3 H | -19.70 | 9 | 9 | 0 |
| | 1/3 O + 2/3 F | -40.76 | 6 | 12 | -6 |
| | 2/3 O + 1/3 F | -32.20 | 12 | 15 | -3 |
| | 1/3 OH + 2/3 H | -14.77 | -3 | -3 | 0 |
| | 2/3 OH + 1/3 H | -18.58 | 3 | 3 | 0 |

| | | | | |
|---|---|---|---|---|
| 1/3 OH + 2/3 F | -40.36 | 3 | 9 | -6 |
| 2/3 OH + 1/3 F | -31.44 | 6 | 9 | -3 |
| 1/3 H + 2/3 F | -36.05 | -3 | 3 | -6 |
| 2/3 H + 1/3 F | -23.37 | -6 | -3 | -3 |

**Table S4.** Same as Table S1 for $Ti_3C_2$.

| Structure | | $\Delta G^O$ | $v(H^+)$ | $v(e^-)$ | $v(F^-)$ |
|---|---|---|---|---|---|
| Single Coverage | Clean | 0 | 0 | 0 | 0 |
| | 1/9 H | -1.11 | -1 | -1 | 0 |
| | 1/3 H | -3.43 | -3 | -3 | 0 |
| | 2/3 H | -6.98 | -6 | -6 | 0 |
| | 1 H | -10.24 | -9 | -9 | 0 |
| | 1/9 OH | -2.65 | 1 | 1 | 0 |
| | 1/3 OH | -7.62 | 3 | 3 | 0 |
| | 2/3 OH | -14.78 | 6 | 6 | 0 |
| | 1 OH | -21.12 | 9 | 9 | 0 |
| | 1/9 O | -3.23 | 2 | 2 | 0 |
| | 1/3 O | -9.90 | 6 | 6 | 0 |
| | 2/3 O | -18.82 | 12 | 12 | 0 |
| | 1 O | -21.91 | 18 | 18 | 0 |
| | 1/9 F | -5.39 | 0 | 1 | -1 |
| | 1/3 F | -16.11 | 0 | 3 | -3 |
| | 2/3 F | -32.34 | 0 | 6 | -6 |
| | 1 F | -48.10 | 0 | 9 | -9 |
| Mixed Coverage A | 1/3 O + 2/3 OH | -23.27 | 12 | 12 | 0 |
| | 2/3 O + 1/3 OH | -23.43 | 15 | 15 | 0 |
| | 1/3 O + 2/3 H | -15.37 | 0 | 0 | 0 |
| | 2/3 O + 1/3 H | -19.38 | 9 | 9 | 0 |
| | 1/3 O + 2/3 F | -40.66 | 6 | 12 | -6 |
| | 2/3 O + 1/3 F | -31.90 | 12 | 15 | -3 |
| | 1/3 OH + 2/3 H | -14.12 | -3 | -3 | 0 |
| | 2/3 OH + 1/3 H | -17.73 | 3 | 3 | 0 |
| | 1/3 OH + 2/3 F | -39.67 | 3 | 9 | -6 |
| | 2/3 OH + 1/3 F | -30.63 | 6 | 9 | -3 |
| | 1/3 H + 2/3 F | -35.31 | -3 | 3 | -6 |
| | 2/3 H + 1/3 F | -22.64 | -6 | -3 | -3 |

| | | | | | |
|---|---|---|---|---|---|
| Mixed Coverage B | 1/3 O + 2/3 OH | -22.97 | 12 | 12 | 0 |
| | 2/3 O + 1/3 OH | -23.06 | 15 | 15 | 0 |
| | 1/3 O + 2/3 H | -15.06 | 0 | 0 | 0 |
| | 2/3 O + 1/3 H | -18.86 | 9 | 9 | 0 |
| | 1/3 O + 2/3 F | -40.37 | 6 | 12 | -6 |
| | 2/3 O + 1/3 F | -31.53 | 12 | 15 | -3 |
| | 1/3 OH + 2/3 H | -14.12 | -3 | -3 | 0 |
| | 2/3 OH + 1/3 H | -17.71 | 3 | 3 | 0 |
| | 1/3 OH + 2/3 F | -39.56 | 3 | 9 | -6 |
| | 2/3 OH + 1/3 F | -30.56 | 6 | 9 | -3 |
| | 1/3 H + 2/3 F | -35.36 | -3 | 3 | -6 |
| | 2/3 H + 1/3 F | -22.75 | -6 | -3 | -3 |
| Mixed Coverage C | 1/3 O + 2/3 OH | -23.05 | 12 | 12 | 0 |
| | 2/3 O + 1/3 OH | -23.20 | 15 | 15 | 0 |
| | 1/3 O + 2/3 H | -15.12 | 0 | 0 | 0 |
| | 2/3 O + 1/3 H | -19.06 | 9 | 9 | 0 |
| | 1/3 O + 2/3 F | -40.46 | 6 | 12 | -6 |
| | 2/3 O + 1/3 F | -31.65 | 12 | 15 | -3 |
| | 1/3 OH + 2/3 H | -14.11 | -3 | -3 | 0 |
| | 2/3 OH + 1/3 H | -17.72 | 3 | 3 | 0 |
| | 1/3 OH + 2/3 F | -39.60 | 3 | 9 | -6 |
| | 2/3 OH + 1/3 F | -30.58 | 6 | 9 | -3 |
| | 1/3 H + 2/3 F | -35.35 | -3 | 3 | -6 |
| | 2/3 H + 1/3 F | -22.71 | -6 | -3 | -3 |
| Mixed Coverage D | 1/3 O + 2/3 OH | -22.91 | 12 | 12 | 0 |
| | 2/3 O + 1/3 OH | -23.09 | 15 | 15 | 0 |
| | 1/3 O + 2/3 H | -14.89 | 0 | 0 | 0 |
| | 2/3 O + 1/3 H | -18.97 | 9 | 9 | 0 |
| | 1/3 O + 2/3 F | -40.35 | 6 | 12 | -6 |
| | 2/3 O + 1/3 F | -31.54 | 12 | 15 | -3 |
| | 1/3 OH + 2/3 H | -14.07 | -3 | -3 | 0 |
| | 2/3 OH + 1/3 H | -17.75 | 3 | 3 | 0 |

| | | | | |
|---|---|---|---|---|
| 1/3 OH + 2/3 F | -39.57 | 3 | 9 | -6 |
| 2/3 OH + 1/3 F | -30.54 | 6 | 9 | -3 |
| 1/3 H + 2/3 F | -35.40 | -3 | 3 | -6 |
| 2/3 H + 1/3 F | -22.71 | -6 | -3 | -3 |

**Appendix E:**

# Supporting Information for "Thermodynamic and Kinetc Study of Hydrogen Evolution Reaction over $V_2C$, insights of HER mechanism"

# Theoretical Study of the Mechanism of the Hydrogen Evolution Reaction on the $V_2C$ MXene: Thermodynamic and Kinetic Aspects

Martí López,[1] Kai S. Exner,[2]* Francesc Viñes,[1]* Francesc Illas[1]

[1]*Departament de Ciència de Materials i Química Física & Institut de Química Teòrica i Computacional (IQTCUB), Universitat de Barcelona, c/ Martí i Franqués 1-11, Barcelona 08028, Spain.*

[2]*University Duisburg-Essen, Faculty of Chemistry, Theoretical Inorganic Chemistry, Universitätsstraße 5, 45141 Essen, Germany; Cluster of Excellence RESOLV, Bochum, Germany; Center for Nanointegration (CENIDE) Duisburg-Essen, Duisburg, Germany*

*Corresponding authors: francesc.vines@ub.edu, kai.exner@uni-due.de

**Table of Contents**

## S1. Hydrogen adsorption on $V_2C$-H

**Figure S1.** Top view of the $V_2C$-H (0001) MXene surface depicted as in Figure 1 from the main text. The two symmetrically different adsorptions sites, top and hollow C, are depicted in blue and orange, respectively.

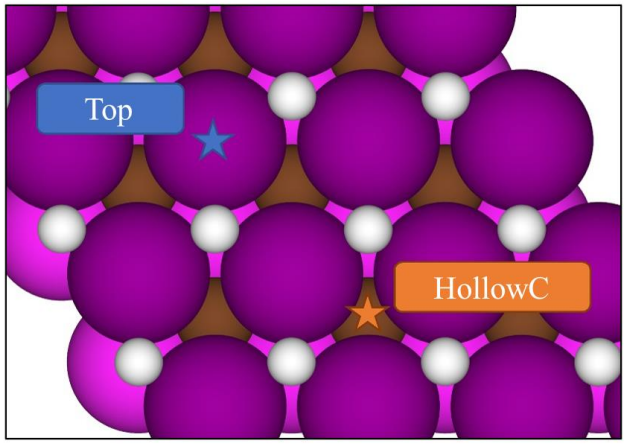

## S2. The case of $V_2C$-H

*Volmer Heyrovsky I*

**Figure S2.** Top view of the tested paths for the Volmer step of the VT-I mechanism over the $V_2C$-H (0001) MXene surface as depicted in Figure 1 of the main text. The nine indirect top adsorption sites corresponding to the adsorption of H1, H2, and H3 are indicated by blue, orange, and green circles respectively. Note that the green top sites a and b are duplicated in the present figure, but they correspond to the same site.

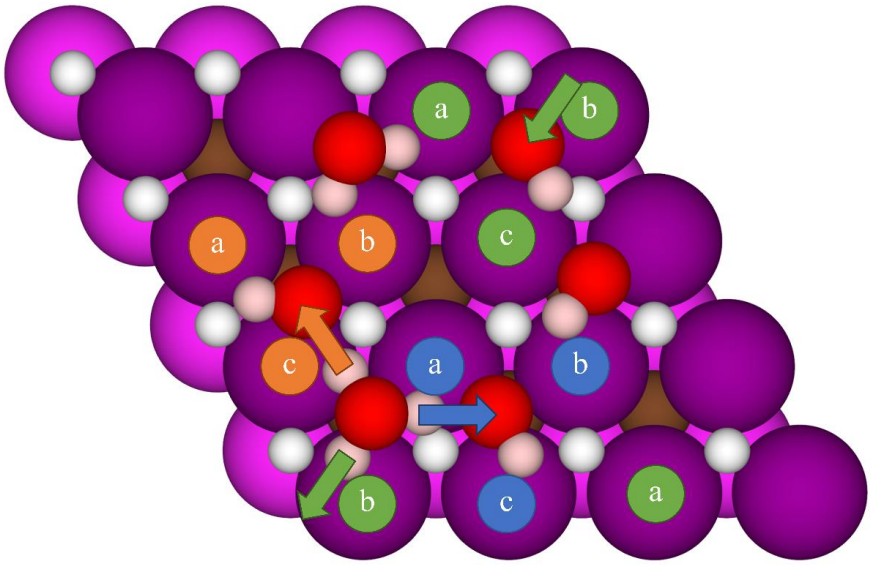

**Figure S3.** Top view of the tested pathways for the Volmer step of the VH-I mechanism over the $V_2C$-H (0001) MXene surface depicted as in Figure 1 of the main text. The three indirect hollow C adsorption sites corresponding to the adsorption of H1, H2, and H3 are labelled by blue, orange, and green circles, respectively. The circles are slightly shifted to avoid an overlapping with the upper oxygen atoms from the water layer.

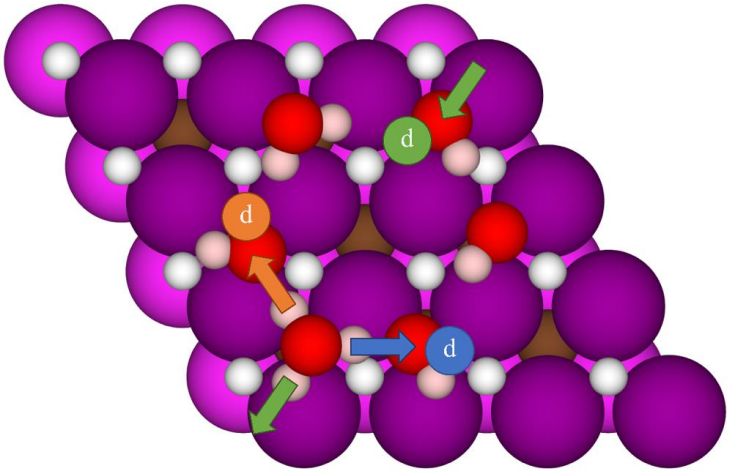


**Figure S4.** Top view of the tested pathways for the Volmer step of the VH-I mechanism over the $V_2C$-H (0001) MXene surface depicted as in Figure 1 of the main text. The three direct top adsorption sites corresponding to the adsorption of H1, H2, and H3 are labelled by blue, orange, and green circles, respectively. Direct adsorption at hollow C involves H1, H2, and H3 at the hollow C site below the oxygen atom where they are initially bond.

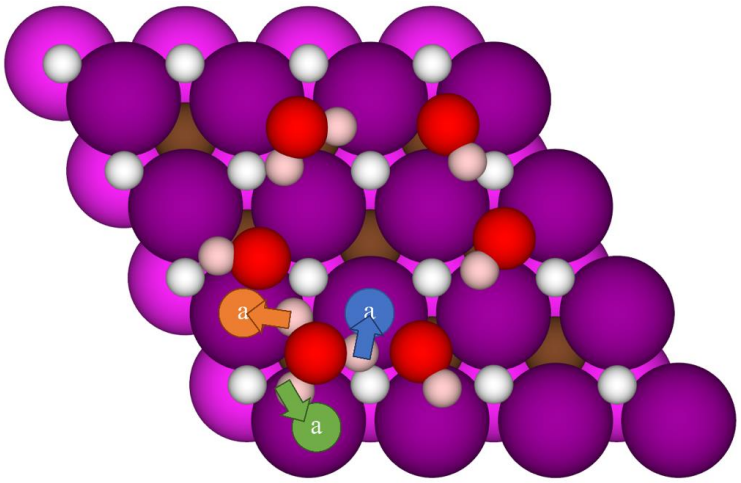

**Table S1.** Hydrogen adsorption free energies, $\Delta G_{ads}$ in eV, of the evaluated Volmer steps.

| Label | Direct/Indirect | Site | $\Delta G_{ads}$ |
|---|---|---|---|
| H1 (blue) | Indirect | Top a | -0.15 |
| | | Top b | 0.17 |
| | | Top c | -0.16 |
| | | Hollow C | 0.30 |
| | Direct | Top | -0.14 |
| | | Hollow C | 0.44 |
| H2 (orange) | Indirect | Top a | 0.19 |
| | | Top b | -0.03 |
| | | Top c | -0.17 |
| | | Hollow C | 0.32 |
| | Direct | Top | -0.11 |
| | | Hollow C | 0.32 |
| H3 (green) | Indirect | Top a | -0.04 |
| | | Top b | -0.15 |
| | | Top c | -0.11 |
| | | Hollow C | 0.30 |
| | Direct | Top | -0.20 |
| | | Hollow C | 0.40 |

## *Volmer Tafel I*

**Figure S5.** Top view of the tested pathways for the second Volmer step of the VT-I mechanism over the $V_2C$-H (0001) MXene surface as depicted in Figure 1 of the main text. The nine indirect top adsorption sites corresponding to the adsorption of H1, H2, and H3 are labelled by blue, orange, and green circles, respectively. Note that the green top sites a and b are duplicated in the present figure, but they correspond to the same exact site.

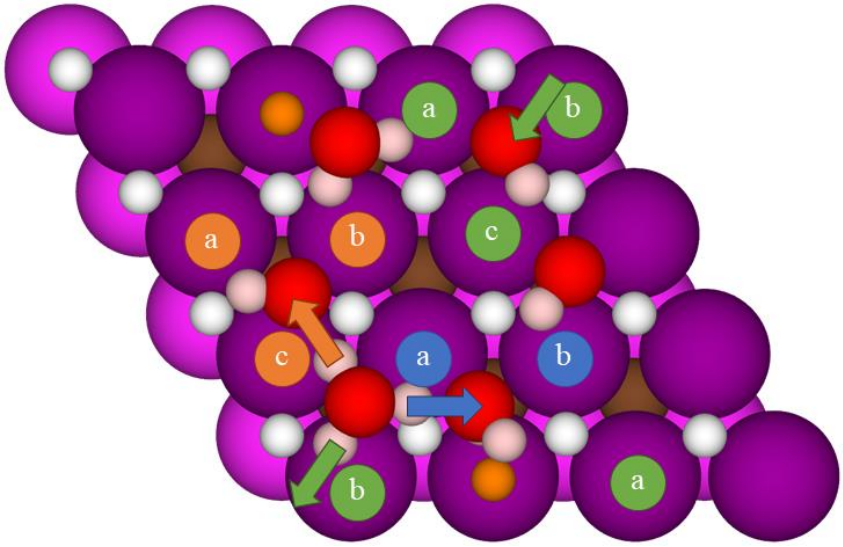

**Figure S6.** Top view of the tested pathways for the second Volmer Step of the VT-I mechanism over the $V_2C$-H (0001) MXene surface as depicted in Figure 1 of the main text. The three indirect hollow C adsorption sites corresponding to the adsorption of H1, H2, and H3 are labelled in blue, orange, and green circles, respectively. The circles are slightly shifted to avoid an overlapping with the upper oxygen atom from the water layer.

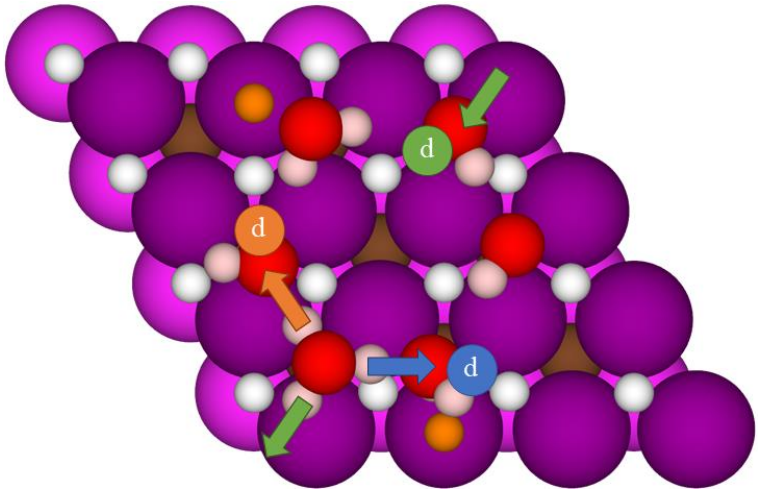


**Figure S7.** Top view of the tested pathways for the second Volmer step of the VT-I mechanism over the $V_2C$-H (0001) MXene surface as depicted in Figure 1 of the main text. The three direct top adsorption sites corresponding to the adsorption of H1, H2, and H3 are labelled by blue, orange, and green circles, respectively. Direct adsorption at hollow C involves H1, H2, and H3 at the hollow C site below the oxygen atom where they are initially bond

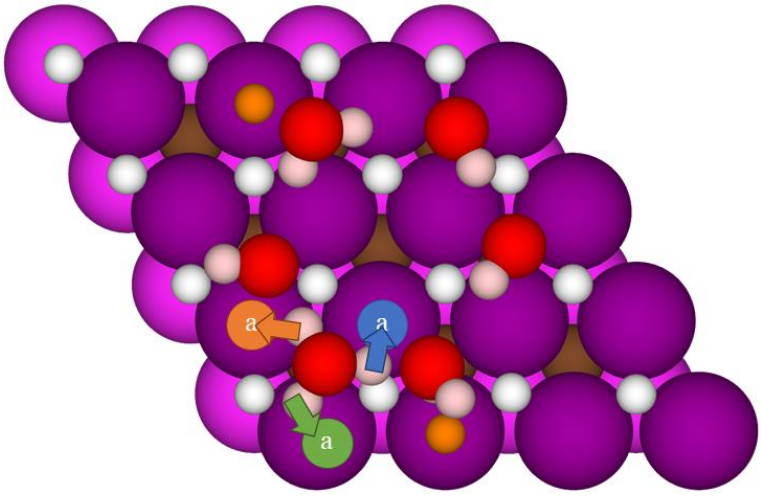

## S3. The case of $V_2C$-OH

*Volmer Heyrovsky II*

**Figure S8.** Top view of the tested pathways for the Heyrovsky step of the VH-II mechanism over the $V_2C$-H (0001) MXene surface as depicted in Figure 1 of the main text. The H atoms used to form the desired $H_2$ molecule are labelled by orange and green circles, respectively. The circles are slightly shifted to avoid an overlapping with the upper oxygen atom from the water layer.